2015

Structural and optical studies of GaAs1-xBix and p-Bi203 for optoelectronic devices

Julian Steele
University of Wollongong, js598@uowmail.edu.au

UNIVERSITY OF WOLLONGONG

AGREEMENT FOR DEPOSIT OF HDR THESIS IN DIGITAL REPOSITORY
KEY DETAILS

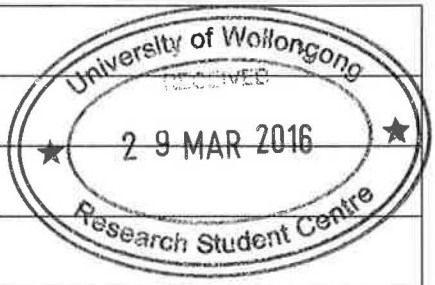

1.	Student Name	**Julian Andrew Steele**
2.	Student No	**3284864**
3.	Email address	**js598@uowmail.edu.au**
4.	School	**School of Physics**
5.	Faculty	**EIS**
6.	Supervisor	**Prof. Roger Lewis**
7.	Title of thesis	**Structural and Optical Studies of $GaAs_{1-x}Bi_x$ and β-Bi2O3 for Optoelectronic Devices**
8.	Keywords	phonons, III-V semiconductors, GaAsBi, Raman scattering, molecular beam epitaxy, high-index zincblende crystal, bismuth oxide, polymorphic
9.	*Field of Research (FoR) codes (optional) See explanation below	0204, 020504, 020403, 020406
10.	Restricted Access The University is committed to making HDR theses publicly available. If a restriction is required, please consult your supervisor prior to completing this section	Is a restriction required for this thesis, or part thereof? ☐ Yes ☒ No If Yes: a) Nominate restriction period: _____ months b) Provide details of the reason for the restriction: ☐ Publishing/patent ☐ Third party copyright ☐ Commercial /in confidence ☐ Other (please specify) _____
11.	Release of thesis automatically at the end of the expiry period (if applicable)	☒ Yes ☐ No (To ensure your thesis is deposited and accessible via the UOW digital repository at the expiry of the restriction period, tick Yes) If No, provide the reason why the thesis should not be released at the expiry of the restriction period. (Note: If you tick No, the Library will contact your supervisor at the end of the expiry period to request release of the thesis)
12.	Third party copyright material that has been used without consent (if applicable)	If the thesis contains material whose copyright belongs to a third party and has been used without consent: a) Would gaining consent to include the third party copyright material in the electronic copy of the thesis be onerous or expensive? ☐ Yes ☐ No b) Would removal of the copyright material compromise the thesis?

		☐ Yes ☐ No

***Field of Research (FoR)** code classifications are used in the measurement and analysis of research and experimental development (R&D) undertaken in Australia,according to the field of research. In this respect, it is the methodology used in the R&D that is being considered. UOW uses FoR codes to classify research outputs, and has been used to report research data to the Commonwealth Government.

The FoR has three hierarchical levels, namely Divisions (at the broadest subject or discipline level), Groups and Fields (at finer levels). Students submitting their HDR thesis have the option to classify their research using the Group level (4 digit code) or Field level (6 digit code). All Divisions, Groups and Fields are assigned unique codes.

TERMS & CONDITIONS

1. Definitions

1.1. In this Agreement:

"**Digital Repository**" means Research Online or any other open access electronic repository operated by UOW or its agents;

"**UOW**" means the University of Wollongong;

"**Work**" means the thesis you are depositing including any abstract, object, text, image and related data;

"**You**" means the Candidate identified in item 1 of the Key Details;

"Third party copyright" means any material where the copyright is owned by another person

2. Your warranties

2.1. You warrant that:

(a) all or part of the Work is your original work;

(b) the Work does not violate or infringe any copyright, trademark, patent other rights of any person;

(c) if you have used another person's copyright work or intellectual property rights:

(i) you have obtained permission from that person for the use of this material as contemplated by this agreement; or

(ii) you have confirmed in item 10 of the Key Details reasons you have not obtained permission to use or to grant to UOW the licence contemplated by this agreement;

(d) if the Work has been commissioned, sponsored or supported in any way, you have fulfilled all obligations required by such contract or agreement;

(e) the Work may be deposited in the Digital Repository without breaching the intellectual property rights of any third party provided UOW complies with any restrictions identified in items 8 and 9 of the Key Details.

3. UOW rights

3.1. You grant UOW a perpetual, non-exclusive, worldwide, royalty-free, sub-licensable licence to:

(a) deposit the Work in the Digital Repository;

(b) distribute copies of the Work (including the abstract) in electronic format;

(c) electronically store and copy the Work; and

(d) convert the Work to any format necessary for the preservation of the Work or the deposit on the Digital Repository.

3.2. UOW:

(a) may remove the Work from the Digital Repository for professional or administrative reasons at its sole discretion;

(b) is not under any obligation to take legal action on your behalf in the event breaches of your intellectual property rights stem from the deposit of the work in the Digital Repository;

(c) is not under any obligation to reproduce, transmit, broadcast or display the work in any particular format; and

(d) is not liable for any loss or damage to the Work whilst stored in the Digital Repository.

3.3. If you have used another person's copyright work without consent as identified under item 10 of the Key Details UOW may:

(a) remove this material from the Work and deposit in the Digital Repository;

(b) deposit only the metadata of the Work in the Digital Repository; or

(c) elect not to deposit the Work in the Digital Repository.

I declare my digital thesis is the final version approved by the University for the award of the degree.

Julian Steele
Student (candidate) signature

Prof. Roger Lewis
Supervisor signature

11/03/16
Date of student (candidate) signature

11/03/16
Date of supervisor signature

Structural and Optical Studies of $GaAs_{1-x}Bi_x$ and β-Bi_2O_3 for Optoelectronic Devices

Julian A. Steele

Bachelor of Science (Physics) (Honours Class I)

A dissertation submitted in fulfilment of the degree of
Doctor of Philosophy

UNIVERSITY OF
WOLLONGONG

School of Physics

2015

CERTIFICATION

I, Julian A. Steele, declare that this thesis, submitted in fulfilment of the requirements for the award of Doctor of Philosophy, in the School of Physics, Faculty of Engineering and Information Sciences, University of Wollongong, is wholly my own work unless otherwise referenced or acknowledged. The document has not been submitted for qualifications at any other academic institution.

Julian A. Steele
September 2015

For my parents...

Table of Contents

List of Tables

List of Figures

Structural and Optical Studies of $GaAs_{1-x}Bi_x$ and β-Bi_2O_3 for Optoelectronic Devices

Julian A. Steele

Abstract

In this thesis, the optical and structural properties of molecular beam epitaxy (MBE) grown dilute $GaAs_{1-x}Bi_x$/GaAs (001)- and (113)B-oriented heterostructures and the laser-induced oxidation dynamics and kinetics of bismuth are investigated.

A general method for determining the polarised Raman backscattering selection rules for an arbitrary (hhk)-oriented zincblende-type crystal surface is first presented, allowing for a full interpretation of the first-order Raman spectrum of strained (001) and (113)B $GaAs_{1-x}Bi_x$ alloys. The introduction of Bi in GaAs induces a two-mode behaviour (GaAs-like and GaBi-like phonon bands) and disorder-activated GaAs-like phonons. The optical mode peak frequencies decrease linearly for higher GaBi molar fractions, which introduce in-plane lattice strain $\varepsilon_{\parallel}$, causing the phonons to shift by $\Delta\omega = \Delta\omega_{\text{alloy}} + \Delta\omega_{\text{strain}}$. X-ray diffraction measurements are used to determine x and $\varepsilon_{\parallel}$, permitting $\Delta\omega_{\text{alloy}}$ to be decoupled.

The *nominally undoped* $GaAs_{1-x}Bi_x$ epitaxial alloys also reveal a Bi-induced (p-type) longitudinal-optical-plasmon-coupled (LOPC) mode for $0.018 \leq x \leq 0.048$. The relative integrated Raman intensities of LO(Γ) and LOPC $A_{\text{LO}}/A_{\text{LOPC}}$ are characteristic of heavily doped p-GaAs, with a remarkable near total screening of the LO(Γ) phonon ($A_{\text{LO}}/A_{\text{LOPC}} \to 0$) for larger Bi concentrations. A method of spectral analysis is set out which yields estimates of hole concentrations in excess of $5 \times 10^{17}\,\text{cm}^{-3}$ and correlates with the Bi molar fraction.

The MBE of GaAsBi is shown to experience the formation of Bi surface droplets which are able to catalyse nanostructures atop the epitaxial surface during growth, through vapour-liquid-solid (VLS) mechanism. In-plane nanotracks exhibiting lateral self-assembly and fascinating out-of-phase height variations across their growth axes are reported. Following a detailed morphological study, an explanation for their unusual shape is found to be beyond the capacity of existing planar growth models and more pertinent semi-empirical growth model is developed. A simulation of nanotrack formation based on the model yields excellent agreement with experiment. The microstructure and light producing properties of the nanostructures are also investigated.

The laser irradiation-induced oxidation of bismuth metal is studied *in situ* by micro-Raman spectroscopy under ambient conditions as a function of irradiation power and time. The purely optical synthesis and characterisation of β-Bi_2O_3 oxide microislands on metallic Bi surfaces is shown to be stable over time, even at room-temperature. By closely examining possible reactions on simple Bi morphologies it is revealed for the first time that the ensuing oxide phase is critically dependent on the final oxide volume and follows a fixed kinetic transformation sequence: $\frac{3}{2}O_2(\text{g}) + 2\text{Bi}(\text{l}) \to \beta\text{-}Bi_2O_3(\text{s}) \to \alpha\text{-}Bi_2O_3(\text{s})$. An electrostatic mechanism involving a changing Bi_2O_3 surface-to-volume ratio is proposed to explain the room-temperature metastability of small β-Bi_2O_3 volumes and the subsequent transformation sequence, as well as unifying the results of previous studies.

An understanding of the dynamical features of Bi_2O_3 phase stability at the nanoscale are then utilised in the controlled oxidation of bismuth surface microdroplets on top of a GaAsBi surface. A detailed Raman study of Bi microdroplet oxidation kinetics yields insights into the laser-induced oxidation process and offers useful real-time diagnostics. The temporal evolution of new β-Bi_2O_3 Raman modes is shown to be well described by Johnson-Mehl-Avrami-Kolmogorov kinetic transformation theory and while this work limits itself to the laser-induced oxidation of GaAsBi bismuth surface droplets, the results will find application within the wider context of bismuth laser-induced oxidation and direct Raman laser processing.

KEYWORDS: phonons, gallium arsenide, III-V semiconductors, GaAsBi, wide-bandgap semiconductors, Raman scattering, molecular beam epitaxy, high-index zincblende crystal, semiconductor epitaxial layers, bismuth oxide, polymorphic

Acknowledgements

This thesis would not have been possible without the guidance, support, advice, suggestions and help from many people during my time as an undergraduate and graduate student at the University of Wollongong – it has been a truly memorable journey!

Thanks to my principal supervisor Prof Roger Lewis for sharing his wisdom, distinguishing logic and developing me into a well-rounded researcher.

Thanks to my co-supervisor A/Prof Joseph Horvat for his keen eye for detail and great sense of humour.

I acknowledge also my fellow research students, for their support and friendship throughout my doctoral work.

Last, but definitely not least, I'm deeply in debt to my loving parents, Robyn and Ted, for teaching me the joy of scientific thinking. Thank you.

List of Publications

Publications arising from the work contained in this thesis are listed below. The following co-authors helped to grow the $GaAs_{1-x}Bi_x$/GaAs samples investigated: M. Henini, O. M. Lemine, A. Alkaoud, D. Fan, Yu. I. Mazur, V. G. Dorogan, P. C. Grant, S.-Q. Yu and G. J. Salamo. Co-authors R. A. Lewis and J. Horvat are respectively the principal supervisor and co-supervisor of my PhD research. M. Nancarrow assisted in performing some of the electron microscopy work. I designed, performed and analysed the experiments and simulations, as well as prepared the manuscripts for publication.

Peer-reviewed journal articles

1. Surface effects of vapor-liquid-solid driven Bi surface droplets formed during molecular-beam-epitaxy of GaAsBi
   J. A. Steele, R. A. Lewis, J. Horvat, M. J. B. Nancarrow, M. Henini, O. M. Lemine, D. Fan, Yu. I. Mazur, V. G. Dorogan, P. C. Grant, S.-Q. Yu and G. J. Salamo
   (Under Review at *Scientific Reports*).

2. Mechanism of periodic height variations along self-aligned VLS-grown planar nanostructures
   J. A. Steele, J. Horvat, R. A. Lewis, M. Henini, O. M. Lemine, D. Fan, Yu. I. Mazur, V. G. Dorogan, P. C. Grant, S.-Q. Yu and G. J. Salamo
   Nanoscale **7**, 20442 (2015).

3. Laser-induced oxidation kinetics of bismuth surface microdroplets on GaAsBi studied *in situ* by Raman microprobe analysis
   J. A. Steele and R. A. Lewis
   Optics Express **22**, 32261–32275 (2014).

4. *In situ* micro-Raman studies of laser-induced bismuth oxidation reveals metastability of β-Bi_2O_3 microislands
   J. A. Steele and R. A. Lewis
   Optical Materials Express **4**, 2133–2142 (2014).

5. Raman scattering reveals strong LO-phonon-hole-plasmon coupling in nominally undoped GaAsBi: optical determination of carrier concentration

J. A. Steele, R. A. Lewis, M. Henini, O. M. Lemine, D. Fan, Yu. I. Mazur, V. G. Dorogan, P. C. Grant, S.-Q. Yu and G. J. Salamo
Optics Express **22**, 11680–11689 (2014).

6. Raman scattering studies of strain effects in (100) and (311)B $GaAs_{1-x}Bi_x$ epitaxial layers
J. A. Steele, R. A. Lewis, M. Henini, O. M. Lemine and A. Alkaoud
Journal of Applied Physics **114**, 193516 (2013).

Peer-reviewed conferences/proceedings

1. Residual effects of vapor-liquid-solid mechanistic bismuth surface droplet formation during molecular beam epitaxy of GaAsBi
J. A. Steele, R. A. Lewis, M. Henini, O. M. Lemine, D. Fan, Yu. I. Mazur, V. G. Dorogan, P. C. Grant, S.-Q. Yu and G. J. Salamo
Talk presented at the 6th International Workshop on Bismuth-Containing Semiconductors, 2015, Madison, United States.

2. In Situ Micro-Raman Studies of Laser-Induced Bismuth Oxidation Dynamics and Kinetics: Application to GaAs(Bi) Photovoltaic Surface Engineering
J. A. Steele and R. A. Lewis
Talk presented at the 6th International Workshop on Bismuth-Containing Semiconductors, 2015, Madison, United States.

3. Residual microstructure effects of mobile bismuth surface droplets formed during MBE of GaAsBi
J. A. Steele, R. A. Lewis, M. Henini, O. M. Lemine, D. Fan, Yu. I. Mazur, V. G. Dorogan, P. C. Grant, S.-Q. Yu and G. J. Salamo
Poster presented at the 39th Annual Condensed Matter and Materials Meeting, 2015, Wagga Wagga, Australia. (Awarded Best Poster)

4. Raman scattering reveals Bi-induced effects in nominally undoped $GaAs_{1-x}Bi_x$
J. A. Steele, R. A. Lewis, M. Henini, O. M. Lemine, D. Fan, Yu. I. Mazur, V. G. Dorogan, P. C. Grant, S.-Q. Yu and G. J. Salamo
Talk presented at the 5th International Workshop on Bismuth-Containing Semiconductors, 2014, Cork, Ireland.

Abbreviations

AFM	atomic force microscopy
BEP	beam equivalent pressure
CB	conduction band
DALA	disorder-activated longitudinal acoustic
DATA	disorder-activated transverse acoustic
DATO	disorder-activated transverse optical
DFT	density functional theory
EDS	energy dispersive x-ray spectroscopy
IR	infrared
JMAK	Johnson-Mehl-Avrami-Kolmogorov
LO	longitudinal optical
LOPC	LO-phonon-plasmon-coupled
MBE	molecular beam epitaxy
ML	monolayer
PL	photoluminescence
PV	photovoltaic
SEM	scanning electron microscopy
SO	split-off band
TO	transverse optical
UHV	ultra high vacuum
UV	ultraviolet
VB	valence band
VLS	vapour-liquid-solid
XRD	x-ray diffraction

Chapter 1

Introduction and motivation

Over the past 50 years human life has been profoundly influenced by technological advances made in the field of semiconductor research. In particular, devices based on these materials have revolutionised the way we harness and utilise light; from telecom-

munications and information storage, to generating clean energy. Materials which are capable of producing and detecting infrared (IR) radiation have laid the optical foundations that power the internet and drive wireless communication, allowing for Wi-Fi, smart phones, solar cells and many other applications. Solid-state optoelectronic devices capable of efficiently generating light are significantly reducing the power consumption required to solve modern lighting solutions and photovoltaic solar cells − based on mixed crystal semiconductors − are positioned to play a central role in the production of clean energy well into the future. These examples of semiconductor alloy applications only begin to scratch the surface on what is currently commercially available, as well as technologies that are yet to be realised.

The endless conception of new applications for these materials is what motivates innovative semiconductor research; each application will necessitate specific material properties. As well as advancing and refining current device concepts, investigating new material systems reveal novel insights into solid-state physics, through state-of-the-art experimentation, and lay the path for the development of new technologies.

1.1 III-V alloys for devices operating in the near-infrared: a spectrum of choices

III-V semiconductors are alloys with elemental constituents derived from column III (boron family) and V (nitrogen family); these are shown in the inset of Fig. 1.1. Alloys made of just two elements constitute binary systems (e.g. GaAs), while three are called ternary (e.g. $GaAs_{1-x}N_{1-x}$) and of four elements are called quaternary (e.g. $Ga_{1-y}In_yAs_{1-x}N_x$), where $0 \leq x, y \leq 1$. The different chemical nature of the heavy and the light group III and V elements offer interesting properties through their alloying. A vast range of different alloys and their intermediates make it possible to

derive materials with highly tunable parameters, such as bandgap energy, bandgap type (direct or indirect), lattice parameter and other properties. In spite of the breadth of potential offered through the alloying of III-V semiconductors, the current palette of technological alloys remains limited, driving a continuing need to develop new materials that add flexibility to the design and performance of optoelectronic devices. III-V crystals have been extensively studied theoretically and experimentally during the last half century, with most studies dedicated to the first four row constituents (i.e. B, Al, Ga, In, N, P, As and Sb). III-V compound semiconductors have several distinct advantages over elemental semiconductors like Si. Namely, many III-V alloys exhibit relatively high carrier mobilities and often possess a direct bandgap. In terms of optoelectronic applications, a direct bandgap is critical for the efficient production (using less power) and absorption (allowing thinner active layers) of light.

The joining of two (or more) dissimilar materials forms what is known as a heterostructure, with the joining interface(s) forming the heterojunction(s). III-V optoelectronic device design relies heavily on the ability to synthesise layered sandwich-like structures with varying material properties; i.e. refractive index, fundamental bandgap, lattice parameter, band offsets and charge transport properties. III-V alloys commonly form a zincblende crystal structure and alloying a binary system with one or more other species from either of the III or V groups typically induces a smooth and tunable variation in the material properties, with changing composition. Of the properties of III-V alloys, the bandgap energy and lattice parameter are central to device design. Figure. 1.1 presents the bandgap energies vs the lattice parameter of many III-V alloys. As the large range of bandgap energies shows, the alloying of classic III-V materials into ternaries (and quaternaries) allows for controlled access to wavelengths spanning the ultraviolet (UV) to the IR. However, the lattice parameter of a layer in a heterostructured device severely restricts the composition of alloys that can be

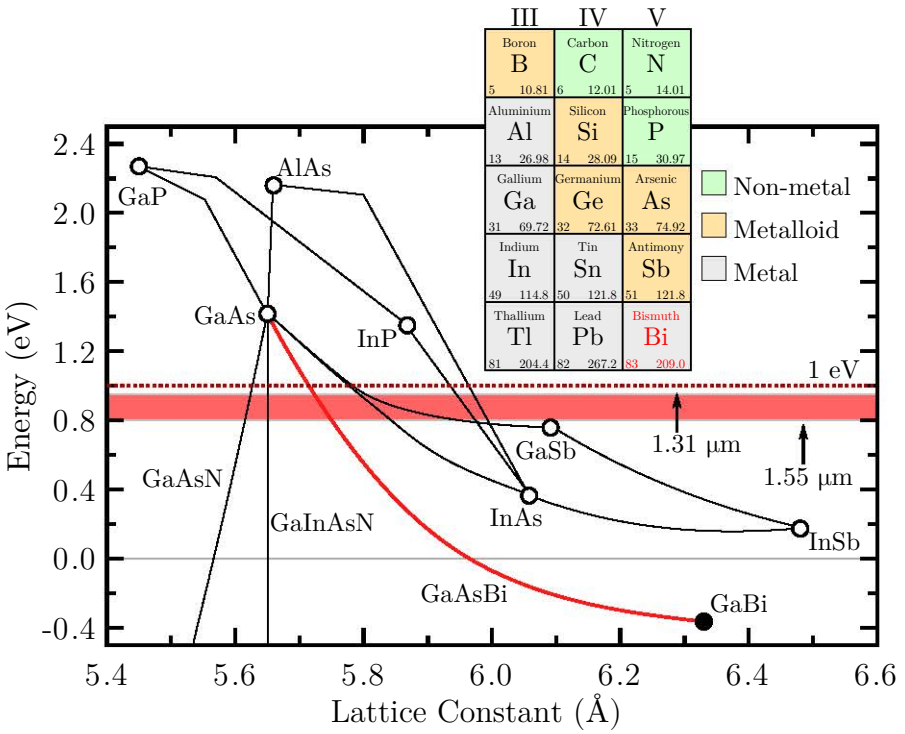

Figure 1.1: Bandgap energy as a function of lattice constant for various III-V alloys[1], including the $GaAs_{1-x}Bi_x$ system[2–4] (red line) experimentally predicted over the complete alloying range[2]. For convenience, the energy of the two IR telecom windows and the desirable 1 eV bandgap energy are also shown. The discontinuities in some of the ternary alloying curves are due to a shift in the type of bandgap exhibited by the semiconductors; direct $\longleftrightarrow$ indirect. The inset shows group III through V of the periodic table of the elements.

incorporated into adjoined layers, without suffering a significant reduction in material quality via strain relaxing dislocations.

In terms of efficiency and function, multi-junction solar cells represent the current highest performing class of commercial solar cells. The structures are composed of semiconductor diodes connected in series with multiple bandgaps to selectively absorb portions of the solar spectrum, to realise an improved fundamental efficiency over single bandgap cells[5]. Common commercial triple-junction cells are available employing differing multi-junction material schemes and efficiencies generally in excess of 40%[6–8]. Next generation high efficiency III-V multi-junction solar cells appear squarely centred around the development of a 1 eV bandgap semiconductor which is lattice matched

to GaAs[8]. Specifically, an optimal heterostructure has been proposed for realizing solar cell efficiencies higher than 50% with the sequential bandgaps of 0.7 eV/ 1.0 eV/ 1.4 eV/ 1.8 eV[9]. GaInP, GaAs and Ge are suitable lattice-matched semiconductors for the top, next to top, and bottom cells. But, until quite recently, there existed no materials lattice matched to GaAs with a bandgap of 1.0 eV.

For telecommunications, there are three main operating windows − relatively free from optical losses − for transporting data-carrying optical signals through optical fibres; light of wavelengths 0.85, 1.31 and 1.55 μm. Each of these wavelengths has its own advantages. For example, while the optical loss of the 0.85 μm operating window is relatively high at $\sim$ 1.8 dB/km, cheap GaAs lasers and Si detectors are well suited in this optical range. At a wavelength of 1.31 μm there is zero dispersion in the fibres with a smaller optical loss of 0.5 dB/km. This second window may seem very appealing, but for "long haul" optical fibre networks, the optical losses per km must be minimised. The 1.55 μm operating window only suffers an optical loss of 0.2 dB/km, making it the preferred window for sending optical signals over very long distances. Thus, semiconductors which efficiently emit and detect light at 1.31 and 1.55 μm wavelengths are vital for telecom technologies. Accessing wavelengths of 1.31 and 1.55 μm requires a direct bandgap of 0.95 and 0.8 eV, respectively, as well as being lattice-matched to readily available GaAs (or even InP) substrates.

Figure 1.1 summarises the different choices for III-V materials capable of operating in the 0.8 to 1 eV regime. Generally, the bandgap energy decreases as the lattice constant increases. Thus, it is difficult to find a III-V alloy with E_g between 0.8 and 1 eV and which is lattice-matched to GaAs. Considering the alloying relationships in Fig. 1.1, the dilute GaAsN system is a special case, in that its bandgap decreases as the lattice constant *decreases*. Adding In to form the $Ga_{1-y}In_yAs_{1-x}N_x$ system[10] is appealing due to the giant lowering in the bandgap[11] whilst retaining a lattice match

to GaAs. Due to this appealing character, the possibility of GaAsN-based materials for optoelectronic devices has been extensively explored in the past 15 years[12,13]. Unfortunately, even for very dilute nitrides, the large size and chemical mismatch between N and As leads to dramatic degradation to the carrier mobility[14], providing challenges for using these materials in device-quality electronics.

Involving larger physical and technical issues, proposals have been put forward for the introduction of GaAsBi-based materials to access light in the 0.8 to 1 eV range, due to its anomalously large reduction in bandgap energy (compared to alloying with other group V elements)[15,16] (see Fig.1.1). The incorporation of Bi into GaAs is difficult. Thus, GaAsBi has received far less attention than its lighter family members as a building block for III-V alloy semiconductors.

1.2 The dilute GaAsBi system and related materials for accessing the infrared

For decades researchers have been interested in III-V alloys containing bismuth for applications in long wavelength devices; for example alloys such as $InSb_{1-x}Bi_x$[17], $InAs_{1-x}Bi_x$[18] and $InAs_{1-y-x}Sb_yBi_x$[18]. This is because Bi inclusion reduces the bandgap energy of these already fairly narrow bandgap semiconductors (the approximate reduction rates are as follows: 55 meV/Bi% for the case of $InAs_{1-x}Bi_x$[18], 35 meV/Bi% for $InSb_{1-x}Bi_x$[19] and 46 meV/Bi% for $InSb_{1-x}Bi_x$[18]), extending the InSb wavelength to reach the 8 - 14 μm atmospheric window. These alloys were first grown using bulk growth techniques and were essentially limited by the low solid solubility of Bi (less than $\sim$3%[17]). In the 1980s, non-equilibrium growth techniques molecular beam epitaxy (MBE) and metalorganic vapour phase epitaxy (MOVPE) were used to grow better refined InSbBi, InAsBi and InAsSbBi mixed crystals, with

higher Bi content[20–22]. While an appealing reduction in bandgap was observed in these materials, the formation of InBi (and $InBi_2$) surface droplets presented significant problems for their applications[21,22]. The issues surrounding droplet formation likely prevented any significant further development of these alloys for optoelectronic devices and discouraged future investigations of III-V-Bi alloys.

Early investigations of $GaAs_{1-x}Bi_x$ semiconductors were motivated by the desire of producing a lasing material with a temperature insensitive bandgap[23]. Another motivation was the possibility to co-alloy bismuth with nitrogen in GaAs (GaAsBiN), in an attempt to lessen the N-induced degradation to the semiconductor transport properties[24]. It was proposed that alloying a semimetal − as many Bi-based compounds tend to be − with GaAs would result in a semiconductor exhibiting a bandgap energy with a reduced response to temperature[25]. Needless to say, such a material would have profound implications for devices striving to possess improved thermal stability.

The first successful growth of the GaAsBi alloy appeared in a report by Oe *et al.*[23] in 1998, employing MOVPE. Since 2003, the MBE technique has been used[2,26] to grow the material by many groups around the world. Like previous investigations of III-V-Bi materials, the difficulties associated with Bi inclusion required relatively low growth temperatures to be employed. Further, GaAsBi growth suffered from a similar presence of Bi-based surface droplets[27], again due to the relatively low miscibility of Bi in GaAs. Nonetheless, among the many promising properties of dilute $GaAs_{1-x}Bi_x$ alloys, an anomalously large Bi-induced bandgap reduction was recorded: $\sim$ 88 meV/Bi%[2,15,16]. This result alone warrants further considerations of how dilute GaAsBi can be applied to optoelectronic devices. Moreover, as the next section highlights, there are additional reasons to find interest in the dilute GaAsBi system for optoelectronic devices.

1.3 GaAsBi alloys for optoelectronic devices

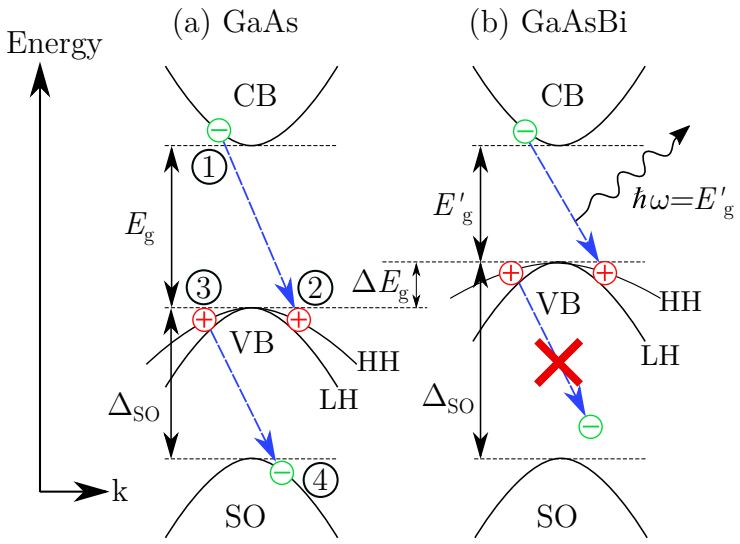

Figure 1.2: Modifications to GaAs band structure through Bi inclusion. (a) Schematic illustration of Auger recombination in the electronic band structure of GaAs: a conduction electron (1) recombines with a valence hole (2) and, instead of emitting a photon, provides the energy for a valence hole (3) to recombine with a spin split-off band (SO) electron (4). Specifically, the process depicted is a primary form of Auger recombination: conduction band to heavy hole band and spin-orbit split-off band to heavy hole band (CHSH Auger recombination). (b) Demonstration of how the Auger recombination mechanism is suppressed for $GaAs_{1-x}Bi_x$, which experiences most of the bandgap reduction from a lifting in the VB edge. In this case, the spin-orbit-splitting energy (Δ_{SO}) becomes lager than the bandgap (E_g), and the conservation of energy renders the Auger recombination forbidden.

The large bandgap reduction observed in $GaAs_{1-x}Bi_x$ with only a small inclusion of bismuth makes it very promising as the active region in many long wavelength devices[2,15,28,29]. For comparison, alloying GaAs with In and Sb only lowers the bandgap by 16 and 21 meV/%, respectively, while nitrogen incorporation induces a 125 meV/% shift in bandgap energy. For the case of alloying GaAsN, the dilute incorporation of nitrogen introduces a resonant state near the conduction band (CB) edge, which narrows the bandgap through a lowering of the CB edge energy[30,31]. The shift observed in GaAsBi is analogous to this, although the resonant state introduced by Bi atoms is near to, and pushes up on, the valence band edge[32–34] (further details

and explanation of this phenomena are given in Chapter 4). A schematic of band structure shifts seen in the $GaAs_{1-x}Bi_x$ system is presented in Fig. 1.2. Regarding the relative energy gap between the VB and spin split-off band (SO in Fig. 1.2 with an energy difference of Δ_{SO}), the Bi-induced modifications to GaAs include a "giant" spin-orbit bowing in the alloy[16].

Despite the low growth temperatures required to achieve Bi inclusion, GaAsBi epitaxial layers have demonstrated strong room-temperature photoluminescence (PL)[4]. Strong electroluminescence has also been shown in GaAsBi light emitting diodes[29] and electrically-pumped single quantum well lasers[37], and lasing has been realised in optically-pumped GaAsBi layers[38]. Efficient semiconductor light emission from telecom diodes are essential for reducing costs. Currently, InGaAsP/InP laser diodes are utilised for long haul telecom applications, for which the current threshold and the slope efficiency strongly vary as the temperature of the device increases[39,40]. A common form of electron-hole recombination experienced in III-V light emitting diodes is Auger recombination, in which electrons and holes recombine in a band-to-band transition but the energy released (nominally E_g) is used to excite another electron hole pair into the CB and VB. This effect is illustrated relative to the GaAs band structure in Fig. 1.2(a). The Auger recombination is a non-radiative process and, hence, considered a "loss". At room temperature, Auger losses account for approximately 50 % and 80 % of the threshold current density for InGaAsP laser operating at 1.31 and 1.55 μm, respectively[41].

Figure. 1.3 presents data for the E_g and Δ_{SO} dependence on Bi content, where alloying induces an increase in Δ_{SO} that is paralleled by a decrease in E_g. Thus, the introduction of Bi into GaAs provides a means of suppressing Auger recombination losses, through a strong reduction in E_g, relative to Δ_{SO}. An international patent application was filed in 2010 by Sweeney[42] to exploit this concept. It was suggested[42]

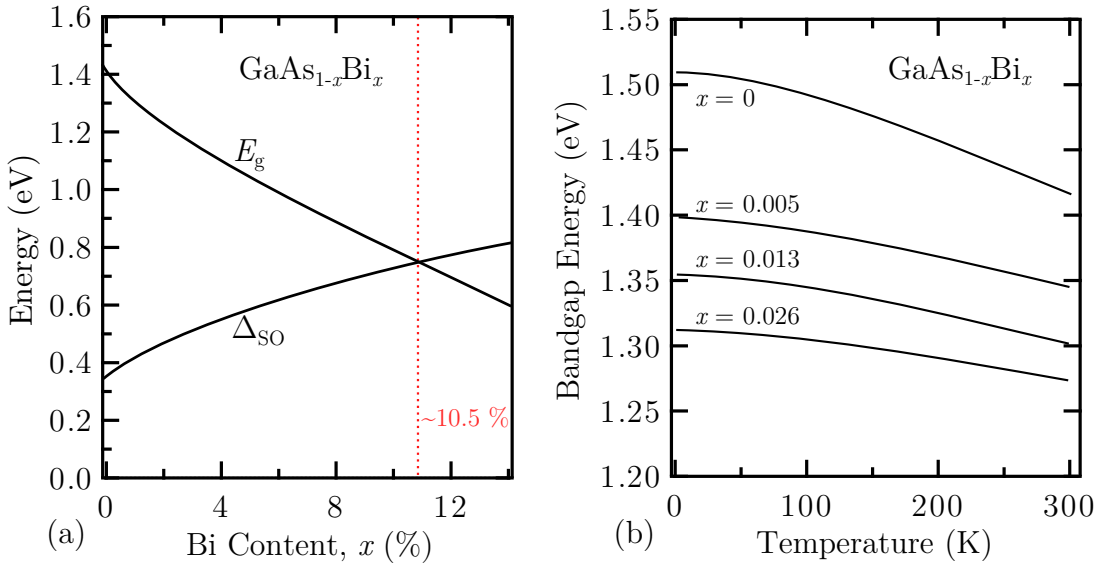

Figure 1.3: (a) $GaAs_{1-x}Bi_x$ bandgap energy (E_g) and spin-orbit-splitting energy (Δ_{SO}) dependence on Bi content (x); data adapted from Ref. 35. (b) Temperature dependence of bandgap energies of dilute $GaAs_{1-x}Bi_x$ alloys; data adapted from Ref. 36.

that employing $GaAs_{1-x}Bi_x$ lasers with Bi content larger than 10.5% will in fact circumvent Auger recombination all together[42–44].

In order to reduce the cost of long haul optical fibre networks, a material with a temperature (T) insensitive bandgap energy (a relatively low $\Delta E_g/\Delta T$ coefficient) is extremely desirable. The phenomena of Auger-related losses in III-V light emitting devices not only drives down efficiency, but also makes device cooling mandatory due to the third carrier (not part of the original electron-hole pair) losing its excess energy to thermal vibrations. The obvious solution is to employ a GaAsBi active region featuring a bismuth content of more than 10.5 %, to completely negate Auger losses. This introduces new alloying restrictions and is not always suitable.

For the case of dilute GaAsBi, there is still a significant reduction in the temperature dependence for the bandgap of the material. Fig. 1.3(b) shows the temperature dependence of dilute GaAsBi alloys measured by photoreflectance[36]. The rate of change of $\Delta E_g/\Delta T$ for GaAsBi with just a few percent of Bi falls dramatically, reducing to about 1/3 to that of GaAs. Like all other semiconductor devices, solar cell function is

sensitive to temperature and susceptible to a lowered performance via the Auger recombination processes. With the high carrier concentrations introduced through heavy doping and/or high level of optically-injected carriers under concentrated sunlight, the Auger recombination lifetime is shortened. In turn, Auger recombination processes can limit the lifetime of carriers, and ultimately efficiency.

The aim of this introductory section was to lay out some of the more interesting properties investigated by researchers in the field, and to highlight the general appeal of the $GaAs_{1-x}Bi_x/GaAs$ epitaxial structure. Like many highly-mismatched alloys, there are several other pertinent phenomena associated with the GaAsBi system not yet told. These include localised and resonant states in the band structure, Bi clustering and the presence of relatively large native hole concentrations. These will be dealt with in detail later in this thesis, at the appropriate place.

1.4 Bismuth oxide

The material system principally under investigation in this thesis is the $GaAs_{1-x}Bi_x/GaAs$ epitaxial structure. As will be shown later, the very low melting point of pure Bi metal (545 K) means it is extremely prone to oxidation. During this research some fascinating observations were made regarding Bi_2O_3 and, as a result, a small portion of the thesis work (Chapter 6) is dedicated to the oxidation of elemental Bi and the phase properties of bismuth oxide. As a binary compound, the properties of bismuth oxide align well with those required for optoelectronic applications, and bismuth oxide has received much attention for these purposes. As such, the work focusing on bismuth oxide is aimed toward photovoltaic (PV) and solar cell applications.

1.4.1 Properties and applications of Bi_2O_3

Bismuth, with an atomic mass of 208.980 g/mol, is the heaviest non-radioactive element in the periodic table. Bismuth is a heavy metal, however it is considered safe, non-toxic, non-carcinogenic[45] and often finds its way into pharmaceutical products. Although its presence in the Earth's crust is relatively rare (only twice as abundant as gold), bismuth oxide (Bi_2O_3) is the most important industrial compound manufactured from bismuth and a common starting point for bismuth chemistry. As demonstrated previously, bismuth-containing III-V semiconductors are attracting much attention in recent years. The same is also true for bismuth(III) oxide (Bi_2O_3). This is because Bi_2O_3 is a very interesting wide-bandgap semiconductor; the bandgap of Bi_2O_3 lies between 2.0 to 2.8 eV, depending of the phase[46]. Characterised by a wide UV bandgap, high permittivity (190) and refractive index (2.9)[47], photocatalytic activity, ionic conductivity, strong absorption and PL (depending on phase) of visible light and intrinsic polarisability, Bi_2O_3 is very much considered an 'optical material'. In fact, the integration of Bi_2O_3 into thin film PV solar cells has recently become common practice[48–50]. Moreover, some groups are exploring how to usefully integrate Bi_2O_3 films into III-V-based multi-junction solar cell devices[48,51,52]. Interest has grown because researchers are now finding practical ways to reliably synthesise and integrate Bi_2O_3 at the nanoscale, in order to exploit some interesting low-dimensional physical properties.

On the other hand, Leontie *et al.*[46] demonstrated that many applications of bismuth oxide are dependent on the phase utilised; the atomic arrangement of Bi_2O_3 strongly dictates the material properties. Since Schumb and Ritter[53] first showed the high polymorphism of bismuth trioxide, four principal phases have been shown to be favoured under typical conditions: α-, β-, γ- and δ-Bi_2O_3. At room temperature, the monoclinic α-phase is the stable form of Bi_2O_3, and transforms into the cubic fluorite δ-phase when heated above 1018 K. The other phases, the tetragonal β-Bi_2O_3 or the

b.c.c. γ-Bi_2O_3, are considered metastable[46] and are reported for temperatures below 750 K when cooled down from the δ-phase.

As each polymorph possesses distinct crystalline structures and physical properties (electrical, optical, photoelectrical, etc.), understanding the crystal dynamics of Bi_2O_3 is of fundamental interest[54–58]. The α-phase modification is often employed because it is robustly stable under ambient conditions. However, it is not the most desirable polymorph for many applications. The δ-phase is best suited for materials requiring high ionic transport (δ-Bi_2O_3 possesses the highest ionic conductivity among all binary metal sesquioxides) and the β-phase is appealing for photocatalytic and PV applications (because of its superior charge separation properties). A greater ability to transfer photo-induced electrons and holes is due to the β-phase exhibiting a more dispersive band structure than the α-phase[59]. Further, the β-phase is a direct bandgap semiconductor while α-phase is indirect[59].

Predicting which phase a transitioning oxide will enter is difficult[60] and is strongly influenced by the presence of trace amounts of impurities[61–65]. Other factors which influence entering the β- and γ-phase include the history of treatment: heating rate, cooling rate, maximum temperature reached in the δ-phase, oxide size/texture and pressure. For the case of a pure Bi_2O_3 system under ambient temperature and pressure, the oxide size and shape plays the key role in defining the total energy of the system, and thus the phase. Besides locking in a particular phase via doping, it is only until very recently that influences such as size and texture have been studied in detail[66,67] and are still yet to be fully understood or exploited.

1.5 Thesis overview

The general motivation and benefits of the $GaAs_{1-x}Bi_x$ alloys and phase-specific Bi_2O_3 have been outlined previously in this chapter. At the beginning of research chapters 3 to

6, a more focused motivation section will prelude the work and outline the current state-of-play for the topics covered, as well as illuminating the importance of the research. Since the GaAsBi system is still relatively new, much of the research is dedicated to the structural and optical charaterisation of this emerging material system. Additional work related to the laser-induced oxidation of bismuth, and specifically Bi droplets atop of GaAsBi surfaces, is also contained in the thesis.

Chapter 2 explains the growth of materials and characterisation techniques used in the work. The principles of MBE, MBE growth of $GaAs_{1-x}Bi_x$, the vapour-liquid-solid (VLS) growth mechanism and sample details are discussed. The principles of Raman scattering, photoluminescence (PL), x-ray diffraction (XRD), scanning electron microscopy (SEM) and atomic force microscopy (AFM) are also outlined.

Chapter 3 will derive the Raman backscattering selection rules for an arbitrarily (hhk)-oriented zincblende crystal and examine them within the context of different polarised Raman backscattering configurations. The selection rules are derived theoretically up to a crystal index of (119) and compared to experiment up to a GaAs crystal index of (115). This chapter reports new findings and can be considered a results chapter. The work here lays the foundation for polarised Raman analysis presented in Chapters 4 and 5.

Chapter 4 presents a compositional study of the Bi-induced effects for (001)- and (113)-oriented $GaAs_{1-x}Bi_x$/GaAs epitaxial layers. The first-order Raman spectrum is examined and, with the aid of XRD experiments, both the structural and electronic origins of the Bi-induced spectral changes are described. A comparison in crystal quality is made for growth of GaAsBi on (001) and (113)B GaAs substrates.

Chapter 5 focuses on the microstructure effects of Bi surface droplets formed during the MBE of GaAsBi, employing a variety of complementary techniques: SEM, AFM, polarised micro-Raman and micro-PL. A morphological study reveals the Bi-catalysed

growth of planar "nanotracks" with periodic height variations. A geometric growth model is presented to explain the origin of their unique shape. The Bi content of the nanotracks, the microstructure and their light emitting properties are also examined.

Chapter 6 studies the laser irradiation-induced oxidation of bismuth metal investigated *in situ* by Raman microprobe analysis, as a function of laser irradiation power and time. A new fixed kinetic transformation sequence is proposed to describe the Bi_2O_3 phase formed immediately after liquid Bi reacts with oxygen (first enters the β-phase), and how is transforms after growing in volume (transforms into the α-phase). The dynamic dependency of phase is then exploited to transform small metallic Bi microislands atop a GaAsBi surface into a room-temperature stable form of β-Bi_2O_3.

Chapter 7 summarises all the results and provides suggestions for future work.

Chapter 2

Experimental methods

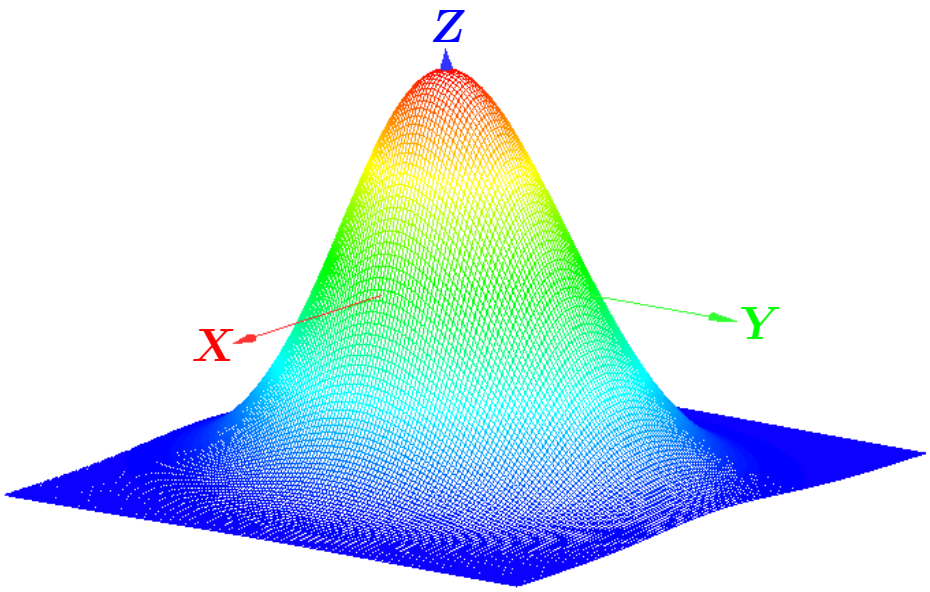

Surface plot of measured Gaussian micro-beam profile for the integrated micro-Raman and micro-photoluminescence system used in this thesis.

2.1 Principles of molecular beam epitaxy

The precision growth of single crystal semiconductors with the high purity (ppb) and low defect density ($5 \times 10^{-3}/\text{cm}^2$ or less) is required for optoelectronic applications.

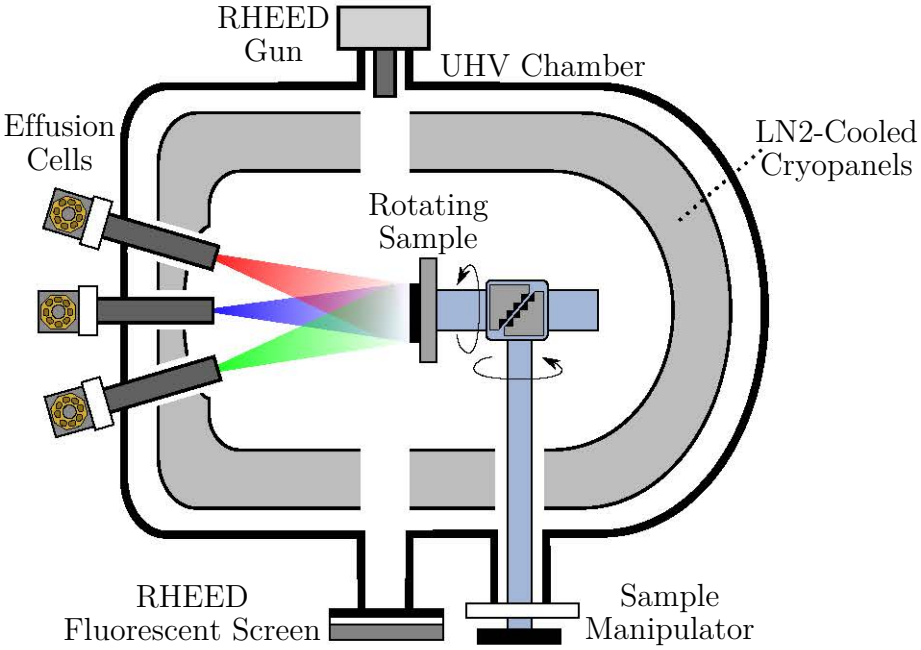

Figure 2.1: Schematic illustration of the growth chamber of an MBE system.

The growth of semiconductor heterostructures must involve a technique which facilitates the deposition and joining of single crystal layers with the same crystal structure; such a process is known as *epitaxy*. For III-V epitaxy, growth can be achieved using several methods, such as metal organic vapour phase epitaxy (MOVPE), molecular beam epitaxy (MBE) and liquid phase epitaxy (LPE). The far simpler approach of LPE meant it was the preferred technique for the early production of semiconductor devices. For III-V growth, both MBE and MOVPE are used in high volume, although a simple distinction can be drawn by their typical application: both are used extensively as production and research tools, however MOVPE is more widely employed by industry due to its commercial appeal. Further, the superior ability of MBE to grow thermodynamically forbidden alloys means it is well suited for research into highly mismatched alloys, like GaAsBi.

Figure 2.1 presents a basic schematic of an MBE system employing three separate effusion cells. In MBE, non-interacting high-purity molecular beams of constituent

materials are evaporated/sublimated and permitted to interact on a heated substrate. The beams of reactants do not interact in the gas phase as their mean free paths through the ultra high vacuum (UHV) are far larger than the nominal source-to-substrate distance (20-30 cm). One of the major advantages of growth by MBE is the extremely clean UHV environment (10^{-10} Torr) − maintained partly by liquid-nitrogen(LN2)-cooled condensing cryopanels − which facilitates high quality crystals to be grown; from purity, interface formation in layered structures, to precise control over the alloying composition and doping. The use of a pure-source environment allows for simplified growth chemistry when the reactants reach the substrate surface (compared to implementing an engineered precursor molecule like trimethylgallium in MOVPE, for example). UHV also lends itself to useful *in situ* monitoring techniques, such as the commonly employed reflection high-energy electron diffraction (RHEED) measurement, which allows one to accurately assess monolayer (ML) inclusions and the epitaxial growth rate.

The growth rate may locally differ over the whole substrate surface due to the angular dependence of the non-normal beam-like flux being emitted by the source effusion cells (see Fig. 2.1). This is particularly pertinent for the growth of semiconductors involving multiple constituents, such as the ternary and quaternary alloys. To reduce such dependencies, a sample manipulator provides continuous sample azimuthal rotation in the MBE chamber throughout growth and promotes a more even distribution of impinging species. The level of control offered by MBE means it is well suited for the growth of high-quality GaAs-based mixed crystals, given the condensation of binary $Ga_{0.5}As_{0.5}$ is thermodynamically favourable over a relatively large window of temperatures and beam pressures. As we will see next, incorporating Bi into GaAs in relatively large proportions − on the order of a few percent − imposes challenging constraints on the MBE growth window.

2.1.1 MBE growth of $GaAs_{1-x}Bi_x$ alloys

Due to the large disparity in atomic size of bismuth relative to arsenic, the MBE growth of $GaAs_{1-x}Bi_x$ requires *very* nonstandard growth conditions. For example, the lowest impurity and defect-related luminescence emissions in GaAs are observed for growth temperatures between 550-600°C. In contrast, the MBE of GaAsBi necessitates far lower substrate temperatures; Bi does not appear to incorporate appreciably above approximately 350°C[26]. Moreover, the V/III flux ratio must also be low, with the Bi incorporation reducing quickly beyond a ratio of V/III$\sim$1.8. While there are significant growth constraints for the successful synthesis of $GaAs_{1-x}Bi_x$ alloys using MBE, it has been suggested that Bi can actually be incorporated at quite substantial quantities: the highest reported value so far is $x = 0.22$[68].

The capacity to grow GaAsBi away from nominal GaAs stoichiometry, and avoid the negative effects typically seen in low-temperature grown GaAs, is due to the ability for Bi atoms to act as a particularly effective surfactant on the surface during growth (Bi atoms lower interface/surface energy between growth species and the GaAs crystal). For the Bi to work effectively as a surfactant, it must continually hold a presence on the surface throughout the growth; i.e. the complete incorporation of incoming Bi flux creates reduced potential for Bi-related surfactancy. On the other hand, the homogeneous incorporation of Bi is plagued by the tendency of Bi atoms to cluster within the GaAs matrix[69–71], and in some cases form Bi-based droplets during growth[27,72,73]. Droplets form because the excess Bi can self-segregate to the surface and unevenly group.

Importantly, the existence of a GaAsBi processing window[74] provides a guide for the growth of alloys with different compositions, through control of important parameters such as substrate temperature or flux ratios.

The vapour-liquid-solid mechanism during MBE

The MBE growth technique synthesises a (thin film) crystal through the direct adsorption of the gas phase onto the solid crystal surface. With the constant arrival of growth species from the effusion cells, and in the presence of a metal catalyst (such as Bi droplets), there are other avenues for which the gas species may form a crystal. For the case of many vapour-based growth techniques at sufficiently high temperatures, a *eutectic* system (a mixed alloy which exhibits a melting point lower than that of the system constituents) can facilitate non-vapour-solid growth. During vapour-based growth a eutectic that is in contact with the crystal substrate surface is able to synthesise new crystal through a process first described by Wagner and Ellis[75] as the vapour-liquid-solid (VLS) mechanism.

MBE has been used in the past 15 years[76] to grow high-quality semiconductor nanowires via the VLS mechanism. In metal-catalysed MBE, the metal particles do not facilitate or catalyse a reaction between species, but rather adsorb vapour phase particles. This is essentially due to the chemical potential of the vapour being lowered by entering the liquid phase. If energetically favourable, the liquid eutectic alloy can deposit material at the liquid-solid interface. It follows that the size and position of the VLS growth on a crystal is determined by the interface made with the metal catalyst. The process of VLS growth has a greatly lowered reaction energy compared to normal vapour-solid growth and the growth rate of the catalysed structure can far surpass that of typical epitaxy.

The options for metal catalysts are limited and often defined by the phase diagram of the eutectic system involved. For the case of GaAs-based VLS growth, some typical metal catalysts include gold and gallium. Recently, Bi was shown to form a eutectic with Ga and As, for VLS growth of GaAs-based nanostructures[77,78].

2.2 $GaAs_{1-x}Bi_x$/GaAs sample details

The uncapped $GaAs_{1-x}Bi_x$/GaAs samples (GaAsBi surfaces exposed) investigated in this thesis were grown by MBE by collaborating groups from both the University of Nottingham and the University of Arkansas. These respective groups performed extensive characterisation (high-resolution transmission electron microscopy and x-ray diffraction) on the samples prior to our research, and their findings indicated that the alloys were coherently grown. The Bi concentration of samples and its coherent structure were further verified more recently during this thesis research, through x-ray diffraction measurements. The compositional details are presented in Table 6.1 in Chapter 4. All the samples but one (sample labelled B7) are included in the compositional study presented in Chapter 4. Note that photoluminescence (PL) is employed in Chapter 5 of this thesis as a means to determine the Bi concentration for a single sample. However, not all samples exhibited PL at room temperature and this method is not always a reliable means for determining Bi concentration (if the GaAsBi is inhomogeneous, for example), thus PL studies were not pursued more broadly.

Samples from University of Nottingham

Two sets of GaAsBi samples were provided by Prof. Mohamed Henini and colleagues. The first set, identified in this thesis as A#, contains three $GaAs_{1-x}Bi_x$/GaAs fully strained heterostructures grown on (001) GaAs substrates (A2 - A4) with Bi concentrations ranging from $0.018 \leq x \leq 0.0301$. The second set, labelled as H#, consists of four high-index (113)B-oriented $GaAs_{1-x}Bi_x$/GaAs samples (H2 - H5) with Bi concentrations ranging from $0.0118 \leq x \leq 0.0391$. Controls were also provided for crystals grown in both crystallographic directions (A1 and H1).

The two sample sets were grown during an investigation[79] into the possible effects that high-index growth planes, such as (113)B, may have on the total Bi inclusion. To

do this, all samples were grown with a constant growth temperature of ∼350°C and the relative As (and Bi) to Ga flux ratios were varied to grow alloys of differing compositions. Atomic Ga and Bi were used as group-III and group-V sources, respectively, while As was in the form of dimers (As_2). To incorporate Bi efficiently into GaAs using MBE, the Ga to As flux needs to be on the brink of As shortage, close to the stoichiometric value. The Ga beam-equivalent pressure (BEP) was set to a fixed value of 9×10^{-7} Torr, while the Bi flux during growth was set to a constant value of $\sim 1.2 \times 10^{-7}$ Torr. Samples with different Bi contents were achieved by varying the As_2 BEP values in the range of 6×10^{-6} - 1.2×10^{-5} Torr. The control samples without Bi were also grown on both (001)- and (113)B-oriented substrates at 350°C and 600°C. The nominal growth rate was roughly 1 μm/h for all samples and the nominal thickness of the epilayers were on the order of 1 μm.

The materials reported by Henini *et al.*[79] constitute some of the samples studied in this thesis. The principal finding and conclusion of the report by Henini *et al.*[79] revealed that the incorporation of Bi is enhanced through growth on a (113)B-oriented GaAs substrate. The origins and implications of this result are further explored in Chapter 4.

Samples from University of Arkansas

A set of seven (001)-oriented $GaAs_{1-x}Bi_x$/GaAs samples were grown at the University of Arkansas and provided to us by Prof. Greg Salamo and colleagues. Six of the samples (B1 - B6) are of a reasonably high quality, exhibiting good x-ray diffraction data; i.e. narrow Bragg peaks with oscillations originating from a clean coherent growth interface.These samples also possessed substantial Bi inclusions, with the concentration ranging from $0.0316 \leq x \leq 0.0478$.

Sample B7, which was omitted from the Raman scattering study in Chapter 4,

possessed a Bi concentration of $x \sim 0.04$. B7 suffered from large Bi segregation during MBE growth, resulting in droplet formation and a substantial lowering of surface quality. The interesting modifications that Bi droplets introduced to the structure, morphology and quality of the GaAsBi materials are the focus of Chapter 5.

Unlike those grown by Henini *et al.*[79], the $GaAs_{1-x}Bi_x$ materials provided by University of Arkansas were all grown with a fixed Ga, As and Bi flux. To vary the Bi inclusion, the substrate temperature was varied between 300 - 365°C instead. For all samples, the nominal growth rate was 0.1 monolayer/s (determined through RHEED measurements) and the final epilayer thickness was approximately 0.3 μm.

2.3 Characterisation techniques

2.3.1 Raman scattering spectroscopy

"Ah, but my effect will play a great role for chemistry and molecular structure!" - Sir Chandrasekhara Venkata Raman

The Raman effect in matter consists of the inelastic scattering of light by elementary excitations. Examples of such excitations include phonons, polaritons, plasmons and coupled phonon-plasmon modes. In general, the incident light interacts with the lattice vibrations (phonons) and the Raman spectra is sensitive to the locally probed environment. The information provided from Raman experiments is extremely important for evaluating material performance and include phase, strain, composition and crystal disorder. Raman scattering spectroscopy is the principal technique used in this thesis for the study of zincblende crystals GaAs, $GaAs_{1-x}Bi_x$ and polymorphic Bi_2O_3. As such, added attention is devoted here to clearly introduce the theoretical principles on which much of the later discussion is built.

Classical theory of Raman scattering

In the illumination of semiconductors with light, several optical processes can occur, such as reflection, scattering, absorption, and luminescence. In Raman scattering spectroscopy, inelastic light scattering processes are analysed, i.e. scattering events in which energy is transferred between the incident photon with energy $\hbar\omega_{\mathrm{i}}$ and the material, producing a scattered photon of a shifted energy $\hbar\omega_{\mathrm{s}}$. The amount of energy transferred corresponds to the eigenenergy $\hbar\Omega_j$ of the jth elementary excitation in the material. Figure 2.2(a) shows a comparison of the three possible processes for scattered photons. The left and right represent inelastic photon scattering (Raman), while the centre process is elastic scattering (Rayleigh; $\hbar\omega_{\mathrm{i}} = \hbar\omega_{\mathrm{s}}$). Treating the processes simply, scattering involves two steps; (i) the excitation of an electron from an initial ground or vibrational state to a higher energy state (which is not real and referred to as a virtual state), through absorbing the photon with energy $\hbar\omega_0$ and wavevector $\mathbf{k}_{\mathrm{i}}$; and (ii) the excited electron decays from the virtual state to either the ground state or some vibrational state (Ω_{j}).

Figures 2.2(b) and (c) present schematic illustrations of a laser Raman setup and spectrum, respectively; scattered monochromatic laser light is dispersed by a monochromator across the excitation frequency (ω_0) range and the intensity is recorded. Experimental Raman scattering experiments yield the eigenfrequencies of the vibrational excitations via an analysis of the peak frequencies (ω_{s}) in the scattered light, given that the frequency of the incident photons (ω_{i}) are well defined by the use of a laser. Thus, due to the conservation of energy, we have

$$\hbar\omega_{\mathrm{s}} = \hbar\omega_{\mathrm{i}} \pm \hbar\Omega_{\mathrm{j}}, \tag{2.1}$$

where the $-$ve sign indicates Raman processes which generate an elementary excitation (Stokes), while the +ve sign stands for their annihilation (anti-Stokes). It follows that

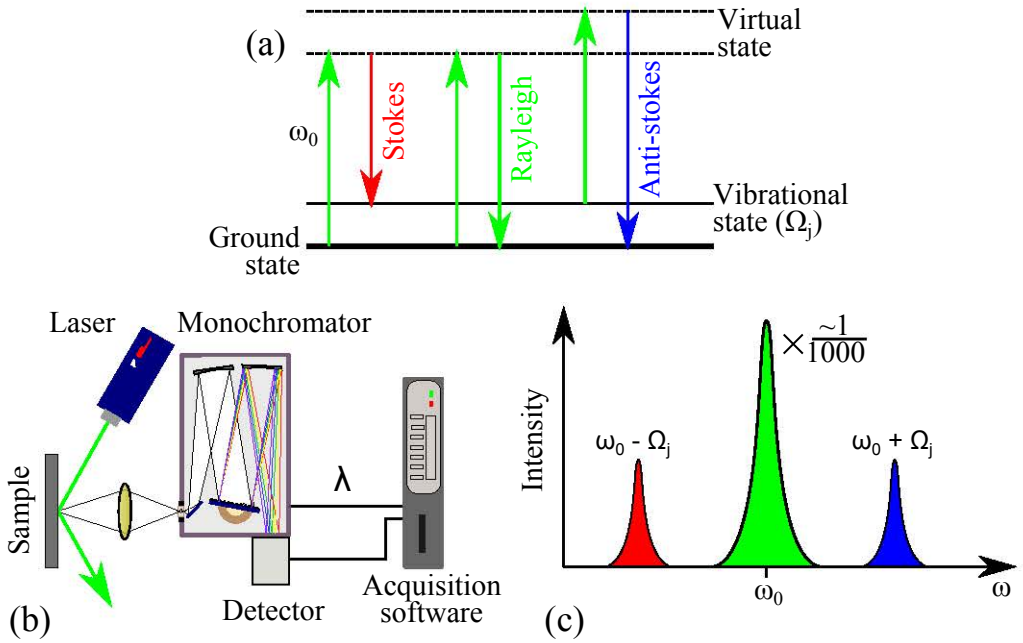

Figure 2.2: Schematic illustrations of (a) Rayleigh and Raman scattering processes, (b) main components of a Raman scattering experimental setup, and (c) Raman spectrum showing the scattered light intensity vs. frequency.

momentum conservation provides a means for correlating all wavevectors involved in the scattering process:

$$\mathbf{k}_\mathrm{s} = \mathbf{k}_\mathrm{i} \pm \mathbf{q}_j. \tag{2.2}$$

Here $\mathbf{k}_\mathrm{s}$ and $\mathbf{q}_j$ represent the wavevectors of the scattered photon and the jth excitation. From within the material the light wavevectors are given by

$$\mathbf{k}_\mathrm{i,s} = n(\omega_\mathrm{i,s})\mathbf{k}^0_\mathrm{i,s}, \tag{2.3}$$

where $n(\omega_\mathrm{i,s})$ represents the index of refraction for light frequencies $\omega_\mathrm{i,s}$.

The investigation of semiconductor epitaxial layers typically employs a backscattering configuration for Raman experiments, whereby $\mathbf{k}_\mathrm{i} \parallel \mathbf{k}_\mathrm{s}$. With absorption coefficient $\alpha \neq 0$, the optical penetration depth of the Raman signal becomes

$$d_\mathrm{opt} = 1/2\alpha. \tag{2.4}$$

For typical α values in the range of $10^6\,\mathrm{cm}^{-1}$, the optical penetration and scattering volume V are quite small (on the order of nm deep, neglecting probe spot size).

In thermodynamic equilibrium the upper vibrational states of the system will be less populated than the ground states. Correspondingly, the intensity of Raman peaks arising from Stokes scattering is larger than anti-Stokes scattering. As in many Raman studies, we will only consider Stokes scattering in this thesis. For the Stokes process, and with the speed of light given by c, it follows that Eq. 2.2 can be reduced to the scalar form

$$q_j = \frac{1}{c}[n(\omega_\mathrm{i})\omega_\mathrm{i} \pm n(\omega_\mathrm{s})\omega_\mathrm{s}]. \tag{2.5}$$

Both conservation of energy and momentum dictate only certain combinations of energy and momentum transfer between the incident light and the material can occur. The quantised nature of semiconductor vibrations means only well-defined (Ω_j, q_j) pairs out of the whole range given by the dispersion relations for a material may be involved in the scattering process. Moreover, Eq. 2.5 suggests a quasi-momentum transfer which is roughly proportional to laser frequency. However, deviations from linearity may arise depending on the excitation wavelength used and the frequency dependence of the refractive index, $n(\omega)$. A practical application of Eq. 2.5 (in our case, red laser light; $\sim$400 THz) yields q-values on the order of $10^6\,\mathrm{cm}^{-1}$. These small values arise because the light wavelengths exceed the typical lattice constants by more than a factor of one hundred. Thus, the excitations involved in Raman scattering are within a few percent from the Brillouin zone centre, Γ. Since the dispersion near Γ is negligible, the energy transfer $\hbar\Omega_j$ is independent of the incident frequency ω_i.

The exact conservation of momentum given by Eq. 2.5 is unrealistic in experiments and real-world limitations enact the process of momentum *non-conservation*. The most stringent of these limitations are imposed by the crystal itself since a well-defined momentum in the system requires the ideal physical homogeneity of the lattice. Crystal

impurities and defects are responsible for relaxing the momentum conservation rule which manifests as broadening in the measured Raman modes. Since Raman bands are approximately the density of phonon states, their lineshape can be used to characterise the degree of disorder in the system.

For laser light above the bandgap, E_g, Raman scattering is mediated by electronic interband transitions which may be influenced by elementary excitations, such as phonons. These transitions define the dielectric susceptibility, χ, in the visible spectral range. The production of scattered light can be described by the generalised susceptibility tensors $\tilde{\chi}(\omega_{\mathrm{i}}, \omega_{\mathrm{s}})$:

$$\mathbf{P}(\omega_{\mathrm{s}}) = \epsilon_0 \tilde{\chi}(\omega_{\mathrm{i}}, \omega_{\mathrm{s}}) \mathbf{E}(\omega_{\mathrm{i}}). \tag{2.6}$$

Here $\mathbf{P}(\omega_{\mathrm{s}})$ is the oscillating polarisation which gives rise to the scattered light wave and $\mathbf{E}(\omega_{\mathrm{i}})$ is the polarisation of the incident light. Given that $\mathbf{P}(\omega_{\mathrm{s}})$ and $\mathbf{E}(\omega_{\mathrm{i}})$ are both vectors, we may drop ϵ_0 and simply write the Cartesian expression:

$$\begin{bmatrix} P_x \\ P_y \\ P_z \end{bmatrix} = \begin{bmatrix} \chi_{xx} & \chi_{xy} & \chi_{xz} \\ \chi_{yx} & \chi_{yy} & \chi_{yz} \\ \chi_{zx} & \chi_{zy} & \chi_{zz} \end{bmatrix} \begin{bmatrix} E_x \\ E_y \\ E_z \end{bmatrix} \tag{2.7}$$

The scattering intensity can now be expressed in terms of the dipole radiation intensity:

$$I_{\mathrm{s}} = I_{\mathrm{s}} \frac{\omega_{\mathrm{s}}^4 V}{(4\pi\epsilon\epsilon_0 c^2)^2} \mid \hat{e}_i \tilde{\chi}(\omega_{\mathrm{i}}, \omega_{\mathrm{s}}) \hat{e}_s \mid^2 . \tag{2.8}$$

Here $I_{\mathrm{i,s}}$ and $\hat{e}_s$ respectively denote the intensity and the polarisation unit vectors of the incident and scattered light, while ϵ_0 is the vacuum permittivity.

We will proceed with α and β respectively representing the directions of $\hat{e}_i$ and $\hat{e}_s$, and writing the tensor components as $\chi_{\alpha,\beta}(\omega_{\mathrm{i}}, \omega_{\mathrm{s}})$. For phonon vibrations with

complex amplitude of the form $Q_j = Q_j^0 exp[i(\Omega_j t - q_j r)]$, the influence of phonons on the generalised susceptibility tensors can be expressed by a Taylor expansion [80]

$$\begin{aligned}
\chi_{\alpha,\beta}(\omega_\mathrm{i},\omega_\mathrm{s}) =& \chi^0_{\alpha,\beta}(\omega_\mathrm{i}) && \mathrm{T1}\\
&+ \sum_j Q_j \cdot \left(\frac{\partial \chi_{\alpha,\beta}(\omega_\mathrm{i})}{\partial Q_j}\right) && \mathrm{T2}\\
&+ \sum_j iQ_j \cdot qj \left(\frac{\partial \chi_{\alpha,\beta}(\omega_\mathrm{i})}{\partial \nabla Q_j}\right) && \mathrm{T3}\\
&+ \sum_j Q_j \cdot E\gamma \cdot \left(\frac{\partial^2 \chi_{\alpha,\beta}(\omega_\mathrm{i})}{\partial Q_j \partial E_\gamma}\right) && \mathrm{T4}\\
&+ \sum_j Q_j Q_{j'} \cdot \frac{1}{2}\left(\frac{\partial^2 \chi_{\alpha,\beta}(\omega_\mathrm{i})}{\partial Q_j \partial Q_{j'}}\right) && \mathrm{T5}\\
&+ ...
\end{aligned} \tag{2.9}$$

Here t and r respectively depict the time and the wave profile displacement and Q_j^0 is the phonon amplitude. Note an additional static electric field in the γ-direction is given here by E_γ, while j' signifies the second mode involved in a two-phonon interaction.

The first five terms here (T1 to T5) capture the origins of the various Raman features discussed throughout this thesis. Beside the susceptibility of the crystal without phonons, $\chi^0_{\alpha,\beta}(\omega_\mathrm{i})$ (T1), terms T2, T3 and T4 give rise to one-phonon processes. The final term (T5) contained in Eq. 2.9 originates from two-phonon processes, with the frequency of the second mode given by $\Omega_{j'}$. Thus, the resultant scattered photon frequency is

$$\omega_\mathrm{s} = \omega_\mathrm{i} \pm (\Omega_j \pm \Omega_{j'}), \tag{2.10}$$

and covers a wide variety of eigenmode combination frequencies.

The one-phonon processes originate from a change in the susceptibility due to lattice deformation Q_j (T2), a deformation gradient ∇Q_j (T3), and the lattice deformation in the presence of a static electric field, $\mathbf{E}_\gamma$ (T4). There are also crystal symmetry considerations to be made which dictate which vibrational modes are "active".

Raman scattering processes involving one, or potentially multiple, phonon amplitudes which leave the crystal symmetry invariant (T2 and T5) are said to be "symmetry-allowed". To observe "symmetry-forbidden" Raman modes, a reduction in symmetry is required through the introduction of deformation gradients and/or static electric fields (T3 and T4).

The partial derivative of T2 in Eq. 2.9 predicts the first-order Raman polarisability. Through introducing a unit vector in the direction of lattice displacement, $\hat{Q} = \boldsymbol{Q}/\mid Q \mid$, we form the Raman tensor:

$$\tilde{\mathcal{R}}_{\hat{Q}} = \hat{Q}_j \cdot \left(\frac{\partial \chi_{\alpha,\beta}(\omega_\mathrm{i})}{\partial Q_j} \right) \tag{2.11}$$

The symmetry of the Raman tensor, and hence the symmetry of the underlying phonon, can be identified by Raman experiments in different polarised configurations; a practical application of the Raman tensors is given in the next chapter.

Quantum theory of Raman scattering

The process described above involves a photon which is scattered by a phonon and has its energy shifted by a quantised value. The coupling of such interactions is extremely weak, while the coupling of photons with electrons is very strong. As already pointed out, the excitation frequencies used in Raman experiments are typically above the bandgap energy. A microscopic assessment of the scattering process thus involves the excitation of an electron to form an electron-hole pair, which occupies an exciton or virtual state. In either case, the creation of an electron-hole pair in the crystal means it is now free to interact with the lattice. From a quantum mechanical view of Raman scattering, one may separate the process into three stages[81]:

(i) an incoming photon of energy $\hbar\omega_\mathrm{i}$ is absorbed and excites an electron-hole pair from the ground state $|0\rangle$ to a higher energy state $|e\rangle$. This process is mediated

by the electron-radiation Hamiltonian H_{e-r}.

(ii) the electron-hole pair is scattered by the lattice and then transitions from $|e\rangle$ to $|e'\rangle$ with the creation of the jth phonon with energy $\hbar\Omega_j$. This is an electron-lattice interaction (phonon creation) and is hence related to electron-phonon Hamiltonia H_{e-ph}.

(iii) the electron-hole pair in the $|e'\rangle$ state decays to the $|0\rangle$ state through radiative recombination, emitting a photon of energy $\hbar\omega_s$.

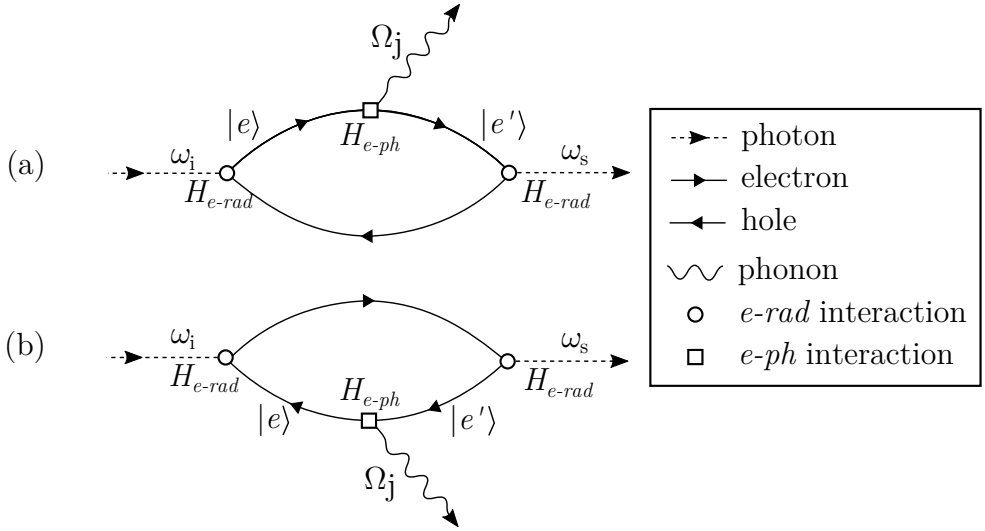

Figure 2.3: Feynman diagrams decribing the 3rd order perturbation calculation of first-order Raman scattering by phonons involving intermediate electron-hole pair states. (a) contribution from electrons and (b) the hole contribution. The terms are explained in the text.

According to Feynman's theory this Raman process can be described by all possible permutations of the interactions described above[81]. Figure 2.3(a) and (b) shows two out of six Feynman diagrams of such a scattering event. For this case, the scattering processes, which can be viewed as the mixing of three waves, is considered to take place in three steps of photon- or phonon-induced electronic transitions; each vertex in the Feynman diagram represents an interaction in the scattering process.

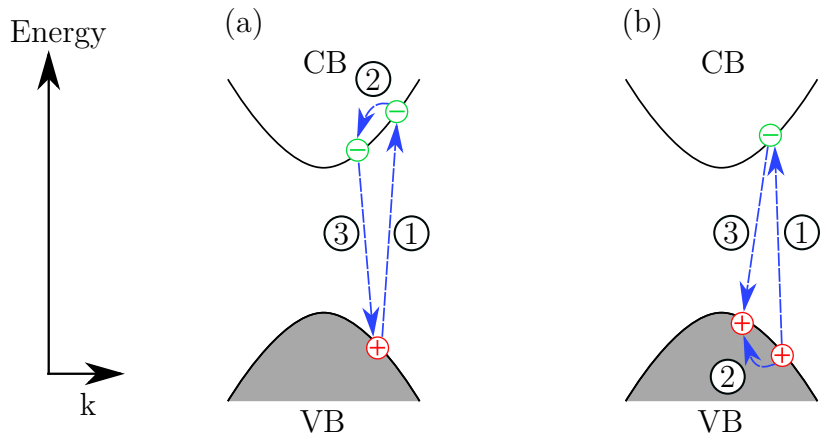

Figure 2.4: Schematic diagram of the interband and intraband electronic transitions involved in two-band Raman processes (Stokes); the order of the transitions are indicated by the numbers. Note for illustrative purposes and simplicity, the schematics depicted do not preserve $\Delta k = 0$ (transitions are not vertical). The processes described by (a) and (b) correspond respectively to the Feynman diagram presented in Fig. 2.3(a) and (b).

A schematic diagram of the transitions involved in the two-band Raman processes of semiconductors if provided in Fig 2.4(a) and (b); the procedures depicted here correspond respectively to those described Fig. 2.3(a) and (b). In terms of the electronic behaviour of a semiconductor, the quantum Raman process described by Figs. 2.3 and 2.4 can be far more powerful in describing Raman scattering events than the description provided by Eq. 2.9. This is because – as shown in Fig 2.4 – the electronic states involved in the light scattering are confined to, and influenced by, the band structure of the material. As we will see in Chapter 4, if one of the intermediate states involved is a *real* state and the incoming or outgoing photon meets the energy of that state, the scattering probability reaches a *resonance*. Further, if these electron-hole states occupy Bloch states in the lattice, they may no longer be confined to scatter light from the Brillouin zone centre.

Instrumentation

Raman scattering data were recorded using an integrated confocal Horiba Jobin-Yvon LabRAM 800HR instrument. Figure 2.5 presents a schematic diagram of the main integrated optical components; 20 mW HeNe 632.8 nm (473.8 THz) laser optics are coupled into a microscope objective which directs scattered light into both the optical dispersion and detection elements, as well as a video camera via a beam splitter. Using a micro-stepper-driven XYZ-stage controlled by the acquisition software, and a video camera, measurements are made at desired locations on the sample surface with relatively high spatial accuracy and stability. Sample rotation around the incident optical axis is achieved using a rotation stage. Eight microscope lenses with differing focal ratios (f-stop) available for the instrument provide an optical objective of either $\times 10$, $\times 50$ or $\times 100$, which define micro-probe sizes in the range of 10 μm to approximately 1 μm. Spot sizes, which coincide with the lateral resolutions, were determined using a combination of highly-attenuated optical images and recording Raman spectra across a cleaved Si crystal edge. For the smallest spot size of $\sim$1 μm (which is slightly larger than the diffraction limit for the system), an Olympus $\times 100$ objective (MPLN100x) with an f-stop=0.9 was used. The measured beam profile for this objective is shown in Fig. 2.5. Laser power densities were controlled by a neutral variable density filter incorporated before the microscope optics and measured using a Thorlabs PM100D power meter.

Where appropriate, Raman (and PL) spectra have been recorded using the laser power density and micro-beam size indicated in corresponding figure captions. Because both high resolution micro-Raman and micro-PL spectroscopy are achievable on the one integrated instrument, the constraints defined here apply equally in describing the limitations of the micro-PL experiments.

For Raman scattering measurements, spectra were recorded by a silicon-based

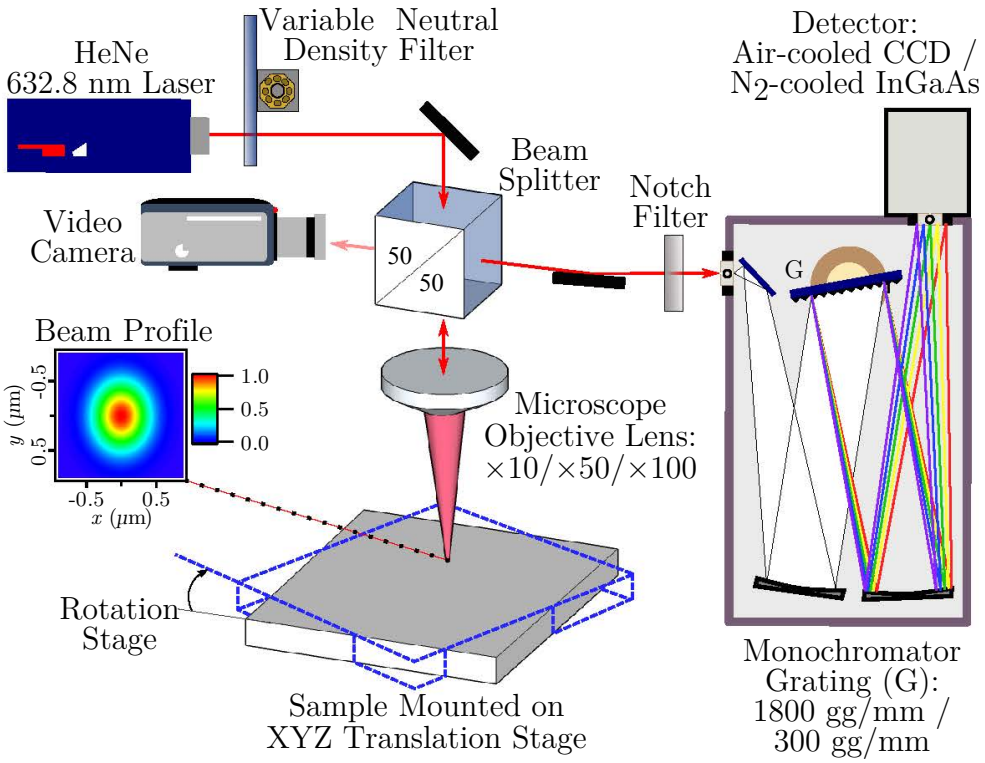

Figure 2.5: Schematic diagram of micro-Raman scattering and micro-PL experimental setup. The key components employed for both techniques are identical, though requiring different optical diffraction (grating) and detection elements. The normalised beam profile data was measured for the smallest incident micro-probe of $\sim$1 μm, using an Olympus $\times$100 objective.

air-cooled CCD detector and dispersed using a 1800 g/mm diffraction grating, which provided a spectral resolution of $\sim$0.2 cm^{-1}. Correct instrument calibration was verified by checking the position of the Si band at $\pm$ 520.7 cm^{-1} (15.6 THz) prior to recording Stokes Raman scattering spectra. With the addition of linear polarisers before and after the microscope optics, polarised Raman scattering measurements were performed in a quasi-backscattering experimental configuration. Implementing an appropriate notch filter to limit Rayleigh backscatter detection meant low-frequency portions of the Stokes Raman spectrum (below 58 cm^{-1}) were partially truncated.

For Raman spectra recorded from the GaAsBi/GaAs epitaxial layers, the epilayer thicknesses are large compared to $d_{opt} = 1/(2\alpha)$,[82] so that there is negligible signal

from the substrate. For the recoding of temporal Ramam data, spectra were recorded with a minimum acquisition time of 3 s, though typically with time intervals larger than this, depending on the Raman signal. These time-based experiments were achieved by measuring a surface map and limiting the spatial acquisition to one defined location; employing such a function ensured the even, rapid and consecutive recording of Raman spectra.

2.3.2 Photoluminescence spectroscopy

Principles of photoluminescence

Photoluminescence (PL) is a very sensitive technique for investigating electronic transitions through the emission of light resulting from the recombination of photo-excited charge carriers. The technique is also simple, non-destructive, often available at room temperature and does not require sample preparation. For incident light with energy near or above the bandgap of a material, photons will be absorbed, exciting an electron from the valence band (VB) to the conduction band (CB) to form an electron-hole pair. The electron-hole pair will then undergo thermalisation via scattering events and eventually recombine and emit a photon (or photoluminescence) with an energy (wavelength) corresponding to the bandgap. Such a process is called band-to-band radiative recombination and is illustrated for a direct bandgap system in Fig. 2.6(a).

Photo-excited electron-hole pairs can also recombine non-radiatively through a defect state (or level) in the bandgap; this process is illustrated in Fig. 2.6(b). The defect states can originate from impurities (i.e. carbon, oxygen etc.) or growth defects introduced through dislocations and point defects (clustering, vacancy or interstitial). The energy released from carriers recombining through defect levels will be converted to crystal vibrations and heat (phonons). It follows that the intensity of the PL emission will be closely related to the density of defects which weaken the emission. Moreover,

the main PL spectral parameters are closely related to the properties of the material and PL intensities yield useful information about the radiative recombination efficiency; understanding the competition between radiative and non-radiative recombination paths is important for device applications. Measuring PL spectra at different excitation intensities can also affect the nature of recombination – a relatively large excitation intensity will dramatically perturb the occupation of states within the VB and CB, and shift the energy of radiation arising from recombination.

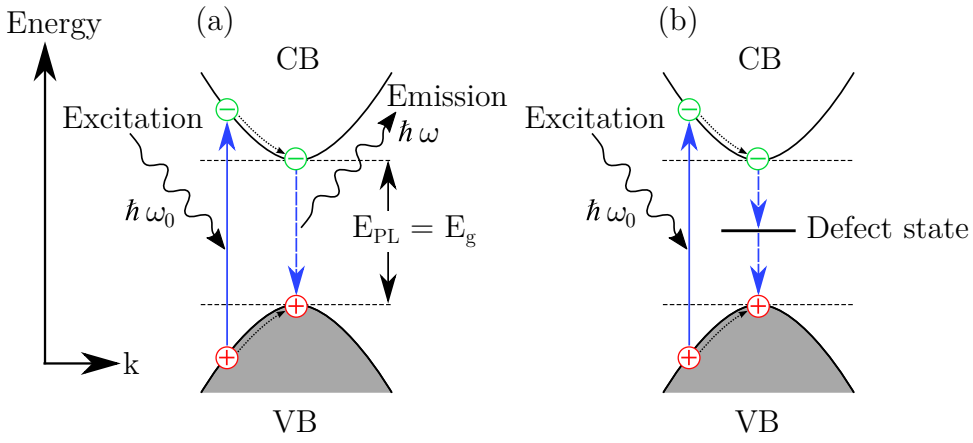

Figure 2.6: Schematic diagram of the basic mechanisms of recombination following photo-excitation. Carrier recombination processes showing (a) band-to-band radiative recombination and (b) non-radiative recombination, via defect states between the CB and VB.

When a PL spectrometer is coupled into an optical microscope (see Fig. 2.5), micro-PL measurements offer the possibility of mapping the light generating properties of optoelectronic materials with high spatial resolution (on the order of $\sim 1\,\mu$m). Semiconductor surface degradation, for example, can be a localised occurrence. Therefore, micro-PL is an extremely powerful tool for the characterisation of optoelectronic surfaces and structures, since it directly investigates their ability to produce light.

Compositional dependence of photoluminescence of $GaAs_{1-x}Bi_x$ alloys

The compositional dependence of the PL signal emitted from $GaAs_{1-x}Bi_x$ was investigated by Lu *et al.*[4], up to $x = 0.106$. The technique of assessing the PL peak energy to determine the Bi concentration is now commonplace. This is because of the systematic way in which the bandgap energy is modified (reduced) through Bi incorporation. The interpolation of bandgap for a changing composition is typically non-linear and a bowing parameter, b, must be introduced. The strong bowing observed in the alloy is well explained by a valence band anticrossing model, which shows that a restructuring of the valence band occurs as the result of an anticrossing interaction between the extended states of the GaAs valence band and the resonant T_2 states of the Bi atoms[83]. For $GaAs_{1-x}Bi_x$, the compositional relationship for the bandgap energy is

$$E_{GaAs_{1-x}Bi_x} = xE_{GaBi} + (1-x)E_{GaAs} - bx(1-x). \tag{2.12}$$

Here $E_{GaAs_{1-x}Bi_x}$, E_{GaBi} and E_{GaAs} are respectively the bandgap energies of $GaAs_{1-x}Bi_x$, GaBi and GaAs. Compounds which have a large difference in electronegativity between the substituted elements, such a GaAsBi, exhibit bowing parameters which vary as a function of x[4,84]. For $GaAs_{1-x}Bi_x$, the bowing decreases with x by,

$$b(x) = \frac{\alpha}{1+\beta x}, \tag{2.13}$$

where Lu *et al.*[4] provided empirically derived values for the fitting parameters: E_{GaBi}, α, and β are -0.36, 9.5, and 10.4, respectively.

Assessing the PL peak energy from $GaAs_{1-x}Bi_x$ alone is not typically a definitive method for determining the Bi concentration. This is because PL emissions will often involve complicated contributions which are difficult to resolve without using a

complimentary method. Moreover, many GaAsBi samples exhibit weak PL at room temperature, or no PL at all. On the other hand, for $GaAs_{1-x}Bi_x$ samples exhibiting unambiguous room-temperature PL, the micro-PL modality does provide the ability to examine the Bi concentration with great spatial resolution ($\sim$1 μm).

Instrumentation

In this work, PL data were recorded using an integrated confocal Horiba Jobin-Yvon LabRAM 800HR instrument sharing the same optical assembly as the Raman experiments previously shown; see Fig. 2.6 for a schematic diagram of PL setup. For PL measurements, spectra were detected by a LN2-cooled InGaAs detector (sensitive to near-IR frequencies) and dispersed using a 300 g/mm diffraction grating, which offered a spectral resolution of $\sim$0.5 nm. Correct instrument calibration was verified by checking the HeNe laser line at 632.8 nm prior to recording PL spectra.

2.3.3 X-ray diffractometry

Principles of XRD

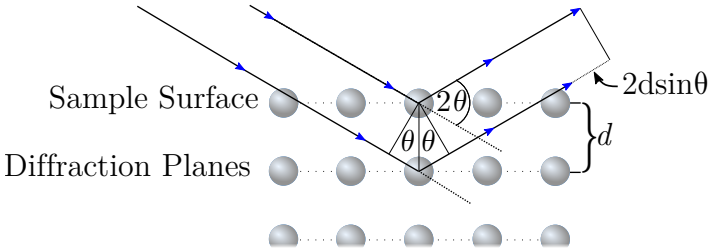

Figure 2.7: Geometrical diagram demonstrating the diffraction of an x-ray beam by planes of a crystal lattice. Note the blue arrow heads represent x-ray beam wavefronts, whereby the deeper penetrating x-rays returning from diffraction planes experience a shifted wavefront (shifted arrow head).

One of the more common tools in the characterisation of epitaxially grown semiconductor layers is x-ray diffraction (XRD). This is because XRD provides a measure of

the long-range order of a material. X-rays penetrate deep into the sample surface and important information about the material composition, epitaxial thickness, quality, strain and relaxation (mismatch), can be determined. X-rays are suitable for this purpose because their wavelength − a Cu source produces $\lambda = 1.54\,\text{Å}$− is comparable to the distance between atoms in the crystal.

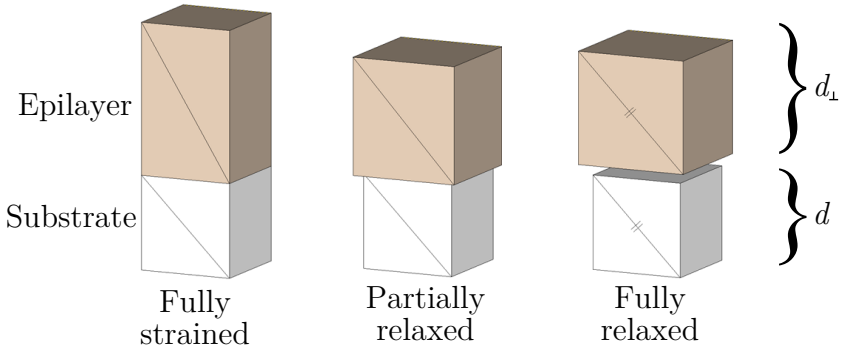

Figure 2.8: Schematic diagram of the different possible biaxial compressive strain statuses for a cubic epitaxial film with lattice parameter larger than that of the substrate material.

An x-ray beam incident on a crystal lattice will be diffracted and interfere with itself to produce constructive and destructive interference. For x-rays of wavelength λ incident on parallel planes of atoms, with a space d between the planes, Bragg peaks (constructive interference) occur when Bragg's law is satisfied:

$$n\lambda_{\text{hkl}} = 2d_{\text{hkl}}\sin(\theta_{\text{B}}), \tag{2.14}$$

where n is an integer, θ_{B} represents Bragg's angle and hkl are the Miller indices for the set of planes analysed. For the diffracted x-ray beam to undergo constructive interference, the difference in the distance travelled by diffracted waves must be an integer multiple of wavelengths. Diffraction measured away off of the Bragg angle will have a significantly reduced intensity, forming a Bragg peak with a finite linewidth. The higher the number of diffraction planes, the larger the diffraction intensity and

the narrower the measured peak. Peak linewidths will approach the bulk crystal limit with greater lattice perfection and will broaden in the presence of defects such as dislocations and structural disorder.

For a compressively strained epitaxial growth on a substrate, XRD will exhibit two Bragg peaks in close proximity that correspond to the lattice parameter of the substrate and the epilayer. This is due to the vertical deformation of the lattice cell in the epilayer, when lattice matched in the growth plane to the substrate. A diagram representing the possible strain states in a compressively strained film is shown in Fig. 2.8. By Eq. 2.14, a larger lattice parameter will diffract at a smaller angle, resulting in negative peak splitting (with respect to the substrate), while the opposite is true for a smaller lattice parameter. In combination with Vegard's law[85], for the relationship between an alloy lattice parameter and composition, XRD measurements allow for an accurate assessment of the composition of ternary alloys (such as $GaAs_{1-x}Bi_x$). The determination of Bi concentration in $GaAs_{1-x}Bi_x$ films is explored in more detail in Chapter 4.

Instrumentation

The penetration of x-rays into the crystal surface is on the order of microns and hence XRD is very sensitive to detecting peaks arising from both the epitaxial layer and substrate. XRD data were recorded from GaAsBi epitaxial layers with thicknesses ranging from approximately 0.3 to 1 μm using a PANalytical X'Pert Pro instrument in line focus geometry. The typical XRD scan on a semiconductor thin film is the 2θ scan. The PANalytical X'Pert Pro is a θ:θ instrument, where the sample is vertically mounted and is fixed as the x-ray tube rotates at a rate of $-\theta^\circ$/min and the detector rotates at a rate of $+\theta^\circ$/min. In this way, the incident angle, ω, is defined between the x-ray source and a stationary sample, and is half of the detector angle, 2θ.

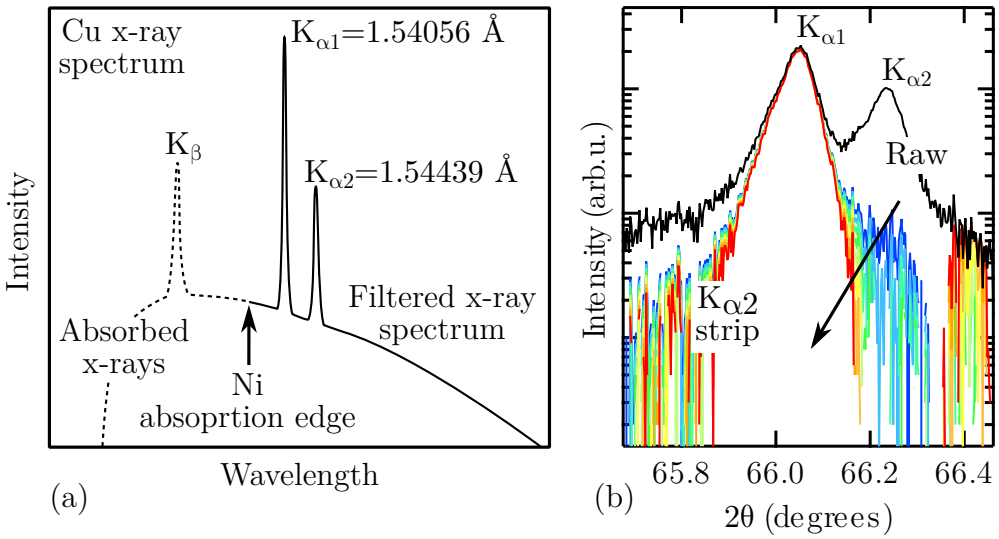

Figure 2.9: (a) Schematic illustration of a Ni-filtered Cu x-ray source (solid trace) showing Cu$K_{\alpha1,2}$ emission peaks, and (b) XRD 2θ-scan from symmetric (004) Bragg reflection of bulk (001) GaAs. The lower intensity traces in (b) (labeled $K_{\alpha2}$ strip) have had Cu$K_{\alpha2}$ contributions removed by employing the Rachinger method, using $K_{\alpha2}/K_{\alpha1}$ ratio values ranging from 0.42 (blue; base of arrow) to 0.58 (red; head of arrow).

The x-rays were generated using a standard Cu x-ray source employing a 10 mA current accelerated by a 40 kV difference between the filament and the copper target. The energy of the electrons incident on the source target is sufficiently high to knock out the inner electrons in the Cu atoms, producing characteristic emission peaks as illustrated in Fig. 2.9(a). For the removal of unwanted K_{β} peaks, a Ni absorber/filter was employed in the x-ray optics, while the $K_{\alpha1,2}$ emissions were employed for diffraction measurements.

In this thesis, 2θ-scans were recorded across the relevant Bragg angle of the investigated crystals and involved the detection of two separate diffraction peaks arising from both the $K_{\alpha1}$ and the $K_{\alpha2}$ emissions. A representative raw 2θ-scan measured from a symmetric (004) reflection of bulk GaAs in the vicinity of 66° is displayed in Fig. 2.9(b). Due to the close proximity of peaks reflected from both the GaAsBi epitaxial layers and GaAs substrates, and the dual nature of characteristic Cu$K_{\alpha1,2}$ x-ray

peaks, it is important to clearly define the procedure employed to remove experimental ambiguities.

To resolve and interpret a single x-ray diffraction peak arising from complementary diffraction planes, Fig. 2.9(b) presents both the raw data (containing $K_{\alpha1}$ and $K_{\alpha2}$ Bragg peaks) and data which has been stripped of the $K_{\alpha2}$ contribution employing the Rachinger correction method[86] using several $K_{\alpha2}/K_{\alpha1}$ ratio values. The Rachinger correction essentially assumes that the intensity of $K_{\alpha2}$ is some proportion of $K_{\alpha1}$, so that for a diffraction peak the contribution from $K_{\alpha2}$ has the same shape as $K_{\alpha1}$, except that it contributes a smaller height and is shifted towards larger angles by $\Delta(2\theta) = 2\tan(\theta)\Delta\lambda\lambda$, where $\Delta\lambda = \lambda(K_{\alpha2}) - \lambda(K_{\alpha1})$.

While the nominal relative intensity of $K_{\alpha1}$ and $K_{\alpha2}$ emissions is close to 2:1, experimental factors can strongly shift the experimentally-detected weighting. Thus, we present nine traces indicating nine different $K_{\alpha2}$ strip procedures made using $K_{\alpha2}/K_{\alpha1}$ ratio values ranging from 0.42 to 0.58. At either of the extremes assigned to this value, we see large distortions on the high scattering shoulder of the $K_{\alpha1}$ peak. Implementing a $K_{\alpha2}/K_{\alpha1}$ ratio value of 0.47 was found to produce the most agreeable stripping of $K_{\alpha2}$ Bragg peaks in the data recorded using our XRD instrument. For all 2θ-scans recorded from the samples under investigation in this thesis, a similar process to that defined in Fig. 2.9(b) was performed in order to accurately revolve scattering features. The XRD data shown in Chapter 4 is presented stripped of $K_{\alpha2}$ contributions.

2.3.4 Scanning electron microscopy

Principles of scanning electron microscopy

Scanning electron microscopy (SEM) is technique used to image materials well beyond the resolvable limits of traditional light microscope systems, and is capable of achieving magnifications on the order of $\times 1\,000\,000$, with 1 nm resolution. The capacity to

examine the very small has seen SEM imaging become a common experimental tool in nanotechnology research.

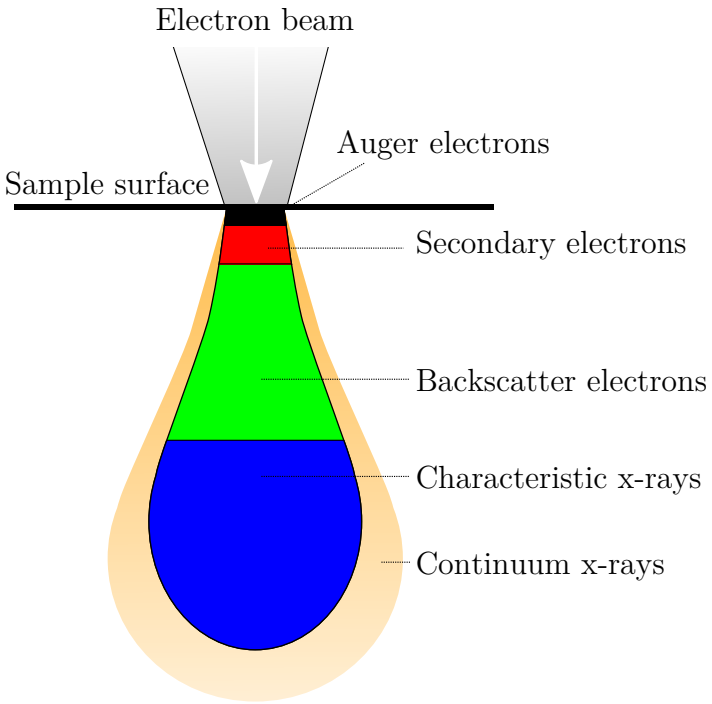

Figure 2.10: Illustration of the teardrop model used to describe the electron interaction volume/depth from which the different electron-solid interactions and signals originate.

In SEM, an electron beam is focused to a spot on the order of 1 nm and scanned across a sample surface. Electrons impinging on the sample surface will generate a variety of signals, and it is the detection of specific signals which produces an image or a material's elemental composition. The three signals which provide the greatest amount of information in SEM are the backscatter electrons (BSEs), secondary electrons (SEs) and characteristic x-rays. Figure 2.10 illustrates the relative interaction volumes and depths for each of the different signals. The depths from which the signals are detected strongly depend on the voltage used to accelerate electrons towards the sample surface. Higher accelerating voltages will produce larger interaction volumes while retaining its 'teardrop' shape/profile.

Inelastic scattering creates SEs which escape from atoms near the surface to produce

an easy-to-interpret image of the sample topology. The contrast in an SE-SEM image is determined by the sample morphology. A high resolution image can be obtained because of the small diameter of the primary electron beam.

BSE are primary beam electrons which undergo elastic backscattering (reflected) from atoms in the sample. For crystalline materials, the contrast in the image produced by BSEs is determined by the atomic number of the elements in the sample as well as the local arrangement of atoms (material crystallinity or orientation) relative to the incident beam. The image will therefore show contrast where the distribution of elements (composition) and their arrangement differ. Because these electrons are emitted from some depth in the sample, the zone of production is relatively large (see Fig. 2.10) and the resolution in a BSE image is far less than that of an SE image.

When the energy of electrons in the incident beam is sufficiently high when striking atoms within the sample, an electron from the inner shell of atom may be knocked out of position. Ionised atoms will refill the inner vacancies with outer electrons − through well-defined transitions − and emit characteristic x-ray photons. Thus, the energy of characteristic x-rays is dependent on the atomic number of the atom. Detection and measurement of the energy permits elemental analysis; energy dispersive x-ray spectroscopy (EDS). EDS can provide rapid qualitative, or with adequate standards, quantitative analysis of elemental composition. The depth from which characteristic x-rays can be produced is of the order of tens of nm to microns, depending on the accelerating voltage. An EDS spectrum will also involve a broadband contribution due to continuum x-rays produced by decelerating the incident electron beam.

Instrumentation

The SEM characterisation in this work was recorded using a JEOL JSM-7001f electron microscope. This instrument is a Schottky field emission microscope and was selected

for its ability for extremely high resolution x-ray analysis (tens of nm) and imaging (∼1.2 nm). As outlined above, the accelerating voltage employed to record data defines the interaction volume of the scanning signals. Where it is important, the accelerating and incident angle of the electron beam (relative to the surface normal) will be defined in the figure caption and an estimated interaction volume will be presented. The EDS modality does not lend itself to the absolute determination of composition in thin semiconductor epitaxial layers, as it usually involves significant components of scaling and relative error. Thus, standardless EDS quantitative analysis is used in this thesis to confirm the relative composition of materials.

2.3.5 Atomic force microscopy

Principles of atomic force microscopy

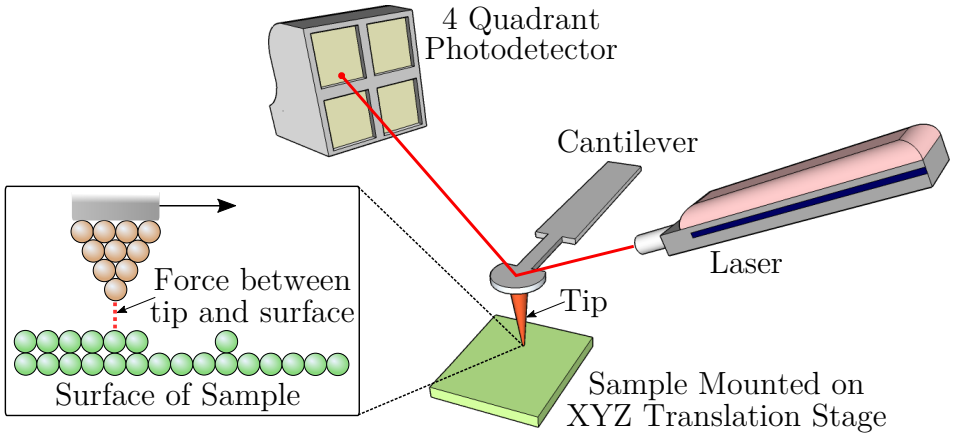

Figure 2.11: Schematic illustration of AFM detection system. As the cantilever is vertically displaced by changes in the surface topography, laser light is reflected off the tip onto a detector which assesses movement.

Atomic force microscopy (AFM) differs from other microscopies in that this method mechanically/physically makes contact with the sample's surface, mapping the height or some other property, rather than focusing light or electrons onto the surface; Fig. 2.11

shows a schematic diagram of an AFM measurement. In this case, a sharp tip attached at the end of a cantilever scans the selected surface area with atomic resolution maintaining a constant force or a force gradient by a feedback loop. Topological changes deflect the tip up or down via the ionic repulsion between tip and surface, and the amount of banding in the cantilever is recorded by the movement of a reflected laser beam incident on a 4 quadrant photodetector. The final surface profile is acquired through a sequence of linescans to form a 3D-AFM image.

Instrumentation

Topographic measurements were performed using a model MFP-3DTM AFM instrument produced by Asylum Research, operating in tapping mode. This instrument offers very low noise and high resolution in both the sample plane ($\sim$0.5 nm) and height ($\sim$0.25 nm), while allowing relatively large areas to be scanned in one measurement (30 μm $\times$30 μm).

Chapter 3

Polarised Raman backscattering selection rules for (hhk)-oriented zincblende crystals

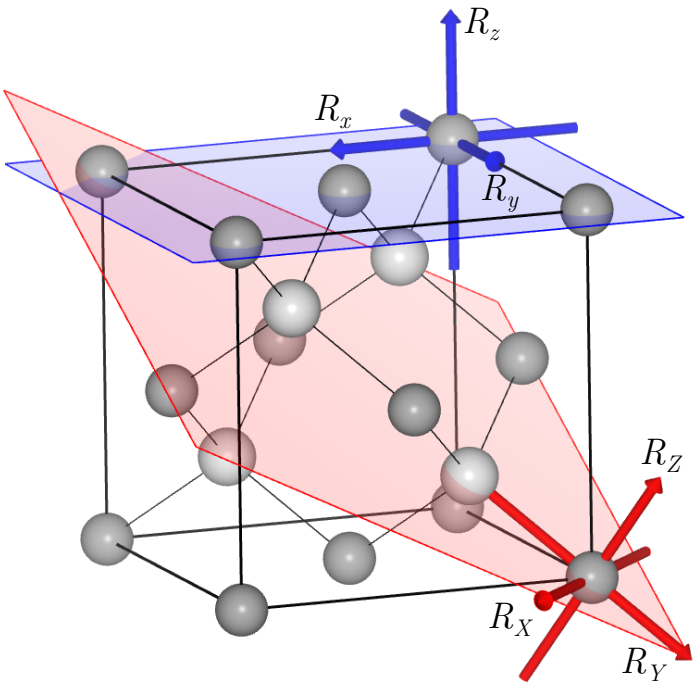

A transformation of a set of orthogonal vectors used to described the crystal geometry.

3.1 Motivation

Recent developments in semiconductor growth technologies have seen new innovative structures grown on ever higher crystal faces, by exploiting orientation-dependent growth procedures[87–89]. The fascinating properties and useful advantages of high-index semiconductor fabrication, as well as heteroepitaxial growth atop high-index substrates, have seen growth directions as high as [119] utilised[88–90]. This is largely due to the surface step structures exhibited by high-index crystal planes, which play an important role in the vapour-solid reaction processes (epitaxial growth). The manner by which atoms are arranged on the crystal surface during growth − known as the surface reconstruction − strongly vary with different crystallographic growth directions. Surface reconstruction can affect the important mechanisms of epitaxial deposition[79,91] as well as the final bulk properties[89]. Studies of $(11k)$ crystal growths misoriented between (001) and (110) planes (see Fig. 3.1(a) to clearly visualise such a misorientation) have seen dramatic changes to dopant incorporation[90], while also offering altered piezoelectric properties[92]. In particular, for polar systems, high-index $(11k)$ faces for $k > 3$ have been shown to have a significantly reduced polarity; these kinds of surface are sometimes termed 'semipolar'[87].

Determining the local orientation and quality of the crystal structure with high lateral resolution is vital to understanding an array of emerging crystal growth techniques at the nano- and micron-scale. Modern micro-Raman scattering systems are powerful tools for such investigations, providing valuable information on structure and phase, while being non-destructive, easy to implement and increasingly accessible to materials research scientists[93]. The so-called quasi-backscattering geometry utilised in micro-Raman scattering is particularly useful in the investigation of semiconductors, because the materials are often opaque to the laser excitation wavelengths typically employed. In this case, the micro-Raman backscattering geometry actually maximises

scattered light collection.

For light backscattered from an arbitrary (hhk)-oriented crystal surface, symmetry determines the Raman activity of the optical phonon modes. The *Raman selection rules* are symmetry considerations, based on group theory, which provide the necessary conditions for phonon modes to be Raman active. Symmetry determines which components of the susceptibility tensor $\tilde{\chi}$ will be nonzero; this predicts the experimental polarisation directions of incident and scattered light for which a nonvanishing Raman scattering intensity may be expected. For backscattering along the crystal growth axis (c axis) and the polarisation vector of incident and scattered light represented respectively by $\hat{e}_i$ and $\hat{e}_s$, the experimental configuration is compactly described using Porto notation[94]: $\bar{c}(\hat{e}_i,\hat{e}_s)c$.

III-V compounds often adopt the zincblende structure (point group T_d), which is analogous to the diamond structure (point group O_h), but where each atom has nearest neighbours of an unlike element. Thus, many of the conclusions drawn in this chapter will actually have direct and transferable implications to diamond structured materials, such as silicon.

For polar alloys, the transverse (TO) and the longitudinal (LO) optical vibration energies are split due to electrostatic interactions. TO phonon scattering is induced by the deformation potential, while LO scattering is usually stronger because it is induced by deformation and electrostatic effects. Relative to a non-polar system, such as silicon, this presents an enhancement of the information content for a given polarised Raman spectrum, due to the existence of TO and LO phonons with different frequencies, intensities and polarisation behaviour.

The Raman tensors for all of the different crystal *symmetries* have been derived previously and are given by Hayes and Loudon[95]. Considering the degrees of freedom between the orientation of the crystal under investigation, and the possibility of control-

ling polarising optics before and after surface scattering, a unique set of Raman tensors is required to accurately explain and evaluate polarised Raman scattering experiments. Concluding crystallographic information via an application of this rigid relation is to implement the Raman selection rules.

While it is now almost thirty years since Mizoguchi and Nakashima[96] first reported an algorithmic micro-Raman measurement designed to determine crystallographic orientations of silicon films, it is surprising that the Raman scattering tensors for crystal indices higher than (113) are yet to be reported. In fact, this anomalous gap in scientific reporting is further worsened for the case of common non-(001) zincblende growth directions, such as [112], where inconsistencies are found between different reports on what the correct Raman tensors actually are − even when employing the *same* coordinate basis sets[97,98].

The aim of this preliminary chapter is to derive the Raman scattering tensors for high-index zincblende crystals up to (119) and examine them within the context of their experimental consequences for common polarised Raman backscattering configurations. Through careful measurement and analysis, polarised Raman scattering data will experimentally validate the derivation of the Raman tensors up to (115)-GaAs. Later, the Raman tensors will assist in Chapter 4 to clearly explain the first-order Raman spectra recorded from (001) and (113)B GaAsBi/GaAs epitaxial layers. In the event of micro-probing crystal surfaces of an unknown direction, we will see in Chapter 5 that their local orientations can be readily determined through detailed polarised Raman analysis.

Note that experimental measurements and analysis of the Raman selection rules for high-index zincblende growth directions beyond [113] are yet to be reported, and constitutes new work.

3.2 Raman tensors for an arbitrary (*hhk*)-oriented zincblende crystal

The nonresonant intensity of the Raman backscattering signal $I(\hat{e}_i,\hat{e}_s)$ can be related to the second-rank Raman tensor

$$\tilde{\mathcal{R}}_j = \begin{bmatrix} \mathcal{R}_{xx} & \mathcal{R}_{xy} & \mathcal{R}_{xz} \\ \mathcal{R}_{yx} & \mathcal{R}_{yy} & \mathcal{R}_{yz} \\ \mathcal{R}_{zx} & \mathcal{R}_{zy} & \mathcal{R}_{zz} \end{bmatrix}, \tag{3.1}$$

which is dependent on the crystal symmetry:

$$I(\hat{e}_i, \hat{e}_s) \propto I_0 \cdot \sum_{j=1}^{3} \mid \hat{e}_i \cdot \tilde{\mathcal{R}}_j \cdot \hat{e}_s \mid^2 . \tag{3.2}$$

Here $\hat{e}_i$ and $\hat{e}_s$ represent the polarisation vectors of the incident and scattered light, respectively, and I_0 contains all fixed experimental parameters (laser intensity, excitation wavelength, integration time, etc.). The index j discriminates the three phonon polarisation directions x, y and z. LO phonons will vibrate in the z direction, while TO phonons will vibrate along the x and y directions.

For a zincblende crystal possessing T_d symmetry, we adopt the notation commonly given for the 3×3 Raman tensors in the main crystal axis system ($x = [100]; y = [010]; z = [001]$), with off-diagonal elements

$$\tilde{\mathcal{R}}_x = \begin{bmatrix} 0 & 0 & 0 \\ 0 & 0 & d \\ 0 & d & 0 \end{bmatrix}; \tilde{\mathcal{R}}_y = \begin{bmatrix} 0 & 0 & d \\ 0 & 0 & 0 \\ d & 0 & 0 \end{bmatrix}; \tilde{\mathcal{R}}_z = \begin{bmatrix} 0 & d & 0 \\ d & 0 & 0 \\ 0 & 0 & 0 \end{bmatrix}. \tag{3.3}$$

Here d indicates the non-zero Raman polarisability elements and are generally different

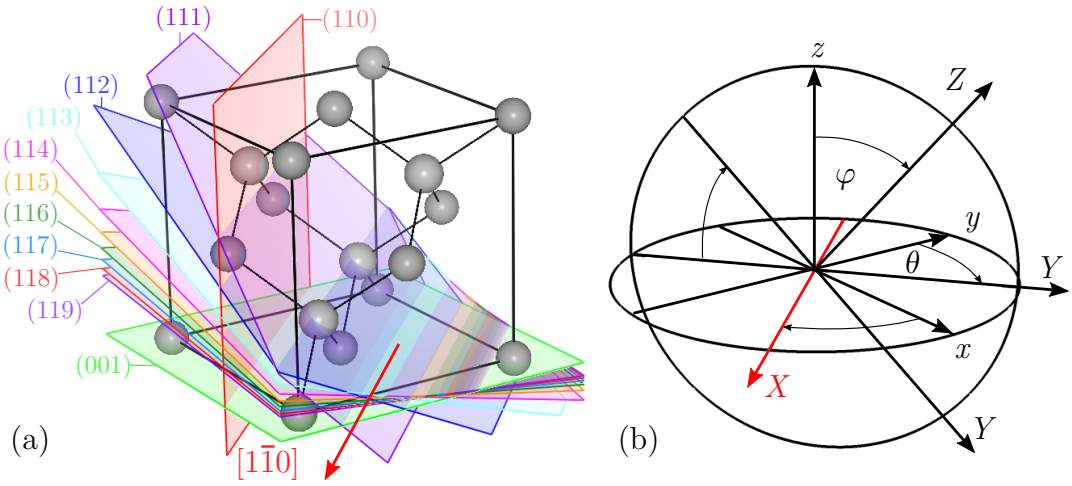

Figure 3.1: (a) Zincblende/diamond structure unit cell showing the various (*hhk*)-oriented crystal planes ranging between (001) and (110), and (b) schematic representation of coordinate system used for a spatial transform between the various *c*-axes. The red X axis shown in (b) and the red $[1\bar{1}0]$ direction in (a) align, where crystallographic rotations around X see its $[1\bar{1}0]$ direction maintained. The two diagrams are related through a rotation of φ around $[1\bar{1}0]$ (X), which translates the Z through each of the (*hhk*) planes in, as depicted in (a).

for the LO and TO modes; i.e. $d_{\mathrm{LO}} \neq d_{\mathrm{TO}}$. These tensors are equal to that described by Eq. 2.11 in Chapter 2, with x, y, and z here providing directions of the phonon-induced lattice deformation. For light Raman backscattered along the z axis, the intensity of the LO phonon mode will be

$$I_{\mathrm{LO}} \propto | \, \hat{e}_i \cdot \tilde{\mathcal{R}}_{\mathrm{LO}_z} \cdot \hat{e}_s \, |^2, \tag{3.4}$$

while for the case of TO phonons, the intensity is described by a proportionality to

$$I_{\mathrm{TO}} \propto | \, \hat{e}_i \cdot \tilde{\mathcal{R}}_{\mathrm{TO}_x} \cdot \hat{e}_s \, |^2 + | \, \hat{e}_i \cdot \tilde{\mathcal{R}}_{\mathrm{TO}_y} \cdot \hat{e}_s \, |^2 \tag{3.5}$$

For light backscattered from different (*hhk*) crystal planes, it is useful to assign Raman tensors with respect to a coordinate system axes (X, Y, Z) which are attached to the (*hhk*)-oriented crystal under investigation, as well as specify the Z direction

to be parallel to the incident/scattered light. A derivation of the new Raman tensors requires the application of three transformation matrices; two rotation matrices to define the new basis sets, and a final matrix associated with the phonon polarisation.

Figure 3.1 presents both the various (hhk) planes of the zincblende crystal and the coordinate system used to rotate the crystal geometry in 3D space. Given we investigate here the specific case of (hhk)-oriented crystal growth, and by way of mathematical convenience, we adopt an easily transformative reference frame; for φ rotations, our $[1\bar{1}0]$ crystal direction is systematically in-plane with the surface, as demonstrated in Fig. 3.1(a) and (b), and allocated as the X axis. As high-index faces are successively accessed, a larger φ rotation is made around the $[1\bar{1}0]$ direction (X).

Figure 3.1(b) shows the unrotated laboratory coordinates (x, y, z), whereby two angles of rotation, θ and φ, are made around z and X, respectively. It follows that axis Y coincides with the $[kk, 2\bar{h}]$ direction, with the different growth orientations characterised by $\varphi = ([001], [hhk])$ in the Y-Z plane.

To calculate the selection rules for (hhk)-oriented zincblende systems, appropriate Raman tensors must be transformed into the experimental coordinate system using general basis

$$(X, Y, Z) = ([1\bar{1}0], [kk, 2\bar{h}], [hhk]). \tag{3.6}$$

The transform of the basis is made in two separate steps, whereby an initial $\theta = \pi/4$ rotation is made around the $z = [001]$ to enter a ($[1\bar{1}0]$,[110],[001]) basis. Then, as illustrated in Fig. 3.1, a φ rotation proceeds around X (in Z-Y plane) to access the different (hhk) growth directions. These rotations can be described by the matrix

$$A(\theta = \frac{\pi}{4}) = \begin{bmatrix} \frac{1}{\sqrt{2}} & \frac{1}{\sqrt{2}} & 0 \\ -\frac{1}{\sqrt{2}} & \frac{1}{\sqrt{2}} & 0 \\ 0 & 0 & 1 \end{bmatrix} \tag{3.7}$$

and a form of Rodrigue's rotation formula [99]

$$R(\varphi) = \cos\varphi \mathrm{I} + \sin\varphi[\hat{u}]_\times + (1-\cos\varphi)\hat{u}\otimes\hat{u}, \tag{3.8}$$

where A denotes the transformation into a system with a $[1\bar{1}0]$-pointing X axis and R is a rotation φ about the X axis (with unit vector $\hat{u} = \frac{1}{\sqrt{2}}[1\bar{1}0]$). Here $[\hat{u}]_\times$ denotes the cross product matrix of $\hat{u}$ and I is the identity matrix, with

$$\hat{u}\otimes\hat{u} = \begin{bmatrix} u_x^2 & u_xu_y & u_xu_z \\ u_xu_y & u_y^2 & u_yu_z \\ u_xu_z & u_yu_z & u_z^2 \end{bmatrix}, \quad [\hat{u}]_\times = \begin{bmatrix} 0 & -u_z & u_y \\ u_z & 0 & -u_x \\ -u_y & u_x & 0 \end{bmatrix}. \tag{3.9}$$

The total transformation matrix, $T = RA$, simplifies to

$$T = \begin{bmatrix} \frac{1}{\sqrt{2}} & \frac{\cos\varphi}{\sqrt{2}} & \frac{\cos\varphi-1}{2} + \frac{\sin\varphi}{\sqrt{2}} \\ \frac{1}{\sqrt{2}} & \frac{\cos\varphi}{\sqrt{2}} & \frac{\sin\varphi}{\sqrt{2}} \\ 0 & -\sin\varphi & \cos\varphi \end{bmatrix} \tag{3.10}$$

where, for our cubic system

$$\cos\varphi = \frac{k}{\sqrt{2h^2+k^2}} \text{ and } \sin\varphi = \frac{h\sqrt{2}}{\sqrt{2h^2+k^2}}.$$

The transformation matrix is orthogonal ($T^T = T^{-1}$) and the transformation takes the form $\tilde{\mathcal{R}'}_j = T\tilde{\mathcal{R}}_jT^T$. Multiplied by the phonon polarisation in the transformed basis, we arrive at the new Raman tensors for the first-order optical modes:

$$\tilde{\mathcal{R}}_{\mathrm{TO}_X,\mathrm{TO}_Y,\mathrm{LO}_Z} = \tilde{\mathcal{R}'}_jQ'_j. \tag{3.11}$$

Here the jth term discriminates the three phonon polarisation directions X, Y and

Z. Inserting the rotated Raman tensors into Eq. 3.2, one can proceed to simply determine the Raman activity of LO and TO vibrations through Eqs. 3.4 and 3.5. The MATLAB code implementing this procedure, as well as the Raman tensors calculated (in units of the Raman polarisability, $d_{\mathrm{LO,TO}}$) for crystal faces up to the (119) plane, are provided in Appendix A. Note that the algorithm in this code was developed with direct correspondence and assistance from Dr. Pascal Puech.

3.3 Experimental consequences of polarised Raman backscattering configurations

It was shown useful in Section 3.2 to specify Raman tensors based on a coordinate system of axes (X, Y, and Z) which are attached to the investigated microstructure. However the polarisation vector terms in Eq. 3.2 for incident ($\hat{e}_i$) and scattered light ($\hat{e}_s$) are yet to receive detailed treatment. Figure 3.2 shows the geometry of a polarised Raman backscattering configuration and relates the employed basis coordinate system to the laboratory coordinates, with backscattering occurring in the $\pm Z$ direction ($Z \parallel c \parallel k$). In the laboratory coordinates, the polarisation of incident and scattered radiation takes the form

$$\hat{e}_i = \begin{bmatrix} \sin(\alpha) \\ \cos(\alpha) \\ 0 \end{bmatrix} \quad \text{and} \quad \hat{e}_s = \begin{bmatrix} \cos(\alpha+\beta) \\ \sin(\alpha+\beta) \\ 0 \end{bmatrix}. \tag{3.12}$$

Here angles α and β are measured relative to Y, and are realised using a rotation stage and rotating polariser (analyser), respectively. Thus all rotations are made relative to a *fixed* $\hat{e}_i$, which was intentional to avoid problems introduced by the intrinsic polarisation of the laser light source (typical for solid-state, ion or otherwise). It

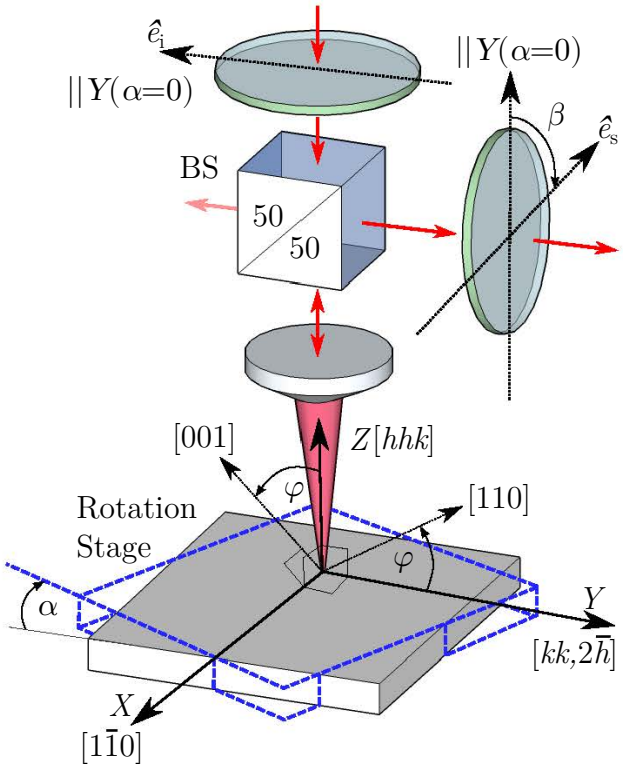

Figure 3.2: Schematic diagram of typical micro-Raman experimental configuration and the coordinate systems employed in the backscattering geometry from (hhk)-oriented crystal faces. Here $\hat{e}_i$ and $\hat{e}_s$ indicates the polarisation of the incident and scattered light, respectively. The other terms are explained in the text.

follows, for the general case, the intensity of the measured first-order optical phonon bands is described by:

$$I \propto \left| \begin{bmatrix} \sin(\alpha) & \cos(\alpha) & 0 \end{bmatrix} \begin{bmatrix} \mathcal{R}_{xx} & \mathcal{R}_{xy} & \mathcal{R}_{xz} \\ \mathcal{R}_{yx} & \mathcal{R}_{yy} & \mathcal{R}_{yz} \\ \mathcal{R}_{zx} & \mathcal{R}_{zy} & \mathcal{R}_{zz} \end{bmatrix} \begin{bmatrix} \cos(\alpha+\beta) \\ \sin(\alpha+\beta) \\ 0 \end{bmatrix} \right|^2 . \tag{3.13}$$

This equation contains all the degrees of freedom possessed in a standard Raman backscattering measurement. For β angles of 0 and $1/\pi$, $\hat{e}_i$ and $\hat{e}_s$ will be parallel and perpendicular, respectively. Thus an appropriate α rotation in these two geometries will allow access to the four main polarised configurations of backscattering measure-

Table 3.1: Raman backscattering selection rules for different experimental configurations given in terms of generalised Raman tensor elements.

Polarised configuration	Selection rules $I_{\mathrm{LO}} \propto I_{\mathrm{LO}_Z}$; $I_{\mathrm{TO}} \propto I_{\mathrm{TO}_X} + I_{\mathrm{TO}_Y}$
$Z(YY)\bar{Z}$	$\lvert\mathcal{R}_{yy}\rvert^2$
$Z(YX)\bar{Z}$	$\lvert\mathcal{R}_{yx}\rvert^2$
$Z(XX)\bar{Z}$	$\lvert\mathcal{R}_{xx}\rvert^2$
$Z(XY)\bar{Z}$	$\lvert\mathcal{R}_{xy}\rvert^2$
$\hat{e}_i \parallel \hat{e}_s(\alpha)$	$\left\lvert\mathcal{R}_{xx}\sin^2(\alpha) + \mathcal{R}_{yy}\cos^2(\alpha) + \frac{(\mathcal{R}_{yx}+\mathcal{R}_{xy})}{2}\sin(2\alpha)\right\rvert^2$
$\hat{e}_i \perp \hat{e}_s(\alpha)$	$\left\lvert\frac{(\mathcal{R}_{xx}+\mathcal{R}_{yy})}{2}\sin(2\alpha) + \mathcal{R}_{yx}\cos^2(\alpha) + \mathcal{R}_{xy}\sin^2(\alpha)\right\rvert^2$
$\hat{e}_i \parallel Y, \hat{e}_s(\beta)$	$\lvert\mathcal{R}_{yx}\sin(\beta) + \mathcal{R}_{yy}\cos(\beta)\rvert^2$
$\hat{e}_i \parallel X, \hat{e}_s(\beta)$	$\lvert\mathcal{R}_{xx}\sin(\beta) + \mathcal{R}_{xy}\cos(\beta)\rvert^2$

ments, which are presented with their respective selection rules in the first four rows of Table 3.1. Fixing $\hat{e}_i$ and $\hat{e}_s$ to be parallel or perpendicular, and rotating the sample through α, will yield the polar-type measurements described by rows 5 and 6, respectively. Polarising the incident light $\hat{e}_i$ in either the Y or X directions (via the necessary α rotation) and rotating the analyser through β will respectively generate the bottom rows, 7 and 8.

Because the alignment of $\hat{e}_i$ or $\hat{e}_s$ with either X or Y basis direction is not assured for a system of unknown orientation, $I(\hat{e}_i \parallel \hat{e}_s(\alpha))$ measurements rotated through α usefully abnegates the need to establish such a reference direction; this can be determined by the analysis. To investigate unknown crystal orientations in Chapter 5, the $\hat{e}_i \parallel \hat{e}_s(\alpha)$ polarised Raman backscattering geometry is employed. Figure 3.3 displays the theoretical intensity of LO and TO modes measured in this configuration, as a function of the sample rotation, α.

Examining these data reveals several general rules for polarised Raman backscattering from different (hhk) zincblende surfaces. First, for light backscattered from a (001) face, only LO phonon modes are active, with the TO band being symmetry forbidden.

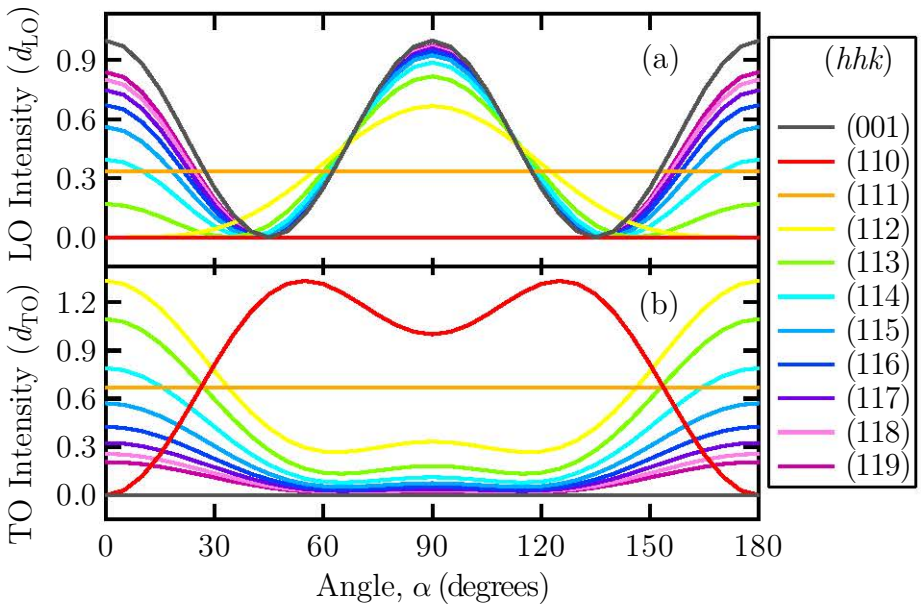

Figure 3.3: Calculated first-order Raman scattering intensity from a zincblende crystal using a parallel-polarised excitation and detection geometry ($\hat{e}_i \parallel \hat{e}_s$) as a function of a rotation around Z, α. (a) intensity of measured LO phonon band, and (b) intensity of the TO phonon modes with contributions from both perpendicular displacements (X and Y).

Conversely the Raman signal from (110)-oriented crystals should only contain contributions from TO phonons, with the LO mode symmetry forbidden for this surface. On the other hand, for Raman backscattering in the high-symmetry [111] direction both LO and TO mode are active, with intensities that are invariant to changes in α. As the crystal plane rotates away from (111) to the high index (112) plane, and higher, through a larger ϕ rotation, we see a transition in general scattering behaviour, becoming more (001)-like nearer the (119) plane. As one would expect examining the relationship between the various (hhk) crystal planes in Fig.3.1, the exhibited changes in the scattering intensities of LO and TO phonons are very systematic and distinguished.

Next we verify the derived Raman tensors for (hhk) zincbelnde-type crystals by experimentally measuring the polarised Raman backscattering spectra from bulk (001), (110), (111), (112), (113), (114) and (115) GaAs crystals, and compare the data to

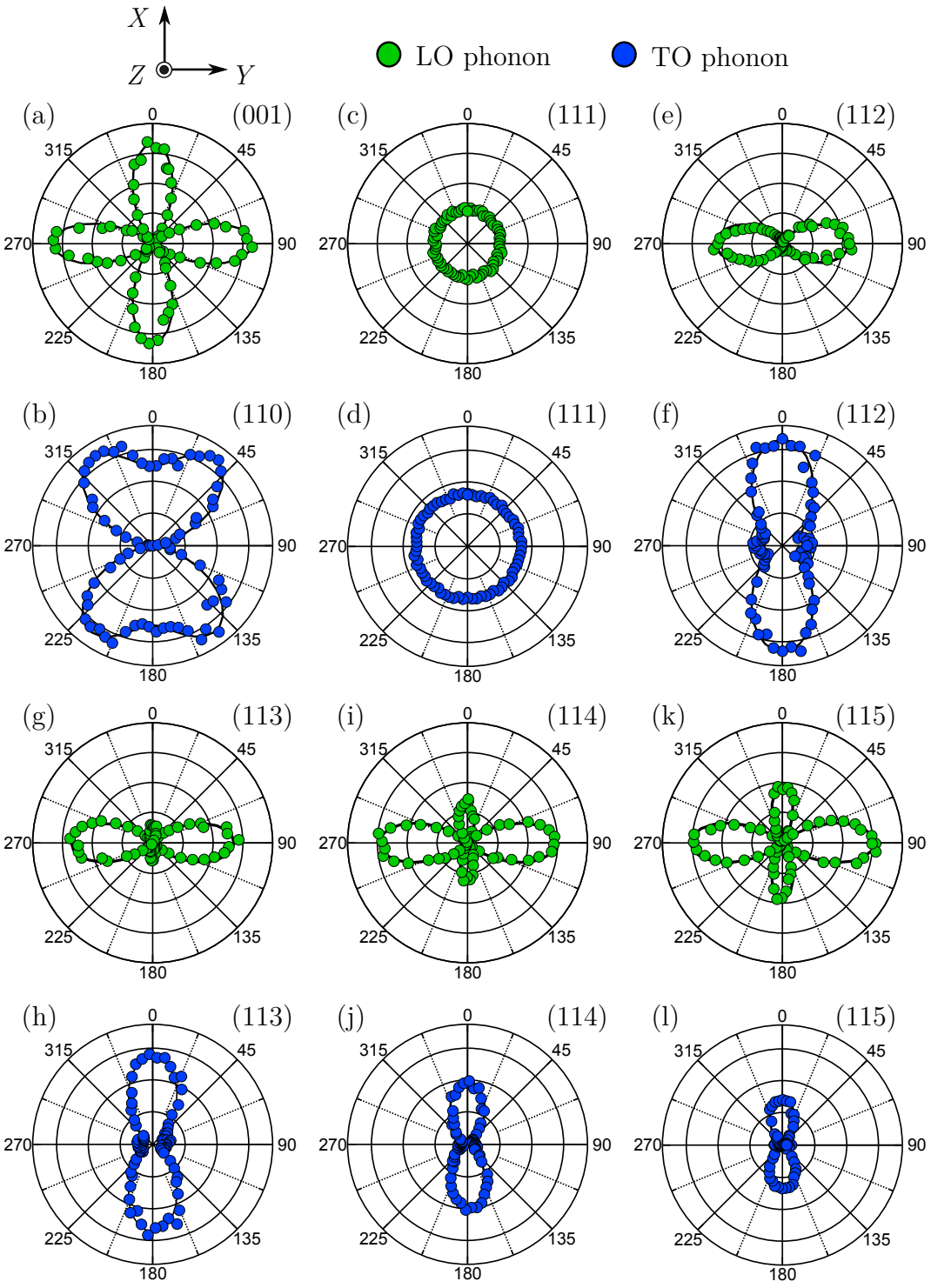

Figure 3.4: Polar plots of calculated (solid black lines) and experimental Raman data measured in a $I(\hat{e}_i \parallel \hat{e}_s(\alpha))$ configuration from bulk (a) (001), (b) (110), (c)-(d) (111), (e)-(f) (112), (g)-(h) (113), (i)-(j) (114) and (k)-(l) (115) GaAs.

theoretical calculations. The experimental geometry implemented for these measurements is the $\hat{e}_i \parallel \hat{e}_s(\alpha)$ configuration, which is described by selection rules presented in Table 3.1. Regardless of the relative direction between the polarisers and the studied crystal, this geometry offers great utility in determining unknown crystal orientation from one $\alpha = \pi$ rotation sequence. Polar plots of the first-order optical Raman peaks for GaAs are presented in Fig. 3.4 for a full $\alpha = 2\pi$ rotation, along with their calculated values. The data is described by the coordinate system (top of figure) and the generalised basis sets in Eq. 3.6, and forbidden vibrational mode (LO and TO bands from (110) and (001) planes, respectively) are not included. There is excellent agreement here between theory and experiment, confirming that the Raman tensors derived here are indeed the correct ones. Of the inconsistencies in the literature for tensors describing [112] Raman backscattering, it becomes clear those reported by Puech *et al.*[98] are accurate, while Bulkin *et al.*[97] appears to be incorrect. Figure 3.4 also reiterates the systematic nature of changes seen in the LO and TO phonons for an increasing crystal index, becoming more (001)-like at (115).

Chapter 4

Raman scattering studies of Bi-induced effects in (001)- and (113)B-oriented $GaAs_{1-x}Bi_x/GaAs$

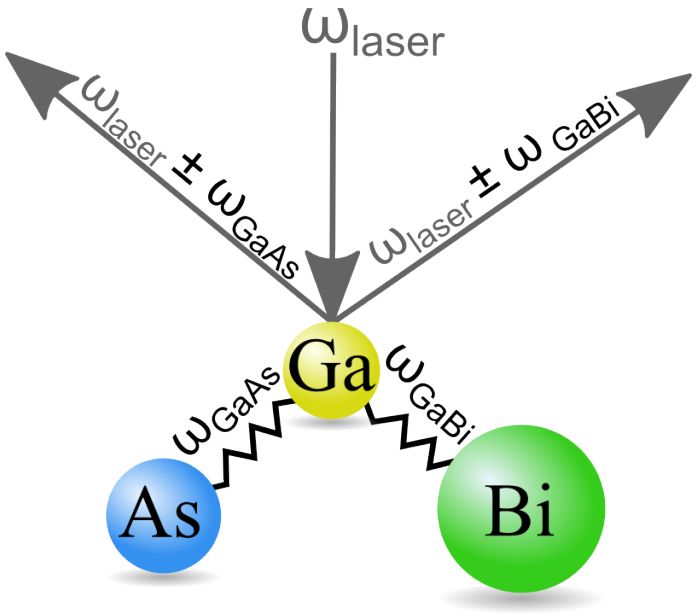

Illustration of the Raman scattering phenomenon and the two-mode vibrational behaviour of the ternary alloy GaAsBi.

4.1 Motivation

While ternary GaAsBi alloys are receiving much attention for the promising physical properties outlined in Chapter 1, many studies are also currently dedicated to methods of increasing the Bi solubility[4,29,72,79,100–102]. This is because growers are at present confronted with some physical and technical issues that have thus far restricted the amount of Bi able to be introduced into the GaAs matrix[103]. In addition to important growth parameters (temperature, species supply etc.), thermodynamic models of this system have indicated that the Bi solubility is a function of the strain state of the alloy[103], with the incorporation significantly stifled by the excess strain introduced via Bi alloying.

The largest Bi incorporation experimentally reported has been $x = 0.22$ for $GaAs_{1-x}Bi_x$ films grown on a bulk (001) GaAs substrate[68]. For films possessing sufficient optical gain and no apparent Bi surface phase separation, the highest Bi concentration still remains below a value nearer to $x = 0.06$[72,104]. Recently, high-index (113)B-oriented substrates were shown to allow for a sizably larger Bi incorporation at stoichiometric conditions, compared to (001) GaAs[79]. These results present a potential approach to improving the Bi incorporation efficiency in (In)GaAsBi(N) materials for long-wave device applications[43], through adopting high-index substrates such as (113)B.

When a bismuth atom bonds with a group III Ga atom in GaAs, the translational symmetry in the lattice is broken and new vibrational modes localised around the bismuth atom are established. Thus, there will exist both GaAs-like and GaBi-like phonon bands propagating through the two sublattices; such a behaviour is known as *two-mode behaviour*. Further, when a large bismuth atom substitutionally replaces a competitively smaller arsenic atom, lattice deformation and strain is introduced into the crystal, impacting the lattice dynamics. Phonon dispersion plays an important role in the physical properties of semiconductors such as carrier mobility and thermal

conductivity[105] and strongly affects device performance. Thus, it is important to first investigate the constituent alloy GaAsBi for its optical, vibrational and electronic properties.

As a tool for investigating the properties of new semiconductors, Raman spectroscopy has proven extremely successful in investigating the electronic and vibrational properties of the now relatively-well-studied GaAs(N, P, Sb) alloys. The relatively large difference in electronegativity and lattice parameter of GaBi (12%) and GaN (20%) to that of GaAs makes these alloys scientifically interesting. As a consequence, alloying introduces biaxial strain when growth is lattice matched to the GaAs substrate, which has a dramatic effect on the Raman spectrum. Both GaAsN and GaAsBi exhibit a two-mode behaviour, consistent with the current work. Both systems are have also been shown to exhibit similar disorder-activated GaAs-type bands, as well as evidence of mixing-of-states via Bi- and N-induced[30,31,106] resonant states existing within the band structure. Thus, it is particularly useful to make the comparison here between the two highly mismatched alloys. We find prior to this thesis work, however, only two Raman studies of GaAsBi epitaxial alloys in the literature[107,108]. Both studies set out to identify new GaBi modes, each focusing on only two (001) GaAsBi samples of relatively low bismuth concentrations ($x \leq 0.024$[107] and $x \leq 0.031$[108]). This highlights the need for further compositional investigations of GaAsBi.

Physical changes in the lattice through dilute Bi incorporation are expected, given the large disparity in atomic size between Bi and As. Far more exotic, and important for optoelectronic applications, are the Bi-induced changes to the electronic properties of the GaAs host[32,83]. Namely, as outlined in Chapter 1, Bi incorporation significantly reduces the bandgap energy; a schematic of the bandgap energy reduction is shown in Fig. 4.1. In the dilute regime, the bandgap decrease is caused largely by an increase in the valence band (VB) edge maxima, relative to the conduction band (CB) minima,

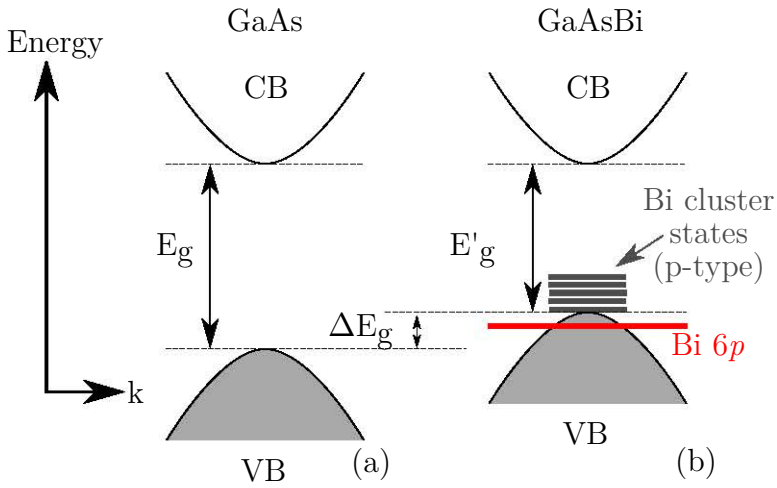

Figure 4.1: Schematic illustration of the (a) GaAs band structure and (b) the Bi-induced band structure changes observed in dilute GaAsBi. In (b) a reduction in the bandgap energy is realised mostly through a shifting of valence band (VB) edge, which is pushed up by the resonant Bi 6*p* orbital state. As well, the presence of Bi pair/clusters in the alloy manifests as localised *p*-type states just above the VB edge, in the forbidden region.

induced by the Bi 6*p* state which is *resonant* with the VB edge[32–34].

Recently, Nargelas *et al.*[109] showed alloying *nominally undoped* GaAs with group V Bi atoms counterintuitively introduces relatively large *p*-type carrier populations: holes thermally excited from Bi-induced acceptor levels lying 26.8 meV above the valence band edge in the forbidden bandgap[110] (see Fig. 4.1(b)). Pettinari *et al.*[111] revealed – through electrical transport measurements – that the hole concentration in fact rises with x up to $p = 2.4 \times 10^{17}\,\mathrm{cm}^{-3}$ at $x = 10.6\%$. They[112] further demonstrated that the acceptor states are passivated through hydrogen incorporation. Needless to say, within the context of current research on GaAsBi applications and device performance, these recent results have large implications for future technological interests.

In polar semiconductors like GaAs, LO(Γ) phonons couple strongly with the collective oscillations of the free-carrier system (plasmons). The extent of coupling, or mixing, is greatest when the two modes are of comparable energies and depends strongly on carrier concentration. For *n*-GaAs this results in two LO-plasmon-coupled (LOPC)

branches, L_+ (upper) and L_- (lower), for a given plasma frequency ω_p. However, due to large carrier damping, only one LOPC mode is generally observed in p-GaAs[113]. For reference, Fig. 4.3 presents the predicted frequencies of these coupled modes in GaAs, for rising hole concentrations.

Given the native acceptors in GaAsBi, one would expect damped LOPC modes in the Raman spectra in the vicinity of the first-order optical modes for sufficiently large carrier concentrations. An early Raman study of $GaAs_{1-x}Bi_x$ uncovered, along with new Ga-Bi centre scattering optical modes, damped LOPC modes for $x \leq 2.4\%$[107]. The free charge carriers were attributed to carbon contamination and the concentration was estimated to be greater than $10^{18}\,\mathrm{cm}^{-3}$[107].

The determination of native hole concentrations in dilute and unpassivated GaAsBi is very important for device fabrication. The Hall effect is typically the method used for measuring the carrier concentration in semiconductors, although it requires the fabrication of ohmic contacts. In this chapter, the first-order Raman scattering spectra from *nominally undoped* $GaAs_{1-x}Bi_x$/GaAs samples is investigated, for $x \leq 0.048$. From a detailed examination of the LO-phonon-hole-plasmon coupled mode, an all-optical method for determining the native free-carrier concentration is derived, revealing a hole concentration in excess of $5 \times 10^{17}\,\mathrm{cm}^{-3}$ and that correlates with the Bi mole fraction. While the absolute size of the hole concentrations determined here diverge from the transport measurements of Pettinari *et al.*[111], likely origins for the discrepancy are discussed.

4.2 The first-order Raman spectrum of GaAsBi

Figure 4.2(a) and (b) presents the typical off-resonance (with respect to the 632.91 nm laser excitation energy) first-order Raman scattering spectra of near-stoichiometric $GaAs_{1-x}Bi_x$ grown on (001)- and (113)B-oriented GaAs substrates, respectively. For

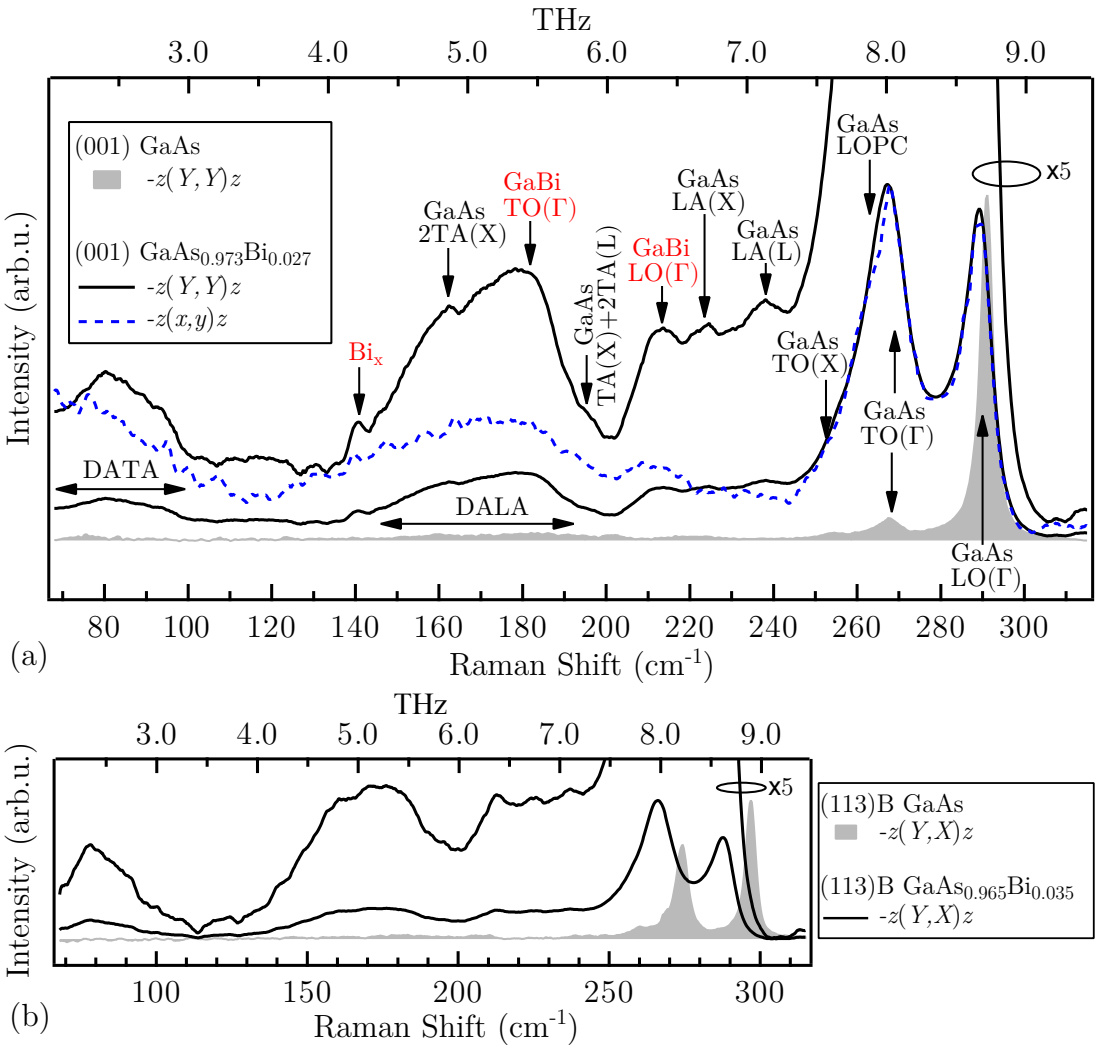

Figure 4.2: Normalised room-temperature Raman spectra of near-stoichiometric $GaAs_{1-x}Bi_x$ epitaxial layers grown on (001)- ($x = 0.027$) and (113)B-oriented ($x = 0.035$) substrates. The spectra were recorded in the polarised quasi-backscattering geometries shown – an explanation of this notation is provided in the text. To reveal weaker features, the upper traces have been reproduced enlarged five times.

comparison, the data have been normalised and spectra recorded from control samples ($x = 0$) is also displayed. Apart from a marked increase in the TO(Γ) mode intensity measured from the high index (113)B GaAsBi surface, the Raman spectra for both orientations are very similar and exhibit a clear two-mode behaviour (GaBi-, GaAs-like optical modes), as well as an interesting array of signature peaks; the assignment of spectral modes in Fig. 4.2(a) also applies to the readily-identifiable features in (b).

Table 4.1: Long-wavelength GaAs phonon frequencies for Brillouin zone high symmetry locations, determined by 296 K neutron scattering experiments [114]

Zone-Boundary	Phonon Mode	Phonon Frequency (cm^{-1})
Γ	TO	267
	LO	286
X	TA	79
	LA	227
	TO	252
L	TA	62
	LA	209
	TO	261
	LO	238

To assist in the interpretation of the GaAsBi first-order Raman scattering spectrum, Table 4.1 shows the vibrational frequencies of related long-wavelength GaAs phonons.

The data in Fig. 4.2(a) measured for both $-z(Y,Y)z$ and $-z(x,x)z$ polarised backscattering geometries; $-z$ and z respectively represent the incident and scattered photon directions (001) and $(00\bar{1})$, while $x = (001)$ and $Y = (110)$. According to the Raman selection rules in a zincblende crystal (T_d site symmetry), the LO(Γ) phonon is allowed for $-z(Y,Y)z$, although forbidden in $-z(x,x)z$, and the TO(Γ) mode is symmetry-forbidden for all (001) backscattering geometries. The relatively strong appearance of TO(Γ) in the Raman spectra (for example, see also Figs. 4.4 and 4.7) can be attributed to bismuth-induced disorder in the lattice, resulting in a relaxation of the Raman selection rules. While the LO(Γ) band is forbidden in the $-z(x,x)z$ geometry, its presence can likewise be linked to the disorder-induced lowering of lattice symmetry and selection rule relaxation.

The GaAs-like optical bands in Fig. 4.2 for both growth orientations exhibit an increase in the full width half maximum (FWHM) and a redshifting to lower frequencies, compared to their respective GaAs controls. The presence of in-plane strain for the (113)B grown sample removes the degeneracy of the TO(Γ) doublet, hindering

a meaningful interpretation of the measured changes for this mode. However, an important comparison can be made between the LO(Γ) phonons measured from the (001)- and (113)B-oriented GaAsBi samples: the LO(Γ) band in the (113)B sample exhibits larger broadening and a greater redshift, compared to the (001) sample. These spectral changes are greatly influenced by structural disorder[115] and suggest a far more severe reduction in crystal quality for GaAsBi grown on the high-index (113)B GaAs substrate, compared to the (001).

We clearly see the two previously discovered GaBi-like modes at $\sim$185 cm^{-1} and $\sim$213 cm^{-1} , which have been identified theoretically[102] as TO(Γ) and LO(Γ) phonons, respectively. The frequency of the GaBi-like phonons do *not* appear to shift over the compositional range studied ($x \leq 0.048$), however, clearly strengthen with increasing Bi concentration. If there was only a very slight shift, it may not be detectable as accurate frequency determinations are made difficult by the superposition of the various nearby disorder-activated bands. Examining the way strain and lattice distortions are accommodated in other (In)GaAs(P)-based systems[116,117], a markedly small redshift in the GaBi-like modes here may actually be expected; under strain, GaAs-based ternary alloys are known to accommodate mechanical distortions predominately in the Ga-As bonds, and not by others. A lack of notable shifting here suggests a similar behaviour for the GaAsBi alloy system.

The Raman peak at $\sim$140 cm^{-1}, labeled Bi$_X$, is of ambiguous origin and no single or combination of GaAs-like phonon modes can be used to explain its appearance. Since we reported this anomalous feature in Ref. 91, an all-optical study by Fitouri *et al.*[118] on localisation effects in GaAsBi alloys has shed light on the matter, attributing this feature to the preferential interaction between electrons localised at Bi atoms and the localised GaBi LO mode.

Just above 250 cm^{-1} appears a broad feature which is assigned to a disorder-

activated TO (DATO) mode. Likewise, in the spectral range from 65 cm^{-1} to 200 cm^{-1}, weak disorder-activated transverse acoustic (DATA) and disorder-activated longitudinal acoustic (DALA) bands (as confirmed by their presence in the $-z(x, x)z$ spectrum in Fig. 4.2(a)) are observed together with second-order Raman signatures of acoustic phonons. These disorder-activated modes are observed for both (001) and (113)B GaAsBi growth directions and indicate large lattice deformation effects. The more prominent of these features is the 2TA(X) acoustic overtone at ∼160 cm^{-1}, which is known to be Raman active even in pure GaAs[119], and agrees well with the neutron scattering data in Table 4.1. This second-order Raman mode conserves momentum, and is allowed, when the two TA(X) phonons are produced sum to zero; i.e. $q_{\mathrm{TA(X)1}} + q_{\mathrm{TA(X)2}} \sim 0$. The small feature at ∼200 cm^{-1} was clearly resolved in many of the Raman spectra recorded from both (001) and (113)B-oriented samples with relatively large Bi concentrations. TA(X)+2TA(L) possess the only adequate Raman shift and thus was attributed to this higher-scattering combination, although further investigations are required to confirm this.

Strong features at ∼228 cm^{-1} and ∼240 cm^{-1} – which have been observed in a previous GaAsBi Raman study[108] – we attribute to GaAs-like LA(X) and LO(L) phonons, respectively, due to their strong alignment with the neutron scattering data presented in Table 4.1. As outlined in Chapter 2, the first-order Raman scattering of these zone-boundary phonons is forbidden in pristine GaAs because of momentum conservation. Broadband spectral features in the vicinity of DATA and DALA are well documented in disordered GaAs-based alloys and their intensities are a good measure of the lack of translational symmetry. The Raman activity is dependent on the derivative of polarisability and needs to be non-zero with respect to the incident wave vector. The strain/disorder set up around larger Bi atoms, as well as Bi pair and cluster point defects, create discontinuities in the electronic wavefunctions and lower the crystal

symmetry, activating these bands. For example, the alloying of $Al_zGa_{1-x}As$ sees a similar presence of DATA and DALA arise in the Raman spectra recorded from alloys with aluminium incorporations larger than $x = 0.4$ [120]. Thus, our clear observations here of broad disorder-induced modes corresponding to the Brillouin-zone edges X and L of the acoustic branches are simply fascinating, particularly given the very dilute nature of the samples studied. Regarding the exotic off-resonance observations of well-resolved LA(X) and LO(L) signatures (as well as the proposed TA(X)+2TA(L) mode), a mechanism of Raman activation based purely on a classical interpretation of Raman scattering and lattice disorder cannot account for their presence. Thus, we must consider the Raman scattering process within the context of the quantum mechanical interpretation outlined in Chapter 2.

For the combination of quantum processes depicted in Figs. 2.3 and 2.4, the dominant term of the third-order perturbation theory is typically used to describe the Raman phenomena, as it directly relates to $\chi_{\alpha,\beta}(\omega_\mathrm{i})$. Adopting the same terminology employed in Fig. 2.3 and its related discussion, we can alternatively consider the Raman scattering probability for the Stokes scattering process as the sum of the probability of the three interactions (the vertices in Fig. 2.3 and the numbered events in Fig. 2.4) involved, by [81]

$$I_{ph}(\omega_s) \approx \frac{2\pi}{\hbar} \sum_{e,e'} \left| \frac{\langle 0 \mid H_{e-r} \mid e\rangle\langle e \mid H_{e-ph} \mid e'\rangle\langle e' \mid H_{e-r} \mid 0\rangle}{(\hbar\omega_\mathrm{i} - \hbar\omega_e - i\Gamma_e)(\hbar\omega_\mathrm{s} - \hbar\omega_{e'} - i\Gamma_{e'})} + C \right|^2 . \tag{4.1}$$

Here $\hbar\omega_{e,e'}$ and $\Gamma_{e,e'}$ respectively represent the energies and the resonance damping constants of the intermediate states $\mid e\rangle$ and $\mid e'\rangle$, and constant C contains contributions from non-resonant scattering (for the case of phonons scattered off-resonance from non-Γ boundaries: $C = 0$). Near-bandgap resonant Raman scattering experiments − measuring Raman spectra with a tunable laser source with energy near that of electronic transitions − are typically required to introduce non-Γ components to the

wavefunctions of the states involved in the centre matrix in Eq. 4.1 (i.e. $\langle 0 \mid H_{e-r} \mid e \rangle$). This is because the electrons (holes) moving through the crystal within the conduction (valence) bands will partake in the intraband scattering of light described in Fig 2.4. Because electron-hole recombination in semiconductors usually occurs between the Fermi levels, an application of Eq. 4.1 involves ground states $\mid 0 \rangle$ that correspond to energies near the valence-band maximum. If $\mid 0 \rangle$ forms a periodically-repeating wavefunction within the lattice (Bloch state), with a well-defined momentum $\mathbf{k}$, then only zone-centre Γ phonons with momentum $q = 0$ will contribute to the classical Raman scattering process described by Chapter 2. On the other hand, if $\mid 0 \rangle$ is localised and does not form a Bloch state, then a single $\mathbf{k}$ quantum number can no longer be used to describe the phonon scattering process and phonons with a variety of $\mathbf{k}$ values may participate in the scattering. For example, if $\mid 0 \rangle$ is a real state with significant non-Γ contributions to its total wavefunction, the first and last matrix elements in Eq. 4.1 (i.e. $\langle 0 \mid H_{e-r} \mid e \rangle$ and $\langle e' \mid H_{e-r} \mid 0 \rangle$) are always non-zero, since all the states involved ($\mid 0 \rangle$, $\mid e' \rangle$ and $\mid e' \rangle$) possess Γ components.

As previously mentioned, the phenomenon of large bandgap reduction (and giant spin-orbit coupling) observed in dilute $GaAs_{1-x}Bi_x$ alloys occurs because of a lifting in the VB maxima, relative to the CB minima, due to the presence of the Bi 6p state which is resonant to the VB edge[121] (see Fig. 4.1). Again, one may draw direct parallels here with the GaAsN material system; the dilute alloying of GaAs with nitrogen (in the order of a few percent) introduces the N 2s state which resides near the CB edge. Similar non-Γ spectral features have been observed in non-resonant Raman studies of dilute $GaAs_{1-x}N_x$ too[30,31], where the activation of the zone-boundary phonons is caused by the mixed symmetry of nitrogen-induced states in the GaAs conduction band[106]. Our observations of X and L boundary phonon modes in the off-resonance Raman spectra of dilute GaAsBi similarly suggests a significant Γ-L-X mixed symmetry

for the Bi 6p state. Unfortunately, very little is known about the exact details of this state, preventing comparison.

At $\sim 260\,\mathrm{cm}^{-1}$ in Fig. 4.2 there appears a relatively large feature just below the TO(Γ) band, which is indicative of LOPC mode scattering in the presence of a large concentration of free charge carriers. According to coupled-mode theory, the frequencies of LOPC modes in a doped polar semiconductor in the limit of long wavelengths, and with no phonon or plasmon damping, are given by [122]

$$L_{\pm}^2 = \frac{1}{2}[(\omega_{LO}^2 + \omega_p^2) \pm \{(\omega_{LO}^2 + \omega_p^2)^2 - 4\omega_p^2 + \omega_{TO}^2\}^{\frac{1}{2}}], \tag{4.2}$$

where $\omega_{LO,TO}$ represent the frequencies of the LO and TO first-order optical modes, and ω_p is the hole plasma frequency defined by

$$\omega_p^2 = \frac{4\pi p e^2}{\varepsilon_\infty m_h^*}. \tag{4.3}$$

Here ε_∞, p, and m_h^* are the optical dielectric constant, the hole concentration, and effective mass mass of the free hole, respectively. Figure 4.3 shows the two calculated frequencies (L_- and L_+) of the undamped coupled LOPC modes near the LO and TO frequencies in p-type GaAs for increasing hole concentration [123]. For p-type GaAs, only a single LOPC mode is observed due to strong hole plasmon damping, moving from LO(Γ) to the TO(Γ) energy with increasing hole densities (the strong damping results mainly from the larger effective masses of holes, compared with electrons) [113].

To investigate the symmetry of the large feature below TO(Γ) in GaAsBi, we examine the Raman backscattering selection rules for this mode with respect to the (001) surface; Fig. 4.4 presents Raman data for (001) $GaAs_{1-x}Bi_x$ (for $x = 0.043$) expanded over the GaAs-like optical phonon range for four different polarised backscattering geometries. The Raman selection rules dictate that the LO(Γ) phonon is allowed for

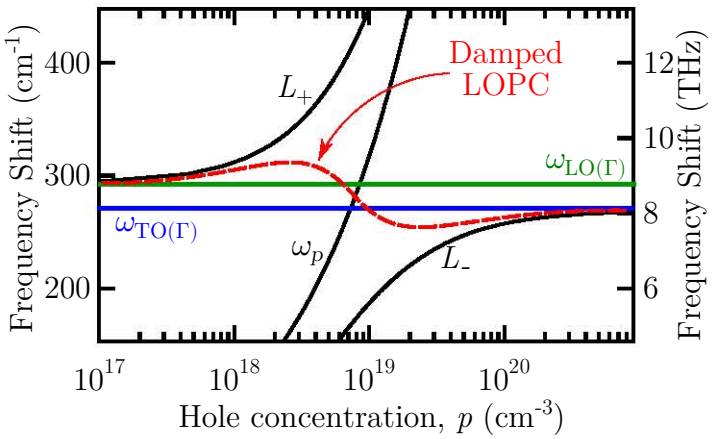

Figure 4.3: Predicted[122] frequencies of the coupled modes (L_+ and L_-) and the plasma mode (ω_p) as a function of hole concentration. The dashed line shows the general behaviour of the single damped LOPC mode observed in p-GaAs.

$-z(Y, Y)z$ and $-z(x, y)z$ but forbidden in $-z(Y, X)z$ and $-z(x, x)z$, while TO(Γ) is always forbidden. Again, the appearance here of the symmetry-forbidden TO mode in all polarisations can be attributed to bismuth-induced disorder in the lattice, resulting in a relaxation of the Raman selection rules. The contribution to the Raman efficiency of the coupled modes from the electro-optic mechanism is not total while the unscreened LO band is present, meaning the observed LOPC modes are phonon-like and should obey the Raman selection rules. The strong feature just below TO ($\sim$266 cm^{-1}) obeys the same Raman selection rules as the LO(Γ) band and is indicative of a LOPC mode in a heavily doped ($>10^{18}$ cm^{-3}) p-GaAs-based system[122–125]. That we do not observe the L_+ branch at higher frequencies confirms the p-type nature of the free carrier present in GaAsBi. It should be noted that while we observe weak GaBi-like centre optical bands over the whole compositional range studied, we do not see hole plasmons interacting with the GaBi-like LO(Γ) phonon since the coupling strength is approximately proportional to the phonon content.

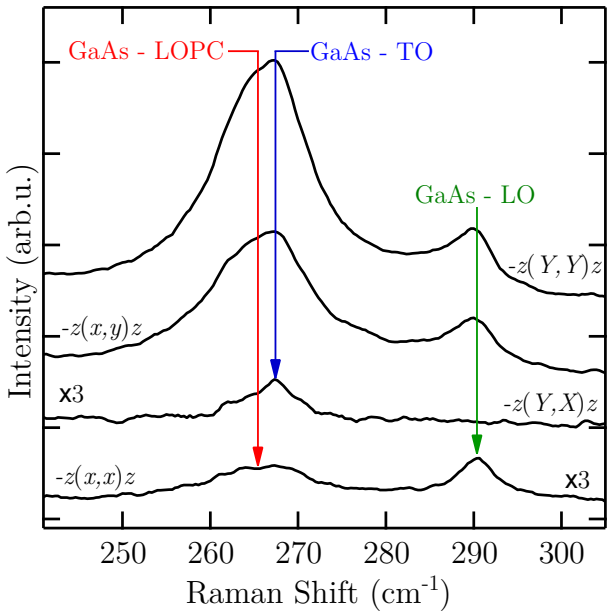

Figure 4.4: Raman spectra of (001) $GaAs_{1-x}Bi_x$ for $x = 0.043$ expanded over GaAs-like optical frequency range for different polarisation configurations (offset vertically for clarity).

4.3 Strain and phonon shifts in GaAsBi alloys

Raman scattering is well-suited for the investigation of mechanical disorder in GaAsBi due to Bi incorporation because it is sensitive to the force constant of the bonds, which in turn will depend on the mechanical properties of the host matrix. Strong shifts in the measured frequencies of the optical phonons will manifest due to modifications to the lattice dynamics of ternary $GaAs_{1-x}Bi_x$ alloys. The total frequency shift will involve two separate contributions; one component accounts for changes in the alloying composition (x) of the ternary material ($\Delta\omega_{\text{alloy}}$) and, in the case of fully strained pseudomorphic structures, another on the strain field present in the alloy ($\Delta\omega_{\text{strain}}$). The total redshift term for the optical phonons can then be quantitatively expressed as

$$\Delta\omega_{\text{LO,TO}} = \Delta\omega_{\text{alloy}} + \Delta\omega_{\text{strain}}. \tag{4.4}$$

Here the dependence of phonon frequencies on the strain is described by the phonon deformation potentials[126,127]. For dilute ternary systems, one may examine the strain-induced shifts independently, and with reasonable accuracy, by simply modelling the host binary system (GaAs in our case). In this section, we examine the compositional influence of pseudomorphic $GaAs_{1-x}Bi_x$/GaAs epitaxial layers on the redshift observed in the GaAs-optical phonons. For reference, Appendix B presents all the physical parameters used in the calculations.

4.3.1 Lattice mismatch and compressive strain in $GaAs_{1-x}Bi_x$/GaAs

In order to calculate the phonon frequency shifts due to stress in the films, one must determine the elastic strains and the three dimensional strain tensor $\tilde{\varepsilon}_{ij}$. The boundary conditions suitable for a bisotropic strain are written in the new basis (XYZ). The equivalence of the strain in two orthogonal in-plane directions sets up the in-plane strain

$$\varepsilon_{XX} = \varepsilon_{YY} = \varepsilon_{\parallel}, \tag{4.5}$$

while the out-of-plane strain is given by

$$\varepsilon_{ZZ} = \varepsilon_{\perp}. \tag{4.6}$$

For an arbitrary (hhk)-oriented growth direction, these two are connected through

$$\varepsilon_{\perp} = \varepsilon_{\parallel} \frac{2 \times [-h^2(h^2+k^2)C_{11} - (3h^4+2h^2k^2+k^4)C_{12} + 2h^2(h^2+2k^2)C_{44}}{[h^4(h^2+k^4)C_{11} + 2h^2(h^2+2k^2)C_{12} + 4h^2(h^2+2k^2)C_{44}}, \tag{4.7}$$

where C_{ij} represent the elastic constants. The assumption of complete adherence to the substrate leads to the orthogonality of the epilayer lattice, namely

$$\varepsilon_{XY} = \varepsilon_{YX} = 0. \tag{4.8}$$

Thus, one arrives at the following expression for the second-rank strain tensor for our biaxially strained system

$$\tilde{\varepsilon} = \begin{bmatrix} \varepsilon_{\parallel} & 0 & \varepsilon_{XZ} \\ 0 & \varepsilon_{\parallel} & \varepsilon_{YZ} \\ \varepsilon_{XZ} & \varepsilon_{YZ} & \varepsilon_{\perp} \end{bmatrix} \tag{4.9}$$

To directly measure the strain state in GaAsBi, x-ray direction (XRD) 2θ scans are recorded from the epitaxial surface of each sample. Because the lattice constant of binary GaBi is larger than the GaAs system, pseudomorphic $GaAs_{1-x}Bi_x$ epitaxial layers will experience a biaxially compressive strain to preserve the in-plane (x-y plane) lattice constant, $a_{\parallel}$.

As illustrated in Fig. 2.8, such lattice matching distorts and further expands the out-of-plane lattice constant, $a_{\perp}$, and the distance between the x-ray scattering planes, $d_{\perp}$. Consequently, there will exist two Bragg peaks in our XRD data: one occurring at θ_{S} from x-rays penetrating through to the pure GaAs substrate, and another peak occupying a negative $\Delta\theta$ angle − relative to θ_{s} − scattering from an expanded epitaxial lattice. From the experimental XRD data, the out-of-plane lattice strain due to the Bi alloying can be determined through[128]

$$\varepsilon_{\perp} = \varepsilon_{ZZ} = \frac{\Delta d_{\perp}}{d} = \frac{\Delta a_{\perp}}{a} = \frac{\Delta\theta}{\tan(\theta_{\mathrm{s}})}. \tag{4.10}$$

The ratios $\Delta d_{\perp}/d$ and $\Delta a_{\perp}/a$ are defined as the relative distance changes between the lattice planes and lattice constants, respectively, while the measured angular shift

is given by $\Delta\theta = \theta - \theta_s$. Regardless of growth direction, the in-plane biaxial strain (lattice mismatch) is

$$\varepsilon_{\parallel} = \varepsilon_{XX} = \varepsilon_{YY} = \frac{(a_{\text{rel}} - a_{\text{GaAs}})}{a_{\text{GaAs}}}, \tag{4.11}$$

and the relaxed lattice parameter in the ternary epitaxial film is calculated by

$$a_{\text{rel}} = a_{\text{GaAs}} \left[1 + P \frac{\Delta d_{\perp}}{d} \right]. \tag{4.12}$$

Here a_{GaAs} indicates the lattice constant of GaAs, while P represents the distortion coefficient of the GaAsBi and is dependent on both the elastic constants and orientation of the sample. The relaxed lattice parameter is typically assumed to follow a linear interpolation of the two binary lattice parameters (i.e. Vegard's law [85]),

$$a_{\text{rel}} = a_{\text{GaAs}_{1-x}\text{Bi}_x} = x a_{\text{GaBi}} + (1 - x) a_{\text{GaAs}}, \tag{4.13}$$

where a_{GaBi} is the relaxed lattice parameter of the binary GaBi system. Given the zincblende GaBi compound is yet to be experimentally realised, we employ the hypothetical lattice parameter proposed Masnadi-Shirazi *et al.* [3], 6.33±0.05 Å, determined via an extrapolation of experiential Rutherford backscattering spectroscopy and high-resolution XRD data recorded over the relatively large compositional range $0 \leq x \leq 0.194$. This value represents the most recent revision of the GaBi lattice parameter and has excellent agreement with the original estimate made by Tixier *et al.* [2], 6.33±0.06 Å. It follows that one may obtain the Bi content of a fully strained GaAsBi film from the XRD data using

$$x = \left[\left(\frac{a_{\text{GaAs}}}{a_{\text{GaBi}} - a_{\text{GaAs}}} \right) \frac{P}{\tan(\theta_s)} \right] \times \Delta\theta. \tag{4.14}$$

Given that the Bi content of our samples is low, we assume the deformation

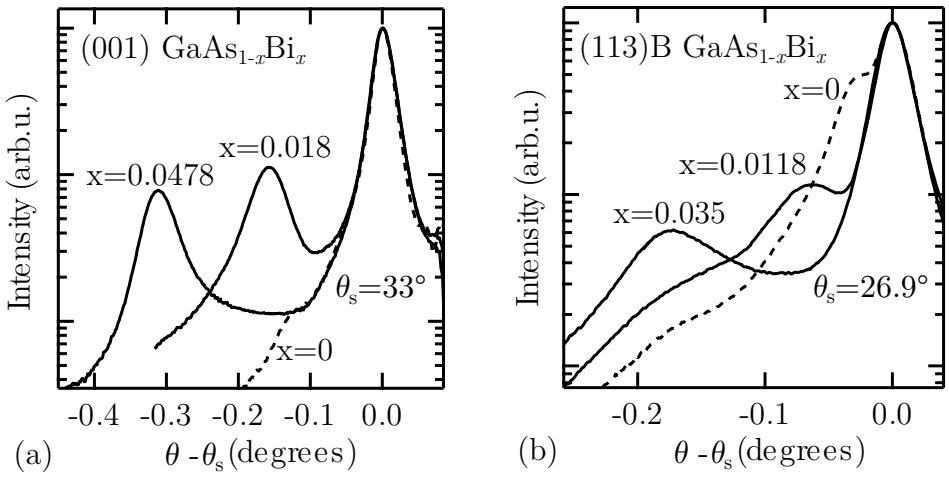

Figure 4.5: Measured XRD scans from symmetric (a) (004) and (b) (113) Bragg reflections for as-grown GaAs (dotted lines) and $GaAs_{1-x}Bi_x$ (solid lines) epilayers grown respectively on (001)- and (113)B-oriented GaAs substrates. θ_s represents the Bragg angle of reflection for the pure GaAs substrates.

constants of our dilute GaAsBi alloys are the same as those for pure GaAs. For the case of (001)-oriented samples, the distortion coefficient is

$$P_{(001)} = \frac{C_{11}}{C_{11} + 2C_{12}} \tag{4.15}$$

whereas for (113)-oriented GaAs, P is given by an interpolation between [001] and [111][129]

$$P_{(113)} = P_{(001)} + \frac{\alpha}{\beta}\frac{2}{3}(2C_{44} - C_{11} + C_{12}). \tag{4.16}$$

Here α=25.24° and is the angle between the [113] and [001] crystallographic directions, while β=54.74° and is the angle between [001] and [111]. Inputting the deformation constants of GaAs, C_{ij}, given in Appendix B, we arrive at $P_{(001)}$=0.527 and $P_{(113)}$=0.691. For samples grown on (001) and (113)B GaAs substrates, the (004) and (113) symmetrical reflections are measured, respectively, using an x-ray wavelength of $\lambda = 1.54\,\text{Å}(\text{Cu}K_{\alpha_1})$. Thus, the Bi concentration in (001)- and (113)B-oriented GaAsBi can be estimated respectively from the 33° and 26.9° Bragg angles and by the linear

Table 4.2: List of samples studied in this work with results from XRD epilayer characterisation. The numbers in parentheses represent the uncertainty for Bi content x in units of the last significant digits. Here '*' indicates control samples ($x = 0$) grown for both substrate orientations.

Sample	$\mid \Delta\theta \mid$ (°)	$\Delta d/d$ ($\times 10^{-3}$)	$\varepsilon_{\parallel}$ ($\times 10^{-3}$)	$x_{(\mathrm{XRD})}$ (%)
		(001)-oriented		
A1*	0	0	0	0
A2	0.152	4.11	2.16	1.8(1)
A3	0.232	6.27	3.28	2.74(2)
A4	0.255	6.90	3.61	3.01(3)
B1	0.267	7.24	3.78	3.16(3)
B2	0.364	9.89	5.15	4.3(1)
B3	0.367	9.98	5.20	4.34(6)
B4	0.369	10.0	5.22	4.36(2)
B5	0.393	10.7	5.56	4.64(4)
B6	0.405	11.0	5.73	4.78(2)
		(113)B-oriented		
H1*	0.025	0.85	0.58	NA
H2	0.0593	2.05	1.41	1.18(1)
H3	0.164	5.68	3.90	3.26(3)
H4	0.176	6.11	4.19	3.5(1)
H5	0.197	6.83	4.68	3.91(2)

relationships

$$x_{001} = 6.77 \times \Delta\theta, \text{ and } x_{(113)} = 11.4 \times \Delta\theta. \tag{4.17}$$

Here $\Delta\theta$ has units of radians. XRD measurements of epilayer lattice constants are widely used to determine the Bi content of $GaAs_{1-x}Bi_x$ epilayers through the proportionality of a_{rel} and the GaBi molar fraction[68,72,100]. Note the rate of change of $x(\Delta d/d)$ for (001)- and (113)B-oriented epilayers differ greatly. This is simply a consequence of the difference in Bragg reflection angle and P value used for corresponding calculations.

Figure 4.5 shows measured XRD data for various near-stoichiometric $GaAs_{1-x}Bi_x$ samples grown on (001) and (113)B GaAs, with controls ($x = 0$) also displayed for comparison. In Fig. 4.5 we see that the XRD shapes for $x = 0$ strongly differ for the

two orientations. There is a small peak appearing at a slightly lower reflection angle for the (113)B GaAs control epilayer. Such XRD lineshapes have been previously observed for (113)A and (113)B GaAs epilayers being attributed to excess As (in the form of As_{Ga} antisites) as a consequence of varying the growth temperatures and/or V:III flux ratios[130,131]. The mechanisms leading to an enhanced concentration of As_{Ga} in (113)B GaAs and the effect it has on the Raman spectral modes are discussed later in detail.

The epilayer XRD peak is seen to be noticeably broader in (113)B-oriented GaAsBi samples. In fact, the FWHM of (113)B epilayers was found to increase with increasing Bi concentrations, whereas only an initial widening was seen for samples grown on (001) substrates. This suggests the quality of the (113)B $GaAs_{1-x}Bi_x$ epilayers is poor, possessing a substantial degree of structural disorder. It is worth noting that while the intensity and width of the substrate reflections are comparable for both orientations, a smaller relative intensity is observed from the (113)B $GaAs_{1-x}Bi_x$ epilayers. This indicates an appreciably thinner epilayer resulting from a lower growth rate in the (113)B direction.

Table 6.1 presents the XRD characterisation results of all the GaAsBi/GaAs samples studied in this thesis, along with their Bi concentration determined using Eqs. 4.17 and the XRD data. For the completeness of later discussion, the small peak appearing in the XRD scan of the (113)B GaAs control ($x = 0$) is also included.

4.3.2 Phonon deformation potentials

The strain in pseudomorphic epilayers and its effect on the lattice dynamics can be analysed through an exact evaluation of the phonon frequencies in the Raman spectrum, since the stress-induced lattice deformation directly affects inter-atomic bonding in the crystal. Given that the elastic strains in the GaAsBi films have been determined, what remains to be calculated are the frequencies of the optical modes in the presence

of strain, due to tetragonal distortions in both the (001) and (113)B directions. The relationship between the optical phonon frequencies and the strain tensor $\tilde{\varepsilon}$ is described by the forth-rank phonon deformation potential tensor $\tilde{K}$ and can be quantified using the procedure given by Cardeira *et al.*[126].

For the cubic GaAs-based system considered here, $\tilde{K}$ has only three independent nonvanishing components: p, q and r. The dimensionless elements of phonon deformation potentials in suppressed notation K_{ij} can be represented using p, q and r, as

$$K_{11} = \frac{p}{\omega_0^2}, \qquad K_{12} = \frac{q}{\omega_0^2}, \qquad K_{44} = \frac{r}{\omega_0^2}. \tag{4.18}$$

Here ω_0 is the phonon frequency of the unstrained crystal. These parameters describe the changes to the spring constant with strain[132] and are provided in Appendix B. Note there are two different values for these parameters − one for LO phonons and another for TO phonons. For Raman backscattering along the crystal c-axis, the tetragonal distortion induces a splitting of the threefold degenerate optical phonons into a singlet mode (LO phonon) whose sublattice displacement is perpendicular to the growth interface, and a doublet mode (TO phonon) with a displacement parallel to the interface. Assuming the threefold degeneracy of the $q \approx 0$ optical phonons in our zincblende material, one arrives at the following secular equation whose solutions yield the frequencies of the optic modes in the presence of strain[133]

$$\begin{bmatrix} p\varepsilon_{XX} + q(\varepsilon_{YY} + \varepsilon_{ZZ}) - \lambda & 2r\varepsilon_{XY} & 2r\varepsilon_{XZ} \\ 2r\varepsilon_{XZ} & p\varepsilon_{YY} + q(\varepsilon_{ZZ} + \varepsilon_{XX}) - \lambda & 2r\varepsilon_{YZ} \\ 2r\varepsilon_{XZ} & 2r\varepsilon_{YZ} & p\varepsilon_{ZZ} + q(\varepsilon_{XX} + \varepsilon_{YY}) - \lambda \end{bmatrix} = 0. \tag{4.19}$$

Here $\lambda = \omega^2 - \omega_0^2$ and ω is the strain dependent frequency. The secular equation is referenced to the main crystallographic basis: ($X = [100]$,$Y = [010]$, $Z = [001]$). Diagonalising this equation yields a set of three eigenvectors of the optic modes in the presence of strain.

For crystal distortion and strain parallel to either the [001] or [111] directions, the first-order optical modes have a singlet component (ω_{S}) and a doublet ($\omega_{\mathrm{D1,D2}}$). For Raman backscattering in these directions the symmetry of the zincblende crystal preserves the degeneracy of the doublet, since $\varepsilon_{XX} = \varepsilon_{YY}$. Thus, for strain in the [001] or [111] directions, we have

$$\Delta\omega_{\mathrm{S}} = \Delta\omega_{\mathrm{LO}(Z)} = \Delta_{\mathrm{H}}\omega + \frac{2}{3}\Delta_{\mathrm{u}}\omega, \tag{4.20}$$

$$\Delta\omega_{\mathrm{D1,D2}} = \Delta\omega_{\mathrm{TO}(X,Y)} = \Delta_{\mathrm{H}}\omega - \frac{1}{3}\Delta_{\mathrm{u}}\omega, \tag{4.21}$$

where the hydrostatic component of the strain given by

$$\Delta_{\mathrm{H}}\omega = \frac{\varepsilon_{\perp}}{6\omega_0}(p+2q)\frac{C_{11}}{(C_{11}-C_{12})(C_{11}+2C_{12})},$$

and the total polar-driven splitting is

$$\Delta_{\mathrm{u}}\omega = \omega_{\mathrm{S}} - \omega_{\mathrm{D1,D2}} = \begin{cases} \frac{\varepsilon_{\perp}}{2\omega_0}\frac{(p-q)}{(C_{11}+C_{12})}, & \varepsilon_{\perp} \parallel [001], \\ \frac{\varepsilon_{\perp}}{2\omega_0}\frac{r}{C_{44}}, & \varepsilon_{\perp} \parallel [111]. \end{cases}$$

For stress parallel to the low-symmetry [110] direction the situation becomes more complex since the triple degeneracy of the optic modes is completely lifted; one component polarised along [110] (LO) and two perpendicular (TO). Employing our standard [111]-oriented basis, Eq. 4.19 yields

$$\Delta\omega_{\mathrm{S}} = \Delta\omega_{\mathrm{LO}(Z)} = \Delta_{\mathrm{H}}\omega + \frac{1}{6}\Delta\omega_{\mathrm{S}}^{(001)} + \frac{1}{2}\Delta\omega_{\mathrm{S}}^{(111)}, \tag{4.22}$$

$$\Delta\omega_{\mathrm{D1}} = \Delta\omega_{\mathrm{TO}(X)} = \Delta_{\mathrm{H}}\omega + \frac{1}{6}\Delta\omega_{\mathrm{S}}^{(001)} - \frac{1}{2}\Delta\omega_{\mathrm{S}}^{(111)}, \tag{4.23}$$

$$\Delta\omega_{\mathrm{D2}} = \Delta\omega_{\mathrm{TO}(Y)} = \Delta_{\mathrm{H}}\omega - \frac{1}{3}\Delta\omega_{\mathrm{S}}^{(001)}. \tag{4.24}$$

Through Eqs. 4.20 - 4.24 the strain-only shift for the optic phonons of GaAs may

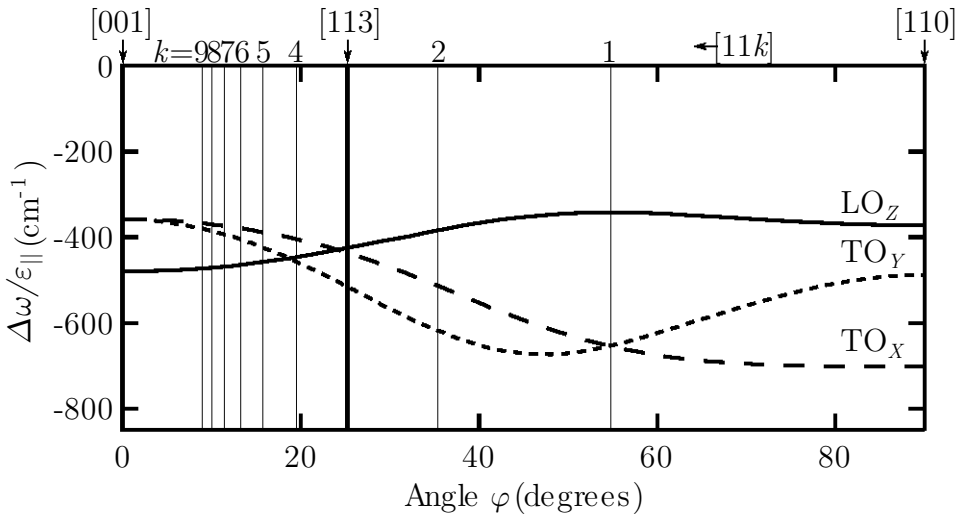

Figure 4.6: Angular dispersion of frequency shift for GaAs optic modes under compressive strain. Here $\varphi = ([001], [hhk])$, representing a rotation in the Y-Z plane using the same coordinate system depicted in Fig. 3.2. The various (hhk) growth directions are indicated, whereby for high-index crystal directions a single number close to the top horizontal axis defines the k value in the set of $[11k]$ vectors.

be determined for backscattering from the (001), (111) and (110) crystal planes. Note only the result for biaxially strained (001) GaAs will be directly used in our analysis, while the values for (111) and (110) will allow an estimate of the phonon strain shifts for an arbitrary angles between [001] and [110] (φ).

The strain-induced phonon shift coefficients for backscattering from a biaxially strained high-index (113)(A or B)-oriented zinceblende or diamond structures are yet to be reported, and special considerations must be given. The initial characterisation of the (113)B GaAsBi alloys suggests a far lower structural quality for these materials. Consequently, we aim to merely assess and compare the magnitudes of the compositional-dependent phonon shifts observed in the (113)B-oriented samples to that of the (001)-oriented ones. As the discussion and analysis presented in Section 4.3.3 will make clear, a reasonable estimation of $\Delta\omega_{\text{strain}}$ component for the (113)B-oriented samples is sufficient for these purposes. To calculate the frequency, the Fresnel dispersion equation gives a relatively close estimation (within 5%[134]) of the energy of phonons

Table 4.3: Strain-induced phonon frequency shifts for GaAs-like LO and TO phonons in dilute (001) and (113)B $GaAs_{1-x}Bi_x$. The numbers in parentheses represent the uncertainty; note that no uncertainties are given for the values related to the [113]B growth direction, since they are approximations.

Growth face	Phonon mode and propagation direction	$\Delta\omega_{\text{strain}}/\varepsilon_{\parallel}$ (cm^{-1})	$\Delta\omega_{\text{strain}}/x$ (cm^{-1})
(001)	TO_X : [100]	$-357(\pm12)$	$-43(\pm2)$
	TO_Y : [010]	$-357(\pm12)$	$-43(\pm2)$
	LO_Z : [001]	$-482(\pm31)$	$-58(\pm4)$
(113)B	TO_X : $[1\bar{1}0]$	-515	-62
	TO_Y : $[33\bar{2}]$	-436	-52
	LO_Z : [113]	-425	-51

when all Raman tensors contribute to the intensity of the mode. The relationship for calculating the frequency of mode in a strained system based on the angle between the main axis and the eigenvector ($\varphi = ([001], [hhk])$) is given by Loudon[135]

$$\omega^2 = [\cos(\varphi)]^2\omega_{\parallel}^2 + [\sin(\varphi)]^2\omega_{\perp}^2, \qquad \text{(TO)} \tag{4.25}$$

$$\omega^2 = [\cos(\varphi)]^2\omega_{\perp}^2 + [\sin(\varphi)]^2\omega_{\parallel}^2. \qquad \text{(LO)} \tag{4.26}$$

Here $\omega_{\parallel}$ and $\omega_{\perp}$ represent the phonon frequency at $\varphi = 0$ and $\pi/2$, and correspond to $\omega_{(001)}$ and $\omega_{(110)}$, respectively. It follows one may estimate $\Delta\omega_{\text{strain}}$ for an arbitrary φ angle. Fig. 4.6 presents this angular dispersion along with the various (hhk) planes clearly marked. This technique has been used effectively by others[98,136] and when comparing to the analytical solution provided by Inoki *et al.*[137], good agreement is found for the (112)-oriented values. Table 4.3 displays the $\Delta\omega_{\text{strain}}$ values determined for the optical modes of dilute (001) and (113)B $GaAs_{1-x}Bi_x$.

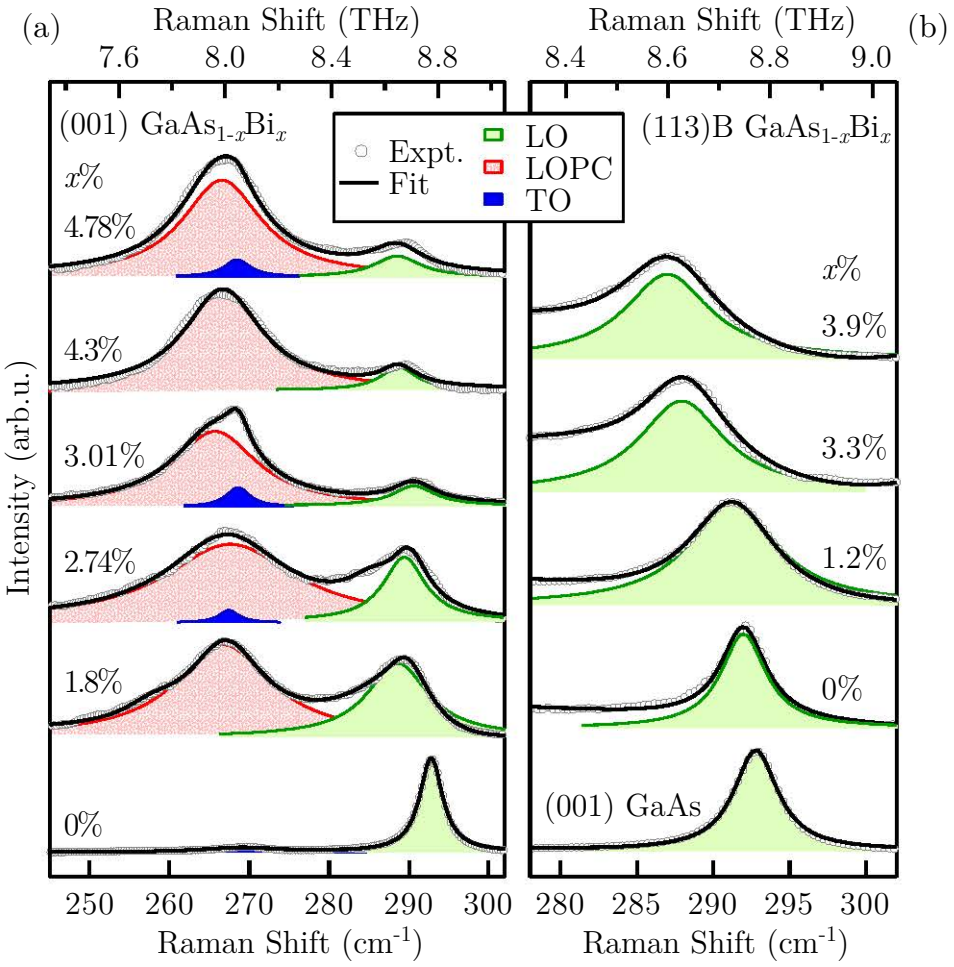

Figure 4.7: Raman spectra of $GaAs_{1-x}Bi_x$ in the vicinity of the GaAs-like optic bands for various Bi concentrations, x. (a) Presents data recorded in $-z(Y, Y)z$ scattering geometry from the (001) growth surface, while (b) was measures in the $-z(Y, X)z$ polarised geometry from the surface of the (113)B-oriented samples and is plotted with the (001) GaAs data for comparison. The filled areas give the contribution of distinct modes to the overall fit (solid line) of our data (open circles). For the case of the (113)B samples in (b), only the LO mode contribution is displayed. For clarity, the traces in (a) and (b) have been normalised respectively to their LOPC and LO peaks, and offset vertically. As well, the spectral contributions from disorder-activated bands are left out (producing vacant areas under the traces). For the case of the (113)B $GaAs_{1-x}Bi_x$ samples, the high-frequency shoulder of the LOPC is also left.

4.3.3 Optical phonon behaviour in (001) and (113)B $GaAs_{1-x}Bi_x$

Next we carry out a detailed analysis of the frequency behaviour of the GaAs-like optical phonons for varying Bi incorporation for both (001) and (113)B growth directions.

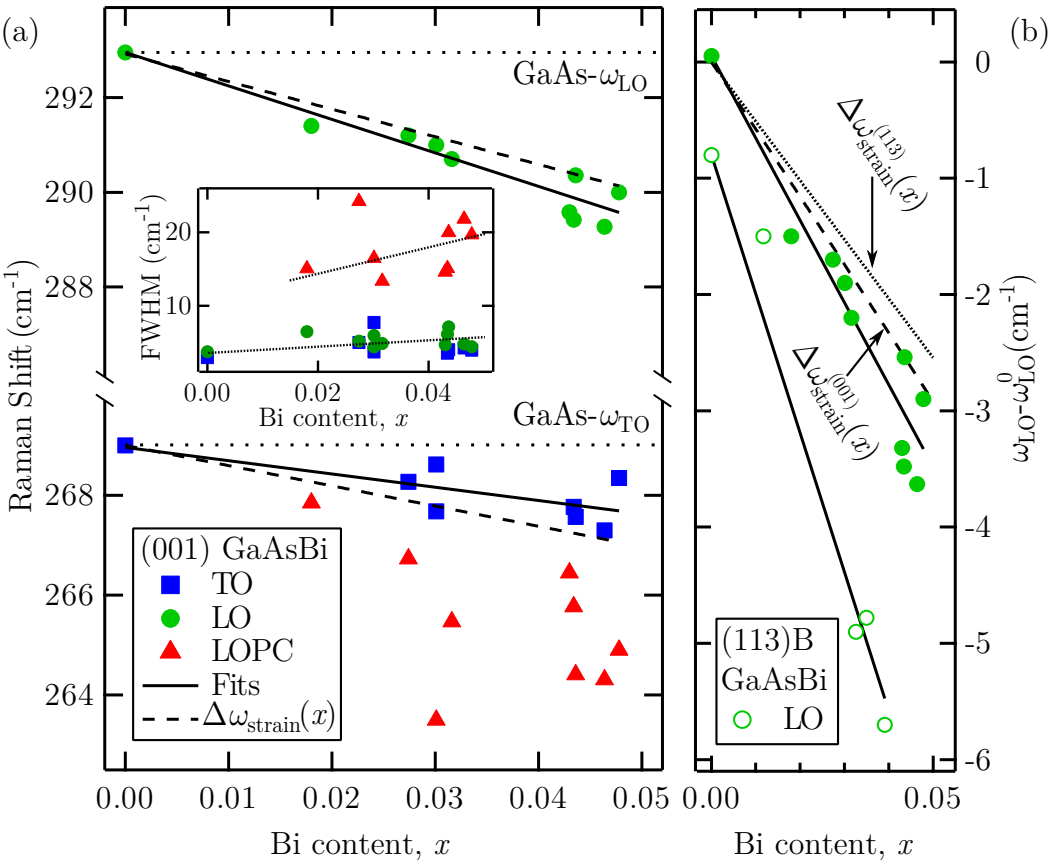

Figure 4.8: (a) Measurement of frequency shifts in (001) GaAsBi for TO, LO and LOPC bands as a function of Bi fraction. Dashed lines represent the frequencies of the dispersionless two centre optical modes for GaAs ($x = 0$) and the inset shows the FWHM of each of the modes. (b) The frequency measured in the (113)B-oriented samples. To highlight the relatively large shift seen in the LO mode of the (113)B samples, (b) offers a direct comparison to the expected strain-induced shift for this growth direction as well as the data for the (001) grown samples; the trace key for (a) also applies to (b).

Raman spectra measured from (001) and (113)B $GaAs_{1-x}Bi_x$ surfaces were recorded respectively in $-z(Y, Y)z$ and $-z(Y, X)z$ polarised backscattering geometries, and are presented in Fig. 4.7, for various compositions. Due to the disorder-induced breakdown of the selection rules, the forbidden TO(Γ) mode is enhanced in the (001)-oriented GaAsBi Raman spectra allowing unambiguous frequency determination.

While Fig. 4.7(a) examines the whole GaAs-like optic band region, (b) simply focuses on the LO phonon mode. Together the strain-induced splitting of the degenerate

TO(Γ) phonons measured in a backscattering geometry and the substantial level of disorder in the (113)B grown samples imposed constraints on a meaningful analysis of this mode. As we will see, a quantitative assessment of only the GaAs-like LO(Γ) phonon yields sufficient insights into the growth GaAsBi on high-index (113)B GaAs substrates.

Examining the data in Fig. 4.7 there are some notable composition-dependent trends. Namely, with even only a small amount of Bi introduced, the GaAs-like phonons mode soften to lower frequencies and significantly broaden (increase in the FHWHM). In Fig. 4.7(a) the peak positions of TO and LO (and subsequently LOPC) are all seen to linearly decrease with alloying. Further, the intensity of the LOPC mode here grows with increases of x relative the uncoupled LO phonon. On the other hand, the intensity of the symmetry forbidden TO mode scattered from (001) surfaces exhibits no clear dependence on composition, though it does appear to systematically redshift. One may also note in Fig. 4.7 the significantly larger redshift experienced for the LO mode in the (113)B-orientated samples. To deconvolute the GaAs-like optical modes of the first-order Raman spectra of $GaAs_{1-x}Bi_x$, Lorentzian oscillators are assigned to each feature.

The peak frequency shift versus Bi content for the (001) and (113)B grown samples is summarised in Fig. 4.8, where a marked shift towards lower energies with increasing x in the epilayers is observed. An initial comparison to the strain contributions incorporated into the data reveal an interesting result for the (001) GaAsBi data set – the TO phonon mode appears to be softening less quickly than the predicted strain-only component, while the LO mode redshift more rapidly.

We define the frequency redshift as the difference in peak position between the $GaAs_{1-x}Bi_x$ epilayer and bulk GaAs;

$$\Delta\omega_{\mathrm{LO,TO}} = \omega_{\mathrm{LO,TO}} - \omega^0_{\mathrm{LO,TO}}, \tag{4.27}$$

where $\omega_{\mathrm{LO,TO}}$ and $\omega^0_{\mathrm{LO,TO}}$ are the measured vibration frequencies for our $GaAs_{1-x}Bi_x$ epilayers and for pristine GaAs, respectively. Although conventionally quadratic equations are used to describe the frequency variations with x in III-V alloys,[138] the small range of x studied here (with respect to other III-V materials, $GaAs_{1-x}Sb_x$ or $GaAs_{1-x}N_x$ for example) warrants only a linear fit. From the linear fit of these data, we obtain the following compositional dependence of the GaAs-like optical modes in strained (001)- and (113)B-oriented $GaAs_{1-x}Bi_x$:

$$\omega^{(001)}_{\mathrm{TO,LO}}(\mathrm{cm}^{-1}) = \omega^0_{\mathrm{TO,LO}} + \Delta\omega^{(001)}_{\mathrm{TO,LO}} \times x, \text{ and} \tag{4.28}$$

$$\omega^{(113)\mathrm{B}}_{\mathrm{LO}}(\mathrm{cm}^{-1}) = \omega^0_{\mathrm{LO}} + \Delta\omega^{(113)\mathrm{B}}_{\mathrm{LO}} \times x. \tag{4.29}$$

The experimentally measured redshift values are:

$$\Delta\omega^{(001)}_{\mathrm{LO}}/x = -71(\pm 3)\,\mathrm{cm}^{-1}, \tag{4.30}$$

$$\Delta\omega^{(001)}_{\mathrm{TO}}/x = -27(\pm 4)\,\mathrm{cm}^{-1} \quad \text{and} \tag{4.31}$$

$$\Delta\omega^{(113)\mathrm{B}}_{\mathrm{LO}}/x = -120(\pm 6)\,\mathrm{cm}^{-1}. \tag{4.32}$$

As the values in Table 4.3 illustrate, the observed slope of the $GaAs_{1-x}Bi_x$ data will have a significant contribution from the effects of strain ($\Delta\omega_{\mathrm{strain}}$), as well as smaller effects due to alloying ($\Delta\omega_{\mathrm{alloy}}$); i.e. the substitutional replacement of As atoms with Bi. Thus, we present Eq. 4.4 describing the total shift again in its general form:

$$\Delta\omega = \Delta\omega_{\mathrm{alloy}} + \Delta\omega_{\mathrm{strain}}. \tag{4.33}$$

Accounting for the strain-induced shift component using our values determined in Table 4.3 we may estimate the values of the alloying-induced component of the shift

to be:

$$(001)\ \text{GaAsBi LO phonon}: \Delta\omega_{\text{alloy}}(\text{LO}) = -13(\pm 7)\,\text{cm}^{-1}, \tag{4.34}$$

$$(001)\ \text{GaAsBi TO phonon}: \Delta\omega_{\text{alloy}}(\text{TO}) = +16(\pm 6)\,\text{cm}^{-1} \quad \text{and} \tag{4.35}$$

$$(113)\text{B GaAsBi LO phonon}: \Delta\omega_{\text{alloy}}(\text{LO}) = -69(\pm 6)\,\text{cm}^{-1}. \tag{4.36}$$

The $\Delta\omega_{\text{alloying}}(\text{LO})$ value determined here for the (113)B-oriented samples should be similar to that of the (001) GaAsBi. That we see a considerable deviation between the two, with the value in the former being over fives times larger, indicates an extreme level of disorder in the (113)B-oriented $GaAs_{1-x}Bi_x$ alloys.

The strain-only redshift estimated theoretically for the (001)-oriented samples is $\Delta\omega_{\text{strain}} = -58\,\text{cm}^{-1}/x$. This is compared to our measured total redshift of $-71(\pm 4)\,\text{cm}^{-1}/x$. The additional redshift component we may attribute to the effects of alloying, whereby the total number of Ga-As bonds is reduced, such that $\Delta\omega_{\text{alloy}}(\text{LO}) = -12(\pm 4)\,\text{cm}^{-1}$.

In fact, a value of $\Delta\omega_{\text{alloy}}(\text{LO}) = -12(\pm 4)\text{cm}^{-1}$ for the alloying shift is rather low when compared to the alloying effects observed for $GaAs_{1-x}N_x$ [139,140] ($\sim 40\,\text{cm}^{-1}/x$) and in considering that most of the alloying-induced shift in the phonon bands is experienced in the dilute range. Further measurements on fully relaxed $GaAs_{1-x}Bi_x$ would aid comparison. Moreover, the relatively large *positive* value yielded for the TO phonon of $\Delta\omega_{\text{alloy}}(\text{TO}) = +16(\pm 6)\,\text{cm}^{-1}$ is surprising. A small alloy-induced blueshift of the GaAs-like TO mode was also reported for strain-free GaAsN materials by Ibáñez *et al.*[140]. An alloy-induced blueshift has the dramatic effect of strongly reducing the TO-LO splitting energy for the GaAs-like optical modes in $GaAs_{1-x}Bi_x$ (see for example Fig. 4.8(a); the TO and LO modes appear to strongly converge). A narrowing of the TO-LO splitting cannot be accounted for through only the influence of biaxial strain, as the consequence of $\Delta\omega_{\text{strain}}(\text{LO}) > \Delta\omega_{\text{strain}}(\text{TO})$. It cannot be explained by the changes to short-range ordering in the semiconductor either, through Bi clustering

or defects (i.e. by a modification in the spring constant or disorder effects), because this should affect both the LO and TO modes in a similar fashion (we see this clearly in the (113)-oriented samples). On the contrary, it is worth emphasising again, we observe the TO mode exhibiting a positive $\Delta\omega_{\text{alloy}}$ value.

To understand this interesting result, we must examine long-range ordering effects on the frequency of the GaAs-like optic branch of $GaAs_{1-x}Bi_x$. In pristine GaAs the TO-LO splitting may be used to calculate the ionic plasma frequency associated with the LO phonon by

$$\Omega^2_{\text{GaAs}} = \omega^2_{\text{LO}} - \omega^2_{\text{TO}}, \tag{4.37}$$

and is be related to the physical properties of GaAs through[141]

$$\Omega^2_{\text{GaAs}} = \frac{4\pi N e^{*2}_{T,\text{GaAs}}}{\epsilon_\infty V \mu_{\text{GaAs}}}. \tag{4.38}$$

Here ϵ_∞ is the high-frequency dielectric constant of GaAs, $e^{*2}_{T,\text{GaAs}}$ is the transverse effective charge of the longitudinal Ga-As oscillators and μ_{GaAs} is the Ga-As reduced mass. Parameter N represents the total number of Ga-As bonds (so there are $2 \times N$ atoms in N primitive cells in the GaAs lattice) and V is the volume of the crystal and is related to N through $V = Na^3_{\text{GaAs}}/4$.

Through independent examination of the components contained in Eq. 4.38, one may shed light on the large reduction in GaAs-like TO-LO splitting for dilute GaAsBi. First, ϵ_∞ will increase with the dilute alloying of GaAs with Bi, thus reducing Ω_{GaAs}; however the change in ϵ_∞ is not expected to be large[142,143]. Likewise, one may anticipate only a very slight modification in $e^{*2}_{T,\text{GaAs}}$ for the Ga-As oscillators within the host sublattice over the dilute range studied here. Adding just a few percent of Bi into GaAs by the substitutional replacement of As will, however, significantly reduce the total number of Ga-As oscillators, N, and thus reduce the total TO-LO splitting.

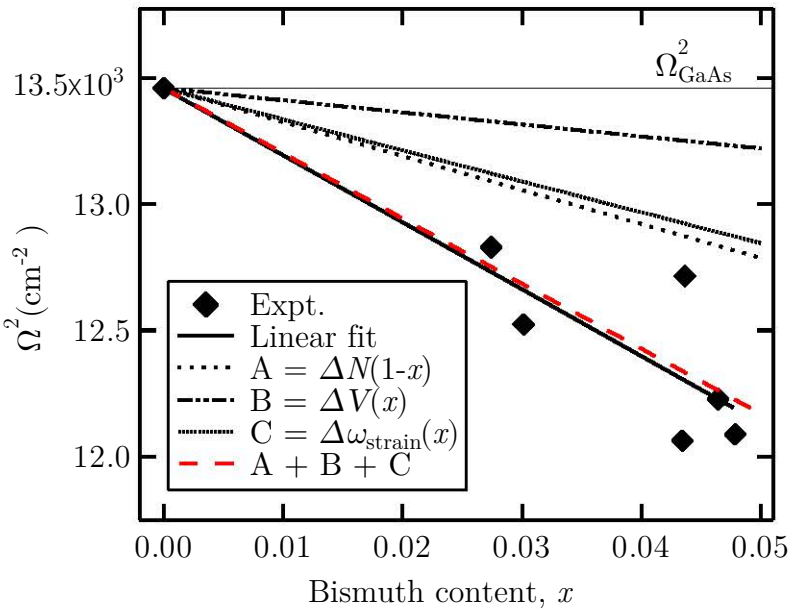

Figure 4.9: The squared ionic plasma frequency for the GaAs-like LO phonon band in dilute $GaAs_{1-x}Bi_x$ for increasing Bi (x). A linear fit has also been made to the data which was derived from measurements of the TO-LO splitting in Fig. 4.8: $\Omega^2 = \omega^2_{LO} - \omega^2_{TO}$. Contributions to the measured splitting, with respect to parameters contained in Eq 4.38, and the total sum of these changes (A+B+C), are also presented. The constant value of Ω^2_{GaAs} is displayed unvarying for composition as a reference to the relative change.

It follows that the total number of bonds represented in Eq. 4.38 may be amended for in $GaAs_{1-x}Bi_x$; $N \rightarrow N(1-x)$. A further reduction in the TO-LO splitting will originate from the lattice expansion caused by the incorporation of relatively large Bi atoms.

Figure 4.9 presents the experimental Raman scattering measurement of the squared ionic plasma frequency in dilute (001) GaAsBi along with estimations for influential contributions to its narrowing, as discussed above. Summing the affects of alloying and strain (trace A + B + C) appears to account for a substantial proportion of the large compositionally-dependent reduction seen in the TO-LO splitting of $GaAs_{1-x}Bi_x$. While an initial comparison of the experimental data and this model appear very agreeable, there are very likely other non-trivial influences at play that have not been mentioned, which act to further modify the TO-LO splitting value. For example, the

large native p-type carrier population introduced into the crystal as a result of alloying presents a unique problem when interpreting compositionally-dependent phonon shifting in polar GaAsBi; the coupling between the LO-phonon mode and the plasmon mode − arising from the collective oscillation of free charge carriers − alters the original frequency of the LO band. There could very well be a fortuitous cancellation of such influences with the contributions from changes in the physical parameters ϵ_∞ or $e^{*2}_{T,\mathrm{GaAs}}$.

In reference to the (113)B $GaAs_{1-x}Bi_x$ data shown in Fig. 4.8(b), it is notable that for the GaAs ($x = 0$) the LO(Γ) mode is dampened by $\sim$0.7 cm^{-1}. This frequency shift was verified through mapping of large areas of the epilayer surface of the control and is also highlighted in Fig. 4.7(b). The samples were grown at near-stoichiometric conditions (i.e. the As flux is nearly the same as Ga flux) in order to incorporate Bi. This large shift in frequency for the control likely arises due to an increased number of As antisite (As_{Ga}) defects inherent in high-index GaAs epitaxial growth [131,144]. The strain determined from the small offset in the XRD scans (0.58×10^{-3}) is less than 1/3 of that required (1.8×10^{-3}) to cause a redshift of $\sim$7 cm^{-1}. Therefore strain caused by the presence of As antisites cannot explain the entire shift. Examining the FWHM of the LO phonon peaks for (001) GaAs and (113)B GaAs control epilayers in Fig. 4.7(b), we find their receptive values to be 2.7 cm^{-1} and 3.8 cm^{-1}, further indicating an inferior structural quality in the latter.

It is interesting that the contribution of strain-only effects in the (113) surfaces are predicted to be less to that of (001)-oriented samples (see Table 4.3 and Fig. 4.8). The total rate of redshift measured here for the (113)B $GaAs_{1-x}Bi_x$ samples is $\Delta\omega_{\mathrm{LO}} = -120(\pm 6)\mathrm{cm}^{-1}/x$, which is unusually large. Evoking the concept of "phonon confinement", the enhanced LO(Γ) phonon redshift arises from increased crystal defects inherent to (113)B crystal growth. Phonon confinement can cause optical phonons

to redshift in frequency, broaden and even become asymmetric. This occurs because the phonon, confined in direct space within a sphere of diameter L, can be described in reciprocal space by a wave packet with a range of k-values, $\Delta k \approx L^{-1}$ [145]. Thus the response observed in the Raman spectra is governed by a convolution of the ω vs. k phonon dispersion and the wave packet. Tiong *et al.*[146] employed the phonon confinement model to interpret the LO(Γ) phonon shift caused by bombardment of (001) GaAs with 270 keV As^+ ions, and its dependence on fluence. They[146] observed a maximum induced redshift before the LO(Γ) peak broadened into a continuum. A Raman spectrum of this kind is indicative of amorphous GaAs, in which the crystal begins to lack long-range order.

We suggest the relatively lower crystal quality of the (113)B-orientated samples is a consequence of the growth chemistry imposed by implementing this high index growth surface, rather than a failure to optimise the MBE growth conditions. The (113) GaAs(Bi) surface contains an equal number of (001)-like atoms having two surface-dangling bonds and (111)-like atoms having one surface-dangling bond. A type-A surface contains (001) As(Bi) atoms and (111)A-like Ga atoms, while a type-B surface contains (001)-like Ga atoms and (111)B-like As(Bi) atoms. It has been explained[144] that a (N11)A surface (where N= $1, 2, 3, \ldots$) has very low affinity for impurities and defect incorporation when compared to the (N11)B surface, since its dangling bond is empty. However, in (N11)B surfaces the two unbonded valence electrons of the As(Bi) atoms become very reactive. While Bi incorporation is enhanced, this makes (113)B growth prone to impurities and defects, significantly reducing material quality and performance. Ultimately this physical constraint limits the potential for integrating (113)B-oriented GaAsBi crystal into optoelectronic devices. Invoking the notion that an increase in defect density is the cause to the large dampening is supported by prior characterisation of these samples[79]. In Ref. 79 Henini *et al.* present transmission

electron microscopy (TEM) images for both the (001) and (113)B GaAsBi samples. These images reveal the presence of structural defects in both layers. In the case of (001) GaAsBi films, such defects consist mainly of minor dislocations. However, for the (113)B sample, the crystalline quality is shown to be fairly good at the growth interface where microtwins are observed, but degrades heavily near the surface. Z-contrast imaging also shows no Bi segregation near the GaAsBi/GaAs interface, despite the large amount of disorder. Coupled with the homogeneous surface mapping of Raman scattering spectra, the increased redshift in (113)B samples cannot be explained by Bi clustering. Thus the clear correlative behaviour of the LO(Γ) redshifted frequency and the Bi concentration x for samples grown on a (113)B-oriented substrate presumably arises from confinement of the phonon in the defective GaAsBi matrix.

Strong dampening effects on the LO(Γ) mode of our (113)B GaAsBi samples can likely be avoided by crystal growth below the critical thickness where defects develop. Raman scattering studies only examine the vibration properties near the surface of solids, thus one can only assume the enhanced redshift would not be observed near the epilayer interface where the crystal is coherently grown. While it is possible to improve the structural properties of these samples through optimizing growth conditions, we speculate that a more accurate Raman study might be achieved with thinner epilayers.

4.4 LO-phonon-hole-plasmon coupling in nominally undoped GaAsBi

Among the Raman active elementary excitations present in the first-order Raman spectrum in $GaAs_{1-x}Bi_x$, the scattering of coupled LO-phonon-hole-plasmon modes plays a significant role. In this section, we examine the scattering LOPC modes within nominally undoped $GaAs_{1-x}Bi_x$. Because of the very low structural quality of the

(113)B-oriented samples, they are omitted from further detailed treatment.

4.4.1 Composition-dependent analysis of LOPC mode

Figure 4.10 presents a reproduction of the predicted[122] carrier concentration-dependent (holes) frequencies of the coupled modes (L_+ and L_-) and the plasma mode (ω_p) shown in Fig. 4.3. Several LOPC traces have been added (dashed lines) which illustrate the general behaviour[113] of this mode for a rising (arrow direction) LOPC damping constant, Γ_p. Here we see that for low hole doping the LOPC mode is slightly blueshifted relative to ω_{LO} before redshifting towards ω_{TO} (crossing at $p \sim 5 \times 10^{18}\,\mathrm{cm}^{-3}$) with increasing hole concentrations and reaching ω_{TO} at higher concentrations ($p \geq 5{\times}10^{20}\,\mathrm{cm}^{-3}$). In our data, as the Bi molar fraction increases, the LOPC mode not only generally increases in intensity, but also softens well below TO for the entire compositional range studied (see Fig. 4.8(a)). The relatively large scatter in the data points for the LOPC frequency arises from the fitting procedure, which must navigate disorder-activated bands that are in close proximity to the LOPC mode, within the Raman spectra. Further, as shown in the inset of Fig. 4.8(a), the LOPC FWHM is relatively large, adding to the difficulty of isolating its true frequency. It is clear when comparing our data with representative p-GaAs LOPC lineshapes in the 10^{18}–$10^{20}\,\mathrm{cm}^{-3}$ doping range[113,123], we are well into the 'final stage' of the asymptotic approach to TO from LO. The further shift can be accounted by the significant reduction in the ionic plasma frequency associated with the LO phonon: $\Omega^2_{\mathrm{GaAs}} = (\omega^2_{\mathrm{LO}} - \omega^2_{\mathrm{TO}})$[141].

The fact the LOPC peak frequency for our lowest Bi content is well below that expected (not actually observed directly for this sample) as well as only having a scattering intensity comparable to that of the LO band, suggests strong damping effects dominate the phonon-hole-plasmon interaction of nominally undoped GaAsBi. The damping constant of the plasma oscillation Γ_p can be evaluated by the hole

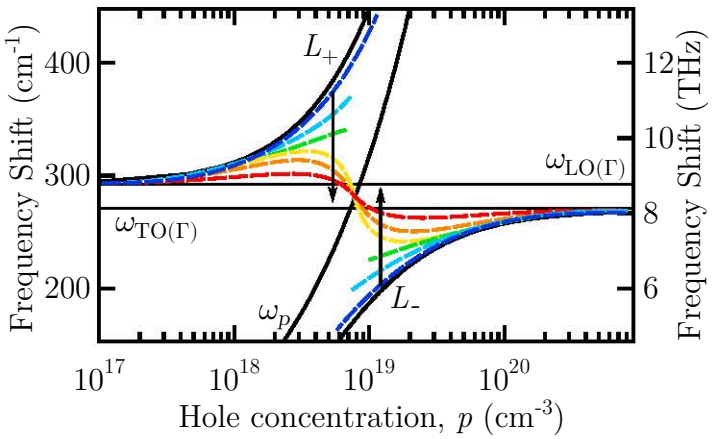

Figure 4.10: A reproduction of Fig. 4.3: a series of damped LOPC mode frequencies have been added (dashed lines) to illustrate the general behaviour for this mode with an increasing damping constant, Γ_p. The direction of the arrows shows the narrowing of the damped coupling path, from a low Γ_p value (blue; base of arrow), to a relatively high Γ_p value (red; head of arrow).

scattering rate as

$$\Gamma_p = \tau^{-1} = \frac{e}{\mu m^*}, \tag{4.39}$$

where e is the electrical charge, τ, μ, and m^* are the average scattering relaxation time, hole mobility, and effective mass of the free carrier, respectively. The intrinsically low hole mobility μ_h, due to large hole effective mass m_h^*, damps the coupled mode and induces broadening. The damping is more severe for GaAsBi than for GaAs since additional scattering mechanisms exist in a highly mismatched ternary alloy. Pettinari *et al.*[111] measured an order of magnitude reduction in μ_h for $GaAs_{1-x}Bi_x$ for $x <$ 6% with corresponding increase in m_h^*. The FWHM data in the inset of Fig. 4.8(a) shows a similar steady increase for both of the optic modes as a result of Bi-induced disorder, while the LOPC peak broadens more rapidly. The coupled linewidth, which corresponds to mode damping, is roughly in inverse proportion to the phonon content of the mode[147]. From Fig. 4.3, the coupled mode should only dampen and broaden in the vicinity of ω_p crossing ω_{LO}. These data further support the notion of a large Bi dependent damping constant, however further measurements on more dilute alloys

($x \leq 0.018$) would aid comparison.

4.4.2 Optical determination of carrier concentration

Conventional spectral analysis of the LOPC to study hole densities in p-type GaAs[123] assumes that the TO and LO frequencies, and other physical parameters of GaAs, do not drastically change over the doping concentrations used. The compositional redshift of the bands observed here introduces a problem in implementing such techniques into our analysis. However, by careful examination of the relative integrated scattering intensities of the LO and LOPC modes, we can spectroscopically estimate carrier concentrations[113].

We must first derive an expression of the Raman scattering cross section by taking into account the presence of a surface depletion region of width d[122] and adopt a simple two-layer (surface depletion layer/bulk material) model[124,148]; a schematic of such a two-layered system is provided in Fig. 4.11. For optical penetration depths greater than the depletion width, $d_{\text{opt}} > d$, the Raman spectra will exhibit both LOPC modes scattered from the bulk and unscreened LO phonon components from the depletion layer. The thickness of the surface depletion layer for large hole concentrations is estimated using the Schottky model

$$d = \left(\frac{2\varepsilon_0 \varepsilon_{\text{S}} \text{V}_{\text{B}}}{ep} \right)^{1/2}, \tag{4.40}$$

where V_{B} and ε_{S} are the band bending and static dielectric constant, respectively. The inverse relationship of d on p implies that as hole concentrations rise, the LO phonon scattering volume approaches zero. When the LOPC mode changes from phonon-like to plasmon-like the LO band is said to be totally screened. Thus, the intensity of the LO phonon scattered within the depletion layer essentially depends on the size of d and the penetration depth of the probe beam; however, we assume the Raman

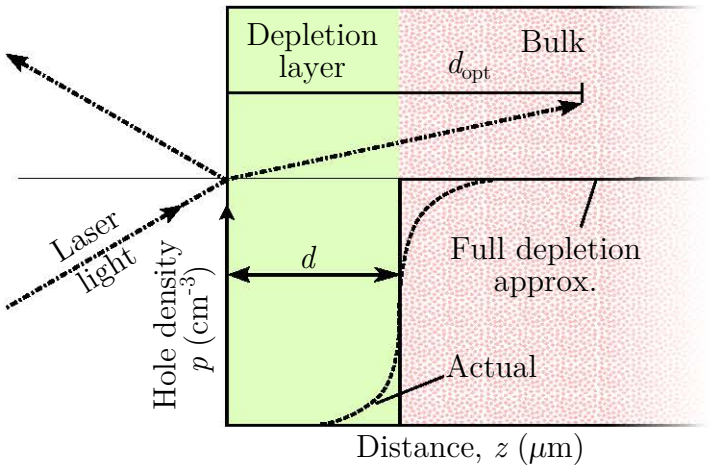

Figure 4.11: Schematic illustration of the Shottky model for "full depletion" and the formation of two scattering sites for LO phonons; uncoupled LO modes scattered within the depleted surface layer of length d and the coupled plasma modes originating from the bulk.

scattering by LO phonons in the depletion layer is similar to that in a undoped crystal. Given the low Bi content of our samples, we estimate that the Raman scattering cross section of the unscreened LO mode is similar to that in pristine GaAs. Light scattering from charge density fluctuations is not considered because the intensity is estimated to be of the order of 10^{-3} less than the phonon scattering intensity in p-GaAs. Then the integrated intensity of the LO phonon band for an opaque semiconductor with absorption coefficient α and $d \leq 1/\alpha$, is[149]

$$A_{\mathrm{LO}} = A_0[1 - \exp(-2\alpha d)]. \tag{4.41}$$

Here A_0 is the intensity observed in a low concentration or undoped crystal, where the plasmon frequency is too low to affect the LO phonon[150]. Since the integrated Raman intensity is proportional to the scattering volume, it follows that

$$A_0 = \zeta_{\mathrm{S}} A_{\mathrm{LOPC}} + A_{\mathrm{LO}}, \tag{4.42}$$

where $\zeta_S = I_{LO}/I_{LOPC}$ is the calculated area cross section from pure LO phonons and LOPC in a volume element, by Eq. 4.41. The depletion layer thickness for large hole concentrations can be estimated experimentally using Eqs. 4.41 and 4.42 by

$$d = \frac{1}{2\alpha}\ln\left(1 + \frac{\zeta_A}{\zeta_S}\right). \tag{4.43}$$

Here $\zeta_A = A_{LO}/A_{LOPC}$ is the ratio of the measured integrated intensities of the unscreened LO band from the depletion layer and the LOPC mode from the bulk. From the decomposition of the superimposed Raman features and equating Eqs. 4.40 and 4.43, we evaluate the hole concentration using

$$p = \frac{8\varepsilon_0\varepsilon_S\alpha^2 V_B}{e\left[\ln(1+\frac{\zeta_A}{\zeta_S})\right]^2}. \tag{4.44}$$

Figure 4.12 gives our experimentally derived values of ζ_A for $GaAs_{1-x}Bi_x$. Comparing I_{LO} for $x = 0$ with I_{LOPC} for $GaAs_{1-x}Bi_x$, leads to the ζ_S values in the inset. The intensity of the LOPC band increases relative to the unscreened LO mode for increasing x (see Fig. 4.7; the unscreened LO phonon contributions are greatly reduced for higher Bi contents). For the small Bi contents studied here, the LO band experiences almost total screening, due to the narrowing of the surface depletion layer. For comparison, the LO phonon in p-GaAs is only rendered invisible ($A_{LO}/A_{LOPC} \to 0$) for $p > 5 \times 10^{19}\,cm^{-3}$, thus our observations here for *nominally undoped* GaAsBi are remarkable.

Pettinari *et al.*[111] performed Hall effect experiments on 30–56 nm thick $GaAs_{1-x}Bi_x$ epitaxial layers for $0.06 \leq x \leq 0.106$ and found that the hole concentration rose from $\sim 4 \times 10^{13}\,cm^{-3}$ for $x = 0.6\%$ to $2.4 \times 10^{17}\,cm^{-3}$ at $x = 10.6\%$. This suggests that in our samples the carrier concentrations should not exceed $p \sim 3 \times 10^{15}\,cm^{-3}$. To quantitatively evaluate p using Eq. 4.44, Bi-induced perturbations in the physical

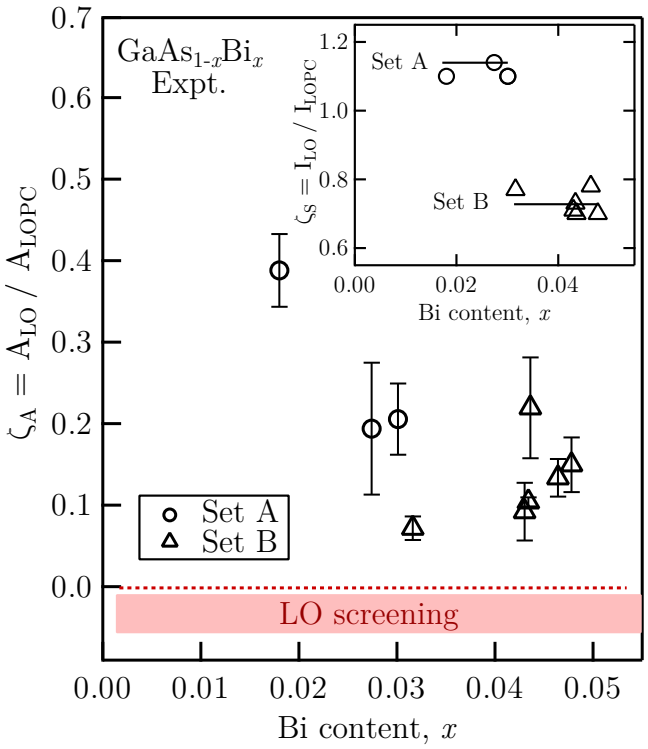

Figure 4.12: Experimentally determined values of ζ_A for all GaAsBi samples. The inset shows ζ_S for samples set A and B, used to calculate the two theoretical traces shown in Fig. 4.13.

constants of the semiconductor must once again be considered. Though the optical constants of GaAsBi are not well known, there are good estimates for changes in complex dielectric function and absorption coefficient [142,143]; the band bending may be estimated assuming Fermi pinning at the Bi-induced acceptor states [110]. However, including these factors increases the spectroscopic estimation of p by only a factor of 2 to 4, rather than by orders of magnitude. Alternatively, the hole concentration strongly depends on the values of ζ_A and ζ_S and the Raman efficiency of the LO phonon in theory can depend on x, which would abnegate use of a constant ζ_S. On close examination we find values for ζ_S differ between sample sets A and B, but are consistent across the same set. Thus it is reasonable to assume that ζ_S has weak Bi dependence over the range studied here and the difference between sets A and B is more likely due to their differing low optical qualities (caused by growing the epilayers

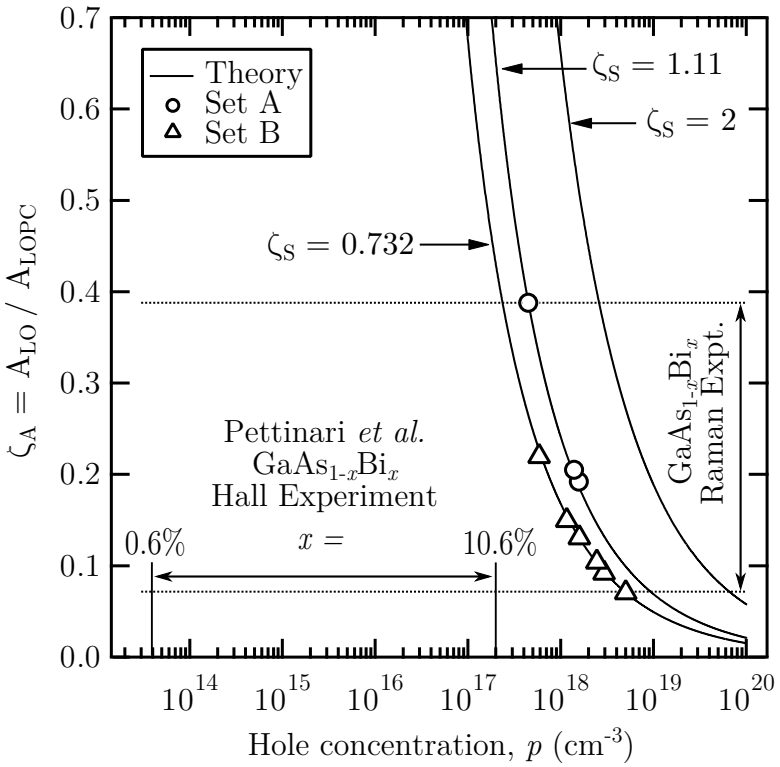

Figure 4.13: The theoretically expected[122] values of ζ_A (solid lines) for p-GaAs as a function of hole concentration. The horizontal and vertical ranges shown are from Pettinari *et al.*[111] and our optical measurements, respectively.

away from stoichiometric conditions to introduce Bi into the GaAs matrix). Thus we present the theoretical[122] p dependence of ζ_A for the host p-type GaAs in Fig. 4.13. With a conservatively low[151,152] value of $\zeta_S = 0.732$ we estimate the hole concentration to exceed $5 \times 10^{17}\,cm^{-3}$. The transport results of Pettinari *et al.*[111] are far smaller.

Since reporting these results in Ref. 153, Li *et al.*[154] echoed similar findings; they revealed relatively large hole concentrations in their nominally undoped 250 nm thick $GaAs_{1-x}Bi_x$ epitaxial alloys ($p > 10^{18}\,cm^{-3}$), and also found that they grew steadily with the Bi concentration. Attempting to reconcile these conflicting reports[111,153,154], we suggest the larger hole concentrations are due to the synthesis of much thicker epitaxial layers. The thinner epilayers of Pettinari *et al.*[111] (~ 50 nm) are closer to a pristine and evenly distributed GaAsBi system, with a lower density of bismuth pair or cluster states than thicker layers[155]. On the other hand, we fully concur that hole

concentrations rise with increasing Bi molar fraction. Theoretical examination into the formation of Bi-induced acceptor states located above the valence band during the growth may shed light on the discrepancy. The source of the single mode behaviour in *p*-type GaAs has been traced to the intra-band heavy hole transitions, though for the simplified analysis presented here, contributions to the Raman spectra from intra-light-hole and inter-valence-band scattering mechanisms are omitted[123]. The GaAsBi band structure experiences most of its shift in the valence band, acceptor states are pinned roughly 26.8 meV above the valence band edge and there exists increased valence band splitting that occurs with increasing strain; these factors cannot be overlooked in better describing the strong damped hole-plasma-coupling phenomena.

Chapter 5

VLS-driven Bi surface droplets during MBE of $GaAs_{1-x}Bi_x$

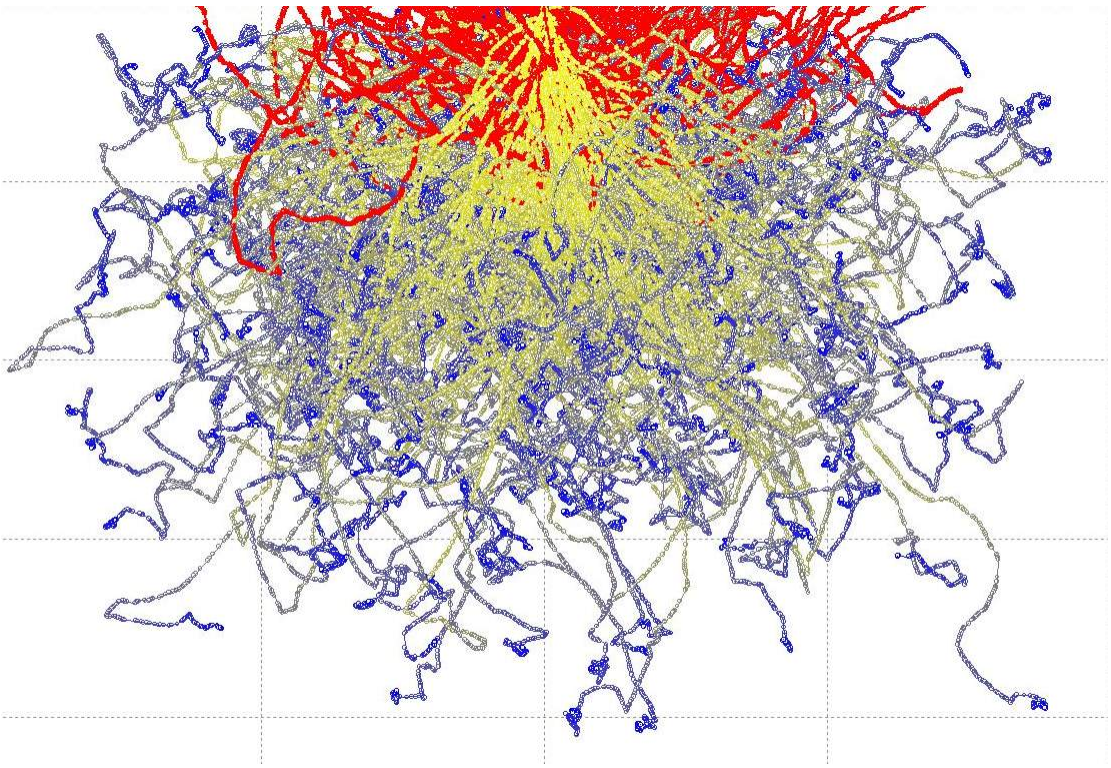

Simulated trajectories of electrons incident normal to a surface. The shift to cooler colours represents the loss of electron energies as they penetrate deeper.

5.1 Motivation

The precision assembly of functional semiconductor nanostructures has experienced a recent explosion of interest[156], as they hold tremendous promise for building future electronic and photonic devices. Since it was first reported by Wagner and Ellis[75], the vapour-liquid-solid (VLS) mechanism has been extensively used in the synthesis of a wide variety of one-dimensional nanowires from the μm to the nm diameter range[157]. Of particular interest are III-V alloy nanowires with direct bandgap and high mobilities, grown by molecular-beam-epitaxy (MBE)[158]. For the pertinent case of dilute $GaAs_{1-x}Bi_x$ materials[2,159], bismuth alloying offers further design freedoms by inducing a tunable reduction in the bandgap energy[28,44,159,160]. Such properties provide appealing avenues for the growth of nanostructured materials accessing longer wavelengths[161]. As already outlined, the large bandstructure modifications are due to the massive disparity in atomic radii and electronegativity between group-V Bi and As atoms, which also imposes physical and technical challenges for growers; Bi exhibits a strong tendency to segregate and form metallic surface droplets[27].

The tendency for Bi to surface-segregate has motivated intense research into how to grow device-quality $GaAs_{1-x}Bi_x$/GaAs structures while retaining appreciable Bi incorporation[162]. On the other hand, in the pursuit of realising record GaBi molar fractions, the attitude of researchers toward the optical and structural quality of high Bi content film appears more relaxed[68]. Recently, several unpublished reports of Bi-rich films exhibiting surface droplets have indicated unusual epitaxial "tracks" left behind the droplet which are formed during the MBE growth, begging the question: are they *moving*?

In the liquid phase, Bi droplets are known to ultimately act as catalysts to several fascinating growth phenomena utilised by nanofabricators[163,164]. Knowledge of the destabilisation process[77] and movement of the Bi droplets (sometimes referred to

as crawling, self-propagating or running), as well as the subsequent formation of a new nanoscale surface structure (in-plane nanowires), is vital to form a complete understanding of GaAsBi growth.

Investigations utilising elemental bismuth to seed the VLS growth of III-V nano- or microstructures are limited[77,78], with studies often tending to focus on alternative material systems; such as Cd(Se,Te)[165], PbTe[166], SnS_2[167] and Si[168] nanowires. Bismuth is a group V species, however it does not readily form a solid binary compound with Ga. Rather than being directly harmful to the electronic properties of the host, like silver- or gold-seed atom incorporation[169,170], bismuth strongly alters the GaAs bandstructure[32–34] (however some anomalous effects are known to occur, which were explored in detail in the previous chapter). Thus the small amount of interest in Bi-assisted III-V nanostructure growth using the VLS mechanism is surprising, given its candidature as an alternative "self-seeded" type of catalyst, able to tune the nanowire properties[171] through intentional incorporation of Bi atoms from the catalyst. The bismuth-assisted growth of III-V (InAs, GaP, GaAs, and InP) nanowires has already been realised employing the solution-liquid-solid (SLS) technique[172]. Since a solution-based synthesis differs considerably from a vapour-based method, it is difficult to directly compare these findings with the current work. However, it is worth mentioning the nanowires grown by SLS demonstrated good crystal quality, with few stacking defects[172].

Besides a number of investigations into GaAsBi quantum well structures, detailed studies of GaAsBi nanostructures are scarce[78,161,173]. Recently, Sterzer *et al.*[173] showed that for static Bi surface droplets the crystalline Bi exhibits preferential lateral ordering with respect to the GaAsBi surface after cool-down. A more recent study published by Essouda *et al.*[78] reported the first synthesis of Bi-catalysed GaAsBi nanostructures atop GaAs, grown by atmospheric pressure metalorganic vapour phase

epitaxy. Simple fully-tapered planar structures were synthesised in the work[78], however none reached over a micron in length. Further, they[78] did not investigate the microstructure of their nanostructures, nor their important optical properties. As far as we can tell, excluding earlier theoretical work into GaAsBi nanowires by Ding *et al.*[161], these two studies by Sterzer *et al.*[173] and Essouda *et al.*[78] encompass the full degree of literary work on the subject.

A comprehensive knowledge of the effects that droplet epitaxy has on the GaAsBi crystal surface is vital to achieving high-performance GaAsBi alloys with large Bi concentration. Several investigations have done well to identify the MBE growth conditions that lead to droplet formation[27,69,72,73,174], however surprisingly little is known about the mechanisms governing their kinetic behaviour or their potentially disruptive interactions with the underlying crystal. Without the aid of a microscope, a significant limitation to the optical and physical characterisation of GaAsBi epitaxial films exhibiting surface droplets is the lateral resolution of the instruments employed (typically in the order of mm to cm). Thus, experimental probes are often far larger than the dimensions of the surface droplets/tracks on the surface (order of nm to μm[27,69,72,73,174]) with measurements unavoidably recording an unresolved average of the entire probed area. While the removal of Bi surface droplets − through selective wet chemical etching − prior to characterisation appears to rid the surface of Bi metal, a number of experimental studies have neglected to consider their lasting impact on the structural and optical properties of the epitaxial surface[3,175,176]. This issue we investigate in the present chapter using micro-optical probes (lateral resolution: $\sim 1\mu$m).

On account of the limitations of modern top-down semiconductor lithography, there is a growing interest in using self-organizing systems to achieve functional nanometre planar structures with reproducible shape and size. Needless to say, understanding

the morphological origins of any nanostructure is paramount to their functional design. Numerous models have highlighted the importance that growth chemistry and parameters have on the VLS process[177], with several growth modes already identified (phase transitions[178,179], diameter oscillating[180,181], kinking[182,183], and crawling[179]) as emerging from different interactions between the catalyst and underlying crystal. Nanostructures possessing non-monotonous morphological variations along the growth direction are offering new avenues for device engineering, with periodic dimensional changes[178,181,184] of particular interest due to novel quantum confinement effects[185–188]. Moreover, the formation of preferentially orientated structures[189] are in parallel with advancing technological aims to employ bottom-up fabrication techniques[179,190–193]. Nanowires which self-align on the surface could play an important role in combining the synthesis and assembly in a single step, while offering compatibility with traditional planar device structures[189,192–195].

In this chapter, we extend the current palette of non-monotonous one-dimensional III-V nanostructures and report a new type of self-aligned planar growth mode (resulting in what we have called nanotracks), which exhibit dual periodic height variations that are out-of-phase across the growth axis, and persist the entire length of the structure (see, for example, Fig. 5.1). It is found that an explanation for their unusual planar shape is outside the scope of the limited number of growth models[179,189] currently available in the literature. Thus we present in this chapter a new type of kinetic growth model; one which geometrically addresses the problem of localised species supply in the MBE growth chamber and links it to an inhomogeneous nucleation interface. Such a proposal is very different to the current commonly-used models of crawling mode growth kinetics[179,189].

5.2 Bi droplets and the formation of planar nanostructure

Due to the Bi-droplet-induced degradation of its epitaxial surface, the single $GaAs_{1-x}Bi_x$ sample investigated in this chapter was omitted from the Raman studies in Chapter 4. For clarity, we will define our planar nanostructures as nanotracks, given their unique aspect ratio (see Figs. 5.1, 5.6 or 5.7). They were synthesised in parallel to the MBE of the 300-nm thick (001) GaAsBi/GaAs epitaxial structure. A relatively large Bi flux was used which was well within the Bi saturation regime[27], where an alloying limit is imposed by the low miscibility of Bi into GaAs. As a consequence, liquid Bi droplets form (Fig. 5.1(a)) through aggregation of unincorporated Bi atoms on the surface. As an essential requirement for the MBE of GaAsBi, growth is carried out at the relatively low substrate temperature (compared to the MBE of other III-V alloys) of 325-330°C. This is well above the Ga-Bi eutectic point (222°C) and low melting point (compared to other group-V metals) of pure Bi metal (271°C). While the local Bi droplet density varied slightly across the sample surface, their size and typical surface effects did not. The MBE geometry employed is a standard Riber 32P design with non-normal MBE effusion cells and a sample mount which rotated throughout growth to promote the homogeneous epitaxial incorporation of Bi. The nominal bismuth concentration in the smooth bulk $GaAs_{1-x}Bi_x$ epilayer is $x = 0.040$, determined through evaluating the micro-photoluminescence (micro-PL) peak energy[4]; raw PL data is provided in Fig. 5.14. When compared to other droplet-free locations on the sample surface this value is found to be consistent, and comparable to known Bi saturation limits for $GaAs_{1-x}Bi_x$ alloys grown under similar conditions[26].

Figure 5.1(a) shows a representative scanning electron micrograph (SEM) of the GaAsBi sample surface, revealing a relatively smooth GaAsBi epitaxial growth over-

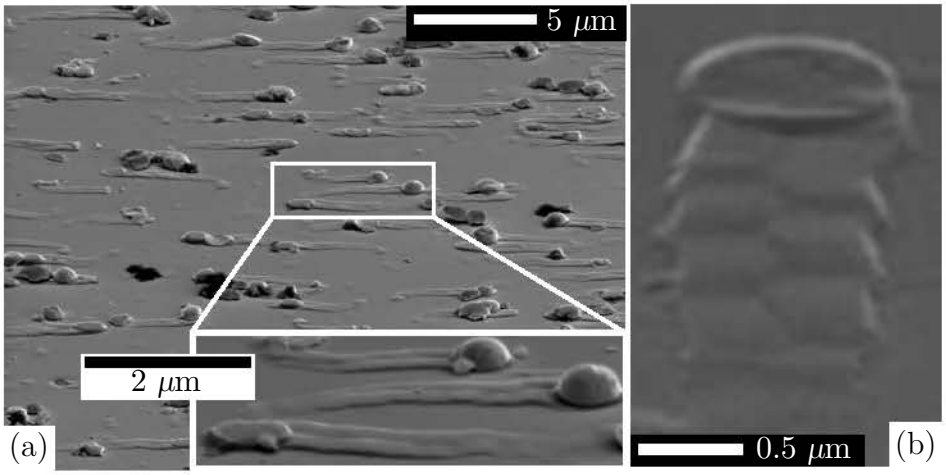

Figure 5.1: Secondary electron SEM images of (a) GaAsBi sample surface, showing the formation of surface droplets and trailing nanotracks. The bottom inset presents an enlargement of the SEM image and exhibits the parallel/antiparallel nature of nanotrack growth. (b) An alternative perspective of nanotrack formation, revealing pronounced out-of-phase height variations across their growth axes.

grown by Bi surface droplets and the formation of in-plane GaAsBi nanotracks. EDS measurements indicated pure Bi droplets are formed on the GaAsBi surface (no final Ga/Bi dual composites[27]), which is indicative of Bi-rich growth and attributed to Bi segregation[27]. The bottom inset in Fig. 5.1(a) focuses on the parallel/antiparallel alignment of the nanotracks and the contrasting forms by which they can terminate − with or without the surface droplet catalyst. The pressure of Bi is high at 330°C and a sufficiently large Bi beam equivalent pressure (BEP) is required to avoid total evaporation of Bi droplets. If the Bi BEP drops well below the Bi desorption rate, none of the bulk Bi will remain. That many nanotracks terminate forming nanodiscs[77] without droplets reflects a partial disruption of this fine balance, likely towards the final stages of growth.

Of one hundred characteristic nanotracks inspected (neglecting disrupted growths), the typical lengths (4-5 μm), heights (45-55 nm), as well as the terminating nanodisc diameters ($\sim$940 nm), appear relatively steady across the whole sample surface. Such a consistent mode of distribution indicates a uniform growth environment, as well as

signifying our Bi liquid droplets necessitate a critical volume before moving. In the absence of direct observation, determining such kinetic features, as well as the exact initial time of nanotrack formation, is difficult. We note that nanotracks formed early on during growth would likely exhibit an overgrown character, due to the rising (and much thicker) epitaxial layer. That all nanotracks possess comparable dimensions, and none appear to be overgrown, suggests a temporally unified deposition of the nanotracks. Further, simultaneous growth likely occurred late during MBE.

Figure 5.1(b) offers a different perspective of the nanotracks. Topologically-sensitive secondary electron imaging (SEI) is employed to highlight the presence of a periodic undulation pattern seen across the nanotrack centre, evidenced by image shadowing. The variation in height exhibited here is archetypal of all inspected nanotracks, a characteristic persisting along the entire nanotrack length. Another fascinating feature is the centre axial line of the nanotrack. As far as we can tell, planar nanostructures exhibiting this unusual morphology are *yet to be reported*.

Unlike for free-standing nanowires, a unified understanding of crawling modes is not yet realised[179,189,190]. Principally, the VLS mechanism[75] underpins our observations of Bi droplet movement and the formation of self-aligning nanostructures. Such VLS-driven growth should not be surprising during the Bi-rich MBE of GaAsBi alloys; Schwarz *et al.*[179] have calculated the stability of different modes of steady-state growth and found a uniquely broad stability range for the promotion of crawling modes, in which lateral, rather than free-standing, nanowires form. While the kinetics of VLS growth are extremely complicated, our aim is to introduce the fundamental processes in the following section, in aid of interpreting our results.

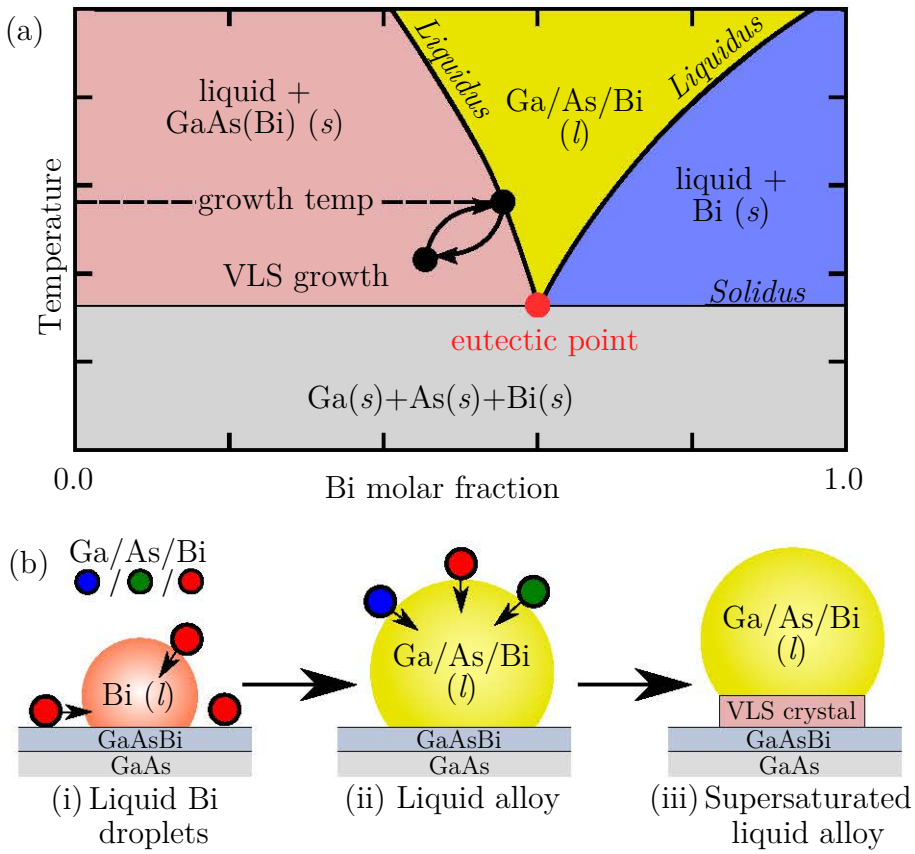

Figure 5.2: (a) Illustration of the pseudobinary (Ga/As)-(Bi) eutectic phase diagram where, for clarity, the scheme has been simplified to treat both Ga and As components together, as one part of a binary system. Note this phase diagram does *not* portray actual data in any way (the true eutectic point is unknown, for example) and is offered purely for demonstrative purposes. Features of this diagram are described in detail in the text. (b) Schematic illustration of (i) Bi segregation and development of liquid surface droplets during MBE, (ii) the adsorption of Ga and As species and the formation of a eutectic liquid alloy and (iii) the deposition of crystal at the liquid-solid interface.

5.2.1 The vapour-liquid-solid mechanism and preferential growth

The use of metals to mediate the growth of high-aspect ratio semiconductor nanostructures is well established[75,156–158]. The general mechanism for VLS growth is most easily described by considering the illustration of a simplified phase diagram for the Ga-As-Bi eutectic system, presented in Fig. 5.2(a). By its very composition and nature, a mixed eutectic system will exhibit a melting temperature far lower than that

possessed by its pure constituents; the minimum melting temperature occurring at some well defined alloying ratio is defined as the *eutectic point*. Note that at precisely the eutectic point, all phases exist simultaneously.

The heavy liquidus line in Fig. 5.2(a) separates the all-liquid phase from the liquid + solid phases, while the light horizontal solidus line separates the liquid + solid phases from the all solid (crystal) phase. Such boundaries are determined through experiment, whereby a systematic mapping of the alloy transition points is measured − such data is not available for the current system. For changes in alloy composition, growth at a constant temperature defines where on the liquidus boundary the alloy phase will transition. VLS growth is indicated Fig. 5.2(a) by the cyclic arrows, in which the system repeatedly fluctuates between a state of liquid + GaAs(Bi) (s) (red region) and an all-liquid state (gold region), by continual equilibrating via VLS growth.

Figure 5.2(b) presents a schematic of the overall process leading to VLS growth. Once surface segregation produces Bi surface droplets, and in the liquid phase, the eutectic will adsorb Ga and As species from a vapour with a higher chemical potential (μ_{v}), relative to the liquid chemical potential (μ_{l}). Thus the difference in these quantities is defined as

$$\Delta\mu_{\mathrm{vl}} = \mu_{\mathrm{v}} - \mu_{\mathrm{l}}, \tag{5.1}$$

where the system is said to be supersaturated (concentration of the components in the liquid phase is higher than the equilibrium concentration; red region of Fig. 5.2(a)) for

$$\Delta\mu_{\mathrm{vl}} > 0. \tag{5.2}$$

If the chemical potential of the solid (μ_{s}) is lower than μ_{l}, and in a state of supersaturation, the droplet may equilibrate via an exchange with the solid crystal surface, rather than desorbing already deposited material back into the vapour. In response to the concentration imbalance the droplet crystallises material at the liquid-solid interface,

as illustrated in Fig. 5.2(b). With a continual supply of vapour, and growth of the epilayer in the solid-state (MBE) proceeding relatively slowly, herein lies the driving force of the VLS mechanism[196]:

$$\mu_{\mathrm{v}} \geq \mu_{\mathrm{l}} \geq \mu_{\mathrm{s}}. \tag{5.3}$$

Generally, nucleation at the liquid-solid interface will be preferentially faceted and growth − as well as motion − will proceed perpendicular to the dominant crystal face. The tendency for facets with low surface energies to form more readily gives rise to self-alignment, evidenced in our case by only a small fraction of our nanotracks taking on nonconforming paths.

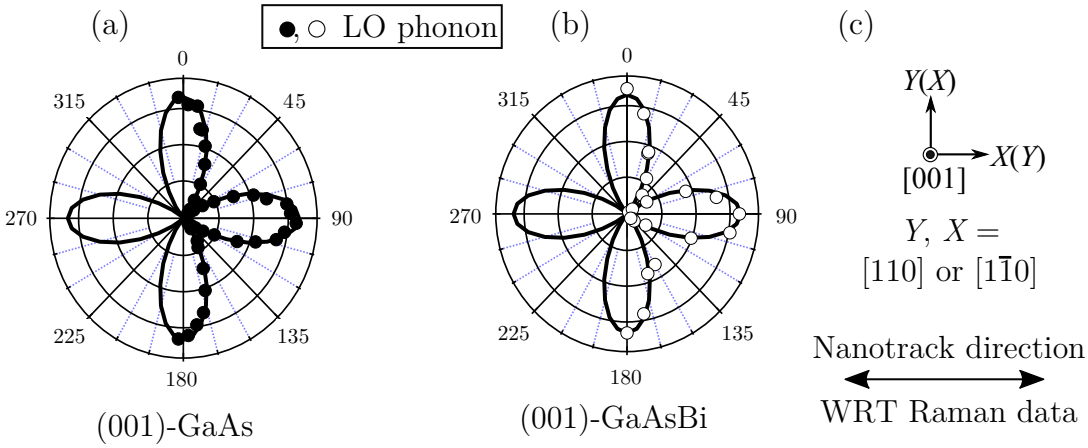

Figure 5.3: Polarised micro-Raman scattering LO phonon polar plots measured from (a) a pure (001) GaAs crystal surface and (b) the (001) GaAsBi surface. (c) Shows the possible basis directions (either [110] or [1$\bar{1}$0]) deduced from the analysis of (b) (and (a)), along with the observed preferential nanotracks growth direction, with respect to (WRT) the Raman data in (b).

To investigate our preferred growth directions, Fig. 5.3 displays polarised micro-Raman backscattering data which were recorded in a $\hat{e}_i \parallel \hat{e}_s(\alpha)$ configuration from the (001) GaAsBi sample surface and the intensity of the LO band was analyzed as a function of scattering geometry. These measurements indicate that the nanotracks align with either the $\pm$[110] or $\pm$[1$\bar{1}$0] crystallographic directions. From a crystallo-

graphic point of view, the orthogonal ±[110] and ±[1$\bar{1}$0] directions on a (001)-oriented zincblende substrate are not equivalent to each other, and growth will occur where interfacial energy is minimised. In zincblende GaAsBi, group-V terminates on (111)B facets, which has the lowest free energy[197].

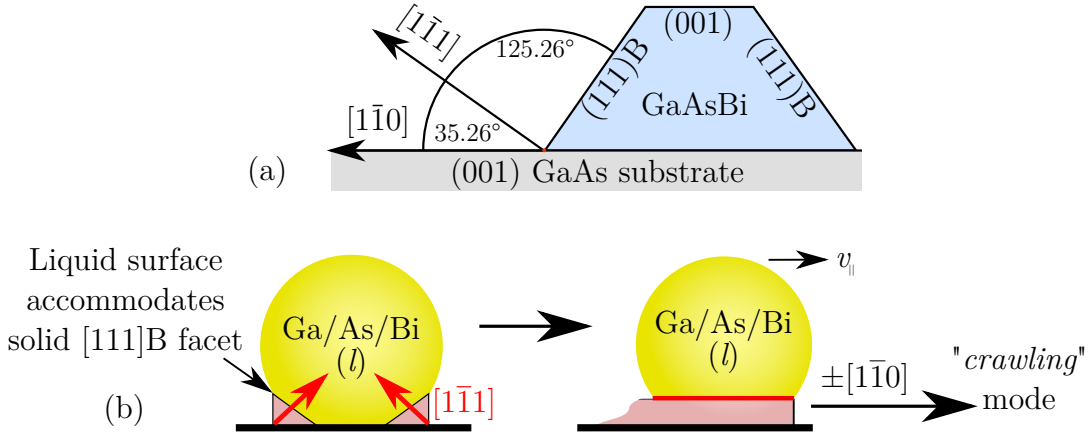

Figure 5.4: (a) Geometric information of relevant crystal faces relative to the [001] growth direction, and (b) a schematic illustration of two simultaneous [111]B growth planes accommodated by the liquid interface, which evolves ultimately into movement in a single planar direction. A "crawling" mode then propagates with in-plane velocity $v_{||}$ in the ±[1$\bar{1}$1] bi-direction, with the liquid droplet pinned on the nanotrack top by surface tension.

Figure 5.4(a) presents the out-of-plane [111]B direction (also written as [1$\bar{1}$1]) relative to the (001) epilaxial growth. Given this directional growth property for zincblende crystals, and the lateral projection of [111]B onto the epitaxial surface, we assign ±[1$\bar{1}$0] as the preferential growth direction for our nanotracks. This bi-directional growth facet agrees well with the literature[189,194,195,198]. Figure. 5.4(b) shows how lateral motion in the [1$\bar{1}$0] is achieved by this process; the mobility of the liquid surface at the interface accommodates the low-energy [111]B facet being synthesised and the droplet motion is restricted in-plane. With simultaneous growth of multiple facets of equivalent energy, the final growth direction is ultimately determined by random small-scale topological or thermal fluctuations. A crawling growth mode then propagates with the liquid droplet pinned to its front via surface tension. That

we see equal movement in opposite directions eliminates thermal gradient or electric field effects underpinning this preference.

5.2.2 Nanotrack composition

To determine the composition of our VLS-grown nanotracks, the EDS modality is employed. Because the structures examined are in the nanoscale regime, it is vital to first consider the interaction volume of our EDS probe; a schematic illustration of the characteristic x-ray contribution to the electron interaction volume is provided in Fig. 2.10. As the voltage used to accelerate the electron beam (e-beam) is increased, the energy of the electrons will also increase, penetrating deeper into the material. Electrons possessing energy high enough to knock out the inner electrons of Ga, As or Bi atoms may produce characteristic x-rays from well below the surface.

In assessing the volume from which characteristic x-rays are generated, there are essentially two impactful experimental parameters to consider for fine tuning. The first parameter is the accelerating voltage used to produce the e-beam, which will scale with the depth, z, from which x-ray signals are detected. Ideally, the lowest possible accelerating voltage should be employed that will produce electrons capable of generating the largest x-ray peak energy examined. The other important parameter to consider is the angle at which the e-beam is incident on the surface; higher incident angles will lift the teardrop-shaped interaction volume toward the surface, and reduce the overall penetration depth (see the simulated electron trajectories in Fig. 5.5(b)). While the exact location of the x-ray detector in the SEM instrument will also influence measured signal intensities, its location is effectively fixed in our experiments to 30° from the sample normal, and defines an azimuthal angle of 40° with respect to the incident e-beam.

The quantitative model used by the instrument software is based on GaP and

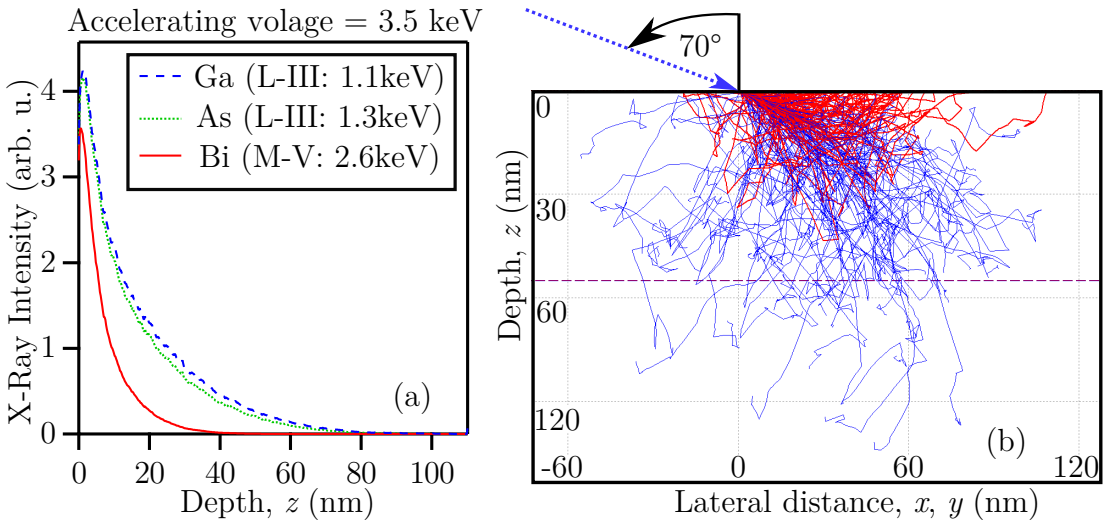

Figure 5.5: Monte Carlo simulated x-ray signal from a 10 nm wide e-beam consisting of 10^4 electrons accelerated at 3.5 keV and incident at an angle of 70°. The simulated crystal structure is $GaAs_{0.968}Bi_{0.032}/GaAs_{0.96}Bi_{0.04}/GaAs$ with relative layer thicknesses of 55 nm/300 nm/500 μm. (a) Simulated x-ray intensity depth profile and (b) 2D tracked paths of 200 electrons from the simulation. The blue paths here show trajectory terminations within the crystal and red indicate paths which escape from the crystal surface (secondary electrons) which do not contribute to the characteristic x-ray emission. For reference, the broken horizontal line in (b) indicates the interface between the two top $GaAs_{1-x}Bi_x$ layers of the simulated structure, at a depth of $z = 55$ nm. The simulation was performed using the monte CArlo SImulation of electroN trajectory in sOlids (CASINO) v2.42 software package[199], implementing the default procedure model.

InAs compounds, and pure Bi metal, making it ineffective at determining the absolute composition of $GaAs_{1-x}Bi_x$. For example, a Bi concentration in the $GaAs_{1-x}Bi_x$ layer was estimated to be over $x = 0.1$ using the compositional analysis algorithm, which is far larger than the expected value of $x = 0.04$. This is in fact a common problem for EDS measurements without the analysing software being specifically calibrated for a particular material system[200]. Thus, standardless EDS is employed and we rely on the signal detected from the $GaAs_{0.96}Bi_{0.04}$ epitaxial film for comparison with the nanotrack.

A reliable EDS measurement can only be made if the Bi-related x-ray signal depth is much lower than the nanotrack height. Maintaining a manageable integration time (∼20 minutes), a reliable EDS measurement is found to be made with a 10-nm-wide

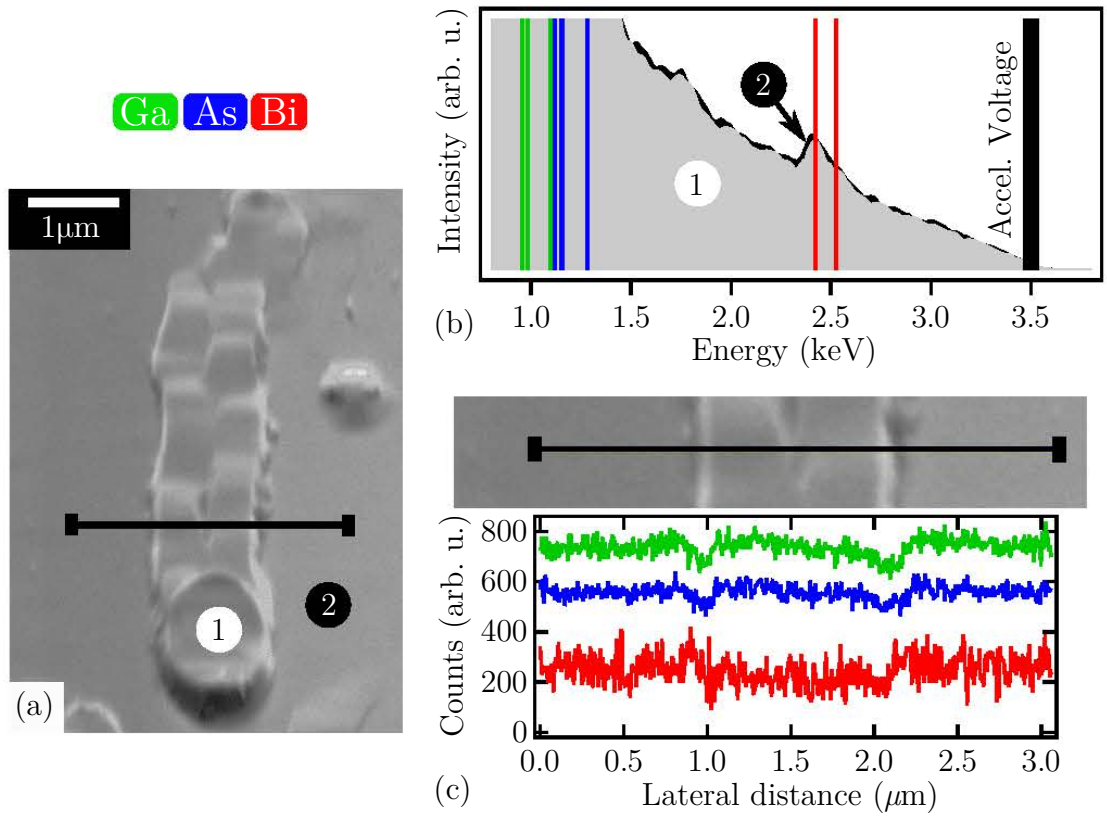

Figure 5.6: (a) Flattened SEM image of nanotrack acquired at 70° to surface normal with the locations of interest indicated. (b) Displays a comparison of the raw EDS spectra focusing on the Bi-related signal, measured from two different locations; (1) on the VLS-grown nanodisc, and (2) from the GaAsBi epitaxial layer. The coloured vertical lines indicate the various L shell lines of Ga and As, and the M shell lines of the Bi atom, used to quantify the x-ray counts. (c) EDS line scan taken across the nanotrack. Because the EDS measurement here is considered standardless, and to avoid confusion, (c) is presented in raw counts rather than a compositional percentage.

e-beam accelerated by a 3.5 kV potential and incident at 70° to the surface normal. To verify, a Monte Carlo simulation of the EDS signal generated implementing such an experimental procedure is presented in Fig. 5.5. The layered structure used in the simulation is based on the alloying composition interpreted from the EDS experiments presented Fig. 5.6 (relative to $x = 0.04$ in the epilayer), the density calculated from elasticity theory and the physical dimension are determined from the AFM morphological data shown in Fig. 5.7: $GaAs_{0.968}Bi_{0.032}(55\,nm)/GaAs_{0.96}Bi_{0.04}(300\,nm)/GaAs(500\,\mu m)$. Figure 5.5(a) shows the theoretical x-ray intensity depth profile for the highest peak

energies generated from each of the constituent Ga, As and Bi species. Note the bottom GaAs layer yields no x-ray signal under the simulated conditions and is simply added for completeness. Examining these data we find that at a depth of $z = 48\,\text{nm}$, one would expect to detect over 99.96 % of the characteristic x-rays emitted from Bi atoms within the nanotrack crystal. Likewise, at a depth of $z = 55\,\text{nm}$, approximately 97% of the Ga and As EDS signal will be detected. Beneficial to our experiments is the fact that we are simply interested in assessing the concentration of Bi atoms, which are detected from a relatively shallower depth because of their large Z number. Defining a large 70° incident angle does reduce the lateral resolution of the measurement, however the local composition of the nanotrack is not expected to deviate greatly. Rather than fix an accurate value for the concentration of Bi within the nanotracks, our aim here is to merely demonstrate that there is an interestingly substantial inclusion, from the droplet catalyst. The chemistry of Bi incorporation into the nanotracks will be extremely complicated, particularly given the VLS structure is more closely lattice-matched atop $GaAs_{1-x}Bi_x$, rather than a GaAs substrate.

Figure 5.6(a) displays a flattened (recorded at 70° to normal and augmented to appear from top-down) SEM image of an undulating nanotrack examined using EDS, whereby point analyses (Fig. 5.6(b)) and a line scan (Fig. 5.6(c)) are also presented, recorded from the locations indicated in the SEM image. Interestingly, an initial assessment of these data clearly indicates a substantial inclusion of Bi into the nanotracks. The raw x-ray data examining the Bi-related energies is included in Fig. 5.6(b) to demonstrate the comparable spectral weight of these x-ray signals measured from the nanotrack and the epitaxial layer. Analysing similar spectra recorded implementing a line scan measurement forms the data shown in Fig. 5.6(c), which further exhibits the considerable inclusion of Bi into the VLS crystal, from the catalyst. The amount of Bi introduced here appears to be only slightly less than of the epilayer. To quantify

the Bi incorporation, the nanotrack is estimated to contain approximately 70% - 80% of the Bi held in the surrounding epilayer ($x_{\text{nanotrack}} = 0.028$ - 0.032), and found to be consistent across all growth.

As we will see later in this chapter, conclusions drawn from the analysis of micro-Raman and micro-PL measurements on nanotracks confirm this substantial level of Bi alloying. While the present work is relatively unrefined compared to a dedicated growth study, this interesting compositional result strongly suggests that a bismuth-based eutectic may be used effectively for the self-catalysed growth of 1D dilute GaAsBi nanostructures, using MBE and the VLS mechanism.

5.2.3 Morphological studies of nanotracks

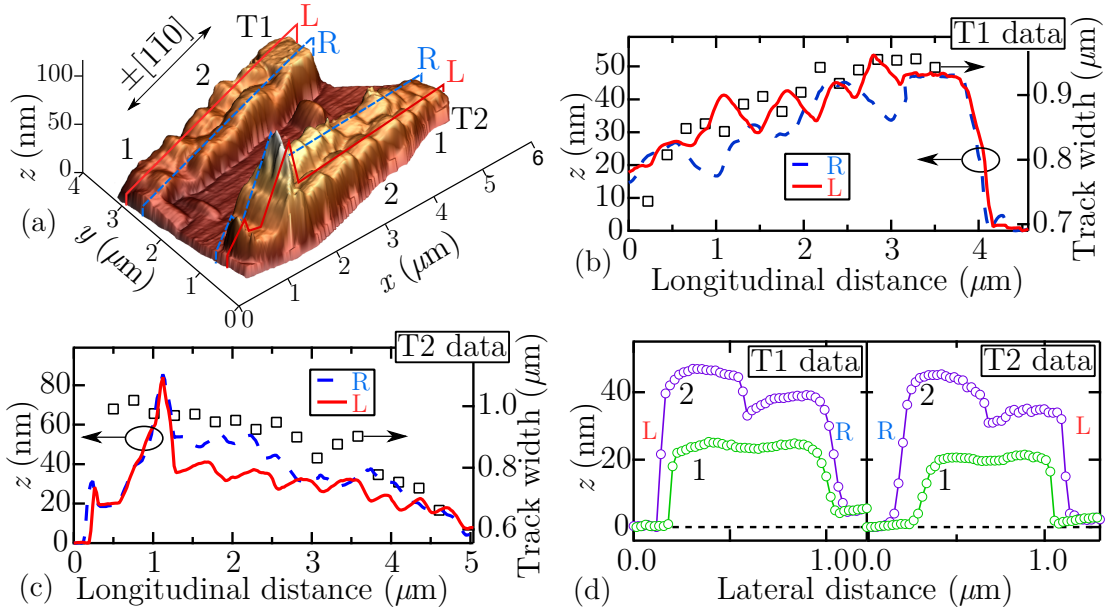

Figure 5.7: (a) AFM micrograph of two antiparallel nanotracks, labeled T1 and T2. The two axial lines along both nanotracks (one solid red and the other broken blue) indicate the paths of the line height scans presented in (b) and (c). The nanotrack width data in (b) and (c) were determined via multiple line height scans measured orthogonally to ±[1$\bar{1}$0], and (d) shows two of these scans obtained for both nanotracks at the locations indicated in (a).

The typical details of the nanotrack morphology are contained in the AFM data

shown in Fig. 5.7(a), displaying two antiparallel planar nanotracks (T1 and T2), side-by-side. At this aspect ratio the central line and height variations along the nanotracks become vivid. The terminating form of T2 is very different to the flat nanodisc of T1, although similar to that observed in the synthesis of in-plane nanowires[190,192] and asymmetric nanoholes[201], counting its preferential assembly of a "pit" along the ±[110] direction. Nanotracks terminating in this way − with high raised lips on the trailing side − were uncommon on the studied sample and only noted here for completeness.

An analysis of the AFM image (using the WSxM v5.0 software[202]) is presented in Fig. 5.7(b)-(d) for both nanotracks, with the paths taken for the line height scans indicated in Fig. 5.7(a). These data are typical of all nanotracks, with several pervasive morphological features.

The width of the nanotracks steadily increases perpendicular to the growth direction by roughly 20% over its whole length, data for which is presented in Fig. 5.7(b)-(c). This is paralleled by a gradual increase in height. Within the framework of VLS processes, one can expect that the size and position of the Bi droplet is related to the width and position of the nanotrack; the area of precipitated crystal is confined to the liquid-solid interface. The increase in our nanotrack width is analogous to tapered nanowires which are shaped by a changing catalyst size during growth[203]. Previous studies have reported an increase in droplet size during motion and this particular aspect of growth kinetics appears to define the resulting width − and in turn, height[204] − of our nanotracks.

A periodic variation in the nanotrack height appears the full length of growth, peaking both at the far left (L) and right (R) hand sides. The line height data in Fig. 5.7(b)-(c) best communicates this nanotrack characteristic, with T1 and T2 together exhibiting comparable periods and amplitudes. In fact, once the steady gain in height is accounted for, the rising and falling angles are found to be even and

approximately equal to 1.5°. Note that the undulation height and period exhibited on L side (in both T1 and T2) appears more regular and cyclic. In contrast, the R side exhibits more disorder in these features (see also, for example, the R side of the nanotrack in Fig. 5.6(a)). The sidewall gradients of the L and R sides also significantly differ, with a steeper lateral rise seen for the L side (see Fig. 5.7(d)). Regarding the relative lateral position of peaks and troughs, they appear approximately out-of-phase across the nanotrack centre. However, this particular morphological feature is made less distinct here due to the disorder of the R side. For reference, we point out that this growth aspect is evidently contained in the SEM data shown in Fig. 5.1(b).

The high aspect ratio in which Fig. 5.7(d) is presented ($z : x, y \approx 1 : 37$) reveals a pronounced centred dip in the cross section of the nanotrack, forming an "M-shape". The central depression in height is less defined at the beginning of the nanotrack growth (traces labelled 1), sharpening up with an increase in nanotrack height and width (traces labeled 2).

5.2.4 Simulations of nanotrack formation

We present now a simple geometric growth model to lend insight to our experimental observations. The numerics of the model were carried out using MATLAB R2015a software, with the implemented code presented in Appendix C.

Geometric models describing nanowire growth rates often monitor only the total rate of species arriving at the droplet surface and assume that growth at the liquid-solid interface proceeds uniformly. For a liquid droplet creating a homogeneous growth interface with the underlying crystal, it follows that lateral motion would only produce a simple and relatively featureless planar structure. To explain our interesting nanotrack morphology it is clear that a meaningful model must account for the localisation of adsorbed species and an *inhomogeneous growth interface*. The main parameters and

limiting processes of our model are summarised in Fig. 5.8 and are discussed in detail below.

We consider a rigid circular liquid-solid interface of radius R and, by studying key supply restrictions, form a dynamic functional describing the nucleation rate over its area, A. Central to the model are the two different modes of species supply: (i) direct impingement from a rotating non-normal beam-like vapour source (creating angle θ with the z-axis), which is shadowed by the 3D droplet surface and (ii) diffusion from various paths crossing the solid-state to reach the *moving* droplet. For simplicity, we only consider mode (i) to be dynamic since it must account for a constantly changing azimuthal angle, α. It follows that a steady-state solution may be estimated to account for diffusion, mode (ii), relative to the lateral droplet velocity, $v_{||x}$ (see Fig. 5.8).

Our model reduces the supply problem to a single type of limiting growth species, the arrival of which at the liquid droplet surface will help to define the nucleation rate at the liquid-solid interface. For the synthesis of III-V semiconductor nanowires (planar or vertical) this is not an oversimplification, given that group-III Ga species limit growth kinetics[205]. In this way, only a single set of θ and α values are required.

The vapour flux can impinge onto the substrate, the nanotrack sidewall and surface, as well as directly onto the liquid droplet surface. The coordinate-dependent concentrations of stationary adatoms on the crystal substrate (n_s) and the nanotrack sidewall (n_t) surfaces obey the diffusion equations

$$D_s \Delta n_s + \Phi \cos(\theta) = \frac{n_s}{\tau_s}, \tag{5.4}$$

and

$$D_t \frac{d^2 n_t}{dz^2} + \Phi \sin(\theta) = \frac{n_t}{\tau_t}. \tag{5.5}$$

Here Δ is the 2D in-plane Laplace operator, and D_s, D_t are the diffusion coefficients

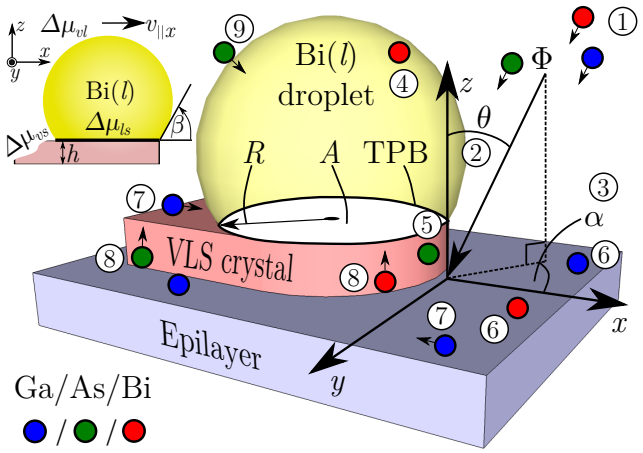

Figure 5.8: Schematic illustrations of geometric model with the parameters described in the text (the processes described in the image are not atomic species specific): (1) incident ion beam flux (Φ) and mass transport in the gas phase; (2) the direction of the incoming non-normal flux is angled θ away from the growth axis (z-axis); (3) the sample is constantly rotated during MBE, forming angle α with the nanotrack growth direction; vapour impinging on the (4) droplet, (5) nanotrack sidewall and (6) the epilayer surface; diffusion of atoms across the (7) epilayer surface and (8) nanotrack sidewall; (9) chemical reaction at the vapour-liquid interface and adsorption of vapour species. The inset shows the relative velocity ($v_{||x}$) of the droplet, the nanotrack height h, and the wetting angle β, which meets at the three phase boundary (TPB).

(with units of m^2/s) for adatoms on the substrate and sidewalls, respectively. The second terms in these equations define the arrival rate of adatoms from the impinging ion beam flux Φ (incident at angle θ to the surface normal), while τ_s and τ_t are the effective lifetimes of diffusing adatoms on the substrate and nanotrack sidewalls, respectively. The numerical values of τ_s and τ_t (with units of s) are principally governed by the rates of surface nucleation. We assume that the surface diffusion process (scheme 7 and 8 in Fig. 5.8; first terms in Eq. 5.4 and 5.5) possesses radial symmetry. Symmetry then dictates that the growth chronology will critically depend on the magnitudes of the adatom diffusion lengths on the epilayer surface

$$\lambda_s = \sqrt{D_s \tau_s}, \tag{5.6}$$

and on the nanotrack sidewall surface

$$\lambda_t = \sqrt{D_t \tau_t}. \tag{5.7}$$

Important to our model are simply the lifetimes and diffusion lengths of adatoms on the crystal surfaces, which are set relative to the droplet speed, v, using a scaling factor. There will be large difference between these two diffusion lengths; the solid-state reaction on the epilayer (MBE) will create a surface which is more atomically flat and less defective than the highly faceted nanotrack surface. After considering rates of impingement, we proceed to flatten the diffusion path of adatoms into two dimensions and simply consider a high diffusion barrier ($\lambda_t << \lambda_s$) imposed by the rough nanotrack crystal surface, of length h, in the x-y plane. This diffusion barrier also exists in the trailing droplet path.

For the impinging flux of the droplet surface, a simplified hemispherical geometry[206] (droplet wetting angle of $\beta = \pi/2$) is adopted where the droplet interception of flux is

$$I_{\mathrm{Bi}(l)} = \frac{1 + \cos(\theta)}{2} \pi R^2 \Phi. \tag{5.8}$$

We ignore the diffusion of species over the "rough"[75] liquid surface and assume the existence of a sufficiently high number of accommodation sites over its entire area. Using Eq. 5.8 and the projection of $I_{\mathrm{Bi}(l)}$ onto the x-y plane (via radial diffusion within the liquid droplet), we then arrive at a steady-state estimate for a fixed α.

Employing a general form[207] to define the dependence of the nucleus formation rate on the various system factors, we have

$$J = \omega Z C \exp(-\Delta G / k_{\mathrm{B}} T), \tag{5.9}$$

where ω is the frequency of attachment of growth species at the interface and is

dependent on the number of nucleation sites, and Z is a statistical dimensionless number known as the Zeldovich factor[208], which is dependent on the change in the Gibbs free energy of nucleation, ΔG. In addition $k_{\mathrm{B}}T$ is the thermal energy and C indicates the magnitude of the concentration of the relevant species in the liquid (not to be confused with n_s or n_t), and is related to the supersaturation and the equilibrium concentration (C_{eq}) by

$$C = C_{\mathrm{eq}}\exp(\Delta\mu_{\mathrm{ls}}/k_{\mathrm{B}}T). \tag{5.10}$$

When C_{eq} is zero, the supersaturation and nucleation rate at the liquid-solid interface are zero. Thus it follows that for a constant temperature, an increase in the concentration C produces a direct rise in the nucleation rate J through Eq. 5.9 (assuming an unchanging critical nucleus size).

We must now consider the important difference between nucleation at the centre of the solid-liquid interface and at the bordering three phase boundary (TPB)[209]. A minimisation of the nucleation barrier (Gibbs free energy) at TPB means it is the preferred nucleation site in a three phase system[196]. Sear[210] demonstrated that nucleation rate at a TPB can be orders of magnitude higher than growth at the other surfaces and interfaces. With adatoms essentially only diffusing across the solid crystal surface, supersaturation is also at its highest at the TPB because it is in direct contact with species supply. Growth near the TPB edge also facilitates non-faceted growth, further roughening the crystal surface. In this case, the supersaturation required for growth near the TPB may actually be further reduced. The VLS synthesis of relatively narrow nanowires (diameters in the order of tens of nm) is considered piecewise[211], as a nucleus at the TPB (or liquid-solid interface) spreads out in steps. These factors contribute to enhanced growth near a TPB edge, which is necessary to explaining our observations. Within the context of our model, this implies that the nucleation rate at the bordering TPB will not only be at its highest, but also locally enhanced

and dispersed towards the interface centre. Thus, we employ a ring-shaped one-sided Gaussian function to describe the elevated growth rate in this region. This function peaks at the TPB (distance R) with the parameters adjusted to obtain the proportions of the growth structures that correspond to the observed proportions.

In reliably estimating the relative nucleation rate across A, for a given α, we depend on empirical data of the nanotrack morphology. Firstly, the sample was continually rotated in the MBE growth chamber at a rate of 5 revolutions per minute. Without direct *in situ* observations[212], it is expected the periodic appearance of peaks and troughs will have formed at equivalent values of α during repeated rotations (i.e. $\alpha = j2\pi$, where $j = 1, 2, 3, \ldots$). Thus analysis of the AFM data suggests the droplets move and deposit VLS crystal with a lateral speed of between 2.5 to 3 μm/minute. This relatively high lateral growth rate is not unreasonable, given the relatively large area of A[204], nanotracks only reach typical heights of approximately 50 nm, and that droplet movement here is in no way comparable to the vertical growth of nanowires; a droplet atop a growing vertical nanowire is moved entirely by displacing itself through VLS growth. The impact of high droplet mobility on the collection of surface diffusing adatoms is large; $v_{||x}$ will induce, and scale with, a supply differential between the front and rear of the droplet. The number of diffusing atoms arriving at the front of the droplet is enhanced by its relative motion. On the other hand, diffusing species reaching the rear of the droplet must traverse h unaided and pass an additional distance across the atomically rough nanotrack top.

Our AFM experiments indicate the nanotracks experience an overall ∼20% steady increases in width during lateral growth. The size of R defines the nanotrack width, thus increases linearly with lateral distance (centred on $y = 0$; see Fig. 5.8) within our model. In fact, the measured lateral period − the distance recorded between consecutive undulation peaks or troughs − is found to be close to the nanotrack width,

and provides a relationship for these values in the model; the undulation period (defined by equivalent values of α) is set equal to twice the droplet radius.

Finally, the model considers a droplet that is large enough to initiate and sustain VLS growth − the effects of the initiation of droplet movement on the nanotrack growth are not considered in the model. Hence the liquid droplet is already moving unilaterally with a constant speed in the model and continually solidifies crystal at the liquid-solid interface. Accepting these kinetic features, we estimate a 2D (x-y plane) steady-state dynamic nucleation rate across A for growth in the z-direction, and for a given α. Figure 5.9 presents our normalised nucleation rate over A for four fixed azimuthal angles covering $0 \leq \alpha \leq \pi$. From these plots it becomes obvious that the dynamic surface A experiences a rotating nucleation "hot spot" and a persisting centre line of low nucleation, existing at the centre and extending out towards its rear. The latter is enhanced by the relatively strong nucleation rate near the TPB, as well as the scarcity of diffusing supply species arriving at the very back of the moving droplet.

In simulating the final nanotrack morphology we essentially take a discrete approach: scaled matrix values of surface A are cumulatively summed through iterations of a shifting centre and rotating α. A total of 2000 iterations are performed in this manner covering a distance just over $10R$. The result of this procedure is presented in Fig. 5.10(a), with line scan analyses of the simulated nanotrack − analogous to that performed in Fig. 5.7 − displayed in Fig. 5.10(b)-(c). There is a good agreement between the simulation and experiment, with the typical nanotrack characteristics clearly present. The periodic and out-of-phase height variations along the nanotrack appear equally spaced across both L and R sides, with a height that steadily rises throughout growth.

Through our narrow definition of the droplet kinetics (including an increasing R) and of a lateral period (with its connection to the frequency of α), it is not unexpected

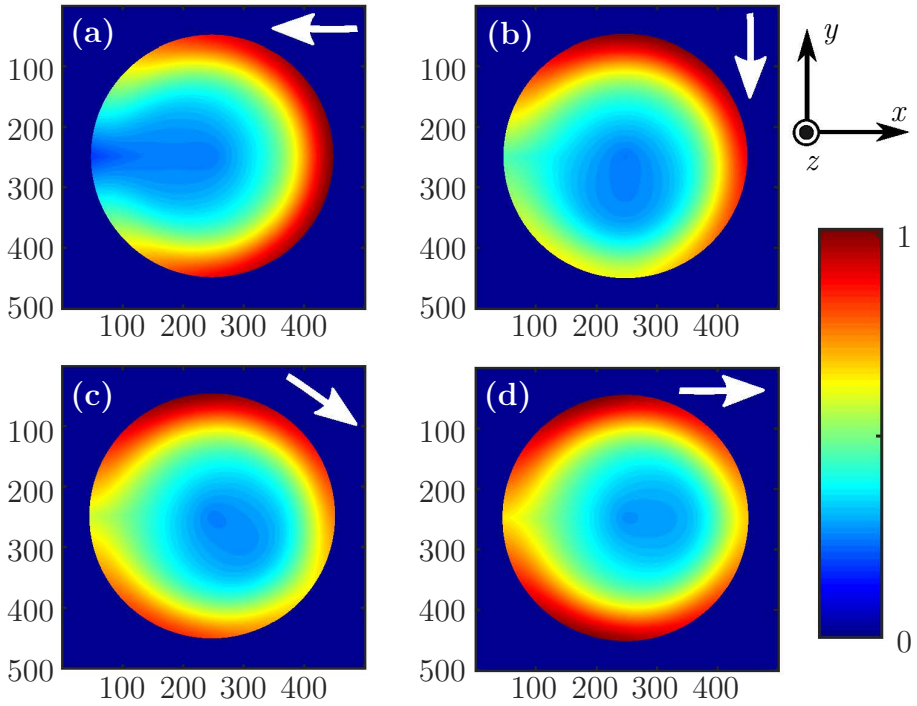

Figure 5.9: Normalised nucleation (in the z-direction) rate determined by the model at the liquid-solid interface A for α values of (a) 0°, (b) 90°, (c) 145° and (d) 180°. The depicted coordinate system relates to the axes shown in Fig. 5.8. The arrows here indicate the relative flux directions for each angle, while both the horizontal (x) and vertical (y) spatial axes are given in units of pixels.

that we arrive at a result which strongly resembles experiment. What is interesting are the correct morphological subtleties existing in these data. Namely, the presence of height dip at the centre of the nanotrack, forming an M-shape through its cross section. In Fig. 5.10(c), this feature strongly resembles the AFM data in Fig. 5.7(d), and likewise becomes more prominent with increasing nanotrack height.

Similar too is the asymmetry of the simulated nanotrack cross section, with very different relative gradients for the left and right sidewalls. For convenience, we allow the steeper wall here to correspond also to the L side, and it follows that the R side inherits a flatter top and more rounded edge. An asymmetrical cross section essentially arises because the sweep direction of the rotating beam-like flux, α, is not equivalent for opposite sides, relative to lateral motion. For a VLS-driven droplet moving with

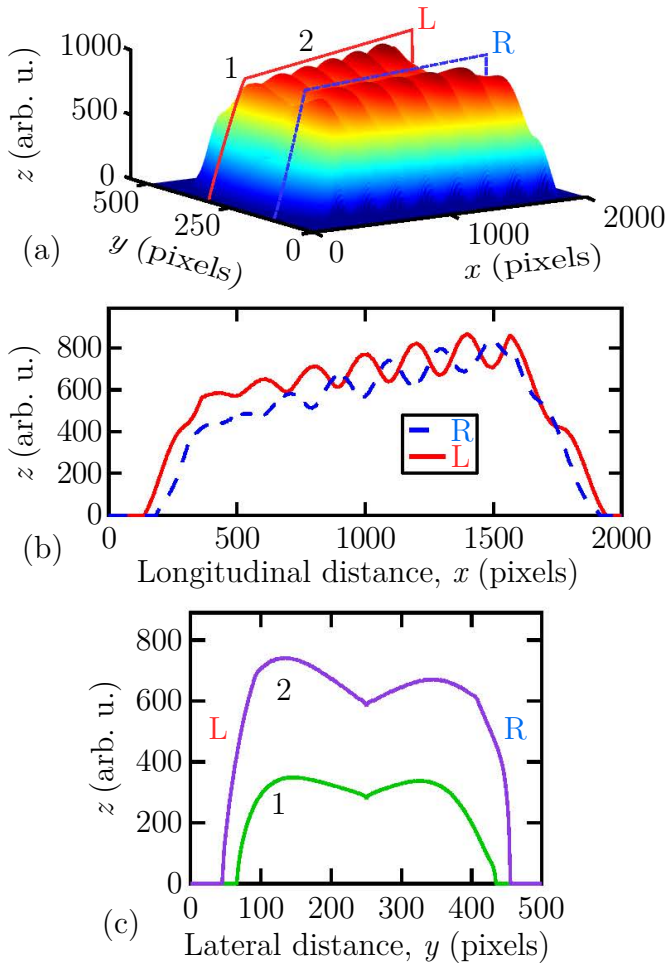

Figure 5.10: (a) Surface plot of simulated nanotrack morphology employing the model described in text. The two axial lines along the simulated nanotrack (one solid red and the other broken blue) indicate the paths of the line height scan data presented in (b). (c) Two cross sectional height scans obtained from the locations indicated in (a). The horizontal axes here are given in pixels.

sufficient unidirectional speed, such growth asymmetry becomes inevitable in the presence of a rotating vapour source.

With the steepness of the R edge reduced, it is expected that the VLS growth dynamics of the R side will be significantly altered (compared to the L side) through elevated sidewall wetting and droplet destabilisation. This may account for the heightened disorder observed experimentally for the R side of the nanotrack top (see Fig. 5.7(b) and (c)).

Within the framework of our model, the origins of particular morphological features become evident. The central nanotrack height minimum − creating an M-shape in the cross sectional data − manifests as a consequence of fewer diffusing supply species arriving at the centre rear of the moving droplet. As h increases, the frequency of adatoms successfully arriving at the droplet rear from the epitaxial surface is greatly reduced, and the shape becomes more pronounced. Likewise, the presence of strong shadowing effects for the 3D droplet and a rotating beam-like vapour source induces a periodic and out-of-phase height variation along opposite sides of the planar growth. These two aspects of growth are independent from each other; without periodic shadowing effects, supply diffusion would only define the M-shape cross section. This offers independently tunable degrees of freedom in the design of planar nanotracks possessing these features.

5.3 Micro-optical characterisation of GaAsBi surface features

As outlined in the motivation section of this chapter, it is important to determine local deviations in the epitaxial properties produced in the presence of VLS-driven Bi surface droplets. A typical problem in modern solid-state physics is finding powerful and accessible tools in the study of semiconducting structures at the micron and nanometer scale. To investigate crystallographic orientation, x-ray and electron diffraction techniques are frequently relied upon. However, in a top-down investigative approach these methods do not possess the interaction volumes required to reliably probe localised structure. In this section, we examine the microstructure and important optical properties of the various nanostructures present on the sample surface by employing room-temperature micro-Raman and micro-PL experiments.

Optical penetration of micro-Raman and micro-PL signals

It is important that we assess the optical penetration depth, d_{opt}, of the Raman and PL measurements. This is because if the optical penetration depth exceeds the thickness of the structures studied, a non-trivial subsurface signal may contribute to the recorded Raman or PL spectrum. Although Raman and PL measurements both employ 632.8 nm HeNe laser light for excitation, the two techniques have very different interaction volumes. The depth analysis is determined by considering the absorption coefficients for both the incoming (α_{in}) and the outgoing (α_{out}) light:

$$d_{\text{opt}} = 1/(\alpha_{\text{in}} + \alpha_{\text{out}}). \tag{5.11}$$

Firstly, Raman backscattered photons (with only a slight energy shift) from a material with absorption coefficient $\alpha \neq 0$ will only provide information from half of the light penetration; $d_{\text{opt}} = 1/2\alpha$ ($\alpha = \alpha_{\text{in}} \approx \alpha_{\text{out}}$). For pure GaAs, d_{opt} will be slightly larger than 100 nm, with the majority of the exponentially decaying signal arising from the topmost 50 nm. For the compositionally perturbed $GaAs_{1-x}Bi_x$ system with $x \sim 0.04$, this depth will be further reduced through an increase in α[142,143].

On the other hand, d_{opt} for the PL measurements will be much larger. PL signals can be detected from deep below the surface, even through a relatively thick $GaAs_{1-x}Bi_x$ epilayer (> 300 nm); observing the substrate GaAs PL peak from $GaAs_{1-x}Bi_x$/GaAs structures is a common feature for PL studies of these films[4,154]. There are two main reasons for this: (i) photons emitted from the material as luminescence will possess longer wavelengths (lower energy) than the excitation wavelength, and will be able to escape from a larger depth ($\alpha_{\text{out}} << \alpha_{\text{in}}$), and (ii) the excited charge carriers may diffuse deeper into the material and recombine (emitting PL) a further distance away from where they were excited. However, again, the majority of the luminescence emitted will arise from just a few tens of nm from the semiconductor surface and small

topological changes are expected to be sensitively resolved.

While an exact value of d_{opt} for the micro-Raman and micro-PL measurements is not defined here, we note the impact that d_{opt} has on the types of conclusions that may be drawn from these measurements. A quantitative spectral analysis of first order Raman spectra − like that presented in Chapter 4 − is not presented in what follows. However, polarised Raman analysis is employed to observe experiential trends (Raman selection rules). It is believed that the magnitude of d_{opt} here will not significantly stifle the ability to draw conclusions about local phase and relative orientation, from polarised micro-Raman analysis. In contrast, we point out that without moving to shorter excitation wavelengths, this particular experimental constraint indeed renders the micro-PL characterisation in this section strictly *qualitative*.

5.3.1 Micro-Raman survey of sample surface

Figure 5.11 presents corresponding micrographs of a particularly disordered location (exhibiting the full variety of surface features found) on the surface of the sample, using optical and scanning electron techniques. The optical image in Fig. 5.11(a) was recorded through topologically-sensitive differential interference contrast (DIC) microscopy, and again reveals a flat epitaxial surface interrupted by metallic surface droplets, and the formation of nanotracks. Of the surface features, six typical locations are identified in the SE-SEM image in Fig. 5.11(c) which receive detailed treatment in this section. The crystal coordinate system specified by the inset Figure 5.11(c) is inferred from the analysis of the Raman data shown in Fig. 5.3.

The segregation of elemental bismuth on the epitaxial surface is readily identified in the EDS micrograph shown in Fig. 5.11(b), however determining the surface quality and form (i.e. microstructure/orientation, metallic purity, crystallinity, or chemical oxidation) requires a phase-specific technique, such as Raman scattering spectroscopy

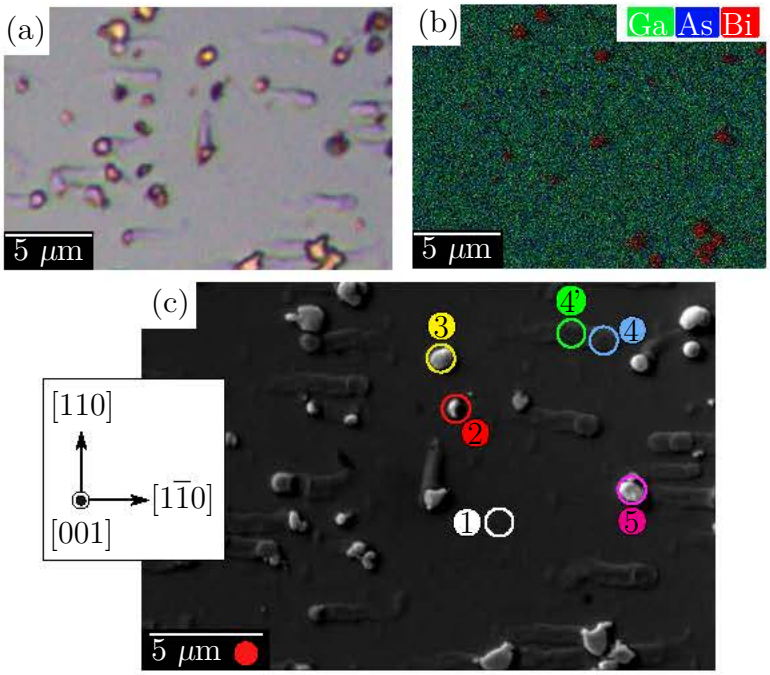

Figure 5.11: Corresponding (a) differential optical (false colour) micrograph (b) EDS micrograph recorded using 3.5 kV accelerating potential and (c) SEM image of the droplet covered GaAsBi surface. In (c), local areas of interest are identified and the inset shows the relative crystal orientation, as determined by combining polarised Raman scattering measurements (Fig. 5.3) and surface energy theory (see section 5.2.1). The solid red circle in (c) indicates the relative spot size of the micro-probe for both micro-Raman and micro-PL measurements. Surface features outside of the presented frames were used to navigate the electron and optical microscopy instruments into place before acquiring the corresponding images.

or XRD. Figure 5.12 presents depolarised micro-Raman spectra recorded from the locations indicated in 5.11(c), along with the vibrational signatures associated with Bi, β-Bi_2O_3, GaBi-like and GaAs-like optical modes. By way of alignment with these signatures, we are able to characterise these surface features using a Raman microprobe.

The spectral features and two-mode behaviour exhibited from ① (smooth droplet-free region) is characteristic of $GaAs_{1-x}Bi_x$ for $x \sim 0.04$; refer to Chapter 4 for a detailed discussion on the GaAsBi first-order Raman spectrum. Due to the Bi-induced structural disorder and matrix deformation, and a subsequent relaxation of the Raman selection rules, we see the weak appearance of the symmetry-forbidden GaAs-like TO

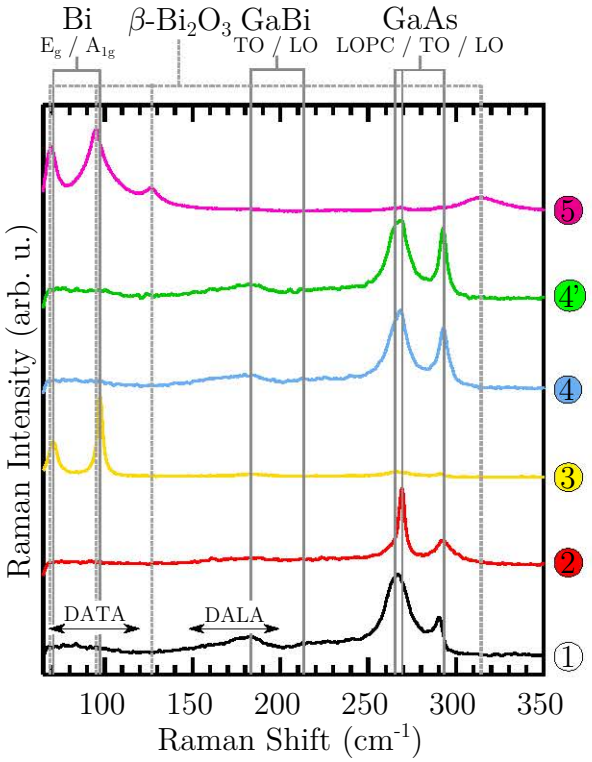

Figure 5.12: Room-temperature micro-Raman spectra recorded from locations of the interest depicted in Fig. 5.11(c). Spectra have been normalised and offset for clarity, with the vertical lines corresponding to the frequencies of Bi, β-Bi_2O_3, GaBi-like and GaAs-like optical modes.

mode as well as the broadband lifting of disorder-activated transverse (DATA) and longitudinal acoustic (DALA) signatures.

The spectrum recorded from the nano-pillar like structure at ❷ has a strong TO mode contribution, which is surprisingly large compared to the LO mode for backscattering from a nominally [001]-oriented growth surface[80]. Such a shift in spectral weighting is indicative of out-of-plane growth which is significantly misorientated away from the original [001] *c*-axis of the substrate. The strength of the GaBi-like vibrations in the ❷ spectrum is considerably less than that observed in ①, reflecting a localised reduction in the Bi concentration and the number of Ga-Bi oscillators. Further, the hole-induced LOPC mode is significantly reduced. The unusual character of ❷, as well as its crystallographic orientation, is examined in detail later using polarised Raman

scattering.

The micro-Raman spectrum recorded from the droplet at ③ exhibits two prominent modes at 73 cm^{-1} and 98 cm^{-1}, which is consistent with the two first-order optical bands of rhombohedral Bi (A7 structure) corresponding to the E_g and A_{1g} phonon modes, respectively[213]. The frequency, linewidths, and second-order harmonics measured indicate a crystalline Bi structure.

The spectra obtained from the microdisc and nanotrack at ④ and ④', respectively, are very similar, exhibiting a two-mode behaviour comparable to that recorded from ①. This confirms successful Bi incorporation within these features. Essentially there are only minor differences between spectra ④ and ④', and ①, which exist mainly in the GaAs-like optical bands; the TO and LO phonons intensify and blueshift, with the strengthening of the TO mode in ④ greater than ④'. While a quantitative interpretation for the symmetry-forbidden TO mode cannot be performed, its relative magnitude is an indicator of local electric field perturbations, leading to its appearance. Comparing to ①, both locations yield weaker GaBi-like vibrational bands. As previously mentioned, their integrated strength here is proportional to the number of Ga-Bi oscillators and infers a slight localised reduction in the Bi concentration (in the nanotrack), in agreement with the EDS results. Due to the similar character of ④ and ④', onward we will focus on location ④ and consider it representative of the whole VLS nanotrack.

The final topological feature to be characterised is ⑤, which exhibits vibrational signatures associated with a room-temperature metastable form of bismuth oxide (Bi_2O_3) in the β-phase[214]. Due to the very low (with respect to other group V semimetals) melting point of bismuth metal (272°C), it has a high tendency to oxidise. Thus, the appearance of bismuth oxide on the droplet-covered surface is not surprising and is not considered any further here. Its interesting tenure of the β-phase[67] – a

typically metastable high-temperature phase – is the focus of Chapter 6.

5.3.2 Polarised micro-Raman characterisation

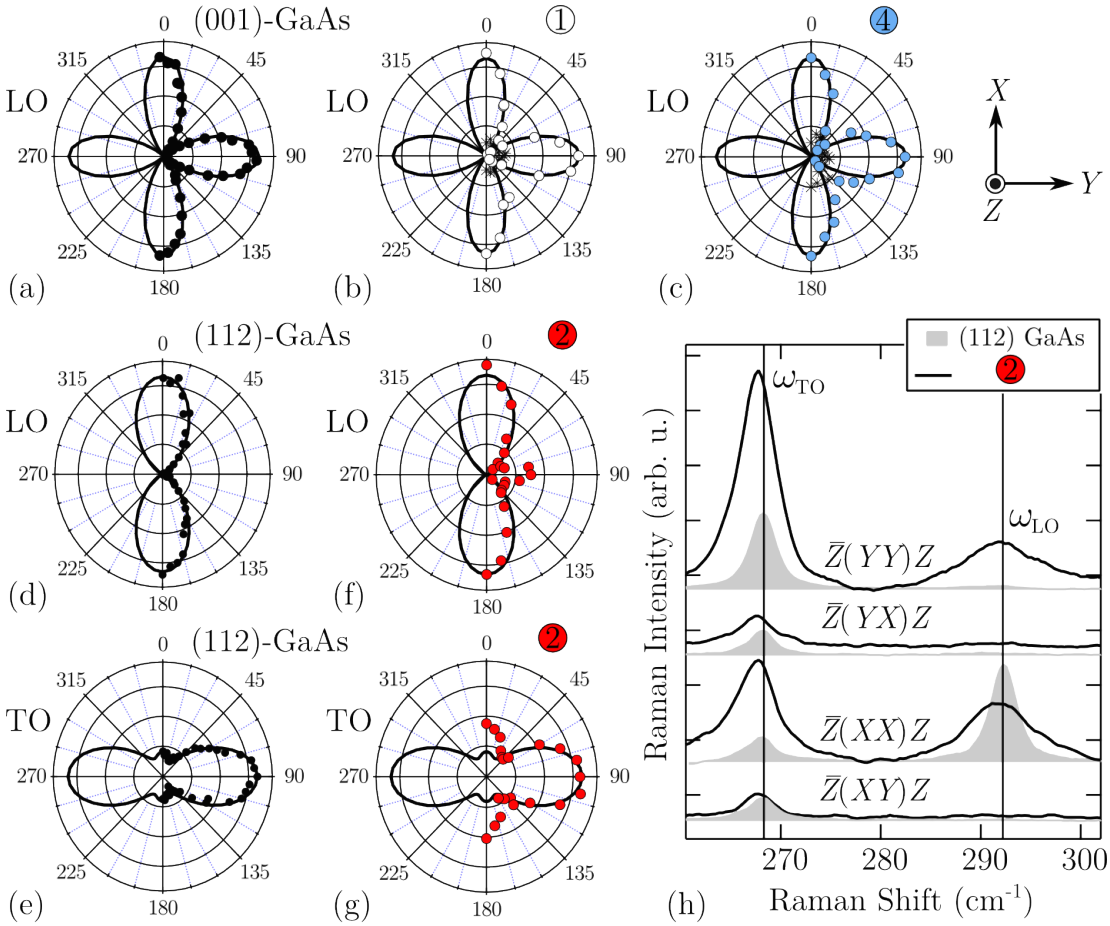

Figure 5.13: Normalised Raman backscattering polar plots of GaAs and GaAs-like optic modes measured in $\hat{e}_i \parallel \hat{e}_s(\alpha)$ configuration: (a) (001)-GaAs single crystal; (b) ①; (c) ④; (d) and (e) (112)-GaAs; (f) and (g) ②. For the case of plots (a)–(c), the TO mode is forbidden in a backscattering geometry, though the observed intensity relative to the LO mode is represented by the asterisk symbols (close to the origin). The bases of all the polar plots are represented by the coordinate system provided in the top right inset and correspond in the laboratory coordinates. (h) Comparison of the selection rules measured from ② and a (112)-oriented GaAs. The vertical lines in (h) indicate the TO and LO frequencies of pure GaAs.

Figure 5.13 displays polarised first-order Raman scattering data recorded from ①, ②, ④ and, for comparison, (001)- and (112)-oriented GaAs single crystals. The

polar data contained in Fig. 5.13(a)-(g) were measured employing a parallel polarised configuration ($\hat{e}_i \parallel \hat{e}_s(\alpha)$) rotated through $0° \leq \alpha \leq 180°$. Here our standard (112)-oriented basis ($X = \frac{1}{\sqrt{2}}[1\bar{1}0]$, $Y = \frac{1}{\sqrt{3}}[11\bar{1}]$, and $Z = \frac{1}{\sqrt{6}}[112]$) is adopted to aid interpretation of the data recorded from ②, along with a comparison to (112) GaAs in Fig. 5.13(h), for the four principal polasised geometries. The Raman selection rules observed for the (112) GaAs single crystal align well with that expected for these polarised configurations and permit a direct reference. To help in assessing the polar data, the calculated intensities − using the tensors provided in Appendix A and Eq. 3.13 − for each mode are presented (solid line).

For the case of ①, the results for the GaAs-like polar LO phonon intensity is essentially the same as that recorded from the (001)-GaAs crystal, with a periodic LO phonon intensity which cycles every 90° and virtually no TO band. The presence of a weak TO peak that is invariant to changes in α is in agreement with its disorder-activated origins. Similar polar data recorded from ④ indicate the planar nanotrack crystal aligns with the epitaxial film (and substrate), with no significant misalignment or rotation around the Z axis. This is not surprising, given the coherent nature in which VLS crystal is deposited on the epitaxial surface. The strength of the disorder-activated TO band in ④ is verified to be stronger and approximately double that of ①. This simply indicates an elevated level of structural disorder present in the nanotrack, compared to the epitaxial surface.

As revealed in Fig. 5.12, an initial inspection of the Raman spectrum recoded from ② suggests the growth of a non-(001) in-plane surface. Further, the large weighting of the GaAs-like TO band, relative to the LO band, indicates significant misalignment away from an original [001] growth direction; such as one of the [hhk] directions described in Chapter 3. Examining the polarised Raman data measured from ② in Fig. 5.13 allows a simple reduction of these possibilities. First, for light Raman scattered

from a (110) surface, the LO is symmetry forbidden and should be relatively weak, while for the case of a (111) surface, the intensity of TO and LO should be invariant to changes in α, ruling these planes out. However, the polar data does resemble that of a [112]-oriented structure, or perhaps even a higher index plane. As expected for a strained and disordered system, the phonon energies measured here for the GaAs-like optical modes are redshifted to lower energies. The reduction in the TO phonon frequency ($\Delta\omega_{\mathrm{TO}}$) is considerably larger than the LO frequency ($\Delta\omega_{\mathrm{TO}}$), measured to be $\Delta\omega_{\mathrm{TO}} = -0.8\,\mathrm{cm}^{-1}$ and $\Delta\omega_{\mathrm{LO}} = -0.3\,\mathrm{cm}^{-1}$, respectively. This is contrast to the strain-induced shifts seen from light Raman scattered from a (001) surface, for which a greater shift in the LO band is typically seen. Inspecting Fig. 4.6, which presents the strain-induced optic mode redshift coefficient values for backscattering from the various $[hhk]$ surfaces, we find that a markedly larger shift in the TO phonon is only seen for plane indices lower than (113). This strongly suggests ❷ to be oriented between [113] and [111].

To further identify the orientation of ❷, we examine its notable deviations from the typical selection rules of (112) GaAs, displayed in Fig. 5.13(h). Again, a likely explanation lies again in the strain state of ❷. In Fig. 5.13(h) the selection rules are comparable for the $\bar{Z}(YX)Z$, $\bar{Z}(XX)Z$ and $\bar{Z}(XY)Z$ polarised geometries; LO is symmetry-forbidden in the crossed polarisations, confirming the relative orientation of the polarisers versus the crystallographic axis. However, for the $\bar{Z}(YY)Z$ geometry, an activation of the LO phonon is observed. Calculations made by Mailhiot and Smith[215] for the three components of the strain-induced electric field in our adopted (112) basis show that the polarisation along the Z direction is strong, while the in-plane polarisation only contains a large Y component[136]. This strain property, along with some likely deviation away from a true [112] direction, may account for this experimental observation.

In line with the coherent nature of VLS growth, note the general retention in ❷ for a common $X = [1\bar{1}0]$, relative to the epitaxial growth. This suggests a crystallographic reorientation − likely due to multifaceting − in the Y-Z plane displayed (see Fig. 3.1). While a more exact evaluation of the crystal orientation of ❷ (with respect to the (001)-oriented substrate/epilayer) is at present lacking, we simply emphasise the interesting nature of this non-(001) growth, catalysed in the presence of Bi surface droplets. Within the context of growing device-quality GaAsBi materials, such a finding is highly undesirable. Next we examine the important light-emitting properties of these surface features.

5.3.3 Micro-photoluminescence characterisation

EDS and micro-Raman characterisation of the nanotracks have already revealed the presence of localised inhomogeneities in the structure and composition of the Bi-catalysed surface features. In particular, nanotracks possess a lower Bi concentration. One would expect, then, for the nanotracks to exhibit a smaller Bi-induced bandstructure modification, i.e. the desirable bandgap reduction is smaller. Further, Eq. 2.12 from Chapter 2 provides a means of quantifying this change in composition through PL analysis. In terms of the scientific and technological drivers for $GaAs_{1-x}Bi_x$ alloys, their bandgap energy and light emitting properties are by far some of most important. This we investigate in the present section.

For investigating the light emitting properties of semiconductor surfaces, micro-PL is an extremely powerful and commonly-employed tool. As well as providing the spatial resolution required to study the features atop our GaAsBi sample, the microscope optics can achieve extremely high excitation power densities (I_{pump}), offering more insightful and dynamical forms of the PL measurement − pump-dependence studies.

Figure 5.14(a) presents the measured PL peak energy and FWHM of low-I_{pump} spec-

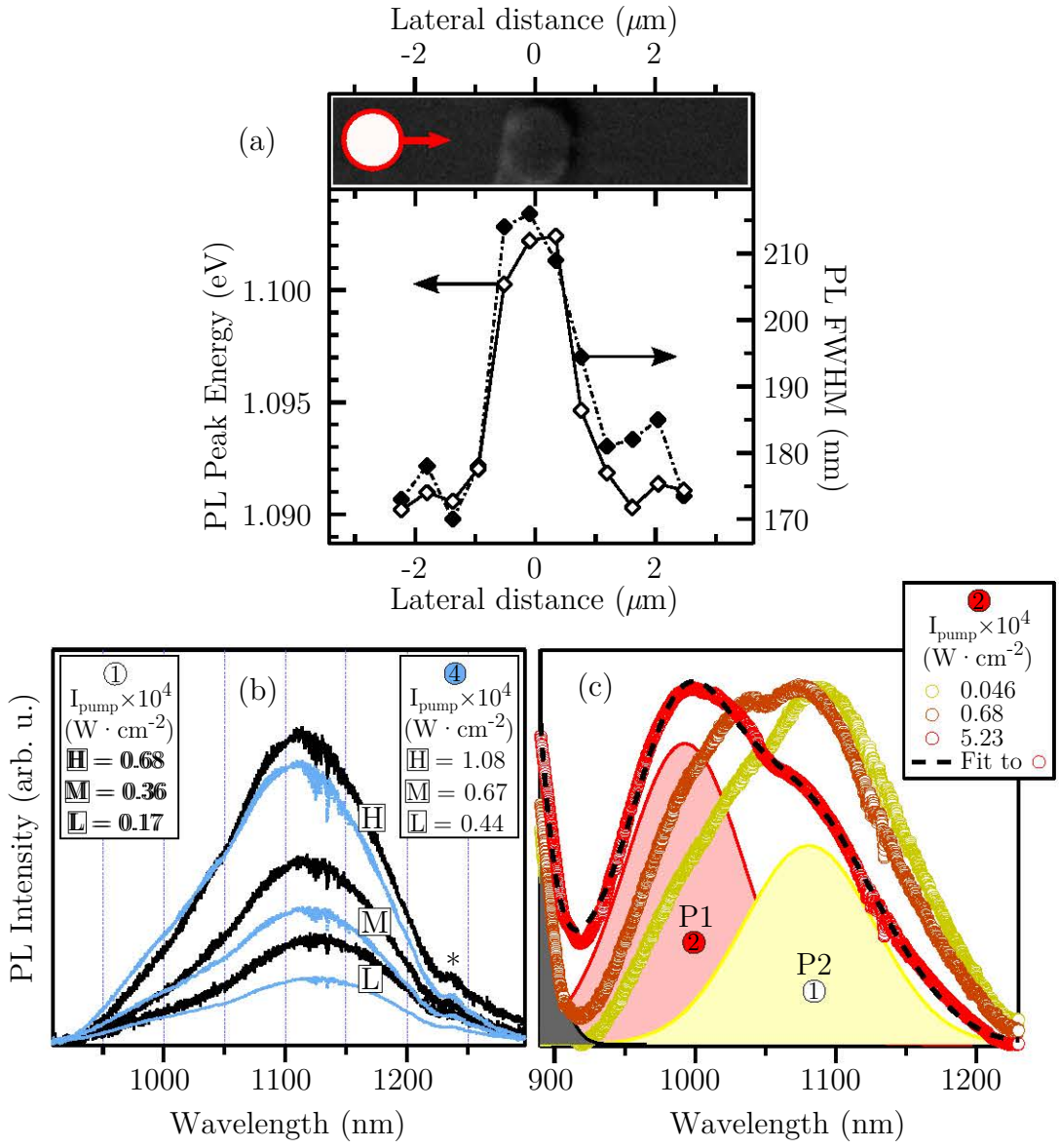

Figure 5.14: (a) PL peak energy and full width half maximum (FWHM) of micro-PL spectra recorded using a relatively low power density ($I_{\text{pump}} = 5 \times 10^2\,\text{W} \bullet \text{cm}^{-2}$) along a line scan across ④. The top micrograph is a scaled SEM image of ④ showing the path taken by the scan and the relative size of the micro-probe. (b) Micro-PL spectra recorded from ① and ④ for three differing laser power densities (I_{pump} = low [L], medium [M] and high [H]), exhibiting the typical spectral changes; signal intensification and a blueshift in peak energy. Here '*' indicates a spectral artifact. (c) Three normalised PL spectra recorded from ② covering two orders of magnitude of I_{pump}, showing the detection of two Gaussian peaks, P1 and P2, originating from feature ② and from the surrounding epilayer, labelled ①.

tra obtained from a line scan across ④. The distinct shift here in the PL peak energy, E_{PL}, and the FWHM measured from ④ clearly demonstrates a local discontinuity in the properties of the VLS growth. The blueshift in energy can be understood as a local decrease in Bi concentration within the nanotrack, while the rise in FWHM has two possible origins: (i) a density of states tail manifested by relatively high structural/mechanical disorder, and (ii) the superposition of an unresolved emission from the GaAsBi epitaxial growth below the nanodisc, contributing to a peak of slightly lower energy. While an increase in E_{PL} is consistent with a reduced Bi mole fraction, in dilute thin films of $\mathrm{GaAs}_{1-x}\mathrm{Bi}_x$ it is has been shown that the PL intensity initially increases with increasing Bi content (up to $x \sim 4\%$)[4]. Consistent with this notion is the measured absolute PL intensity of the GaAsBi emission across ④, which experiences a marked dip within the microdisc region (data not shown).

Figure 5.14(b) displays micro-PL spectra recorded from locations ① and ④ for three increasing values of I_{pump}. A steady increase in the overall PL signal is seen for a rising I_{pump}, due to the pump light producing more electron-hole pairs for radiative recombination. Interestingly, we also see the PL peak energy shift to shorter wavelengths for increasing irradiance. Lu *et al.*[4], as well as other investigators[216,217], have already reported this type of excitation-dependence for PL signals measured from $\mathrm{GaAs}_{1-x}\mathrm{Bi}_x$. These types of dependencies are signatures often seen in high-mismatched alloys involving localised states and, once more, parallels may be drawn here to the PL dynamics of the GaAsN system[218,219]. The mismatch between Bi (and N) with As induces an unusual optical response by introducing an impurity-like localised character in the host GaAs band structure, as a consequence of its hybridisation with the Bi-induced (N-induced) wavefunction.

Figure 5.14(c) focuses on the more complex PL spectra recorded from ②. In the normalised PL data two separate Gaussian peaks of differing energies are resolved

and, for higher excitation intensities, the spectra display a similar blueshift in the peak energy. A preliminary analysis of the pump-dependence indicates a dominant high-energy emission arising from ② (P1), with a second PL peak (P2) exhibiting a character (peak energy and FWHM values) similar to that measured from ①, and is attributed to PL emitted by the underlying epitaxial layer.

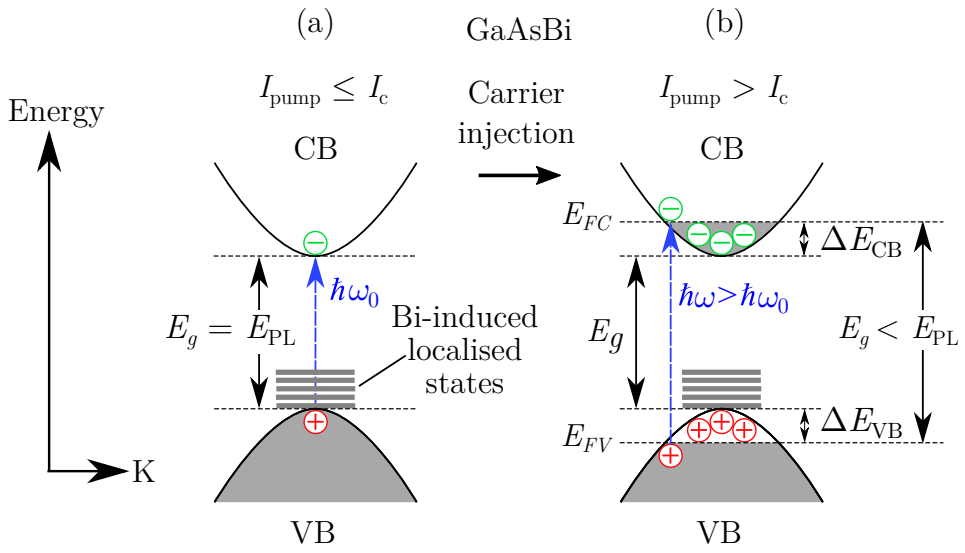

Figure 5.15: Schematic illustration of band filling effect in electronic band diagram of GaAsBi. (a) The measured E_{PL} equal to the intrinsic direct bandgap of GaAsBi for I_{pump} below a critical excitation intensity, I_c. (b) For I_{pump} above I_c, the "apparent" optical bandgap is widened due to a large carrier injection and recombination occurs between the Fermi levels in the CB (E_{FC}) and VB (E_{FV}); between states which no longer lie at their respective band edges.

In Fig. 5.14(b) and (c), the shift in the PL peak energy (E_{PL}) under high illumination is due to the band filling effect; this effect leads to a blueshift in the observed luminescence for increasing photo-induced carriers. Figure 5.15 shows a schematic illustration of this phenomenon and considers both possible photo-induced perturbations of the quasi-Fermi energy levels for the CB (ΔE_{CB}) and VB (ΔE_{VB}). For the case of GaAsBi alloys, this effect is known to be exaggerated [4] by the high level of Bi-induced localised states near the VB maximum [33], causing a degenerate charge distribution in this region. Consequently, due to the Pauli exclusion principle, radiative recombination

between occupied states in CB and VB are forbidden and the possible transitions are pushed to higher energies. Considering the VB edge in GaAs experiences most of the change from Bi incorporation, it is reasonable to assume that ΔE_{VB} is the dominant contributor to the pump dependent shift in E_{PL}. For comparison, in an attempt to optically induce a Burstein-Moss shift (band filling with only states close to the CB minimum being populated) in pure GaAs, high I_{pump} measurements show very little shift in E_{PL} over the pump intensity range studied here. This data is shown in the inset of Fig.5.16. In fact, one sees a redshift, rather than a blueshift, for an extremely high I_{pump}. This is likely due the local temperature increase within the high intensity micro-probe, which would slightly reduce the bandgap energy.

To study in detail the interesting excitation dependence of locations ①, ❷ and ❹, micro-PL spectra were measured with I_{pump} values over approximately three orders of magnitude: 1.5×10^2 to 1.4×10^5 $\mathrm{W \bullet cm^{-2}}$. Figure 5.16 presents the excitation intensity dependence of the PL peak energy measured from these locations. For low I_{pump}, the shape and energy of the emission from all three locations remains stable over an order of magnitude. The peak energy measured under low irradiance accurately portrays the intrinsic bandgap energy of the probed material. Consistent with the data contained in Fig. 5.14(a), we see a slight blueshift in E_{PL} recorded at low I_{pump} from ❹, compared to ①, as well as a large blueshift in ❷. Both of the shifts in PL peak energies measured from ❷ and ❹ are presumed to originate from a relative reduction in the local Bi molar fraction contained in these locations.

On the other hand, above a critical excitation intensity threshold in Fig. 5.16 (indicated by I_{c}), we observe a monotonic increase in the PL peak energy when I_{pump} is plotted on a log scale. With rising I_{pump} more photo-excited charge carriers are created and the energy for recombination is broadened, increasing E_{PL}. Over the excitation range studied in Fig. 5.16 a relatively large total shift of $\sim 50\,\mathrm{meV}$ is experienced.

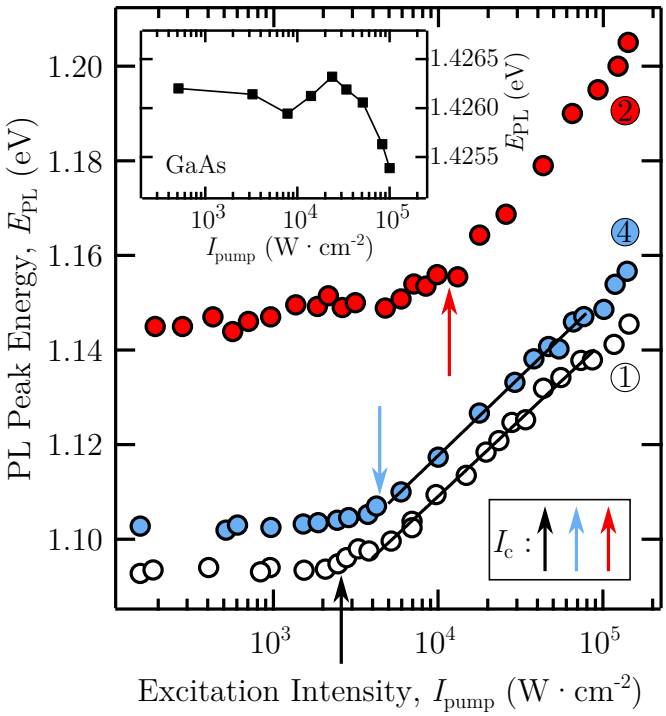

Figure 5.16: Measured micro-PL peak energy dependence on excitation intensity, I_{pump}. The arrows indicate the differing critical intensities (I_c) measured from ①, ② and ④, where a strong monotonic blueshift is seen in the PL peak energies due to band filling. The inset shows similar measurements made on pure GaAs.

In quantifying the rate of blueshift observed in the PL peak energy, Lu *et al.*[4] showed that the thermalisation depth ε experiences the following pump-dependence:

$$\varepsilon(\text{ev}) = -\frac{k_B T}{2} \ln(I_{\text{pump}}) + C. \tag{5.12}$$

Here T is temperature, k_B is the Boltzmann constant and C is a constant. Fitting the comparable gradients of traces ① and ④ in Fig. 5.16 with this equation yields temperature determinations of 328 K and 335 K, respectively. This appears to reasonably reflect the physical system studied and is consistent with measurements performed at room temperature.

Interestingly, the values of I_c in Fig. 5.16 differ between the different locations. Factors influencing the exact value of I_c are vague, though Lu *et al.*[4] did suggest an

inverse relationship with the bismuth content, and thus density of Bi-related localised states. Here we see a similar compositional trend (Bi content inferred from PL peak energy measured at low I_{pump}) across three different locations on one GaAsBi surface; the value of I_{c} is lowered for materials exhibiting PL peak energies with larger Bi-induced reductions.

Investigating the dependence of the integrated PL signal (I_{PL}) on the excitation intensity can yield insights into the dominant recombination mechanism present within the optical microprobe[220,221]. The presence of dominant nonradiative recombination is closely linked to the density of defects that provide mediating recombination avenues. Typically the measured PL intensity is proportional to the injected carrier density through a power law[220]. For a fixed microprobe volume, therefore, the integrated PL intensity I_{PL} will scale with the excitation intensity by[220,221]

$$I_{\text{PL}} = A I_{\text{pump}}^{m}, \tag{5.13}$$

where A is a scaling factor and, through theoretical considerations, exponent m will acquire a value typically between 1 and 2, depending on the proportions of radiative and nonradiative recombination. For $m = 1$, excitonic radiative recombination dominates. However for $m = 2$, Shockley-Read-Hall recombination occurs[220] relating to the presence of nonradiative deep-level traps, induced through defect states, which provide a shunt path for the carriers.

Figure 5.17 displays a log-log plot of the excitation dependence of the I_{PL} measured from ①, ②, and ④. The straight line fits are made using the equation in the inset and yield the values of m displayed. Three different exponent values m are acquired from the locations studied on our GaAsBi surface. For the case of the epitaxial film, a value of $m(①) = 1.20 \pm 0.04$ is measured and suggests radiative recombination to dominate. Agreeing with the micro-Raman characterisation of the nanotrack/nanodisc,

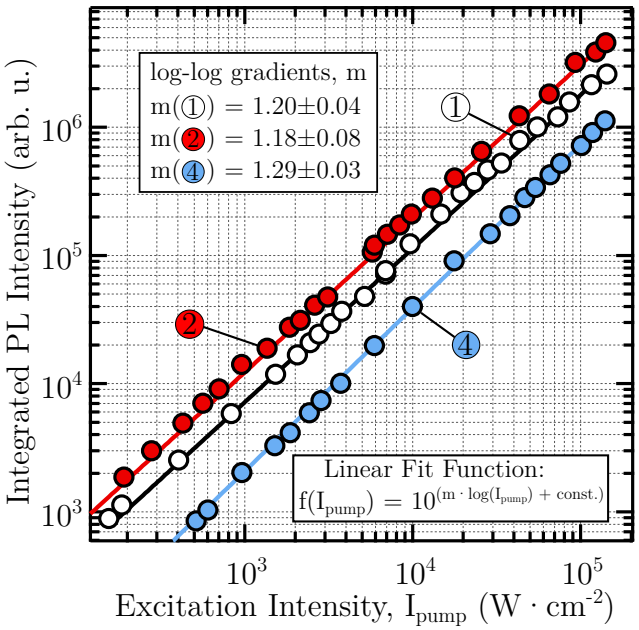

Figure 5.17: PL intensity, E_{PL}, recorded from ①, ② and ④, as a function of the pump intensity, I_{pump}.

the relatively higher value of m(④)$= 1.29 \pm 0.03$ indicates an increase in the defect density within the probed region, leading to a greater proportion of carrier recombining through Shockley-Read-Hall processes. Conversely, the exponent value m(②)$= 1.18 \pm 0.07$ is comparable to m(①), if only marginally less. This suggests less defects may be serving as nonradiative recombination centres within ②. From the PL peak energy measured from ②, a significant reduction in the Bi content is expected to exist and may account for a relative increase in the structural quality of the crystal. While it is difficult to accurately isolate the causal influences that locally vary m, these findings further exhibit non-trivial inhomogeneities across the Bi-droplet covered surface. In this case, an inhomogeneity in a very important optical parameter related to the light emitting efficiency of the semiconductor.

Chapter 6

In Situ micro-Raman studies of laser-induced bismuth oxidation: application to GaAs(Bi) photovoltaic surface engineering

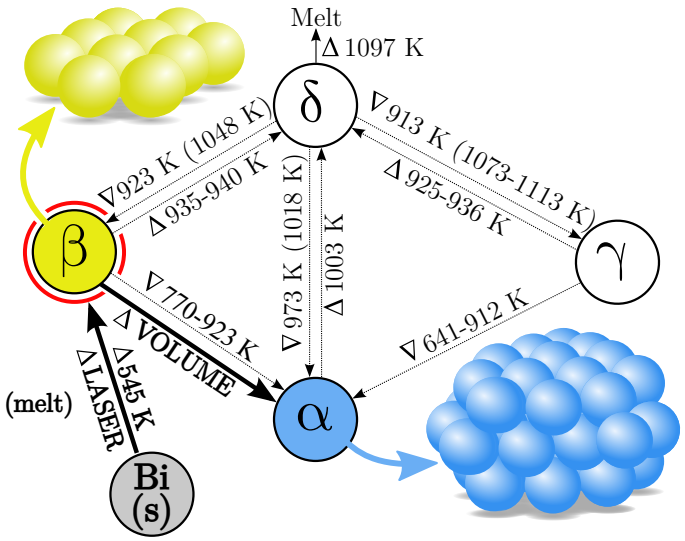

Thermal transformation relations for polymorphic Bi_2O_3 with an illustration of morphological-electrostatic dependencies.

6.1 Oxidation dynamics of metallic Bi

6.1.1 Motivation

Bismuth trioxide (Bi_2O_3; also known as bismuth oxide and bismuth sesquioxide) polymorphs are fascinating optical materials with wide bandgap (2.5 - 3.5 eV), high permittivity (30 - 45), large dielectric permittivity, remarkable photoconductivity, and ionic conductivity. The versatility of Bi_2O_3 nanomaterials has fostered considerable attention for scientific and technological advances over the past decade, with applications spanning electrical ceramics, solid-state electrolytes, gas sensors, medical disinfection/sterilisation, and energy generation[49,222–224]. Within the context of current research on Bi_2O_3, surprisingly little is known about its phase properties at the nano- and micron-scale.

Of the four main Bi_2O_3 polymorphs[55–58], by far the most interesting are the high temperature metastable β and δ modifications, because of their extremely high oxygen ion conductivity (δ-Bi_2O_3 possessing the highest among all binary metal sesquioxides) and their strong visible-light-driven photocatalytic activity (β-Bi_2O_3 being the most active). While thermal oxidation of bismuth is inexpensive and easily controlled[46,225,226], synthesis of the desirable β-Bi_2O_3 and its stabilisation at room temperature is not straightforward[61–65]. Attempts to better understand phase transformation relations among Bi_2O_3 polymorphs are currently underway[60], however a comprehensive model of the transient stages of oxidation is yet to fully explain the varied and seemingly anomalous oxidation phase results reported in the literature[52,226–237]. From the nucleation of Bi_2O_3 molecules on the bismuth surface, to the coalescence of a thermodynamically stable oxide, represent a scientifically challenging and technologically important *terra incognita*. In most studies of bismuth oxidation to date, the only real-time *in situ* diagnostics have been through thermogravimetric analysis or X-ray diffraction (XRD)

measurements. Usually, neither of these techniques is versatile enough to provide information suitable for process control or for elucidating transformation dynamics [238–241].

In this section, we shed light on the bismuth oxidation process through novel laser irradiation-induced oxidation experiments, monitored *in situ* by micro-Raman scattering. Our findings reveal that the resultant Bi_2O_3 phase is critically dependent on oxide volume (at the micron-scale) and follows a fixed transformation sequence. An electrostatic mechanism − based on a changing Bi_2O_3 surface-to-volume ratio − is invoked to explain how small volumes of undoped β-Bi_2O_3 acquire room-temperature metastablity, as well as permitting the interpretation of previous studies.

6.1.2 In situ Raman laser-induced Bi oxidation experiments

The bismuth samples described in this section (see Fig 6.1) were prepared using a high purity (99.99% pure) bismuth ingot purchased from Rotometals Inc. Flakes scraped off by scalpel allowed measurements on larger (bulk) samples, while the production of smaller bismuth particles (0.3 - 3 μm) was achieved using a mortar and pestle, followed by selection under microscope. No further sample preparation was required.

The melting point of bismuth is much lower than that of Bi_2O_3 (see Fig. 6.3), so atomic rearrangement immediately after oxide formation is inhibited. The tendency for Bi_2O_3 to be glass-forming on metallic Bi surfaces [242] means it is useful to investigate small-scale surface reactions. Figure 6.1 shows optical microscope images of the three kinds of bismuth surfaces examined in this study, along with a typical bismuth Raman spectrum exhibiting two modes at 71 cm^{-1} and 98 cm^{-1}. Modes at these frequencies are consistent with the two first-order optical bands of rhombohedral bismuth corresponding to doubly degenerate E_g and non-degenerate A_{1g} phonon modes, respectively [213]. Enlarged in the inset are the weak second-order bands at $\sim$188 cm^{-1} consisting of three overtones of similar frequencies [243].

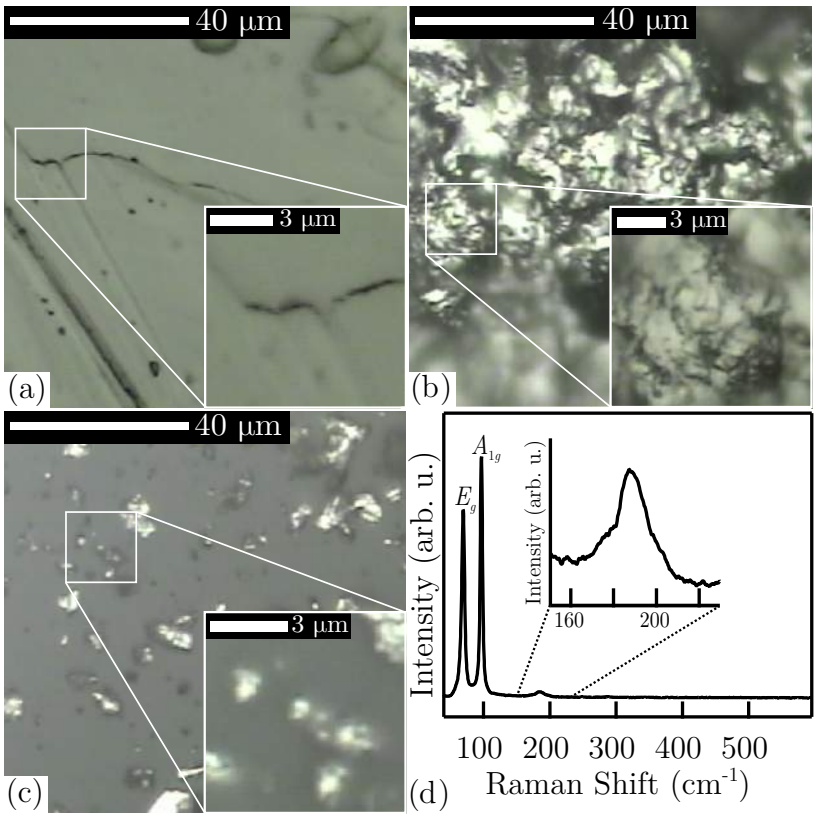

Figure 6.1: Optical micrographs of representative Bi surfaces examined in this study. (a) Smooth, (b) rough, and (c) small particulates on a glass slide. (d) The micro-Raman spectra measured at very low laser power density ($5 \times 10^2\,\mathrm{W} \bullet \mathrm{cm}^{-2}$) from a smooth Bi surface with the inset expanded over the second-order bismuth harmonics.

The development of laser-induced oxidation on a smooth Bi surface is plotted in Fig. 6.2(a) for increasing laser power densities from 0.6×10^4 to $12.5 \times 10^4\,\mathrm{W}\cdot\mathrm{cm}^{-2}$, where additional modes at 128, 315, and $461\,\mathrm{cm}^{-1}$ contribute to the Raman lineshape for irradiances in excess of $2.7 \times 10^4\,\mathrm{W}\cdot\mathrm{cm}^{-2}$. These three bands correspond to unique Bi-O stretches and are attributed to the β-phase Bi_2O_3 [214]. Their appearance confirms laser irradiation-induced oxidation of the bismuth surface (using ambient oxygen) and indicates that, for sufficiently large power densities, there are two induced effects: an oxidation reaction followed by the arranging into β-Bi_2O_3. The second-order scattering mode (with heavy A_{1g} phonon composition [243]) also intensifies and appears connected to the surface oxidation; however, it is not. As the laser power increases the probed

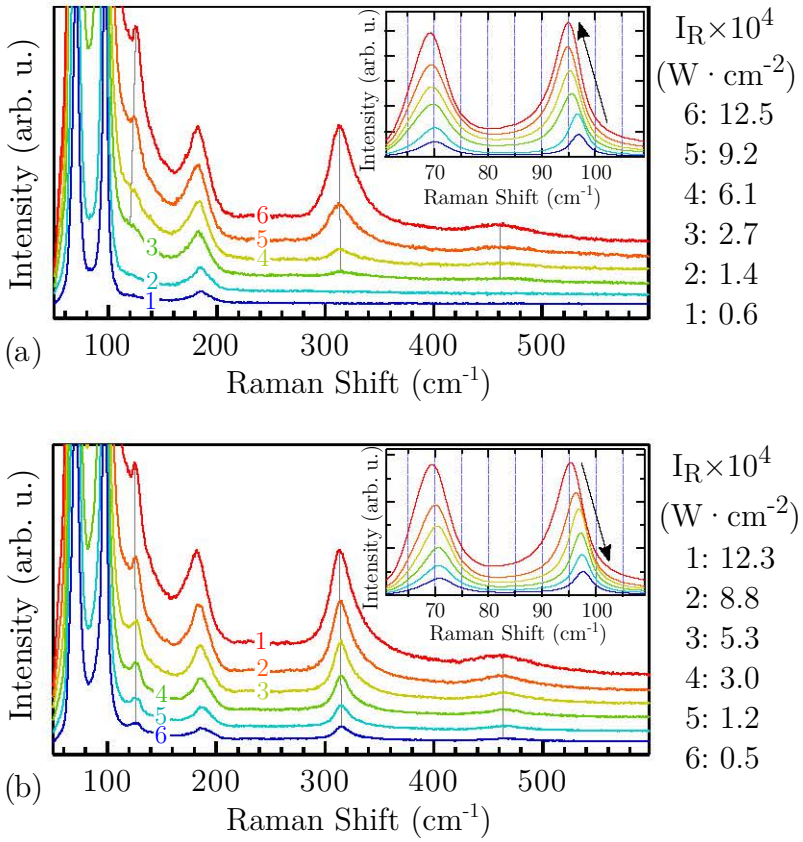

Figure 6.2: Raman spectra of smooth bismuth surface (see Fig. 6.1(a)) for (a) increasing laser power, and (b) decreasing laser power. The insets expand these data over the first-order bismuth optical phonon range. For decreasing power, time was spent between each measurement to allow for cooling. The three solid vertical lines at 128, 315, and 461 cm^{-1} represent the three modes of β-Bi_2O_3. Spectra have been scaled and shifted vertically for clarity.

area rises in temperature and causes first-order bands to grow. Consequently, this also increases the intensity of the second-order harmonics. Figure 6.2(b) presents similar data for a decreasing probe irradiance. Note a two-minute delay was allocated between consecutive measurements to ensure adequate material cooling, as no control was employed. Here the β-Bi_2O_3 signatures represent a prominent and unchanging contribution to the overall Raman lineshape. Local temperature estimates based on the measured frequency of the non-degenerate A_{1g} vibration (this method is clearly outlined in Section. 6.2.3) for the spectrum recorded using a laser power density of

$0.5 \times 10^4\,\mathrm{W\cdot cm^{-2}}$ place the bismuth crystal close to room temperature. Thus, no structural changes are observed once the synthesised oxide is returned to ambient conditions.

Given that 632.8 nm HeNe laser light is used for excitation, the photolytically activated influences are small compared to the isothermally driven process[244]. Many metal oxidation reactions promoted by laser irradiation are largely thermally driven, and isolating non-thermal radiation effects is difficult. For the specific case of a specular bismuth surface[245] irradiated by low intensity 632.8 nm laser light, Raman measurements demonstrated no evidence of oxidation following long exposures; only once temperatures in the laser heated volume surpass the bismuth melting point will an oxidation reaction occur. This is verified by the insets of Figs. 6.2(a) and 6.2(b), where phonon mode redshifting is attributed to large changes in local temperature[246,247]. Decreasing laser powers reveal these phonon bands returning to their original energies. This is important, as it removes factors such as laser-induced defects, resulting in quantum confinement, from influencing the observed redshift; the shifting is driven by non-destructive and purely thermal mechanisms.

The stability of the transformed β-Bi_2O_3 material was investigated over time. Raman spectra were recorded before and after exposure to high irradiance and in both cases an extremely low power density of $I_\mathrm{R} < 5\times10^2\,\mathrm{W\cdot cm^{-2}}$ was used. The absence of Bi-O stretches before irradiation and their presence two weeks after irradiation reveal a stable synthesis of β-Bi_2O_3. Furthermore, no decrease in the relative Raman scattering intensities of these peaks are observed. Thus laser-induced β-Bi_2O_3 oxidation is not only demonstrated, but shown to be stable at room temperature.

Figure 6.3 displays the traditional existence domains and transformation relations (broken light arrows) for the four main Bi_2O_3 polymorphs[55–58], represented as α-(monoclinic), β- (tetragonal), γ- (bcc), and δ-phase (fcc), along with the oxidation

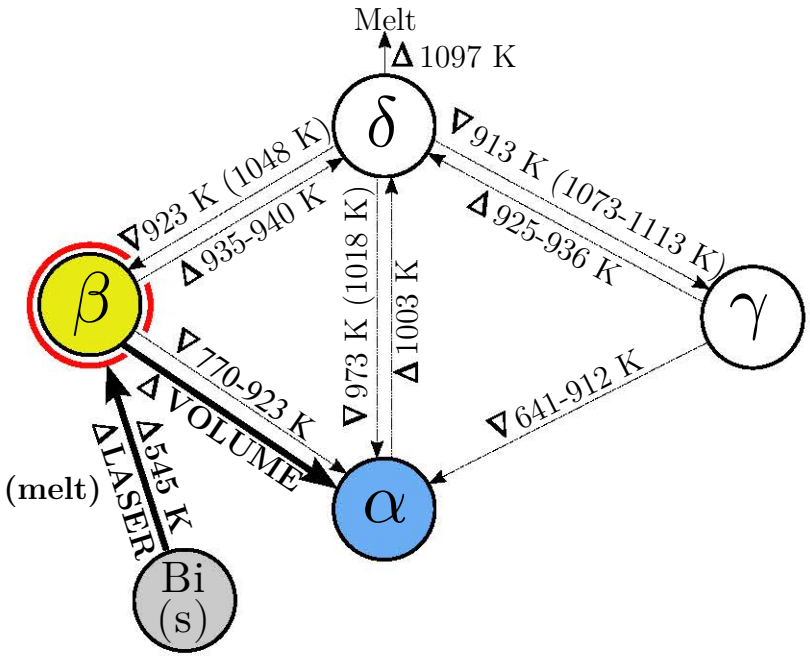

Figure 6.3: Existence domains and transformation relations of Bi and the four main Bi_2O_3 polymorphs[57,222]. The light broken arrows represent bulk isotherm transformations, while the heavy solid arrows represent the micro-probe laser-induced transformations observed in this study. The processes of heating and cooling are indicated here by Δ and ∇, respectively. Temperature ranges without parentheses represent transition temperatures while the values in parentheses represent required minimum initial temperatures.

sequence observed in this study (solid heavy arrows). The existence of at least three other modifications have been realised (ω, ε and η), although these are synthesised under atypical conditions[248–250] and are omitted for clarity. A striking feature of Fig. 6.3 is a tendency for all polymorphs to transform into the δ-phase at sufficiently high temperatures, and ultimately to transform into the α-phase when cooled to room temperature. Of the phases, α-Bi_2O_3 is thermodynamically stable from room temperature up to 1003 K, where it transforms into the δ-Bi_2O_3 phase, which is stable until melting at 1097 K. When cooling from δ-Bi_2O_3, large thermal hysteresis effects regulate the transformation into one of two high-temperature metastable phases, β-Bi_2O_3 or γ-Bi_2O_3. Below approximately 641-923 K the metastable phase transforms into α-Bi_2O_3, unless chemically stabilised[61]. Within this framework, our findings are

unusual for two reasons. Firstly, the laser-induced oxidation results reveal a purely β-Bi_2O_3 oxide layer. This is directly verified through *no* observation of α-Bi_2O_3 vibrations (see Fig. 6.4(a)) in the Raman spectra. Secondly, the laser-induced β-Bi_2O_3 violates the traditional temperature domains for Bi_2O_3 by exhibiting phase stability at room temperature.

6.1.3 Reaching a metastable β-phase oxide

To understand these results, we next investigate the laser-induced changes which are possible with the more textured Bi surfaces of Figs. 6.1(a)–(c). Laser-induced oxidations were carried out using a maximum irradiance of $12.5 \times 10^4\,\mathrm{W\cdot cm^{-2}}$ and $3.2 \times 10^4\,\mathrm{W\cdot cm^{-2}}$ for $1.7\,\mu$m and $4.2\,\mu$m laser spots, respectively, and spectra recorded at fixed time intervals. Final resultant phases were determined *in situ* only after temporal changes in the Raman spectra ceased. Due to the micro-beam profile, laser spot sizes are not equal to the size of the oxide formed, but rather represent the size of the probed area. Depending on incident power densities and surface morphology, the laser-induced oxides can be much smaller.

Plotted in Fig. 6.4(a) are representative Raman spectra of bismuth [213] and the two single β- [251] and α-phase [252] oxides achievable with our experimental setup. The arrows between traces here indicate observed sequential intermediates. While a laser-induced δ-phase transformation was recently realised [238] in Bi_2O_3, the characteristic $625\,\mathrm{cm^{-1}}$ Raman signature was never observed in our data. A remarkable aspect of these results is that we observe an initial β-phase (or Bi + β) in all transformations; laser-induced oxidation of α-Bi_2O_3 is *never* achieved without first passing through an intermediate β-phase. This is highlighted by the temporal data shown in Fig. 6.4(b), where for longer exposure times the β Raman spectrum is shown to evolve into single-phase α (these spectra have been normalised to the bottom β trace by the factors

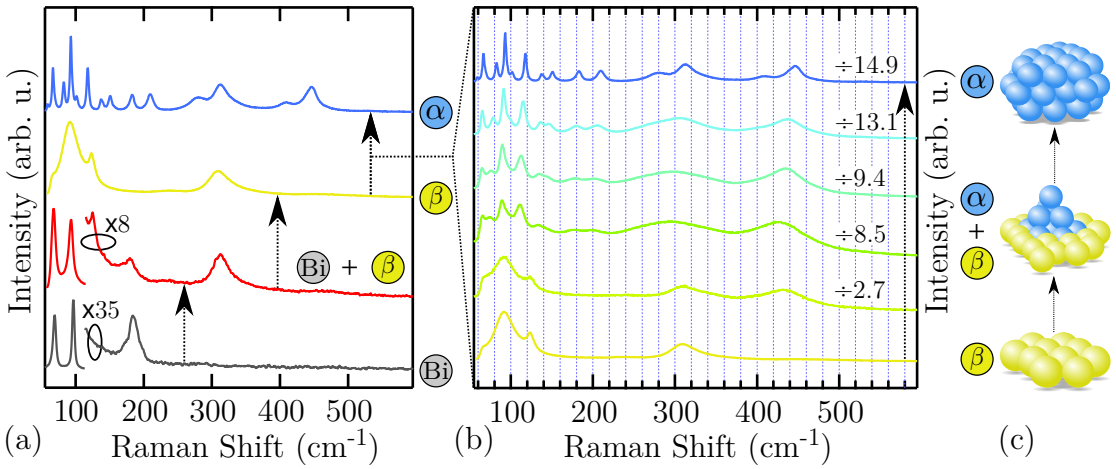

Figure 6.4: (a) Representative unpolarised Raman spectra from bismuth metal and resultant laser-induced Bi_2O_3 phases. Traces labeled Bi, β and α represent the pure phase spectra, while the spectra labeled Bi + β portray an initial (and sometimes final) combined phase. (b) Chosen $\beta \rightarrow \alpha$ transitional dual spectra for longer irradiation exposures. Arrows between traces indicate the observed oxidation phase sequence and all spectra have been normalised (normalisation factors given) and offset for clarity. (c) Schematic of oxide aggregation leading to $\beta \rightarrow \alpha$ transition.

given). The phase transition is matched by broadband temporal growth of the Raman signal, increasing by a factor of approximately 15. The increase in Raman signal here is evenly weighted for both existing β-Bi_2O_3 modes and transitioning α-Bi_2O_3 modes (for example, the peak just above 300 cm^{-1} undergoes a continuous intensification during the transformation), indicating a dramatic change in the scattering volume and the formation of new oxide material, rather than a pronounced shift in scattering cross-section. The tipping point between phases appears to be connected to the size of Bi_2O_3 produced and is schematically represented in Fig. 6.4(c); after some well-defined critical volume, the Bi_2O_3 transforms its structure from β-phase to α-phase.

Table 6.1 summarises the laser-induced oxidation results for all bismuth surface types examined. Here 'smooth' corresponds to a highly specular surface (Fig. 6.1(a)) and 'rough' represents a granulated surface on the scale of 0.2 - 4 μm (Fig. 6.1(b)). Smaller particles ranging from roughly 0.3 to 3 μm were also examined (Fig. 6.1(c)). Differences in the relative texture of the particulates were insignificant (when compared

Table 6.1: Laser-induced bismuth oxide phase results for varying bismuth surfaces (corresponding to those shown in Figs. 6.1(a)–6.1(c)) irradiated by a large (4.2 μm) and small (1.7 μm) focused 632.8 nm laser beam. Representative Raman spectra of resulting phase(s) match with those given in Fig. 6.4(a).

Beam size (μm)	Bulk surface type		Particle size (μm)	
	smooth	rough	1.5 - 3	<1.5
1.7	Bi + β	Bi + β	Bi + β, β	Bi + β, β
4.2	Bi + β	Bi + β, β, α	β, α	β

to size) in determining oxide phase and are not considered further. The oxidation results in Table 1 suggest an inability for Bi_2O_3 to retain β-phase structure above the critical dimension ($\sim$1.5 μm). This is highlighted by a complete absence of α-Bi_2O_3 when irradiating with a 1.7 μm laser spot. This is a consequence of the small ($< 1.7\,\mu$m) and limited volume of oxides formed when employing this beam spot size. Raman spectra revealing a combination of Bi and β were most favoured, with the notable exception of using a 4.2 μm beam on smaller particles. To this point, measurements made with the larger spot size proved to be a better gauge for assessing size dependencies; a distinct shift in subsequent phase was observed for particles transitioning across $\sim$1.5 μm range. Furthermore, rough surfaces with elevated structure were more likely to produce α-Bi_2O_3.

Given the 632.8 nm laser-induced oxidation process is thermally driven, the observation of a new governing oxidation/transformation sequence

$$\frac{3}{2}O_2(g) + 2Bi(l) \rightarrow \beta{-}Bi_2O_3(s) \rightarrow \alpha{-}Bi_2O_3(s), \tag{6.1}$$

extends the traditional phase relations of Fig. 6.3 and should hold true for all thermal oxidations of bismuth. It is emphasised that a laser-induced β-$Bi_2O_3 \rightarrow \alpha$-$Bi_2O_3$

transition occurs in direct opposition to conventional isothermal existence domains, since longer laser exposures generally increase local temperatures rather than decrease them.

Examining the varied Bi oxidation studies in the literature we make the observation that the sequence described by Eq. 6.1 is both accurate for high temperature annealing methods[52,227–231] and laser-induced techniques[226,232–234]. For the specific cases of thermally-treated nanoparticles[52,229] and nanotextured films[230,231], lower oxidation temperatures produced single-phase β-Bi_2O_3, while higher temperatures resulted in single-phase α-Bi_2O_3. More importantly, scanning electron microscope (SEM) images revealed an increased tendency for bismuth oxide microislands to coalesce and form larger aggregated oxide volumes (see Fig. 6.4(c)) with increasing temperature, depicting a critical oxide size comparable to ours, for which the β-$Bi_2O_3 \rightarrow \alpha$-$Bi_2O_3$ transition is observed. It was even demonstrated by XRD measurements that for temperatures between the synthesis of pure β-phase or α-phase oxides, a transitional mixed phase is observed − reminiscent of Fig. 6.4(b) − which bridged the two single-phases[230]. Huang *et al.*[231] also inadvertently reported similar results, however, accounting for their findings using a model based on the differing crystallographic orientations of electrodeposited Bi films. In the pursuit of laser-induced oxidation of Bi nanowires[234] and nanotextured films[226,232], several authors have pointed to the role laser power plays in determining the resulting oxide phase(s). In brief, all studies demonstrated an initial β-phase and oxidations under higher irradiance favoured α-Bi_2O_3 formation. Similar to elevated temperatures in thermal annealing processes, the increased α-Bi_2O_3 formation demonstrated an enhanced capacity for the laser-heated area to produce larger oxides[226,232]. The consistency of results across the very different oxidation schemes means oxide/metal interface effects (i.e. mismatch or strain relief/dislocations) can be neglected. In light of these findings, the one feature which unifies the synthesis

of room-temperature metastable β-Bi_2O_3 becomes clear: *size*.

The fundamental relationships between bismuth oxidation and ensuing phases are still unresolved. For example, why is an initial β-phase favourable over an α-phase and how does undoped β-Bi_2O_3 oxide remain stable at room temperature? From the view point of joining small β-Bi_2O_3 volumes to form an aggregated α-phase, a likely explanation lies in their respective molecular structures; the β-phase Bi_2O_3 polyhedra are proposed to be BiO_6 octahedra with all Bi-O bonds equivalent at 2.4 Å and very similar to that of α-Bi_2O_3. However, given the volumic nature of the results, a detailed answer presumably resides in how the electrostatics of the ionic Bi_2O_3 crystal change with an evolving surface-to-volume ratio[253].

The total electrostatic energy of an arbitrarily shaped ionic Bi_2O_3 crystal can be described by a generalised two part equation[254]:

$$E(\mathcal{L}, P) = \underbrace{E_0(\mathcal{L})}_{\text{Term 1: morphology-independent}} + \underbrace{J(\mathbf{M}, P).}_{\text{Term 2: morphology-dependent}} \tag{6.2}$$

Here $E_0(\mathcal{L})$ represents the morphology-independent term and is simply dependent on the electrostatic energy of the crystal unit cell, E_0, and the total crystal volume, $\mathcal{L}$. On the other hand, $J(\mathbf{M}, P)$ deals with the morphology dependencies of E, and varies with the crystal shape and size (encompassed by variable P), as well as the distribution of ions within a unit cell inducing a dipole moments, $\mathbf{M}$. Term 2 is equal to zero if the dipole moment of the unit cell is zero.

In Tasker's model of ionic crystal surfaces[255], Bi_2O_3 has a dipole moment perpendicular to its surface and is exposed favourably in a practical environment. Moreover the surface is electrostatically unstable. The electrostatic energy of the whole Bi_2O_3 volume therefore is the electrostatic energy of a unit cell multiplied by the number of unit cells (Term 1) plus the corrections proportional to the surface energy of the crystal (Terms 2)[254]. Thus, like all ionic crystals, the bulk energy of diminutive Bi_2O_3

is heavily dependent on surface-to-volume ratio. Harwig and Weenk[256] have already pointed out that there is only a very small difference in the electrostatic energy of α-phase and β-phase Bi_2O_3, with a Madelung energy − representing the majority of the crystal energy[257] − marginally lower for the α-phase (14.49 kJ/mol), compared to the β-phase (14.56 kJ/mol). The surface stability has also been shown to relate to the stability of different crystal planes and, if polar or nonpolar terminations are present, due to alternate stacking of Bi layers and O layers. However, since α-Bi_2O_3 is never seen in the initial oxidation of bismuth (within this study, or otherwise), it is not likely that crystal-plane effects are significant.

The temporal data shown in Fig. 6.4(b) permits the evaluation of real-time phase and structure, as well as allowing the general assessment of mode shifting magnitude and direction. Through a purely empirical interpretation of phonon frequencies, the Bi-O stretching frequency is inversely related to the bond lengths[214]. While α-phase nucleation points take hold in the β-Bi_2O_3 volume, new interactions are established between Bi and O atoms in the transitioning oxide. Early in the transformation, new bonds formed within the oxide experience very little of the pressures exerted by a surrounding external network. New vibrational frequencies are set up and appear at lower frequencies due to this lack of internal pressure and longer bond lengths. With the notable exception of the Bi-Bi vibration just below 70 cm^{-1}, all modes appear to *strongly* harden to higher frequencies for longer laser exposure times. This is paralleled by the entire spectra intensifying over the course of the transformation, until a pure α-phase is reached. It is reasonable to assume, therefore, a correlation between an increasing oxide volume and the direction of the transformation. Rising pressure introduced by a growing crystal network reduces bond lengths and results in phonon mode hardening. As the budding α-Bi_2O_3 condenses, the electrostatic potential of unit cells is further reduced and the dipole moment is lowered toward a final equilibrium.

For reasons that are at present unclear, the synthesis and stabilisation of β-Bi_2O_3 is much easier than that of γ-Bi_2O_3 − this is again likely linked to the comparable Madelung energies of the β-phase and the room-temperature stable α-phase. This suggests β-Bi_2O_3 has a strong tendency to remain stable when its electrostatic energy occupies a local minimum, by possessing a small surface-to-volume ratio or through doping. As far as we know, there is little information about the relative stability, geometries, and electronic structures of Bi_2O_3 polymorph surfaces, which hinders the understanding of their properties and reactivity at small scales.

It is worth pointing out that attempts were made during this thesis work to compute the necessary density functional theory (DFT) calculations to isolate the above suggested electrostatic phase-stabilising mechanism. The principal difficulty in such a simulation is the absolute crystal size at which the size-dependent phase-flip ($\beta \rightarrow \alpha$) is expected to occur − in the order hundreds of nm. While the work contained in this section was under review before appearing in Ref. 67, a study was published by Guenther and Guillon[66] which corroborated our findings (using a variety of complementary techniques). In short, they[66] too provided experimental evidence that the room-temperature stable form of β-Bi_2O_3 is achieved by restricting the size of the oxide to the nanoscale, aptly calling it the "nanophase".

While a comprehensive physical model to aid explanation is lacking, the results and conclusions support merely a plausibility argument; one that points toward oxide volume at small scales as playing a central role in defining Bi_2O_3 phase. This aspect of bismuth oxidation has thus far been overlooked and is particularly significant. In terms of engineering practical Bi_2O_3 elements for optoelectronic applications, fine control over the transformation process is favourable to the exacting preparation of functional materials with specific crystal structure. This we explore in the next section of this chapter.

6.2 Laser-induced oxidation kinetics of bismuth surface microdroplets on GaAsBi

6.2.1 Motivation

Observations of metallic Bi surface droplets following the MBE growth of GaAsBi has been explored repeatedly in this thesis. For the case of our MBE sample, pure Bi droplets are formed. While much of the current work on molecular-beam-epitaxy (MBE) growth of GaAsBi has done well to identify growth conditions which lead to Bi surface segregation[27], the exact composition of the droplets remains unknown. Interestingly, and somewhat suitably, there are many similarities between the surface Bi droplets observed on GaAsBi and those intentionally grown on GaAs-based substrates for the purposed of enhancing the photonic surface absorption; *light-trapping*.

Light-trapping can increase the light absorption ratio which allows decreasing the volume of the active layer. The inclusion of surface metallic nanostructures in GaAs-based solar cells was recently shown to enhance efficiency and function[258], and the droplet epitaxy of semimetal bismuth nanodroplets on a GaAs surface recently realised group-V based MBE nanoscale droplet formation for low-dimensional photovoltaic applications[259]. Further oxidizing the nanodroplets[52] on the GaAs surface forms bismuth trioxide (Bi_2O_3) and an assembly subject to increasing interest for potential applications in energy generation due to its useful optical response[222–224]. The intrinsic polarisability of paired $6s^2$ lone electrons in trivalent bismuth favours the separation of photo-excited electron-hole pairs and the transfer of these carriers[260]. Consequently, the integration of Bi_2O_3 nanoislands was recently shown to be suitable for thin-film solar cells[49].

The optical response and functionality of polymorphic bismuth oxides[55–58] (α-, β-, γ- or δ-phase) are inherently dependent on the phase utilised. In the previous

section, it was revealed that following bismuth oxidation the ensuing oxide phase is critically dependent on the final oxide volume and adheres to a fixed kinetic transformation sequence: $\frac{3}{2}O_2(g) + 2Bi(l) \rightarrow \beta - Bi_2O_3(s) \rightarrow \alpha - Bi_2O_3(s)$. Moreover, it was demonstrated that the often desirable β-Bi_2O_3 − with high oxygen ion conductivity and strong visible-light-driven photocatalytic activity − acquires room-temperature metastability below a critical oxide microisland volume.

The thermal oxidation of metallic bismuth provides a low-cost and easily controlled method for synthesising Bi_2O_3 [46,225], however a recent investigation of high-temperature oxidation of bismuth nanodroplets on a GaAs substrate highlighted the indiscriminate nature of bulk thermal treatments [52]. High-temperature annealing of GaAsBi alloys ultimately changes the opto-electronic properties of the as-grown semiconductor [261–265] and offers limited options for real-time *in situ* diagnostics [67,238–241]. In the interest of controlled surface engineering of such arrangements, alternative techniques ought to be explored.

In this section, we perform micro-Raman studies of GaAsBi metallic Bi surface droplets and investigate the possibility of inducing a local and permanent Bi $\rightarrow$ β-Bi_2O_3 transformation by laser irradiation (HeNe; 632.8 nm, 437.8 THz). By utilizing the transformation dynamics imposed by Eq. 6.1, and oxidizing isolated micron-sized Bi surface droplets, a high level of control is introduced over the transformation, which ensures a final pure β-Bi_2O_3 is always achieved. The ability to locally modify the electrical conductivity and optoelectronic properties of a wide range of materials is the focus of much current research and laser irradiation-induced oxides tend to be compact with good adherent properties with a well-defined metal/oxide interface [244]. Within this context, local laser irradiation for surface engineering of structure, composition, and physical properties, bypassing conventional bulk thermal treatments, is important.

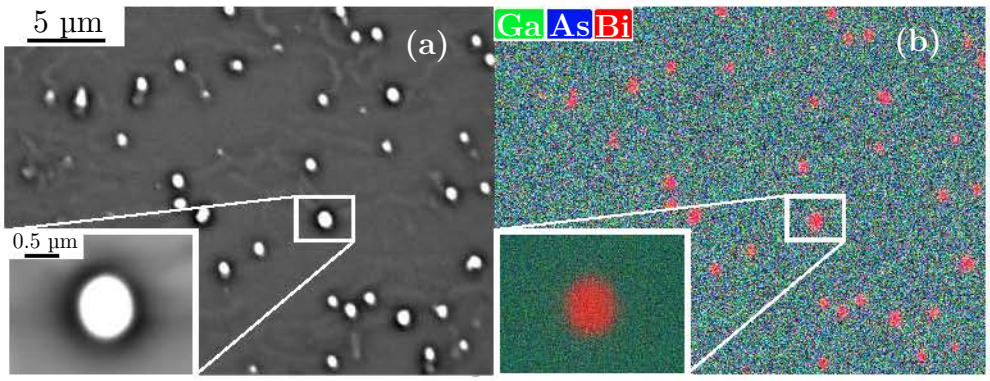

Figure 6.5: (a) SEM image of GaAsBi sample surface showing droplet formation, with (b) the corresponding EDS image. The insets show an enlargement of a typical surface droplet. The EDS data of the droplet reveals a pure bismuth structure which is free from any dual (Ga/Bi) metallic segregation [27].

6.2.2 In situ Raman laser-induced Bi oxidation experiments

The MBE-grown $GaAs_{1-x}Bi_x$ sample studied in this section has Bi concentration $x = 0.048$ and a nominal epilayer thickness of $0.3\,\mu$m. The sample was grown at a substrate temperature of 330°C and with a relatively large Bi flux, and found to be in a saturation regime resulting in the formation of Bi microdroplets covering its epitaxial surface. Figure 6.5 shows representative scanning electron microscope (SEM) and corresponding energy-dispersive x-ray spectroscopy (EDS) images obtained from the GaAsBi expilayer surface. The appearance of pure Bi droplet formation (no Ga/Bi dual composites) on the (100) GaAsBi surface is indicative of bismuth-rich growth (Bi saturation) and attributed to Bi segregation [27]. SEM micrographs revealed the droplets ranged in diameter from 0.1 to $2\,\mu$m, with a mean of roughly $1.5\,\mu$m over the entire sample surface. While the observed surface droplet size and density can fluctuate over different regions, the Raman scattering measurements indicated that the GaAsBi epilayer was highly homogeneous with respect to phonon frequencies and the general Raman lineshape (see Fig. 6.6(b)).

Elemental bismuth can readily be identified in metallic surface droplets using methods such as EDS (see Fig. 6.5(b)), however the bismuth form (i.e. pure metal, de-

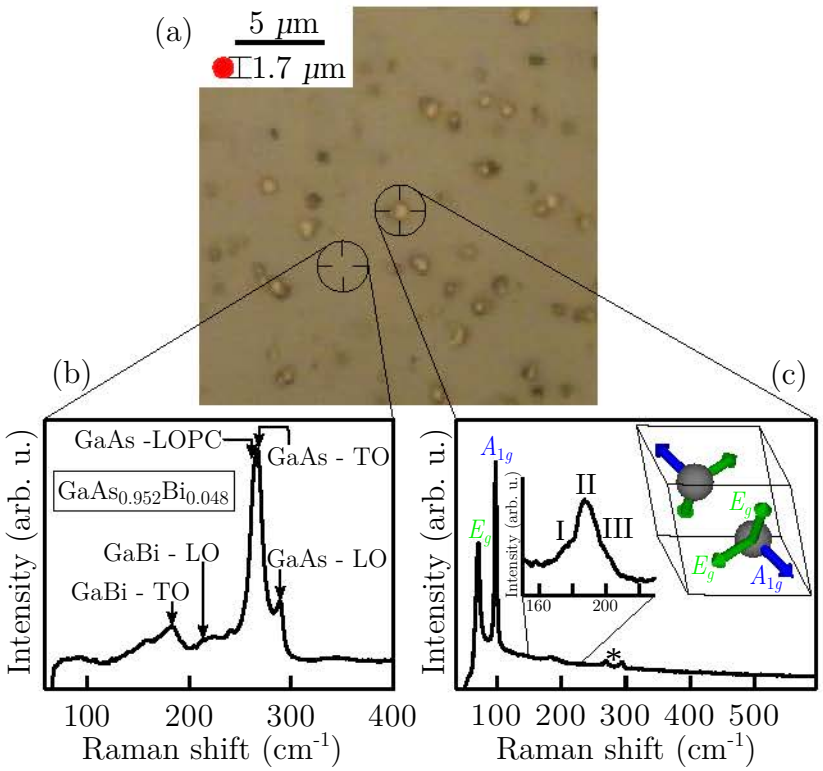

Figure 6.6: (a) Optical micrograph of $GaAs_{0.952}Bi_{0.048}$ sample surface and relative laser spot size. Micro-Raman spectra obtained using a relatively low[67] laser power density ($I_R < 5 \times 10^2\,W/cm^2$) from (b) a droplet-free GaAsBi surface exhibiting characteristic two-mode and free-carrier (hole) plasmon behaviour and (c) the Bi droplet indicated in the optical image above. Here '*' denotes substrate features emerging from scattered probe light. Left inset: spectra expanded and resolved over the second-order bismuth harmonics. Right inset: trigonal two-atom unit cell of bismuth with arrows showing the direction of atomic displacement for non-degenerate A_{1g} and doubly degenerate E_g phonon modes.

fected/polycrystalline or oxidised) must be determined using phase-specific techniques such as Raman spectroscopy or XRD. Figure 6.6(a) shows an optical micrograph of the GaAsBi sample surface with corresponding micro-Raman spectra measured from a smooth, droplet-free region (Fig. 6.6(b)) and from a metallic surface droplet (Fig. 6.6(c)). The spectral features and two-mode behaviour exhibited in Fig. 6.6(b) are characteristic of $GaAs_{1-x}Bi_x$ for $x = 0.048$[91,153]. Figure 6.6(c) displays two strong modes at $73\,cm^{-1}$ (2.1 THz) and $98\,cm^{-2}$ (2.9 THz), which are consistent with the two first-order optical bands of rhombohedral bismuth corresponding to E_g and A_{1g}

phonon modes, respectively[213]. Contrary to the amorphous state suggested by Ciatto *et al.*[69], and in agreement with the data shown in Fig. 6.1, the frequency, linewidths and second-order harmonics measured here indicate a good crystalline Bi structure. From the inset of Fig. 6.6(b), bismuth is shown to crystallise in a trigonally distorted cubic lattice (A7 structure) with two atoms per primitive cell. Thus, for centre point scattering ($q = 0$), there are three optical modes: totally symmetric A_{1g} singlet and the doubly degenerate E_g. Our GaAsBi sample was typically stored under ambient conditions and Raman measurements indicated a negligible presence of naturally-forming bismuth oxide[233].

Enlarged in the inset of Fig. 6.6(c) are the resolved weak bismuth second-order harmonics near $\sim$188 cm^{-1} ($\sim$5.64 THz) consisting of three overtones of similar frequencies which do not originate from GaBi-like modes scattered from the GaAsBi epilayer. Note the large central peak (II) is primarily composed of the A_{1g} symmetry component[243]. Since the laser spot is comparable in size to the Bi island, the relatively weak bands between 270 to 290 cm^{-1} (indicated in Fig. 6.6(c) by *) do originate from the GaAsBi epilayer surface due to light scattering off the droplet and correspond to the GaAs-like TO(Γ), LO(Γ), and LO-phonon-hole-plasmon coupled (LOPC) modes[153].

As exhibited previously in this chapter, the high power densities used in micro-Raman experiments can increase local temperatures due to the intense optical focus. The temperature increase can be hundreds of degrees and will cause wavenumber shifts in Raman modes and potentially induce chemical/structural alterations of the probed surface. Due to its low thermal conductance and very low melting point (545 K), several micro-optical studies of bismuth have demonstrated its tendency to oxidise while under intense illumination[67,226,232–234].

In a comparable procedure to that outlined in Section 6.1.2, Fig. 6.7(a) shows Raman spectra obtained for increasing laser power densities incident on the Bi droplet

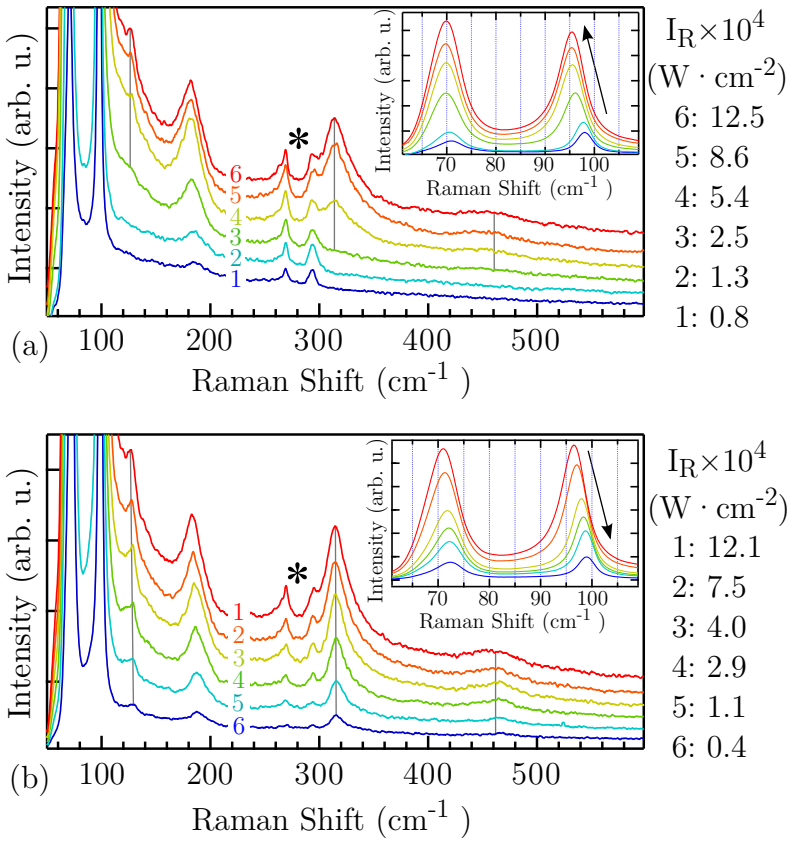

Figure 6.7: Raman spectra of droplet studied in Fig. 6.6(c) for (a) increasing laser power, and (b) decreasing laser power. Here '*' denotes GaAsBi substrate features due to scattered probe light and the insets expand these data over the first-order bismuth optical phonon range. For decreasing power, time was spent between measurements to allow for cooling. The three solid vertical lines at 125, 315, and 460 cm^{-1} represent the three β-Bi_2O_3 vibrational signatures. Spectra have been scaled and shifted vertically for clarity.

studied in Fig. 6.6(c). For laser power densities in excess of $7.4 \times 10^4\,\mathrm{W/cm^2}$, three additional modes at 125, 315, and 460 cm^{-1} are introduced into the Raman spectra which correspond to unique Bi-O vibrations and are attributed to β-phase Bi_2O_3 [67,214]. Again, low-laser-power Raman measurements obtained after oxidation indicated the β-Bi_2O_3 possessed phase stability over time at room-temperature, in agreement with the previous results. The laser-induced oxidation of Bi irradiated with 632.8 nm (473.8 THz) laser light has insignificant photolytic contributions and is thermally driven. Only once temperatures in the laser-heated volume surpass the bismuth melting point will an

oxidation reaction occur; $\frac{3}{2}O_2(g) + 2Bi(l) \rightarrow \beta - Bi_2O_3(s)$. The isolation and small size of the Bi microdroplets impose constraints on the transformation sequence presented in Eq. 6.1, permitting the formation of only a purely β-phase Bi_2O_3 [67].

The insets of Fig. 6.7(a) and 6.7(b) demonstrate the migration of phonon peak frequencies with rising and falling local temperatures, respectively [246,247]. The shifts essentially emerge from the changing atomic bond lengths as a result of the thermal expansion of the bismuth matrix. That modes ultimately return to their original frequencies (see inset of Fig. 6.7(b)) verifies purely thermal mechanisms.

Zayed *et al.* [245] highlighted the variability of the Bi melting point in low dimensions and that the temperature is significantly lower for sub 0.1 μm structures. Given the shallow penetration depth of laser light, the small probe beam size, and the unique morphology of different metallic surfaces, this effect should not be overlooked. However, we only consider the laser-induced oxidation of isolated and smooth micron-sized Bi droplets, studies of which yielded findings consistent with bulk Bi properties.

6.2.3 Temporal Raman study of bismuth laser-induced oxidation

In this section the power and versatility of micro-Raman direct laser processing is demonstrated via a complete *in situ* spectral interpretation of a laser-induced Bi oxidation reaction. Oxidation reactions were investigated for an isolated $\sim 1.5\,\mu$m GaAsBi surface droplet (similar to that studied Fig. 6.6(c)) using a constant laser power density and recording spectra at fixed time intervals. A laser power density of $5.73\times10^4\,W/cm^2$ was selected as it allowed an oxidation reaction to occur on a resolvable timescale.

Figure 6.8 shows chosen Raman spectra obtained *in situ* at different times during the laser-induced oxidation. The low-frequency bands of the spectra (associated with

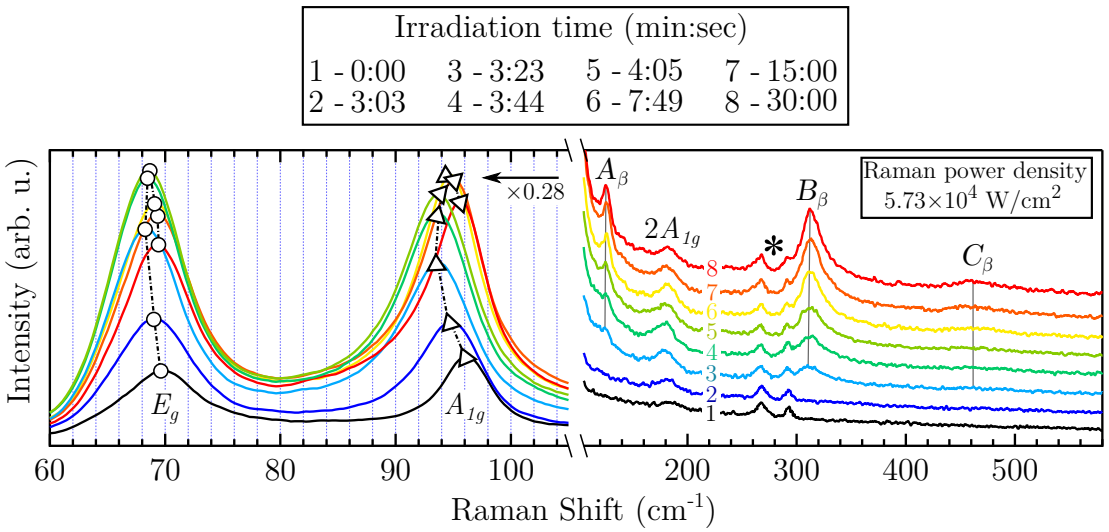

Figure 6.8: Mirco-Raman spectra of an isolated $\sim 1.5\,\mu$m bismuth surface droplet acquired *in situ* at different times of an oxidation reaction using a laser power density of $5.73\times10^4\,\mathrm{W/cm^2}$. The spectra have been offset and the lower frequency portion rescaled for clarity. Here '*' denotes GaAsBi substrate features due to scattered probe light. The vertical lines act as an aid for the eye in identifying the three Raman modes of β-Bi_2O_3 labeled A_β, B_β, and C_β, which are assigned to 125, 315, and $460\,\mathrm{cm^{-1}}$ vibrations, respectively.

the Bi vibrations) strongly redshift during laser heating, reaching a minimum frequency at $\sim$3 min 20 s. A visibly larger shift is observed for the A_{1g} mode than for the E_g. Typically, higher frequency Raman modes are prone to larger shifts, however the difference here is attributed to the anisotropy in bismuth thermal expansion [266] and the fact that nuclear displacements of A_{1g} and E_g are perpendicular and parallel to the basal plane, respectively. Oxidation coincides with maximum phonon redshifts and is indicated by the introduction of three new β-Bi_2O_3 signatures, identified in Fig. 6.8 as A_β, B_β, and C_β. For longer exposure times, the β-Bi_2O_3 bands intensify before temporal changes in the Raman spectra effectively cease. The weak features in Fig. 6.8 identified by * originate from stray light Raman scattered from the GaAsBi epilayer surface and appear unchanging during the reaction.

Spectroscopic real-time temperature estimates of bismuth requires an accurate knowledge of the properties of the metal both in solid and liquid phase. Surprisingly,

there are very few reports on the properties of molten Bi. Since the efficiency of Stokes and anti-Stokes processes has a characteristic temperature dependence, traditional methods of spectroscopically estimating local temperatures involve measuring the anti-Stokes/Stokes ratio ($I_{\mathrm{AS}}/I_{\mathrm{S}}$). However, this method does not lend itself to our attempts to time-resolve or to the use of a Raman microprobe[267]. Alternatively, the phonon shifting for bismuth under laser irradiation can be approximated as a purely thermal occurrence (assumed to be non-destructive) and a relatively simple semi-empirical model can be developed[240,247].

By attributing the change in frequency to the change in the interatomic distance d within the bismuth matrix, and assuming the bismuth is excited in equilibrium conditions (meaning the temperature of heated lattice and electrons are the same), the redshift can be understood by considering the binding energy ϵ_b. Rising temperatures see d increase and the binding energy decrease. Thus the phonon frequency scales with the binding energy and inter-atomic distance by

$$\omega^2 = \epsilon_b/(M_{Bi}d^2) \implies \omega = \omega(T_0) + \Delta\omega(\Delta d, \Delta\epsilon_b), \tag{6.3}$$

where M_{Bi} is the mass of Bi atom, $\omega(T_0)$ is the phonon frequency under ambient conditions, and $\Delta\omega$ represents a shifting term caused by changes in d and ϵ_b. Since the restoring force is non-linear in the displacement, the phonon frequencies are heavily dependent on d, and thus the resulting molar volume V_{m}. The desired temperature T is related to the molar volume through

$$V_{\mathrm{m}}(T) \equiv V_{\mathrm{m0}} \times \exp\left(-3\int_{T_0}^{T} \alpha(T')\partial T'\right), \tag{6.4}$$

where V_{m0} is the molar volume of bismuth under ambient conditions and $\alpha(T') = 1/3[2\alpha_{\perp}(T') + \alpha_{\parallel}(T')]$ is the thermal expansion coefficient[268]. We can examine the

thermal dependence of Bi optical phonon shifts by only considering changes in V_{m}. Neglecting phonon-phonon interactions, the frequency of the phonon is approximated through the isothermic Grüneisen parameter[269]

$$\gamma_{\mathrm{therm}}^{E,A} = -\frac{\partial[\ln\omega_{E,A}]}{\partial[\ln V_{\mathrm{m}}]}. \tag{6.5}$$

The superscript here indicates the two different Grüneisen parameters, $\gamma_{\mathrm{therm}}^{E}$ and $\gamma_{\mathrm{therm}}^{A}$, for the two first-order bismuth optical modes E_g and A_{1g}, respectively. By integrating Eq. 6.5 for only the centre scattering phonons ($q = 0$) we arrive at an expression relating the experimentally observed phonon frequency and local temperature T by

$$\omega_{E,A}(T) = \omega_{E,A}(T_0) \times \exp\left(-3\gamma_{\mathrm{therm}}^{E,A}\int_{T_0}^{T}\alpha(T')\partial T'\right). \tag{6.6}$$

For T_0 and $T \gg 100\,\mathrm{K}$, this can be approximated by the linear equation

$$\omega_{E,A}(T) \;\simeq\; \omega_{E,A}(T_0) + \Delta\omega_{E,A} \times \Delta T. \tag{6.7}$$

Here $\Delta\omega_{E,A}$ is the coefficient of temperature change and $\Delta T = T - T_0$. Höhne *et al.*[247] accurately determined the isothermal Grüneisen parameters for the two first-order optical modes of bismuth to be $\gamma_{\mathrm{therm}}^{E} = 4.9$ and $\gamma_{\mathrm{therm}}^{A} = 2.9$. Inserting these values into Eq. 6.6 we calculate the coefficients to be $\Delta\omega_E = -0.0134\,\mathrm{cm}^{-1}/\mathrm{K}$ and $\Delta\omega_A = -0.0195\,\mathrm{cm}^{-1}/\mathrm{K}$. This suggests upon melting the bismuth E_g and A_{1g} first-order modes should experience a total redshift of approximately $-3.7\,\mathrm{cm}^{-1}$ and $-4.8\,\mathrm{cm}^{-1}$, respectively.

Figure 6.9 displays the temporal analysis from fits made to all spectra measured in the droplet oxidation shown in Fig. 6.8 and is separated into three time intervals, as interpreted by the Raman data. Figure 6.10 displays the estimated Bi droplet temperature using the measured two first-order Bi optical phonon peak frequency

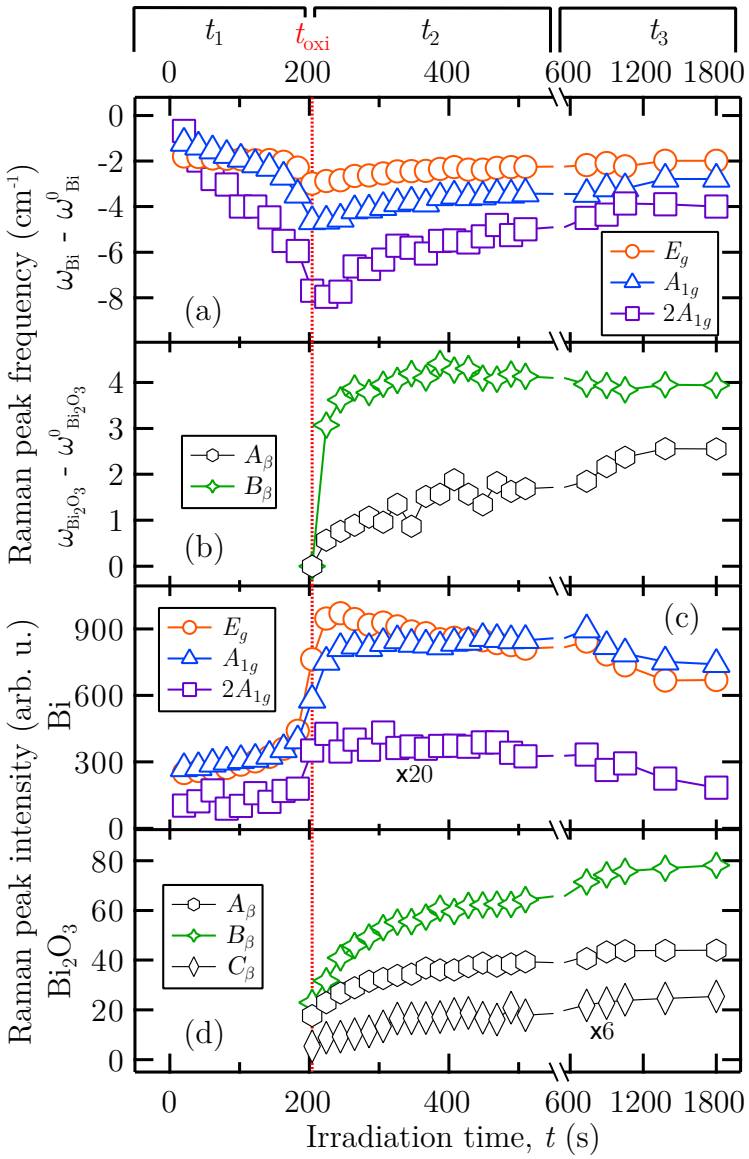

Figure 6.9: Temporal results from fitting all spectra measured during the laser-induced oxidation reaction shown in Fig. 6.8. Values of Raman peak frequency shifts are shown for (a) bismuth modes, and (b) β-Bi_2O_3 modes. Measured Raman peak intensities are shown for (c) bismuth modes, and (d) β-Bi_2O_3 modes. Data is broken into three time intervals which are indicated across the top time axis. The broken vertical line at ~200 s separates time intervals t_1 and t_2 and indicates observation of β-Bi_2O_3 Raman modes, t_{oxi}.

shifts and Eq. 6.7. Early in the reaction the two temperature determinations are very different and extrapolating backward in time to $t = 0$ s for the A_{1g} phonon yields a temperature of approximately 350 K, which is larger than the expected 300 K. A small

initial redshift offset in the A_{1g} phonon can be attributed to the altered dynamics of bismuth in response to a relatively high incident fluence[270]. In general, the analysis of the A_{1g} phonon peak frequency using Eq. 6.7 yields a reasonable account of the changes in temperature leading up to oxidation; increasing from just above room temperature to the melting point of bismuth.

On the other hand, a practical application of Eq. 6.7 in micro-Raman experiments must take into account the degeneracy of the E_g band. Initial laser heating sets up large local temperature differentials and strain-induced symmetry changes lift the double degeneracy of E_g. The E_g linewidth was measured to be approximately $9\,\mathrm{cm}^{-1}$ during the whole reaction, changing very little throughout. This value is much larger than that reported by Höhne *et al.*[247], even at elevated temperatures ($\sim$4-6 cm^{-1}), reflecting the large splitting in the two degenerate E_g phonons. Moreover, while the E_g band is redshifted to lower frequencies it becomes partially truncated by the Rayleigh filter. Thus the temporal analysis of the E_g modes in Fig. 6.9 is included only for completeness and we therefore use the temperature estimates determined from shifts in the A_{1g} phonon (before oxidation) as a basis to the data plotted in the insets of Fig. 6.10(a) and 6.10(b). Note that the error associated with the temperature derived from a Raman spectrum using Eq. 6.7 is relatively large; an accuracy of approximately $\pm 40\,\mathrm{K}$ was assigned by Shebanova *et al.*[240] when comparing the use of a similar technique (assessment of optical phonon shifts) with more conventional methods of temperature determination.

Time interval $\mathbf{t}_1$

Linear (or non-linear) mechanisms of photon absorption occur on the Bi droplet surface which raises local temperatures. In relation to Fig. 6.9, the initial rate of energy absorption and subsequent temperature increase is linear, causing bismuth first-order (and second-order) Raman peaks to intensify and redshift. At approximately $t = 160\,\mathrm{s}$

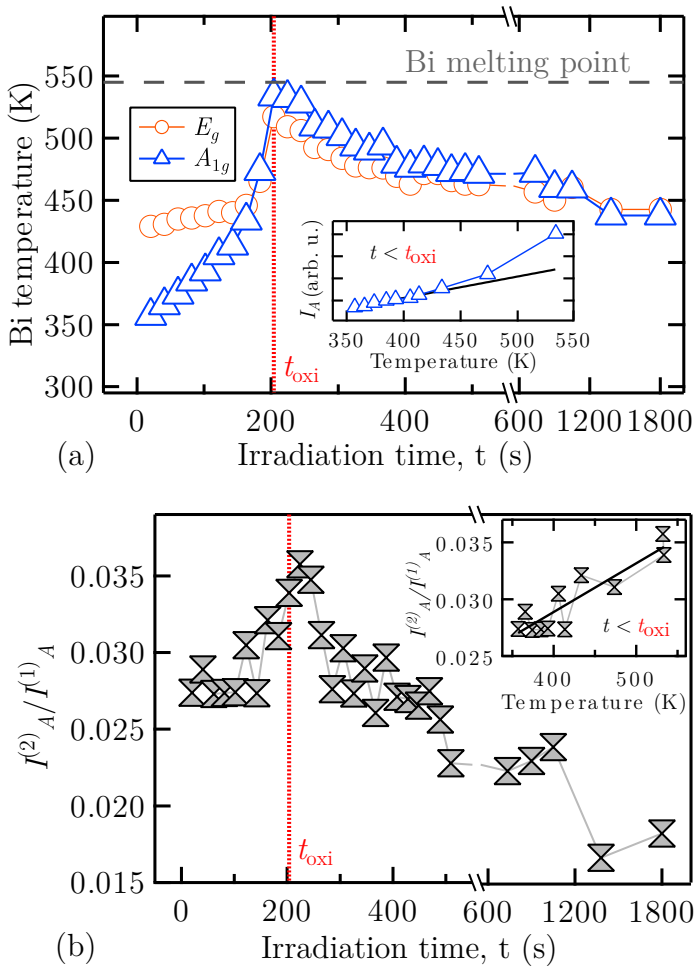

Figure 6.10: (a) Temporal analysis of local bismuth temperature determined using Eq. 6.7 for both E_g and A_{1g} wavenumber shifts. The broken vertical line represents time of bismuth oxidation, t_{oxi}, while the dashed horizontal line indicates the bismuth melting temperature. Inset presents A_{1g} peak intensity as a function of temperature with a linear fit made to data acquired prior to thermal runaway. (b) Ratio $I_A^{(2)}/I_A^{(1)}$ of second- to first-order scattering intensities vs t. Inset shows $I_A^{(2)}/I_A^{(1)}$ as a function of temperature for $t < t_{\text{oxi}}$ with a linear fit acting as an aid for the eye. The temperature basis used in both insets was calculated using Eq. 6.7 and A_{1g} phonon shifts.

the laser heating is accelerated to melting point through a thermal runaway effect. The small bandgap of bismuth gives rise to a relatively large population of intrinsic carriers which will, by their very nature and composition, exhibit free-carrier absorption. The tipping point is defined by the rate of phonon redshifting; it changes from linear to nonlinear and occurs at $\omega_A = 95.3\,\text{cm}^{-1}$ (2.86 THz), corresponding to approximately

$T = 440\,\mathrm{K}$ using Eq. 6.7. This value appears fairly constant when compared to results obtained from laser-induced oxidations of different sized droplets, and regardless of laser intensity. Examining the varied Bi oxidation studies in the literature we make the observation that a thermal runaway study of bismuth is yet to be reported, preventing comparison.

The rise in Raman scattering intensity can be evaluated through the rate of Stokes scattering

$$R_{\mathrm{S}} = A_{\mathrm{S}}[n(\omega) + 1], \tag{6.8}$$

where $n(\omega)$ is the population of frequency ω phonons at lattice temperature T and given by the Plank distribution $n(\omega) = 1/(e^{\hbar\omega/k_{\mathrm{B}}T} - 1)$. Thus we have

$$R_{\mathrm{S}} = \frac{A_{\mathrm{S}}}{1 - e^{-\hbar\omega/k_{\mathrm{B}}T}}, \tag{6.9}$$

where k_{B} is Boltzmann's constant. The rate of Stokes scattering R_{S} is proportional to A_{S}, which includes optical parameters such as Raman susceptibility, which depend on wavelength and temperature. If we simply consider A_{S} to be independent of T, the value of dA_{S}/dT should be roughly constant for temperatures well above 0 K. This suggests deviations from linearity arise due to temperature dependencies in A_{S} when exciting with constant 632.81 nm (473.8 THz) laser light.

Renucci *et al.*[271] have closely examined the bismuth Raman scattering cross-section for E_g and A_{1g} phonons as a function of excitation frequency and determined that for 632.81 nm (HeNe; 1.96 eV, 473.8 THz) excitation the scattering cross-section is off resonance and resides low on the high-energy shoulder of the E_2 transition peak ($\sim$1.6 eV). An increase in temperature would only lower the energy of E_2, rather than increase it, and thus reduce the Raman cross-section when using 632.81 nm (473.8 THz) excitation. From the inset of Fig. 6.10(a), however, we observe the A_{1g}

scattering intensity increases away from a linear relationship with higher temperatures. The departure from linearity coincides with the beginning of the thermal runaway effect (at $\sim T = 440\,K$), accelerating the energy transfer. A pronounced shift in the concentration of free electrons at this temperature can account for both observations. Increases in laser heating reflect an enhancement of photon absorption and their conversion into heat energy, through free-carrier absorption. Likewise, the electron-phonon contribution of A_S in Eq. 6.9 for A_{1g} modes is large; the A_{1g} phonon corresponds to a vibration of different crystal planes with respect to each other and produces a strong coupling between phonons and electrons[247,271].

For contrast, we examine the measured ratio of second- to the first-order scattering intensities $I_A^{(2)}/I_A^{(1)}$ for bismuth in Fig. 6.10(b) as a function of exposure time and spectrally derived temperature (Fig. 6.10(b) inset). The initial value measured near room temperature is similar to that reported by Lannin *et al.*[243] for a comparable excitation frequency (647.1 nm, 463.3 THz). The value of $I_A^{(2)}/I_A^{(1)}$ is seen to steadily increase over time with rising temperatures. These observations of higher-harmonic behaviour discount the notion of dramatic changes in system anharmonicity having any influence over the observed thermal runaway, leading into laser-induced oxidation.

Time interval $\mathbf{t_2}$

The time of initial oxidation is represented in Fig. 6.9 by t_{oxi} and the broken vertical line at $t = 204\,\text{s}$. In the liquid phase, the bismuth droplet reacts with ambient oxygen forming Bi_2O_3 molecules that dissociate and adhere to the droplet surface. They then establish nucleation sites and form weak Bi-O stretches in the Raman spectra. The temporal frequency of the new oxide modes appear to harden strongly during the oxidation reaction (see Fig. 6.9(b)). Just after nucleation the newly-formed β-Bi_2O_3 is relatively free from the pressures of a large oxide network. As the oxide grows, it builds internal pressure which reduces bond lengths and manifests as mode hardening.

The speed at which the vibrations stiffen is related to the rate of growth for the oxide layer. A purely empirical interpretation of metal-oxide stretching frequencies is related to the Bi-O bond length d (in units of Å) by

$$\omega_{\mathrm{Bi-O}} = L \times \exp(-Nd), \tag{6.10}$$

where L and N are fitting parameters. Using experimental results of Raman stretching frequencies and crystallographic bond length, Hardcastle *et al.*[214] determined L and N to respectively be 92 760 cm^{-1} and 2.511 $\mathrm{Å}^{-1}$. A calculation reveals a relative change in the bond lengths over the hardening period of 0.22% and 0.27% for A_β and B_β mode frequencies, respectively. This agrees, at least qualitatively, with a non-linear bonding potential. As the oxidation progresses the increase in Raman signal from β-Bi_2O_3 slows whereby further oxidation reactions can only proceed by solid-state diffusion of reactants through the oxide. The scale thickness determines the absorption which leads to a temperature decrease in the bismuth – inferred from Bi optical phonon blueshifting – and further reduces the chemical reaction rate. Our measurements of A_{1g} intensity appear to grow continually through t_{oxi}. This is simply due to an overlap of the β-Bi_2O_3 and Bi Raman spectra, with Bi-Bi vibrations within the oxide contributing to a similar frequency which is difficult to resolve. Indeed, it is for this reason the temperature basis in Fig. 6.10 does not extend past t_{oxi}.

Time interval $\mathbf{t_3}$

The rate of new oxide formation dramatically slows and, towards 1800 s, effectively ceases. The frequency and intensity of the bismuth modes in Fig. 6.9 flatten out and stabilise, though small temperature fluctuations manifest as small variations in the quantities; the process settles into an approximately equilibrium state.

6.2.4 Modeling of bismuth microdroplet oxidation reaction

The purpose of oxidation experiments is generally to assess the reaction kinetics and the mechanisms of oxidation of the metal (or alloy) under a particular set of exposure variables. We perform here analysis for a single laser-induced Bi oxidation reaction under ambient conditions (reaction displayed in Fig. 6.8 and further analysed in Figs. 6.9 and 6.10), although this could readily be extended to include changes in environmental conditions. Because the Raman scattering cross-section is proportional to the total scattering volume, the evolving Raman peaks allow a direct measure of oxidation in real-time and can be used to analyse the reaction. Therefore the measured temporal intensity of B_β band is presented again in Fig. 6.11 for detailed treatment.

Parabolic oxidation equations are often used for metallic surfaces exposed to high temperatures and free oxygen, with solid-state migration across the scale being the rate-controlling process. However, a parabolic oxidation rate does not describe our data (see Fig. 6.11; the data does not trend parabolically) because of two system factors: (i) while laser heating propels the Bi droplet toward melting point, the surface rapidly cools soon after and forms a protective scale which effectively blocks the radiation required to sustain the oxidation reaction; and (ii) bismuth microislands provide limited Bi reactants which, in turn, also controls rate.

Our data exhibits an initially rapid reaction rate which quickly slows and looks typical of metal surface oxidizing under exposure to relatively low temperatures. This behaviour is reflective of factor (i) and is usually found to conform to rate laws described by logarithmic functions. The interpretation of the logarithmic laws are based on the adsorption of oxygen reactants on the metal surface and the forming of an extremely well-defined metal/oxide interface[272]. Beyond 800 s, however, the reaction is no longer logarithmic as it asymptotically approaches its maximum final volume. This behaviour is indicative of the phase transformation kinetics of solids

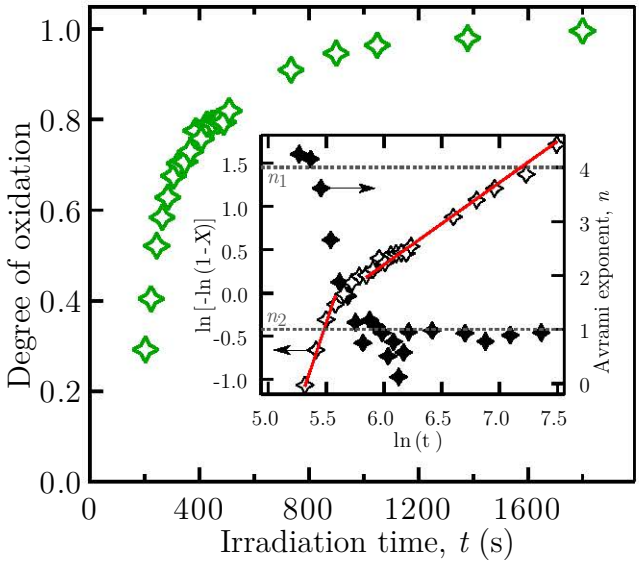

Figure 6.11: Degree of Bi droplet oxidation obtained from normalized B_β Raman intensity vs time t. The inset shows the Avrami plot ln[-ln(1-$X(t)$)] vs ln(t) of the data plotted with corresponding Avrami exponent as derived from the gradient value. Two separate regimes of the Avrami plot are fitted using n_1=4 and n_2=1 (dashed horizontal lines).

(crystallisation), as both are strongly limited by the availability of reactants. The universal method to describe nucleation to coalescence of thin films is the Johnson-Mehl-Avrami-Kolmogorov (JMAK) theory[273–275], which has been successfully applied to describe the oxidation kinetics of metallic systems[276]. The JMAK theory presumes that the transformed volume fraction $X(t)$ will follow an exponential dependency on time through

$$X(t) = 1 - \exp[-k(t - t_{\text{oxi}})^n]. \tag{6.11}$$

Here t is time, and k and n are fit parameters that depend on the surface mechanisms of transport, nucleation, and growth. By theoretical considerations, the Avrami exponent n acquires an integer or half integer value in the range 0.5 to 4, depending on the dimensionality of the transformation and is defined as the local slope in a double logarithmic Avrami plot ln[-ln(1-$X(t)$)] vs ln(t). A nonconstant Avrami exponent as a function of time can be considered as a deviation from normal JMAK behaviour.

In relation to our data, we assume that the integrated Raman intensity of mode B_β − chosen for its relatively strong Raman signal − is proportional to the volume of transformed β-Bi_2O_3 material within the Raman microprobe. The intensity of B_β has been normalised in Fig. 6.11 with corresponding Avrami plot and exponent data presented in the inset. The Avrami plot reveals a time-dependent Avrami exponent with two clear regimes, transitioning from $n = 4$ to $n = 1$, which is used for two separate linear fits of the data. An initial Avrami exponent of $n_1 = 4$ suggests, based on nucleation theory, the transformation is tri-dimensional and interface controlled with a decreasing number of nucleation sites. After a well-defined critical time, the Avrami exponent transitions to $n_2 = 1$, describing a bi-dimensional reaction with nucleation site saturation which is diffusion controlled. Interpreting the oxidation reaction using JMAK theory here appears to yield a reasonable reconstruction of the evolving surface dynamics, suggesting it could prove useful under more elaborate environmental conditions.

Chapter 7

Conclusions

Motivated by conflicting reports in the literature of what the *true* Raman tensors are, we first presented a general method for determining the polarised Raman backscattering selection rules for an arbitrary (hhk)-oriented zincblende-type crystal surface. A direct comparison of the theory and Raman backscattering experiments performed on high-index GaAs crystals (up to (115)) demonstrated that the tensors derived in this thesis are the correct ones. Considering the degrees of freedom available for both the orientation of the investigated material system and the possibility to employ polarising optics before and after the backscattering surface, we examined the full range of consequences imposed by the selection rules for common Raman backscattering configurations.

We have studied the influence of bismuth incorporation on the Raman spectra of strained (100) and (311)B $GaAs_{1-x}Bi_x$/GaAs heterostructures grown by molecular beam epitaxy (MBE), for $0.012 \leq x \leq 0.048$. The first-order Raman spectra of GaAsBi alloys display a two-mode behaviour as well as clear disorder-activated GaAs-like bands arising from a large lattice deformation. This is not surprising, given the large differences in natural bond lengths for GaBi and GaAs. The anomalous appearance of well-resolved non-Γ scattering modes is attributed to the Bi-induced resonant state near

the valence band maximum. The introduction of Bi into GaAs is shown to redshift the optical phonon modes, with a larger shift experienced for the LO(Γ) mode, resulting in a strong narrowing of the optic band splitting. Once effects due to biaxial strain are removed, the contribution to the total narrowing of the TO and LO modes is well described by employing a simple model that takes into account the effects of alloying. $GaAs_{1-x}Bi_x$ samples grown on (311)B GaAs substrates are reported to experience large dampening, $-120(\pm 6)\text{cm}^{-1}/x$, nearly twice that of the (100) grown samples. This is contrary to expected strain-only effects. XRD scans and Ramam scattering measurements reveal that large amounts of disorder in the GaAsBi matrix is the likely origin for the discrepancy.

We also observed damped LOPC modes through Raman scattering experiments for *nominally undoped* $GaAs_{1-x}Bi_x$. By examining the redshifts and broadening of the GaAs-like LO, TO and LOPC bands, strong damping is found to dominate the phonon-hole-plasmon coupling, which softens well below ω_{TO} for large x. Our spectral analysis reveals that the native hole concentration correlates with the Bi molar fraction and exceeds $5 \times 10^{17}\,\text{cm}^{-3}$. The comparatively large carrier densities measured here in a purely optical experiment are attributed to the relatively large thicknesses of our samples.

In the presence of Bi surface droplets, the MBE of GaAsBi is shown to suffer from the formation of planar nanostructures we have called "nanotracks". The characterisation of the self-aligned GaAsBi planar nanotracks reveals them to exhibit periodic height variations along their length. Based on a detailed morphological study of the nanotracks we developed a semi-empirical geometric model to account for three interesting characteristics observed: (i) a cross section resembling an "M-shape", (ii) asymmetrically rising left and right edges, and (iii) a periodic and out-of-phase undulation pattern across the nanotrack growth axis. These features are found to originate

from strong diffusion and shadowing effects. The asymmetry in the nanotrack cross section is expected to promote a disorderly growth process for the less sheer sidewall, a feature observed in experiment. It is shown that the assumption of a skewed distribution of enhanced growth rate near the TPB reproduces the nanotrack pattern with high precision, implying this approach to be accurate. While diffusion and shadowing effects are typically avoided during MBE growth, we conclude they might actually be utilised in the design and growth of planar nanostructures with controlled periodic non-monotonous structure. On the other hand, should the formation of such nanostructures be undesirable, our model can help design the growth procedure for that purpose.

Following a careful assessment of the interaction volume when implementing a 3.5 kV electron beam incident at 70 °, energy dispersive x-ray spectroscopy (EDS) measurements demonstrate a substantial inclusion of Bi atoms into the nanotracks: $x_{\text{nanotrack}} = 0.028$ - 0.032. Through analysis of polarised micro-Raman scattering measurements, the nanotrack crystal is shown to align with the substrate, however they also possess elevated structural disorder, relative to the epitaxial film. Large discontinuities in the optical properties − bandgap and light emitting efficiency − are found to occur over the nanotrack covered surface.

In situ micro-Raman scattering experiments elucidated the dynamics of Bi oxidation. Our optical results reveal the unexpected and seemingly fixed bismuth oxidation sequence: $\frac{3}{2}O_2(g)+2Bi(l) \rightarrow \beta\text{-}Bi_2O_3 \rightarrow \alpha\text{-}Bi_2O_3$. The phenomenon of room-temperature metastable β-Bi_2O_3 is examined within this sequence and the tipping point is attributed to Bi_2O_3 volume dependencies. An electrostatic model based on the changing Bi_2O_3 surface-to-volume ratio is invoked to account for the findings and also to unlock the interpretation to previous studies. Considering the wide variety of applications for bismuth oxide nanomaterials, these findings represent a timely stimulus to further

theoretical and experimental investigation of bismuth oxidation, as well as possible methods of material synthesis/fabrication.

Further real-time *in situ* studies of laser-induced oxidation of GaAsBi bismuth surface droplets are studied by means of Raman microprobe analysis. The synthesised oxide microisland is β-Bi_2O_3, which exhibits phase stability at room temperature. Spectra acquired at fixed time intervals during the oxidation yield insights into laser-induced bismuth oxidation kinetics and permit the meaningful interpretation of oxidation dynamics within Johnson-Mehl-Avrami-Kolmogorov (JMAK) theory.

From the above summary of the technical results and findings of this thesis there are several important implications for the application of GaAsBi and polymorphic Bi_2O_3 materials in optoelectronic devices. For the relatively undeveloped III-V alloy GaAsBi, a common theme throughout this thesis are the fundamental challenges associated with how to successfully incorporate relatively large Bi atoms into the host GaAs matrix, something which has thus far stifled the growth of genuine device-quality alloys. Until overcome, these problems are likely to relegate devices based GaAsBi to the world of the research laboratory. Of the issues studied here, two stand out as particularly problematic moving forward: (i) the surface segregation of Bi atoms during growth and the formation of potentially harmful VLS-driven surface droplets and nanotracks, and (ii) the presence of relatively large native hole concentrations in the nominally undoped alloy. Fortunately, the path to mitigating these concerns appears relatively straightforward, through both employing optimised growth conditions (free from Bi surface droplets) and avoiding the growth of excessively thick epilayers. Within the context of current research on functional Bi_2O_3 nanomaterials for optoelectronic devices, harnessing the anomalous undoped room-temperature stable β-phase (the 'nanophase') will help extend the palette of functional design parameters available to material scientists and engineers. In terms of engineering practical Bi_2O_3 elements,

the level of control over local β-Bi_2O_3 synthesis demonstrated in this thesis (using all-optical means) is favourable to the exacting preparation of functional materials at the micron scale.

7.1 Future work

There are many more investigations/experiments that can be done to further understand the relatively new $GaAs_{1-x}Bi_x$ material system, as well as the phase properties of Bi_2O_3. Moreover, a better knowledge of ternary GaAsBi may be of particular interest for the III-V-Bi family, given its candidature as a building block for further quaternary alloys, i.e. GaAsBiP and GaAsBiN.

The origin of well-resolved non-Γ phonons in the non-resonant Raman spectra of dilute $GaAs_{1-x}Bi_x$ is not yet completely understood. However, there is anecdotal evidence that the X and L zone-boundary phonons are activated by the mixed symmetry of bismuth-induced 6p state in the GaAs valence band. To confirm this, resonant Raman scattering measurements are required to shed further light on this interesting phenomenon. Using the resonant Raman technique, tuning the excitation energy of the Raman laser and analysing the changes in the Raman spectrum near resonance will provide insights into the nature of the electronic state(s) involved.

The Raman data recorded from GaAsBi shows a strong redshift in the GaAs-related modes which are characteristic of Bi-alloying. However, the more significant result is that strongly damped LO-phonon-hole-plamson (LOPC) modes are observed which are associated with large hole concentrations ($> 5 \times 10^{17}\,\mathrm{cm}^{-3}$: determined from Raman spectra) in these *nominally undoped* materials. This is a fascinating result, which however unavoidably begs the question − what would other measurements of carrier concentration (e.g. Hall) give? The issue here is the destructive nature by which transport measurements are made, with the fixing of ohmic contacts. A systematic

comparison of the hole concentrations determined using the spectral method outlined in this thesis, with transport measurements, will help to clarify this issue.

The model proposed to explain the periodic height variations still needs refining. Again, the limited access we have to the growth of GaAsBi materials greatly hinders studies of a systematic nature. This would allow for a deeper understanding of the growth conditions leading to the formation of nanostructures possessing these interesting morphologies. Further, the geometric growth model could be tested against many experiments to determine growth parameters (like diffusion lengths), and examine how it scales up or down for the growth of nanostructures of different sizes.

To unambiguously confirm an electrostatic mechanism underpinning the room-temperature metastability of β-phase Bi_2O_3, nanocrystal simulations of the total energy for the two competing phases (α and β) are required. As outlined briefly in Chapter 6, the major issue here is how to approach such a large scale simulation; an order of magnitude calculation places the number of simulated atoms in a 500 nm by 500 nm α-phase Bi_2O_3 crystal at $\sim 2 \times 10^7$. Molecular mechanics calculations are most likely the method to use here. This is because they are orders of magnitude faster than DFT or quantum chemistry calculations, and often scale much better with system size.

Appendix A

Raman tensor for arbitrary (hhk)-oriented zincblende crystal

MATLAB code

Listing A.1: Tensor-rotation.v - An algorythm (MATLAB code) for calculating Raman tensors up to a zincbelnde crystal face up to (119).

```
clear all
close all
clc  %clears inputs

format long %output is in long 15 sig fig format
d1=[0 0 0; 0 0 1; 0 1 0]; %x
d2=[0 0 1; 0 0 0; 1 0 0]; %y
d3=[0 1 0; 1 0 0; 0 0 0]; %z        % Raman tensors in main
    crystal basis set
t=cat(3,d1,d2,d3);  %Concatenate arrays along 3 dimensions -->
    Raman matrices
```

```
s1 = size(t);

for h=0:9  %for h values 0 to 9; (110) --> (119)(h instead of k,
    to use i,j,k terminology later

 v1=[1,-1,0];v11=v1/norm(v1); %X %norm of vector components --> 2-
     norm, |x|2 = RMS(x)= sqrt(x1^2 x2^2 + x3^2)^1/2
 v2=[h,h,-2];v22=v2/norm(v2);
 v3=[1,1,h];v33=v3/norm(v3);

a=[v11;v22;v33]; % rotation matrix
D1=norm(v1);

disp('rotation matrix')
disp(a)

%rotation
tr=zeros(size(t)) ; %returns a set of three 3x3 zero matrices
for i=1:3
    for j=1:3
        for k=1:3
            for l=1:3
                for m=1:3
                    for n=1:3
                        tr(i,j,k)=tr(i,j,k)+a(i,l)*a(j,m)*a(k,n)*t
                            (l,m,n);
                    end
                end
            end
        end
    end
end
```

```
disp(['Raman tensor, phonon polarisation X=[',num2str(v1(1)),',',
    num2str(v1(2)),',',num2str(v1(3)),']'])
disp(tr(:,:,1)) %display Rx

disp(['Raman tensor, phonon polarisation Y=[',num2str(v2(1)),',',
    num2str(v2(2)),',',num2str(v2(3)),']'])
disp(tr(:,:,2)) %display Ry

disp(['Raman tensor, phonon polarisation Z=[',num2str(v3(1)),',',
    num2str(v3(2)),',',num2str(v3(3)),']'])
disp(tr(:,:,3)) %display Rz

end
```

Table A.1: Raman tensors calculated for (hhk)-oriented zincblende crystals.

Crystal surface	Basis (X, Y, Z)	Raman tensors (Rx ; Ry ; Rz)		
(001)	$([1\bar{1}0], [110], [001])$	$\begin{bmatrix} 0 & 0 & 1 \\ 0 & 0 & 0 \\ -1 & 0 & 0 \end{bmatrix}$	$\begin{bmatrix} 0 & 0 & 0 \\ 0 & 0 & 1 \\ 0 & 1 & 0 \end{bmatrix}$	$\begin{bmatrix} -1 & 0 & 0 \\ 0 & 1 & 0 \\ 0 & 0 & 0 \end{bmatrix}$
(110)	$([1\bar{1}0], [00\bar{2}], [110])$	$\begin{bmatrix} 0 & 1 & 0 \\ 1 & 0 & 0 \\ 0 & 0 & 0 \end{bmatrix}$	$\begin{bmatrix} 1 & 0 & 0 \\ 0 & 0 & 0 \\ 0 & 0 & -1 \end{bmatrix}$	$\begin{bmatrix} 0 & 0 & 0 \\ 0 & 0 & -1 \\ 0 & -1 & 0 \end{bmatrix}$
(111)	$([1\bar{1}0], [11\bar{2}], [111])$	$\begin{bmatrix} 0 & 0.8165 & -0.5774 \\ 0.8165 & 0 & 0 \\ -0.5774 & 0 & 0 \end{bmatrix}$	$\begin{bmatrix} 0.8165 & 0 & 0 \\ 0 & -0.8165 & -0.5774 \\ 0 & 0.5774 & 0 \end{bmatrix}$	$\begin{bmatrix} -0.5774 & 0 & 0 \\ 0 & -0.5774 & 0 \\ 0 & 0 & 1.1547 \end{bmatrix}$
(112)	$([1\bar{1}0], [22\bar{2}], [112])$	$\begin{bmatrix} 0 & 0.5774 & -0.8165 \\ 0.5774 & 0 & 0 \\ -0.8165 & 0 & 0 \end{bmatrix}$	$\begin{bmatrix} 0.5774 & 0 & 0 \\ 0 & -1.1547 & 0 \\ 0 & 0 & 0.5774 \end{bmatrix}$	$\begin{bmatrix} -0.8165 & 0 & 0 \\ 0 & 0 & 0.5774 \\ 0 & 0.5774 & 0 \end{bmatrix}$
(113)	$([1\bar{1}0], [33\bar{2}], [113])$	$\begin{bmatrix} 0 & 0.4264 & -0.9045 \\ 0.4264 & 0 & 0 \\ -0.9045 & 0 & 0 \end{bmatrix}$	$\begin{bmatrix} 0.4264 & 0 & 0 \\ 0 & -1.0466 & 0.4112 \\ 0 & 0.4112 & 0.6202 \end{bmatrix}$	$\begin{bmatrix} -0.9045 & 0 & 0 \\ 0 & 0.4112 & 0.6202 \\ 0 & 0.6202 & 0.4934 \end{bmatrix}$
(114)	$([1\bar{1}0], [44\bar{2}], [114])$	$\begin{bmatrix} 0 & 0.333 & -0.9428 \\ 0.3333 & 0 & 0 \\ -0.9428 & 0 & 0 \end{bmatrix}$	$\begin{bmatrix} 0.3333 & 0 & 0 \\ 0 & -0.8889 & 0.6285 \\ 0 & 0.6285 & 0.5556 \end{bmatrix}$	$\begin{bmatrix} -0.9428 & 0 & 0 \\ 0 & 0.6285 & 0.5556 \\ 0 & 0.5556 & 0.3143 \end{bmatrix}$
(115)	$([1\bar{1}0], [55\bar{2}], [115])$	$\begin{bmatrix} 0 & 0.2722 & -0.9623 \\ 0.2722 & 0 & 0 \\ -0.9623 & 0 & 0 \end{bmatrix}$	$\begin{bmatrix} 0.2722 & 0 & 0 \\ 0 & -0.7560 & 0.7484 \\ 0 & 0.7484 & 0.4838 \end{bmatrix}$	$\begin{bmatrix} -0.9623 & 0 & 0 \\ 0 & 0.7484 & 0.4838 \\ 0 & 0.4838 & 0.2138 \end{bmatrix}$
(116)	$([1\bar{1}0], [66\bar{2}], [116])$	$\begin{bmatrix} 0 & 0.2294 & -0.9733 \\ 0.2294 & 0 & 0 \\ -0.9733 & 0 & 0 \end{bmatrix}$	$\begin{bmatrix} 0.2294 & 0 & 0 \\ 0 & -0.6520 & 0.8196 \\ 0 & 0.8196 & 0.4226 \end{bmatrix}$	$\begin{bmatrix} -0.9733 & 0 & 0 \\ 0 & 0.8196 & 0.4226 \\ 0 & 0.4226 & 0.1537 \end{bmatrix}$
(117)	$([1\bar{1}0], [77\bar{2}], [117])$	$\begin{bmatrix} 0 & 0.1980 & -0.9802 \\ 0.1980 & 0 & 0 \\ -0.9802 & 0 & 0 \end{bmatrix}$	$\begin{bmatrix} 0.1980 & 0 & 0 \\ 0 & -0.5708 & 0.8649 \\ 0 & 0.8649 & 0.3728 \end{bmatrix}$	$\begin{bmatrix} -0.9802 & 0 & 0 \\ 0 & 0.8649 & 0.3728 \\ 0 & 0.3728 & 0.1153 \end{bmatrix}$
(118)	$([1\bar{1}0], [88\bar{2}], [118])$	$\begin{bmatrix} 0 & 0.1741 & -0.9847 \\ 0.1741 & 0 & 0 \\ -0.9847 & 0 & 0 \end{bmatrix}$	$\begin{bmatrix} 0.1741 & 0 & 0 \\ 0 & -0.5064 & 0.8952 \\ 0 & 0.8952 & 0.3323 \end{bmatrix}$	$\begin{bmatrix} -0.9847 & 0 & 0 \\ 0 & 0.8952 & 0.3323 \\ 0 & 0.3323 & 0.0895 \end{bmatrix}$
(119)	$([1\bar{1}0], [99\bar{2}], [119])$	$\begin{bmatrix} 0 & 0.1552 & -0.9879 \\ 0.1552 & 0 & 0 \\ -0.9879 & 0 & 0 \end{bmatrix}$	$\begin{bmatrix} 0.1552 & 0 & 0 \\ 0 & -0.4545 & 0.9165 \\ 0 & 0.9165 & 0.2992 \end{bmatrix}$	$\begin{bmatrix} -0.9879 & 0 & 0 \\ 0 & 0.9165 & 0.2992 \\ 0 & 0.2992 & 0.0714 \end{bmatrix}$

Appendix B

Physical parameters

Table B.1: Physical parameters used in the calculations performed in this thesis.

Parameter (units)	Value	Ref.
GaAs LO phonon deformation potentials		
K_{11}	-1.4	126
K_{12}	-1.9	126
K_{44}	-0.54	126
GaAs TO phonon deformation potentials		
K_{11}	-1.9	126
K_{12}	-2.2	126
K_{44}	-0.8	126
lattice parameter		
a_{GaAs} (Å)	5.65325	278
a_{GaBi} (Å)	6.33($\pm$0.05)	2,3
GaAs elastic deformation constants		
C_{11} (GPa)	118.80	277
C_{12} (GPa)	53.70	277
C_{44} (GPa)	59.40	277
GaAs dielectric constant		
ε_{S} (low frequency)	12.9	278
ε_{∞} (high frequency)	10.88	278

Appendix C

MATLAB code for simulated nanotrack morphology

The model describing the formation of VLS-grown nanotracks in Chapter 5 simplifies the species supply problem into two parts: (i) surface diffusion and (ii) direct impingement onto a hemispherical droplet. Discussion hereon assumes the reader is familiar with the details of the model.

The MATLAB code implemented to model growth estimates the nucleation rate over A by addressing the limiting factors of species transport which define the nucleation, and thus VLS growth. The restrictions to the supply problem are dealt with separately through the development of what are called "masks". Once a mask is formed, it is hierarchically overlaid to form a master mask, or "stamp", which is added to the overall nanotrack structure before another iteration begins. Many of the inputs/variables are empirical and derived from experimental observation and scaled through a relation to the droplet radius, R. On the other hand, there are also a number of parameters available for tuning, in order to better develop a structure resembling experiment. Tunable variable parameters in the MATLAB code include the comment tag '%[VP]'. While it appears to be computationally expensive, note that to system-

atically increase R throughout the procedure, and preserve reasonable resolution, all masks are recalculated for each iteration.

(i) Surface diffusion

Surface diffusion occurs in the presence of a concentration gradient of energised mobile particles. Fick's laws of diffusion [280] are often used to describe these atomic migrations, in which atoms (or particles) will move/disperse to remove the concentration gradient. Fick's first law relates the diffusive flux J vector to the concentration n under the assumption of steady-state. The theory assumes that the surface flux points from areas of high concentration to areas of low concentration and is related to the 2D (surface) concentration gradient through

$$J = -D\nabla n, \tag{C.1}$$

where D is the diffusivity (or diffusion coefficient) and will be constant for a fixed temperature. Fick's second law predicts how the diffusion of species causes the spatial concentration to change with time, by

$$\frac{\partial n}{\partial t} = D\Delta n. \tag{C.2}$$

This equation is identical to the coordinate-dependent diffusion equations given in Chapter 5 (Eqs. 5.4 and 5.5). The analytical solution to Fick's laws yields the time-dependent concentration c of adatoms at r using

$$c(r,t) = c_0 \left[1 - \mathrm{erf}\left(\frac{r}{2\sqrt{Dt}}\right)\right], \tag{C.3}$$

where c_0 is the initial concentration at $C(r = 0, t = 0)$, $2\sqrt{Dt}$ is the diffusion length and the statistical complementary Gaussian error function is given by

$$\mathrm{erf}(r) = \frac{2}{\sqrt{\pi}} \int_0^r \exp(-t^2) dt, \tag{C.4}$$

with its derivative

$$\nabla \mathrm{erf}(r) = \frac{2\exp(-r^2)}{\sqrt{\pi}} \propto \exp(-r^2), \tag{C.5}$$

which can be used to determine Δn across the surface, and thus J through Eq. C.1. By assuming radial diffusion from an homogenous concentration of adatoms outside the droplet path/track, symmetry confines J to a wavefront parallel to either the x- or y-directions. Figure C.1(a) and (b) present plots of the masks employed to calculate the nucleation rate due to surface diffusion, in Fig. C.1(c).

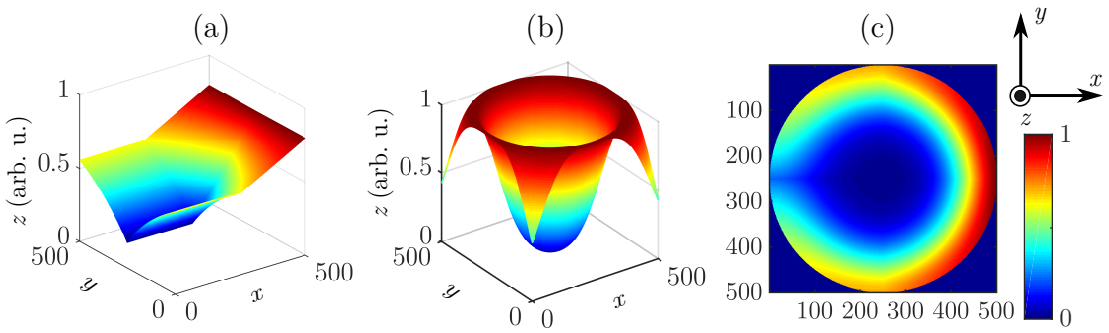

Figure C.1: (a) Surface diffusion mask with the relative supply rate defined for the droplet perimeter, at a distance $r = R$, (b) Gaussian ring function peaking at $r = R$ and (c) is a top-down look at (a) and (b) combined with a circular logic matrix of radius R, for the diffusion only contribution to the nucleation rate over A. The coordinate system in (c) is relative to the axes described in (a) and (b). For (a), (b) and (c) the x and y axes are given in pixels.

(ii) Direct impingement

To solve the direct impingement supply problem, a 3D surface mask must first be created and the local intensity of the flux intercepted by the hemispherical droplet

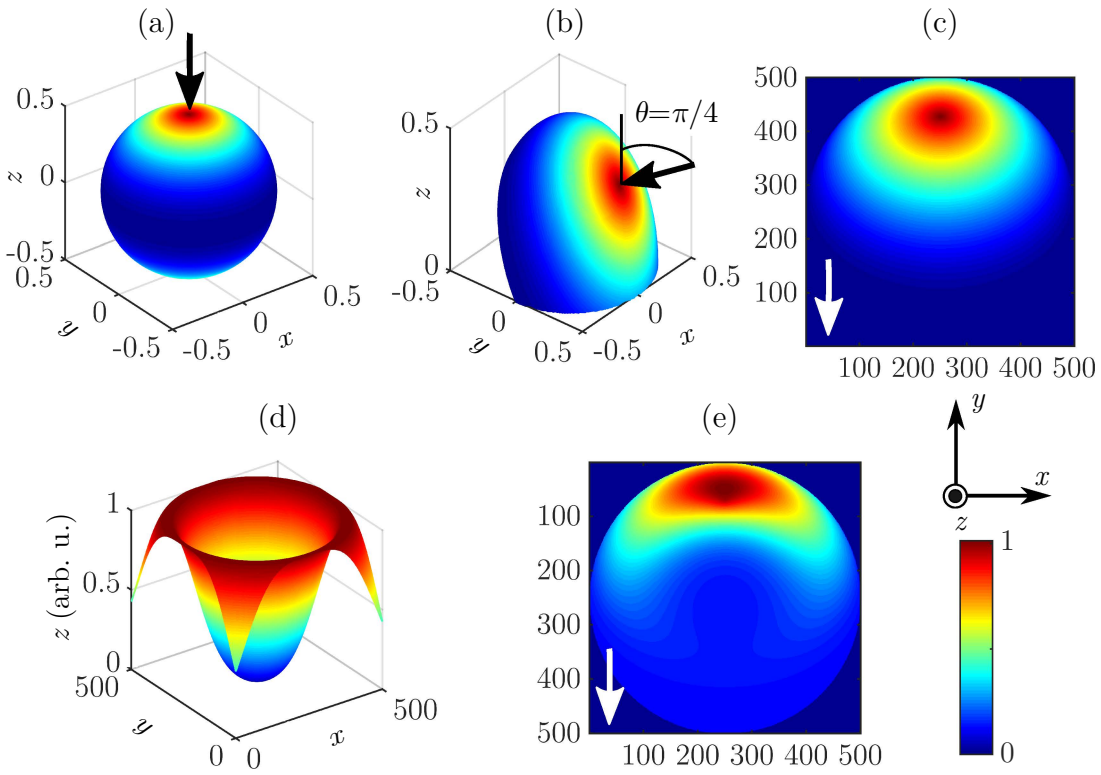

Figure C.2: (a) Surface flux interception for a downward flux incident on a sphere, (b) the hemisphere contribution rotated by $\theta = \pi/4$, and (c) flattened into 2D. (d) Shows the Gaussian function used − as well as a circular logic matrix of radius R − to modify mask (c) into that shown in (e) the impinging flux only contribution to the nucleation rate over A. Note the colour scale provided applies to all plots, while the coordinate system is only in reference to (c) and (e). The arrows here indicate the relative flux directions, while both the horizontal (x) and vertical (y) spatial axes for (c) and (e) are given in units of pixels.

(Equ. 5.8) mapped over its exposed surface. For a downward flux, with zenith (0, 0, R), the relative intensity will decay radially as

$$\frac{I_{\mathrm{HS}}(r)}{I^0_{\mathrm{HS}}} = \frac{r}{R}, \tag{C.6}$$

where I_{HS} and I^0_{HS} are respectively the flux intensity over the surface and at the zenith point.

In the molecular beam epitaxy (MBE) growth chamber, the Ga ion beam makes an angle with the sample normal of approximately $\pi/4$. Figures C.2(a) and (b) show such

a surface for a homogeneous flux beam incident along the z direction and off to $\theta = \pi/4$, respectively. Note the absence of surface values on the backside of Fig. C.2(b), which are caused by shadowing of the 'hidden' surface from the non-normal flux. Figure C.2(c) is the x-y projection of (b) and (d) is the Gaussian function used to modify (C) into the impinging-flux-only contribution to the nucleation, plotted in (e). Combining the diffusion mask (Fig. C.1(c)), direct impingement mask (Fig C.2(e)) and a baseline nucleation mask (a constant value over all of A) yields the normalised nucleation rates for the various α values given in Fig. 5.9.

Listing C.1: MATLAB code implemented to geometrically model the supply of Ga species to the nucleation interface.

```
clear all
colormap jet

%% Simulation Variables
res = 500;       % resolution [pix/um] @500, 1 iteration takes ~60s
    with 8 GB RAM
steps= 2000;     % numbers of steps/iterations used for stamping
   --> 2000 is the nominal value used
Dl = 50 ; %[VP] Scaling factor for diffusion length

R0 = 0.4;        % initial radius [um]
Rf = 0.5;         % Final radius [um]

D = 10*R0;         % total length required to produce final
   nanotrack [um]

M_size = R0*2.5*res;  % mask template sizes

d = linspace(0,D-M_size/res,steps)'; % creates a row vector of No
```

```
    .(steps) evenly spaced points for the distance traveled through
     the whole procedure
d_pix = round(d*res); %avoids pix conversion errors

I = zeros(M_size,D*res);    % Integral of the template stamps

% Angles to rotate surface about (prior to azimuthal rotation)
thx = 0;
thy = 45; %  Incident flux angle from surface normal [deg]
thz = 0;

% Mask differential constants
M_rad_min = 0;
M_rad_max = 1;

%FWHM of ringed Gaussian functions for TPB
FWHM_diff = 0.02 ; % [VP] Gaussian function FWHM for diffusion
    mask
FWHM_flux = 0.02 ; % [VP] Gaussian function FWHM for flux mask

% T mask details --> max - min will scale with velocity of droplet
M_T_min = 0.8 ;
M_T_max = M_T_min*1.1;

% Flux mask
M_F_min = 0.5;
M_F_max = 2;

C_diff = 1 ; % [VP] Scaling coefficient of diff mask
C_flux = 0.4  ; % [VP] Scaling coefficient of flux mask
C_base_flux = 0.1 ; % [VP] Base rate of nucleation
```

```
d_F = 1.1*R0;              % [um] distance from centre of droplet to
    source 2 is good

Rf_F = d_F - R0;     % [um] edge of mask from wrt flux source (
   change this to be dynamically based on R)
gam = R0*1;              % [um/cycle] wavelength of peaks - fixed to
   R0, though can be made to be dynamic
alpha0 = 0;              % initial phi
alpha = -d/gam*360 + alpha0; % [degz] Angle of incidence of source
    wrt from; azimuthal angle (cw positive)

tic %begins tic-toc time counter
% Begin the loop for changes in phi and distance etc.
for i = 1:length(alpha)
alpha(i);

%% Create preliminary masks variables
R = R0*(1-(i/steps)) + Rf*(i/steps) ;         % [um] dynamic value
   of radius of droplet

x = (-M_size/res)/2:1/res:(M_size/res)/2-1/res;
y = (-M_size/res)/2:1/res:(M_size/res)/2-1/res;

[X, Y] = ndgrid(x,y); %generate grid
X0 = 0;
Y0 = 0;
r = sqrt((X-X0).^2 + (Y-Y0).^2); % 2D vector, r

% Circle Mask - Binary
M_circ = r<=R; %Exclude any matrix values for r>R

%% (i) Surface diffusion of of species
```

```
%T Mask for diffusion at front and back
offset = 0.08*R ; % [um] empirical approximation of dynamic
    nanotrack side wall height 'h'

M_T_f_b =    ( M_T_min*(1 - (exp(-abs(X.*(Dl/res) + offset)^2)))
    .*(1 - Y/R)  + (M_T_min + abs(Y)/(R)*(M_T_max-M_T_min)).*(Y/R)
       )  .* (X>=0) .* (Y>=0) ; % front (x>=0) of droplet top (y>0)
M_T_f_t =( M_T_min*(1 - (exp(-abs(X.*(Dl/res) - offset)^2))).*(1 -
     Y/R)  + (M_T_min + abs(Y)/(R)*(M_T_max-M_T_min)).*(Y/R)     )
    .* (X<0) .* (Y>=0) ; % front (x>=0) of droplet top (y>0)
M_T_b_b = M_T_min*(1 - (exp(-(abs(X.*(Dl/res) + offset)^2)))) .* (
    X>=0) .* (Y<0) ; % back (x<0) of droplet top (y>0)
M_T_b_t = M_T_min*(1 - (exp(-(abs(X.*(Dl/res) - offset)^2)))) .* (
    X<0) .* (Y<0) ; % back (x<0) of droplet top (y>0)

M_T = (M_T_b_b + M_T_b_t) + (M_T_f_b + M_T_f_t); % front and back
    summed

figure (1) ; mesh(M_T);

%% (ii) Direct impingement of flux onto hemispherical droplet
    surface

%Map sphere
[Xs Ys Zs] = sphere((res-1)); % Generates new grid

% Scale sphere to radius
Xs = Xs.*R;
Ys = Ys.*R;
Zs = Zs.*R;
```

```
rs = sqrt((Xs-X0).^2 + (Ys-Y0).^2) ; %vector used to build sphere
    flux intercept
M_zs = 1 - rs./R ; % radial function for sphere flux intercept
    mask: I(rs)

% Plot unrotated 3D flux mask with zenith initially (0,0)
figure (2); surf(Xs, Ys, Zs, M_zs, 'EdgeColor','none'); axis
    square;

% rotate about y axis
Drot = [];
for(ix = 1:size(Xs,1))
    for(iy = 1:size(Xs,2))
        if(Zs(ix,iy) > 0 )
            P = [Xs(ix,iy) Ys(ix,iy) Zs(ix,iy)]'; % original point
                in 3d space
            P2 = transrot(P, thx, thy, thz); % rotated point to be
                queried
            if(P2(3) >= 0); % exclude the rotated surface which
               now lies below z<0
                Drot = [Drot; [P2' M_zs(ix,iy)]]; % if we are
                    happy, store the new point with the existing
                    M_zs value as a column vector [X Y Z V]
            end
        end
    end
end

figure (3); scatter3(Drot(:,1), Drot(:,2), Drot(:,3) , 10, Drot
    (:,4), 'filled') ; axis square;
figure(4); scatter(Drot(:,1), Drot(:,2), 10, Drot(:,4), 'filled');
    axis square;
```

```
% Flatten and interpolate back to XY plane and regular matrix grid
F = scatteredInterpolant(Drot(:,1), Drot(:,2), Drot(:,4),'linear',
    'none');
Df = F(X(:,:,1),Y(:,:,1)); % Revome Z component to flattened
figure(5); imagesc(Df); axis square;

Dfr = imrotate(Df,alpha(i),'crop').*1; % azimuthal rotating
Dfr(isnan(Dfr))= 0; % Set all NaN elements from underside of
   rotated sphere to 0
figure(6); imagesc(Dfr); axis square;


%% Gaussian ring masks
Rexp = abs(r)-R ;
M_g_flux = M_rad_min + exp((-Rexp.^2)/(2*FWHM_flux))*(M_rad_max-
   M_rad_min);
M_g_diff = M_rad_min + exp((-Rexp.^2)/(2*FWHM_diff))*(M_rad_max-
   M_rad_min);

%  Combined masks
M_diff = M_circ.*M_T.*M_g_diff; %compiled diffusion mask

M_flux = M_circ.*Dfr.*M_g_flux +  C_base_flux.*M_circ  ;

M_comb = C_diff.*M_diff + C_flux.*M_flux ;

I_temp = zeros(size(I));
I_temp(:,d_pix(i)+1:(d_pix(i)+M_size)) = M_comb; % temporary
   formation of stamp before added to summation

% Shift position and integrate combined mask
```

```
I  = I + I_temp;


end
toc %end time counter
```

Listing C.2: transrot – Transformation function employed to rotate an object/image in 3D space.

```
function b = transrot(p,thx,thy,thz)
%TRANSROT(p, thx, thy, thz)
% p is the point to be rotated [x y z]
% b is the newly oriented point
% thx is theta_x, the rotation about x axis, in degrees* excluded
    for speed
% thy is theta_y, the rotation about y axis, in degrees
% thz is theta_z, the rotation about z axis, in degrees

% 3D rotation tranform matrices
Rx = [  1            0            0;
        0            cosd(thx)   -sind(thx);
        0            sind(thx)    cosd(thx)];

Ry = [  cosd(thy)    0            sind(thy);
        0            1            0;
       -sind(thy)    0            cosd(thy)];

Rz = [  cosd(thz)   -sind(thz)    0;
        sind(thz)    cosd(thz)    0;
        0            0            1];

% Multiply the transformation matricies
```

```
b = (Rx*Ry*Rz*p);


end
```

References

[1] Vurgaftman, I., Meyer, J. R. & Ram-Mohan, L. R. Band parameters for III-V compound semiconductors and their alloys. *Journal of Applied Physics* **89**, 5815–5875 (2001).

[2] Tixier, S., Adamcyk, M., Tiedje, T., Francoeur, S., Mascarenhas, A., Wei, P. & Schiettekatte, F. Molecular beam epitaxy growth of $GaAs_{1-x}Bi_x$. *Applied Physics Letters* **82**, 2245–2247 (2003).

[3] Masnadi-Shirazi, M., Lewis, R. B., Bahrami-Yekta, V., Tiedje, T., Chicoine, M. & Servati, P. Bandgap and optical absorption edge of $GaAs_{1-x}Bi_x$ alloys with $0 < x < 17.8\,\%$. *Journal of Applied Physics* **116**, 223506 (2014).

[4] Lu, X., Beaton, D. A., Lewis, R. B., Tiedje, T. & Zhang, Y. Composition dependence of photoluminescence of $GaAs_{1-x}Bi_x$ alloys. *Applied Physics Letters* **95**, 041903 (2009).

[5] Yamaguchi, M., Takamoto, T., Araki, K. & Ekins-Daukes, N. Multi-junction III-V solar cells: Current status and future potential. *Solar Energy* **79**, 78–85 (2005).

[6] Dimroth, F. High-efficiency solar cells from III-V compound semiconductors. *Physica Status Solidi (c)* **3**, 373–379 (2006).

[7] Dimroth, F., Grave, M., Beutel, P., Fiedeler, U., Karcher, C., Tibbits, T. N. D., Oliva, E., Siefer, G., Schachtner, M., Wekkeli, A., Bett, A. W., Krause, R., Piccin, M., Blanc, N., Drazek, C., Guiot, E., Ghyselen, B., Salvetat, T., Tauzin, A., Signamarcheix, T., Dobrich, A., Hannappel, T. & Schwarzburg, K. Wafer bonded four-junction GaInP/GaAs//GaInAsP/GaInAs concentrator solar cells with 44.7 % efficiency. *Progress in Photovoltaics: Research and Applications* **22**, 277–282 (2014).

[8] Philipps, S. P., Dimroth, F. & Bett, A. W. *High-Efficiency III-V Multijunction Solar Cells* (Academic Press, 2012).

[9] Thomas, T., Mellor, A., Hylton, N. P., FuÌĹhrer, M., Alonso-Álvarez, D., Braun, A., Ekins-Daukes, N. J., David, J. P. R. & Sweeney, S. J. Requirements for a GaAsBi 1 eV sub-cell in a GaAs-based multi-junction solar cell. *Semiconductor Science and Technology* **30**, 094010 (2015).

[10] Harris, J. S. GaInNAs long-wavelength lasers: progress and challenges. *Semiconductor Science and Technology* **17**, 880–891 (2002).

[11] Wei, S.-H. & Zunger, A. Giant and Composition-Dependent Optical Bowing Coefficient in GaAsN Alloys. *Physical Review Letters* **76**, 664–667 (1996).

[12] Henini, M., Misiewicz, J., Kudrawiec, R. & Sek, G. *Dilute Nitride Semiconductors* (Elsevier, 2005).

[13] Mircea Guina, S. M. W. *Molecular beam epitaxy : from research to mass production* (Elsevier, 2013).

[14] Fahy, S. & O'Reilly, E. P. Intrinsic limits on electron mobility in dilute nitride semiconductors. *Applied Physics Letters* **83**, 3731–3733 (2003).

[15] Francoeur, S., Seong, M.-J., Mascarenhas, A., Tixier, S., Adamcyk, M. & Tiedje, T. Band gap of $GaAs_{1-x}Bi_x$, $0 < x < 3.6\,\%$. *Applied Physics Letters* **82**, 3874–3876 (2003).

[16] Fluegel, B., Francoeur, S., Mascarenhas, A., Tixier, S., Young, E. C. & Tiedje, T. Giant Spin-Orbit Bowing in $GaAs_{1-x}Bi_x$. *Physical Review Letters* **97**, 067205 (2006).

[17] Joukoff, B. & Jean-Louis, A. Growth of $InSb_{1-x}Bi_x$ single crystals by Czochralski method. *Journal of Crystal Growth* **12**, 169–172 (1972).

[18] Ma, K. Y., Fang, Z. M., Jaw, D. H., Cohen, R. M., Stringfellow, G. B., Kosar, W. P. & Brown, D. W. Organometallic vapor phase epitaxial growth and characterization of InAsBi and InAsSbBi. *Applied Physics Letters* **55**, 2420 (1989).

[19] Rajpalke, M. K., Linhart, W. M., Yu, K. M., Birkett, M., Alaria, J., Bomphrey, J. J., Sallis, S., Piper, L. F. J., Jones, T. S., Ashwin, M. J. & Veal, T. D. Bi-induced band gap reduction in epitaxial InSbBi alloys. *Applied Physics Letters* **105**, 212101 (2014).

[20] Oe, K., Ando, S. & Sugiyama, K. $InSb_{1-x}Bi_x$ Films Grown by Molecular Beam Epitaxy. *Japanese Journal of Applied Physics* **20**, L303–L306 (1981).

[21] Noreika, A. J. Indium antimonide-bismuth compositions grown by molecular beam epitaxy. *Journal of Applied Physics* **53**, 4932 (1982).

[22] Humphreys, T. P., Chiang, P. K., Bedair, S. M. & Parikh, N. R. Metalorganic chemical vapor deposition and characterization of the In-As-Sb-Bi material system for infrared detection. *Applied Physics Letters* **53**, 142 (1988).

[23] Oe, K. & Okamoto, H. New Semiconductor Alloy $GaAs_{1-x}Bi_x$ Grown by Metal

Organic Vapor Phase Epitaxy. *Japanese Journal of Applied Physics* **37**, L1283–L1285 (1998).

[24] Mascarenhas, A., Zhang, Y., Verley, J. & Seong, M. J. Overcoming limitations in semiconductor alloy design. *Superlattices and Microstructures* **29**, 395–404 (2001).

[25] Kunishige, O. E. & Asai, H. Proposal on a temperature-insensitive wavelength semiconductor laser. *IEICE Transactions on Electronics* **E79-C**, 1751–1758 (1996).

[26] Yoshimoto, M., Murata, S., Chayahara, A., Horino, Y., Saraie, J. & Oe, K. Metastable GaAsBi Alloy Grown by Molecular Beam Epitaxy. *Japanese Journal of Applied Physics* **42**, L1235–L1237 (2003).

[27] Vardar, G., Paleg, S. W., Warren, M. V., Kang, M., Jeon, S. & Goldman, R. S. Mechanisms of droplet formation and Bi incorporation during molecular beam epitaxy of GaAsBi. *Applied Physics Letters* **102**, 042106 (2013).

[28] Fuyuki, T., Yoshioka, R., Yoshida, K. & Yoshimoto, M. Long-wavelength emission in photo-pumped $GaAs_{1-x}Bi_x$ laser with low temperature dependence of lasing wavelength. *Applied Physics Letters* **103**, 202105 (2013).

[29] Lewis, R., Beaton, D., Lu, X. & Tiedje, T. $GaAs_{1-x}Bi_x$ Light Emitting Diodes. *Journal of Crystal Growth* **311**, 1872–1875 (2009).

[30] Mascarenhas, A. & Seong, M. J. Raman and resonant Raman studies of $GaAs_{1-x}N_x$. *Semiconductor Science and Technology* **17**, 823–829 (2002).

[31] Mintairov, A. M., Blagnov, P. A., Melehin, V. G., Faleev, N. N., Merz, J. L., Qiu, Y., Nikishin, S. A. & Temkin, H. Ordering effects in Raman spectra of coherently strained $GaAs_{1-x}N_x$. *Physical Review B* **56**, 15836–15841 (1997).

[32] Francoeur, S., Tixier, S., Young, E., Tiedje, T. & Mascarenhas, A. Bi isoelectronic impurities in GaAs. *Physical Review B* **77**, 085209 (2008).

[33] Zhang, Y., Mascarenhas, A. & Wang, L.-W. Similar and dissimilar aspects of iii-v semiconductors containing bi versus n. *Physical Review B* **71**, 155201 (2005).

[34] Usman, M., Broderick, C. A., Lindsay, A. & O'Reilly, E. P. Tight-binding analysis of the electronic structure of dilute bismide alloys of gap and gaas. *Physical Review B* **84**, 245202 (2011).

[35] Broderick, C. A., Usman, M., Sweeney, S. J. & O'Reilly, E. P. Band engineering in dilute nitride and bismide semiconductor lasers. *Semiconductor Science and Technology* **27**, 094011 (2012).

[36] Yoshida, J., Kita, T., Wada, O. & Oe, K. Temperature Dependence of $GaAs_{1-x}Bi_x$ Band Gap Studied by Photoreflectance Spectroscopy. *Japanese Journal of Applied Physics* **42**, 371–374 (2003).

[37] Ludewig, P., Knaub, N., Hossain, N., Reinhard, S., Nattermann, L., Marko, I. P., Jin, S. R., Hild, K., Chatterjee, S., Stolz, W., Sweeney, S. J. & Volz, K. Electrical injection Ga(AsBi)/(AlGa)As single quantum well laser. *Applied Physics Letters* **102**, 242115 (2013).

[38] Tominaga, Y., Oe, K. & Yoshimoto, M. Low Temperature Dependence of Oscillation Wavelength in $GaAs_{1-x}Bi_x$ Laser by Photo-Pumping. *Applied Physics Express* **3**, 62201 (2010).

[39] Yano, M., Imai, H. & Takusagawa, M. Analysis of electrical, threshold, and temperature characteristics of InGaAsP/InP double- heterojunction lasers. *IEEE Journal of Quantum Electronics* **17**, 1954–1963 (1981).

[40] Childs, G. N., Brand, S. & Abram, R. A. Intervalence band absorption in semiconductor laser materials. *Semiconductor Science and Technology* **1**, 116–120 (1986).

[41] Phillips, A., Sweeney, S., Adams, A. & Thijs, P. The temperature dependence of 1.3- and 1.5- μm compressively strained ingaas(p) mqw semiconductor lasers. *Selected Topics in Quantum Electronics, IEEE Journal of* **5**, 401–412 (1999).

[42] Sweeney, S. J. Light emitting semiconductor devices - GB patent application no. 2010/001249 (2010).

[43] Sweeney, S. J. & Jin, S. R. Bismide-nitride alloys: Promising for efficient light emitting devices in the near- and mid-infrared. *Journal of Applied Physics* **113**, 043110 (2013).

[44] Hossain, N., Marko, I. P., Jin, S. R., Hild, K., Sweeney, S. J., Lewis, R. B., Beaton, D. A. & Tiedje, T. Recombination mechanisms and band alignment of $GaAs_{1-x}Bi_x$/GaAs light emitting diodes. *Applied Physics Letters* **100**, 051105 (2012).

[45] Leonard, N. M., Wieland, L. C. & Mohan, R. S. Applications of bismuth(III) compounds in organic synthesis. *Tetrahedron* **58**, 8373–8397 (2002).

[46] Leontie, L., Caraman, M., Alexe, M. & Harnagea, C. Structural and optical characteristics of bismuth oxide thin films. *Surface Science* **507-510**, 480–485 (2002).

[47] Fan, H. T., Teng, X. M., Pan, S. S., Ye, C., Li, G. H. & Zhang, L. D. Optical properties of δ-bi_2o_3 thin films grown by reactive sputtering. *Applied Physics Letters* **87**, 231916 (2005).

[48] Liu, Z. & Yan, F. The Application of Bismuth-Based Oxides in Organic-Inorganic Hybrid Photovoltaic Devices. *Journal of the American Ceramic Society* **95**, 1944–1948 (2012).

[49] Hu, Q., Wang, J., Zhao, Y. & Li, D. A light-trapping structure based on Bi_2O_3 nano-islands with highly crystallized sputtered silicon for thin-film solar cells. *Optics Express* **19**, A20–A27 (2011).

[50] Som, T., Troppenz, G. V., Wendt, R., Wollgarten, M., Rappich, J., Emmerling, F. & Rademann, K. Graphene Oxide/α-Bi_2O_3 Composites for Visible-Light Photocatalysis, Chemical Catalysis, and Solar Energy Conversion. *ChemSusChem* **7**, 854–865 (2014).

[51] Lai, C.-F., Chang, C.-C., Wen, M.-H., Lin, C.-K. & Wu, M.-K. Enhanced efficiency in InGaN-based photovoltaic devices combined with nanocrystalline Bi_2O_3 /P3HT heterojunction structures. *Physica Status Solidi (a)* **210**, 1133–1136 (2013).

[52] Fitouri, H., Boussaha, R., Rebey, A. & El Jani, B. Oxidation of bismuth nanodroplets deposit on GaAs substrate. *Applied Physics A* **112**, 701–710 (2013).

[53] Schumb, W. C. & Rittner, E. S. Polymorphism of bismuth trioxide. *Journal of the American Chemical Society* **65**, 1055–1060 (1943).

[54] Zhukov, V. P., Zhukovskii, V. M., Zainullina, V. M. & Medvedeva, N. I. Electronic structure and chemical bonding in bismuth sesquioxide polymorphs. *Journal of Structural Chemistry* **40**, 831–837 (1999).

[55] Harwig, H. A. On the Structure of Bismuthsesquioxide: The α, β, γ, and δ-phase. *Zeitschrift für anorganische und allgemeine Chemie* **444**, 151–166 (1978).

[56] Miyayama, M., Katsuta, S., Suenaga, Y. & Yanagida, H. Electrical Conduction in β-Bi_2O_3 Doped with Sb_2O_3. *Journal of the American Ceramic Society* **66**, 585–588 (1983).

[57] Harwig, H. A. & Gerards, A. Electrical properties of the α, β, γ, and δ phases of bismuth sesquioxide. *Journal of Solid State Chemistry* **26**, 265–274 (1978).

[58] Medernach, J. W. & Snyder, R. L. Powder diffraction patterns and structures of the bismuth oxides. *Journal of the American Ceramic Society* **61**, 494–497 (1978).

[59] Jiang, H.-Y., Li, P., Liu, G., Ye, J. & Lin, J. Synthesis and photocatalytic properties of metastable β- Bi_2O_3 stabilized by surface-coordination effects. *Journal of Materials Chemistry A* **3**, 5119–5125 (2015).

[60] Deng, H.-Y., Hao, W.-C. & Xu, H.-Z. A Transition Phase in the Transformation from α-, β- and ϵ- to δ-Bismuth Oxide. *Chinese Physics Letters* **28**, 056101 (2011).

[61] Tran, T. B. & Navrotsky, A. Energetics of disordered and ordered rare earth oxide-stabilized bismuth oxide ionic conductors. *Physical chemistry chemical physics* **16**, 2331–7 (2014).

[62] Wang, Y., Wen, Y., Ding, H. & Shan, Y. Improved structural stability of titanium-doped β-Bi_2O_3 during visible-light-activated photocatalytic processes. *Journal of Materials Science* **45**, 1385–1392 (2010).

[63] Schlesinger, M., Schulze, S., Hietschold, M. & Mehring, M. Metastable β-Bi_2O_3 nanoparticles with high photocatalytic activity from polynuclear bismuth oxido clusters (2013).

[64] Zyryanov, V. V. Mechanochemical synthesis of complex oxides. *Russian Chemical Reviews* **77**, 105–135 (2008).

[65] Zyryanov, V. V. & Uvarov, N. F. Mechanochemical Synthesis and Electrical Conductivity of $Bi_{1.6}M_{0.4}O_{3-x}$ (M = Ca, $Ca_{0.5}Sr_{0.5}$, In, Y, La) Metastable Fluorite Solid Solutions. *Inorganic Materials* **40**, 729–734 (2004).

[66] Guenther, G. & Guillon, O. Solid state transitions of Bi_2O_3 nanoparticles. *Journal of Materials Research* **29**, 1383–1392 (2014).

[67] Steele, J. A. & Lewis, R. A. In situ micro-Raman studies of laser-induced bismuth oxidation reveals metastability of β-Bi_2O_3 microislands. *Optical Materials Express* **4**, 2133 (2014).

[68] Lewis, R. B., Masnadi-Shirazi, M. & Tiedje, T. Growth of high Bi concentration $GaAs_{1-x}Bi_x$ by molecular beam epitaxy. *Applied Physics Letters* **101**, 82112 (2012).

[69] Ciatto, G., Thomasset, M., Glas, F., Lu, X. & Tiedje, T. Formation and vanishing of short range ordering in $GaAs_{1-x}Bi_x$ thin films. *Physical Review B* **82**, 201304 (2010).

[70] Ciatto, G., Young, E. C., Glas, F., Chen, J., Mori, R. A. & Tiedje, T. Spatial correlation between Bi atoms in dilute $GaAs_{1-x}Bi_x$: From random distribution to Bi pairing and clustering. *Physical Review B* **78**, 1–5 (2008).

[71] Sales, D. L., Guerrero, E., Rodrigo, J. F., Galindo, P. L., Yáñez, A., Shafi, M., Khatab, A., Mari, R. H., Henini, M., Novikov, S., Chisholm, M. F. & Molina, S. I. Distribution of bismuth atoms in epitaxial GaAsBi. *Applied Physics Letters* **98**, 101902 (2011).

[72] Lu, X., Beaton, D. A., Lewis, R. B., Tiedje, T. & Whitwick, M. B. Effect of molecular beam epitaxy growth conditions on the Bi content of $GaAs_{1-x}Bi_x$. *Applied Physics Letters* **92**, 192110 (2008).

[73] Moussa, I., Fitouri, H., Rebey, A. & El Jani, B. Atmospheric-pressure metalorganic vapour phase epitaxy optimization of GaAsBi alloy. *Thin Solid Films* **516**, 8372–8376 (2008).

[74] Ptak, A., France, R., Beaton, D., Alberi, K., Simon, J., Mascarenhas, A. & Jiang, C.-S. Kinetically limited growth of GaAsBi by molecular-beam epitaxy. *Journal of Crystal Growth* **338**, 107–110 (2012).

[75] Wagner, R. S. & Ellis, W. C. Vapor-Liquid-Soild mechanism of single crystal growth. *Applied Physics Letters* **4**, 89–90 (1964).

[76] Mamutin, V. V. Growth of A^3N whiskers and plate-shaped crystals by molecular-beam epitaxy with the participation of the liquid phase. *Technical Physics Letters* **25**, 741–744 (1999).

[77] Dejarld, M., Nothern, D. & Millunchick, J. M. Droplet destabilization during Bi catalyzed vapor-liquuid-solid growth of GaAs. *Journal of Applied Physics* **115**, 114307 (2014).

[78] Essouda, Y., Fitouri, H., Boussaha, R., Elayech, N., Rebey, A. & Jani, B. E. Bismuth catalyzed growth of GaAsBi nanowires by metalorganic vapor phase epitaxy. *Materials Letters* **152**, 298–301 (2015).

[79] Henini, M., Ibáñez, J., Schmidbauer, M., Shafi, M., Novikov, S. V., Turyanska, L., Molina, S. I., Sales, D. L., Chisholm, M. F. & Misiewicz, J. Molecular beam epitaxy of GaBiAs on (311)B GaAs substrates. *Applied Physics Letters* **91**, 251909 (2007).

[80] Cardona, M. (ed.) *Light Scattering in Solids I* (Springer Berlin Heidelberg, 1983), topics in edn.

[81] Yu, P. Y. & Cardona, M. *Fundamentals of Semiconductors*, vol. 1 (2010).

[82] Aspnes, D. E. & Studna, A. A. Dielectric functions and optical parameters of Si, Ge, GaP, GaAs, GaSb, InP, InAs, and InSb from 1.5 to 6.0 eV. *Physical Review B* **27**, 985–1009 (1983).

[83] Alberi, K., Dubon, O. D., Walukiewicz, W., Yu, K. M., Bertulis, K. & Krotkus, A. Valence band anticrossing in $GaAs_{1-x}Bi_x$. *Applied Physics Letters* **91**, 051909 (2007).

[84] Iliopoulos, E., Adikimenakis, A., Giesen, C., Heuken, M. & Georgakilas, A. Energy bandgap bowing of InAlN alloys studied by spectroscopic ellipsometry. *Applied Physics Letters* **92**, 191907 (2008).

[85] Vegard, L. Die Konstitution der Mischkristalle und die Raumfüllung der Atome. *Zeitschrift für Physik* **5**, 17–26 (1921).

[86] Rachinger, W. A. A Correction for the 1 2 Doublet in the Measurement of Widths of X-ray Diffraction Lines. *Journal of Scientific Instruments* **25**, 254–255 (1948).

[87] Ravash, R., Blaesing, J., Dadgar, A. & Krost, A. Semipolar single component GaN on planar high index Si(11h) substrates. *Applied Physics Letters* **97**, 10–13 (2010).

[88] Schmidbauer, M., Seydmohamadi, S., Grigoriev, D., Wang, Z. M., Mazur, Y. I., Schäfer, P., Hanke, M., Köhler, R. & Salamo, G. J. Controlling planar and vertical ordering in three-dimensional (In,Ga)As quantum dot lattices by GaAs surface orientation. *Physical Review Letters* **96** (2006).

[89] Liang, B. L., Wang, Z. M., Mazur, Y. I., Strelchuck, V. V., Holmes, K., Lee, J. H. & Salamo, G. J. Ingaas quantum dots grown on b-type high index gaas substrates: surface morphologies and optical properties. *Nanotechnology* **17**, 2736–2740 (2006).

[90] Beneking, H., Narozny, P. & Emeis, N. High quality epitaxial GaAs and InP wafers by isoelectronic doping. *Applied Physics Letters* **47**, 828–830 (1985).

[91] Steele, J. A., Lewis, R. A., Henini, M., Lemine, O. M. & Alkaoud, A. Raman scattering studies of strain effects in (100) and (311)B $GaAs_{1-x}Bi_x$ epitaxial layers. *Journal of Applied Physics* **114**, 193516 (2013).

[92] A., P., Levin, A., Polimeni, A., Schindler, F., Main, P. C., Eaves, L. & Henini, M. Piezoelectric effects in $In_{0.5}Ga_{0.5}As$ self-assembled quantum dots grown on (311)B GaAs substrates. *Applied Physics Letters* **77**, 2979 (2000).

[93] Turrell, G. & Corset, J. *Raman Microscopy: Developments and Applications* (Academic Press, 1996).

[94] Damen, T. C., Porto, S. P. S. & Tell, B. Raman Effect in Zinc Oxide. *Physical Review* **142**, 570–574 (1966).

[95] Hayes, W. & Loudon, R. *Scattering of Light by Crystals* (Courier Corporation, 2012).

[96] Mizoguchi, K. & Nakashima, S. Determination of crystallographic orientations in silicon films by Raman-microprobe polarization measurements. *Journal of Applied Physics* **65**, 2583–2590 (1989).

[97] Bulkin, J. G. & Grasselli, B. J. (eds.) *Analytical Raman Spectroscopy* (John Wiley, New York, 1991).

[98] Puech, P., Landa, G., Carles, R., Pizani, P. S., Daran, E. & Fontaine, C. Strain relaxation in [001]- and [111]-GaAs/CaF2 analyzed by Raman spectroscopy. *Journal of Applied Physics* **77**, 1126 (1995).

[99] O. Rodrigues. Des lois géometriques qui regissent les déplacements d' un systéme solide dans l' espace, et de la variation des coordonnées provenant de ces déplacement considérées indépendent des causes qui peuvent les produire. *Journal de Mathématiques Pures et Appliquées* **8**, 380–440 (1840).

[100] Chine, Z., Fitouri, H., Zaied, I., Rebey, A. & El Jani, B. Growth of GaAsBi alloy under alternated bismuth flows by metalorganic vapor phase epitaxy. *Journal of Crystal Growth* **330**, 35–38 (2011).

[101] Achour, H., Louhibi, S., Amrani, B., Tebboune, A. & Sekkal, N. Structural and electronic properties of GaAsBi. *Superlattices and Microstructures* **44**, 223–229 (2008).

[102] Belabbes, A., Zaoui, A. & Ferhat, M. Lattice dynamics study of bismuth III-V compounds. *Journal of Physics: Condensed Matter* **20**, 415221 (2008).

[103] Jacobsen, H., Puchala, B., Kuech, T. F. & Morgan, D. Ab initio study of the strain dependent thermodynamics of Bi doping in GaAs. *Physical Review B* **86**, 085207 (2012).

[104] Mohmad, A. R., Bastiman, F., Hunter, C. J., Ng, J. S., Sweeney, S. J. & David, J. P. R. The effect of Bi composition to the optical quality of $GaAs_{1-x}Bi_x$. *Applied Physics Letters* **99**, 042107 (2011).

[105] Petritz, R. L. & Scanlon, W. W. Mobility of electrons and holes in the polar crystal, PbS. *Physical Review* **97**, 1620–1626 (1955).

[106] Seong, M. J., Mascarenhas, A. & Geisz, J. F. Γ-L-X mixed symmetry of nitrogen-induced states in $GaAs_{1-x}N_x$ probed by resonant Raman scattering. *Applied Physics Letters* **79**, 1297 (2001).

[107] Verma, P., Oe, K., Yamada, M., Harima, H., Herms, M. & Irmer, G. Raman studies on $GaAs_{1-x}Bi_x$ and $InAs_{1-x}Bi_x$. *Journal of Applied Physics* **89**, 1657–1663 (2001).

[108] Seong, M. J., Francoeur, S., Yoon, S., Mascarenhas, A., Tixier, S., Adamcyk, M. & Tiedje, T. Bi-induced vibrational modes in GaAsBi. *Superlattices and Microstructures* **37**, 394–400 (2005).

[109] Nargelas, S., Jarašiūnas, K., Bertulis, K. & Pačebutas, V. Hole diffusivity in GaAsBi alloys measured by a picosecond transient grating technique. *Applied Physics Letters* **98**, 082115 (2011).

[110] Pettinari, G., Engelkamp, H., Christianen, P. C. M., Maan, J. C., Polimeni, A., Capizzi, M., Lu, X. & Tiedje, T. Compositional evolution of Bi-induced acceptor states in $GaAs_{1-x}Bi_x$ alloy. *Physical Review B* **83**, 201201 (2011).

[111] Pettinari, G., Patane, A., A., P., Polimeni, A., Capizzi, M., Lu, X. & Tiedje, T. Bi-induced p-type conductivity in nominally undoped Ga(AsBi). *Applied Physics Letters* **092109**, 092109 (2012).

[112] Pettinari, G., Patané, A., Polimeni, A., Capizzi, M., Lu, X. & Tiedje, T. Effects of hydrogen on the electronic properties of Ga(AsBi) alloys. *Applied Physics Letters* **101**, 222103 (2012).

[113] Irmer, G., Wenzel, M. & Monecke, J. Light scattering by a multicomponent plasma coupled with longitudinal-optical phonons: Raman spectra of p-type GaAs:Zn. *Physical Review B* **56**, 9524–9538 (1997).

[114] Waugh, J. L. T. & Dolling, G. Crystal Dynamics of Gallium Arsenide. *Physical Review* **132**, 2410–2412 (1963).

[115] Pizani, P. S., Lanciotti, F., Jasinevicius, R. G., Duduch, J. G. & Porto, A. J. V. Raman characterization of structural disorder and residual strains in micromachined GaAs. *Journal of Applied Physics* **87**, 1280 (2000).

[116] Armelles, G., Sanjuán, M. J., González, L. & González, Y. Strain and phonon shifts in $GaAs_{1-x}P_x$ alloys. *Applied Physics Letters* **68**, 1805 (1996).

[117] Proietti, M., Martelli, F., Turchini, S., Alagna, L., Bruni, M., Prosperi, T., Simeone, M. & Garcia, J. Microscopic investigation of the strain distribution in InGaAs/GaAs quantum well structures grown by molecular beam epitaxy. *Journal of Crystal Growth* **127**, 592–595 (1993).

[118] Fitouri, H., Essouda, Y., Zaied, I., Rebey, A. & El Jani, B. Photoreflectance and photoluminescence study of localization effects in GaAsBi alloys. *Optical Materials* **42**, 67–71 (2015).

[119] Venkateswaran, U. D., Cui, L. J., Weinstein, B. A. & Chambers, F. A. Forward and reverse high-pressure transitions in bulklike AlAs and GaAs epilayers. *Physical Review B* **45**, 9237–9247 (1992).

[120] Jusserand, B. & Sapriel, J. Raman investigation of anharmonicity and disorder-induced effects in $Ga_{1-x}Al_xAs$ epitaxial layers. *Physical Review B* **24**, 7194–7205 (1981).

[121] Joshya, R. S., Ptak, A. J., France, R., Mascarenhas, A. & Kini, R. N. Resonant state due to Bi in the dilute bismide alloy $GaAs_{1-x}Bi_x$. *Physical Review B* **90**, 165203 (2014).

[122] Fukasawa, R. & Perkowitz, S. Raman-scattering spectra of coupled LO-phonon-hole-plasmon modes in p-type GaAs. *Physical Review B* **50**, 14119–14124 (1994).

[123] Wan, K. & Young, J. F. Interaction of longitudinal-optic phonons with free holes as evidenced in Raman spectra from Be-doped p -type GaAs. *Physical Review B* **41**, 10772–10779 (1990).

[124] Fukasawa, R., Katayama, S., Hasegaw, A. & Ohta, K. Analysis of Raman Spectra from Heavily Doped p-GaAs. *Journal of the Physical Society of Japan* **57**, 3632–3640 (1988).

[125] Mlayah, A., Carles, R., Landa, G., Bedel, E. & Muñoz-Yagüe, A. Raman study of longitudinal optical phonon-plasmon coupling and disorder effects in heavily Be-doped GaAs. *Journal of Applied Physics* **69**, 4064 (1991).

[126] Cerdeira, F., Buchenauer, C. J., Pollak, F. H. & Cardona, M. Stress-induced shifts of first-order Raman frequencies of diamond- and zinc-blende-type semiconductors. *Physical Review B* **5**, 580–593 (1972).

[127] Wickboldt, P., Anastassakis, E., Sauer, R. & Cardona, M. Raman phonon piezospectroscopy in GaAs: Infrared measurements. *Physical Review B* **35**, 1362–1368 (1987).

[128] Bartels, W. J. Characterization of thin layers on perfect crystals with a multipurpose high resolution x-ray diffractometer. *Journal of Vacuum Science & Technology B* **1**, 338–345 (1983).

[129] Ibáñez, J., Kudrawiec, R., Misiewicz, J., Schmidbauer, M., Henini, M. & Hopkinson, M. Nitrogen incorporation into strained (In, Ga) (As, N) thin films grown on (100), (511), (411), (311), and (111) GaAs substrates studied by photoreflectance

spectroscopy and high-resolution x-ray diffraction. *Journal of Applied Physics* **100**, 093522 (2006).

[130] O'Hagan, S. & Missous, M. The effect of substrate orientation on the properties of low temperature molecular beam epitaxial GaAs. *Journal of Applied Physics* **82**, 2400 (1997).

[131] Daeubler, J., Glunk, M., Schoch, W., Limmer, W. & Sauer, R. Lattice parameter and hole density of (Ga,Mn)As on GaAs(311)A. *Applied Physics Letters* **88**, 051904 (2006).

[132] Ganesan, S., Maradudin, A. & Oitmaa, J. A lattice theory of morphic effects in crystals of the diamond structure. *Annals of Physics* **56**, 556–594 (1970).

[133] Anastassakis, E. Selection rules of Raman scattering by optical phonons in strained cubic crystals. *Journal of Applied Physics* **82**, 1582–1591 (1997).

[134] Puech, P. *Analyse par spectrométrie Raman des déformations dans les structures d'arséniure de gallium orientées [hhl].* Ph.D. thesis (1996).

[135] Loudon, R. Polaritons, Raman Scattering, Electro-Optic Effect and Parametric Amplification. In *International Conference on Light Scattering Spectra in Solids*, 25–41 (George B. Wright, 1969).

[136] Puech, P., Landa, G., Carles, R., Pizani, P. S., Daran, E. & Fontaine, C. Raman scattering study of [hhk]-GaAs/(Si or CaF2) strained heterostructures. *Journal of Applied Physics* **76**, 2773 (1994).

[137] Inoki, C. K., Lemos, V., Cerdeira, F. & Vásquez-López, C. Strain determination in $In_xGa_{1-x}As$/GaAs strained-layer superlattices by photomodulated reflectance. *Journal of Applied Physics* **73**, 3266 (1993).

[138] Chang, I. & Mitra, S. Long wavelength optical phonons in mixed crystals. *Advances in Physics* **20**, 359–404 (2006).

[139] Prokofyeva, T., Sauncy, T., Seon, M., Holtz, M., Qiu, Y., Nikishin, S. & Temkin, H. Raman studies of nitrogen incorporation in $GaAs_{1-x}N_x$. *Applied Physics Letters* **73**, 1409–1411 (1998).

[140] Ibáñez, J., Alarcón-Lladó, E., Cuscó, R. & Artús, M., L ans Hopkinson. Optical phonon behavior in strain-free dilute Ga(As,N) studied by Raman scattering. *Journal of Applied Physics* **102**, 013502 (2007).

[141] Lucovsky, G., Martin, R. M. & Burstein, E. Localized Effective Charges in Diatomic Crystals. *Physical Review B* **4**, 1367–1374 (1971).

[142] Ben Sedrine, N., Moussa, I., Fitouri, H., Rebey, A., El Jani, B. & Chtourou, R. Spectroscopic ellipsometry study of $GaAs_{1-x}Bi_x$ material grown on GaAs substrate by atmospheric pressure metal-organic vapor-phase epitaxy. *Applied Physics Letters* **95**, 011910 (2009).

[143] Mbarki, M. & Rebey, A. First-principles calculation of the physical properties of $GaAs_{1-x}Bi_x$ alloys. *Semiconductor Science and Technology* **26**, 105020 (2011).

[144] Li, X. Amphoteric doping of Si in InAlAs/InGaAs/InP(311)A heterostructures grown by molecular-beam epitaxy. *Journal of Vacuum Science & Technology B* **11**, 912 (1993).

[145] Richter, H., Wang, Z. & Ley, L. The one phonon Raman spectrum in microcrystalline silicon. *Solid State Communications* **39**, 625–629 (1981).

[146] Tiong, K. K., Amirtharaj, P. M., Pollak, F. H. & Aspnes, D. E. Effects of As+ ion implantation on the Raman spectra of GaAs: "Spatial correlation" interpretation. *Applied Physics Letters* **44**, 122 (1984).

[147] Yuasa, T., Naritsuka, S., Mannoh, M., Shinozaki, K., Yamanaka, K., Nomura, Y., Mihara, M. & Ishii, M. Raman scattering from coupled plasmon-LO-phonon modes in n-type $Al_xGa_{1-x}As$. *Physical Review B* **33**, 1222–1232 (1986).

[148] Dubois, L. H., Zegarski, B. R. & Persson, B. N. J. Electron-energy-loss study of the space-charge region at semiconductor surfaces. *Physical Review B* **35**, 9128–9134 (1987).

[149] Pinczuk, A. Raman scattering studies of surface space charge layers and Schottky barrier formation in InP. *Journal of Vacuum Science and Technology* **16**, 1168 (1979).

[150] Murase, K., Katayama, S., Ando, Y. & Kawamura, H. Observation of a Coupled Phonon-Damped-Plasmon Mode in n -GaAs by Raman Scattering. *Physical Review Letters* **33**, 1481–1484 (1974).

[151] Seong, M. J., Chun, S. H., Cheong, H. M., Samarth, N. & Mascarenhas, A. Spectroscopic determination of hole density in the ferromagnetic semiconductor $Ga_{1-x}Mn_xAs$. *Physical Review B* **66**, 033202 (2002).

[152] Yoon, I. T. & Kang, T. W. Analysis of Raman scattering of $GaAs_{1-x}Mn_x$ dilute magnetic semiconductor. *Journal of Magnetism and Magnetic Materials* **321**, 2257–2259 (2009).

[153] Steele, J. A., Lewis, R. A., Henini, M., Lemine, O. M., Fan, D., Mazur, Y. I., Dorogan, V. G., Grant, P. C., Yu, S. Q. & Salamo, G. J. Raman scattering reveals strong LO-phonon-hole-plasmon coupling in nominally undoped GaAsBi: optical determination of carrier concentration. *Optics Express* **22**, 11680–11689 (2014).

[154] Li, J., Forghani, K., Guan, Y., Jiao, W., Kong, W., Collar, K., Kim, T.-H., Kuech, T. F. & Brown, A. S. $GaAs_{1-y}Bi_y$ Raman signatures: illuminating relationships between the electrical and optical properties of $GaAs_{1-y}Bi_y$ and Bi incorporation. *AIP Advances* **5**, 067103 (2015).

[155] Kreitman, M. M. & Barnett, D. L. Probability Tables for Clusters of Foreign Atoms in Simple Lattices Assuming Next-Nearest-Neighbor Interactions. *The Journal of Chemical Physics* **43**, 364 (1965).

[156] Yang, P., Yan, R. & Fardy, M. Semiconductor Nanowire: What's Next? *Nano Lett.* **10**, 1529–1536 (2010).

[157] Dasgupta, N. P., Sun, J., Liu, C., Brittman, S., Andrews, S. C., Lim, J., Gao, H., Yan, R. & Yang, P. 25th anniversary article: Semiconductor nanowires - Synthesis, characterization, and applications. *Advanced Materials* **26**, 2137–2183 (2014).

[158] Hurle, D. *Handbook of crystal growth*, vol. 1 (Elsevier, Boston, 1993).

[159] Oe, K. Characteristics of Semiconductor Alloy $GaAs_{1-x}Bi_x$. *Japanese Journal of Applied Physics* **41**, 2801–2806 (2002).

[160] Ferhat, M. & Zaoui, A. Structural and electronic properties of III-V bismuth compounds. *Physical Review B* **73**, 115107 (2006).

[161] Ding, L., Lu, P., Cao, H., Cai, N., Yu, Z., Gao, T. & Wang, S. Bismuth alloying properties in GaAs nanowires. *Journal of Solid State Chemistry* **205**, 44–48 (2013).

[162] Li, J., Forghani, K., Collar, K., Kuech, T. F., Brown, A. S., Jiao, W. & Kong, W. Growth of $GaAs_{1-x}Bi_x$ by molecular beam epitaxy: Trade-offs in optical and structural characteristics. *Journal of Applied Physics* **116**, 043524 (2014).

[163] Hayashi2, I. (Oxford).

[164] Lu, Z., Zhang, Z., Chen, P., Shi, S., Yao, L., Zhou, C., Zhou, X., Zou, J. & Lu, W. Bismuth-induced phase control of GaAs nanowires grown by molecular beam epitaxy. *Applied Physics Letters* **105**, 162102 (2014).

[165] Lee, S. K. C., Yu, Y., Perez, O., Puscas, S., Kosel, T. H. & Kuno, M. Bismuth-Assisted CdSe and CdTe Nanowire Growth on Plastics. *Chemistry of Materials* **22**, 77–84 (2010).

[166] Volobuev, V., Stetsenko, A., Mateychenko, P., Zubarev, E., Samburskaya, T., Dziawa, P., Reszka, A., Story, T. & Sipatov, A. Bi catalyzed VLS growth of PbTe (001) nanowires. *Journal of Crystal Growth* **318**, 1105–1108 (2011).

[167] Yella, A., Mugnaioli, E., Panthöfer, M., Therese, H. A., Kolb, U. & Tremel, W. Bismuth-catalyzed growth of SnS_2 nanotubes and their stability. *Angewandte Chemie - International Edition* **48**, 6426–6430 (2009).

[168] Yu, L., Fortuna, F., O'Donnell, B., Jeon, T., Foldyna, M., Picardi, G., Roca I Cabarrocas, P., O'Donnell, B., Jeon, T., Foldyna, M., Picardi, G. & i Cabarrocas, P. R. Bismuth-catalyzed and doped silicon nanowires for one-pump-down fabrication of radial junction solar cells. *Nano Letters* **12**, 4153–4158 (2012).

[169] Perea, D. E., Allen, J. E., May, S. J., Wessels, B. W., Seidman, D. N. & Lauhon, L. J. Three-dimensional nanoscale composition mapping of semiconductor nanowires. *Nano letters* **6**, 181–5 (2006).

[170] Bar-Sadan, M., Barthel, J., Shtrikman, H. & Houben, L. Direct imaging of single Au atoms within GaAs nanowires. *Nano letters* **12**, 2352–2356 (2012).

[171] Kuykendall, T., Ulrich, P., Aloni, S. & Yang, P. Complete composition tunability

of InGaN nanowires using a combinatorial approach. *Nature Materials* **6**, 951–956 (2007).

[172] Fanfair, D. D. & Korgel, B. A. Bismuth nanocrystal-seeded III-V semiconductor nanowire synthesis. *Crystal Growth and Design* **5**, 1971–1976 (2005).

[173] Sterzer, E., Knaub, N., Ludewig, P., Straubinger, R., Beyer, A., Stolz, W. & Volz, K. Microscopical investigation of metallic droplets on Ga(AsBi)/GaAs. *Journal of Crystal Growth* **408**, 71–77 (2014).

[174] Fitouri, H., Moussa, I., Rebey, A., Fouzri, A. & El Jani, B. AP-MOVPE of thin $GaAs_{1-x}Bi_x$ alloys. *Journal of Crystal Growth* **295**, 114–118 (2006).

[175] Forghani, K., Guan, Y., Losurdo, M., Luo, G., Morgan, D., Babcock, S. E., Brown, A. S., Mawst, L. J. & Kuech, T. F. $GaAs_{1-y-z}P_yBi_z$, an alternative reduced band gap alloy system lattice-matched to GaAs. *Applied Physics Letters* **105**, 111101 (2014).

[176] Rajpalke, M. K., Linhart, W. M., Yu, K. M., Jones, T. S., Ashwin, M. J. & Veal, T. D. Bi flux-dependent MBE growth of GaSbBi alloys. *Journal of Crystal Growth* **425**, 241–244 (2015).

[177] Wang, H., Zepeda-Ruiz, L. A., Gilmer, G. H. & Upmanyu, M. Atomistics of vapour-liquid-solid nanowire growth. *Nature communications* **4**, 1956 (2013). 1305.0038.

[178] Wen, C. Y., Tersoff, J., Hillerich, K., Reuter, M. C., Park, J. H., Kodambaka, S., Stach, E. A. & Ross, F. M. Periodically changing morphology of the growth interface in Si, Ge, and GaP nanowires. *Physical Review Letters* **107**, 25503 (2011).

[179] Schwarz, K. W. & Tersoff, J. Multiplicity of steady modes of nanowire growth. *Nano Letters* **12**, 1329–1332 (2012).

[180] Wang, H., Wang, J.-T., Cao, Z.-X., Zhang, W.-J., Lee, C.-S., Lee, S.-T. & Zhang, X.-H. A Surface Curvature Oscillation Model for Vapour-Liquid-Solid Growth of Periodic One-Dimensional Nanostructures. *Nature Commun.* **6**, 6412 (2014).

[181] Oliveira, D. S., Tizei, L. H. G., Ugarte, D. & Cotta, M. A. Spontaneous Periodic Diameter Oscillations in InP Nanowires: The Role of Interface Instabilities. *Nano Letters* **13**, 9–13 (2013).

[182] Tian, B., Xie, P., Kempa, T. J., Bell, D. C. & Lieber, C. M. Single-crystalline kinked semiconductor nanowire superstructures. *Nature Nanotechnology* **4**, 824–829 (2009).

[183] Schwarz, K. W., Tersoff, J., Kodambaka, S. & Ross, F. M. Jumping-catalyst dynamics in nanowire growth. *Physical Review Letters* **113**, 55501 (2014).

[184] Dowdy, R. S., Zhang, C., Mohseni, P. K., Fortuna, S. A., Wen, J.-G., Coleman, J. J. & Li, X. Perturbation of Au-assisted planar GaAs nanowire growth by p-type dopant impurities. *Optical Materials Express* **3**, 1687 (2013).

[185] Ma, D. D. D., Lee, C. S., Au, F. C. K., Tong, S. Y. & Lee, S. T. Small-diameter silicon nanowire surfaces. *Science* **299**, 1874–1877 (2003).

[186] Sorokin, P. B., Avramov, P. V., Chernozatonskii, L. A., Fedorov, D. G. & Ovchinnikov, S. G. Atypical quantum confinement effect in silicon nanowires. *The journal of physical chemistry. A* **112**, 9955–9964 (2008).

[187] Kowalczyk, P. J., Mahapatra, O., Brown, S. A., Bian, G., Wang, X. & Chiang, T. C. Electronic size effects in three-dimensional nanostructures. *Nano Letters* **13**, 43–47 (2013).

[188] Brönstrup, G., Jahr, N., Leiterer, C., Csáki, A., Fritzsche, W. & Christiansen, S. Optical Properties of Individual Silicon Nanowires for Photonic Devices. *ACS Nano* **4**, 7113–7122 (2010).

[189] Zi, Y., Jung, K., Zakharov, D. & Yang, C. Understanding self-aligned planar growth of InAs nanowires. *Nano Letters* **13**, 2786–2791 (2013).

[190] Cao, Y. Y. & Yang, G. W. Vertical or horizontal: Understanding nanowire orientation and growth from substrates. *Journal of Physical Chemistry C* **116**, 6233–6238 (2012).

[191] Breuer, S., Hilse, M., Trampert, A., Geelhaar, L. & Riechert, H. Vapor-liquid-solid nucleation of GaAs on Si(111): Growth evolution from traces to nanowires. *Physical Review B* **82**, 075406 (2010).

[192] Zhang, G., Tateno, K., Gotoh, H. & Nakano, H. Parallel-Aligned GaAs Nanowires With <110> Orientation Laterally Grown on [311]B Substrates Via the Gold-Catalyzed Vapor-Liquid-Solid Mode. *Nanotechnology* **21**, 95607 (2010).

[193] Sun, W., Guo, Y., Xu, H., Gao, Q., Hoe Tan, H., Jagadish, C. & Zou, J. Polarity driven simultaneous growth of free-standing and lateral GaAsP epitaxial nanowires on GaAs (001) substrate. *Applied Physics Letters* **103**, 223104 (2013).

[194] Zhang, C., Miao, X., Mohseni, P. K., Choi, W. & Li, X. Site-Controlled VLS Growth of Planar Nanowires: Yield and Mechanism. *Nano letters* **14**, 6836–6841 (2014).

[195] Fortuna, S. A., Wen, J., Chun, I. S. & Li, X. Planar GaAs nanowires on GaAs (100) Substrates: Self-aligned, nearly twin-defect free, and transfer-printable. *Nano Letters* **8**, 4421–4427 (2008).

[196] Wacaser, B. A., Dick, K. A., Johansson, J., Borgström, M. T., Deppert, K. & Samuelson, L. Preferential interface nucleation: An expansion of the VLS growth mechanism for nanowires. *Advanced Materials* **21**, 153–165 (2009).

[197] Braun, W., Kaganer, V. M., Trampert, A., Schönherr, H. P., Gong, Q., Nötzel, R., Däweritz, L. & Ploog, K. H. Diffusion and incorporation: Shape evolution during overgrowth on structured substrates. *Journal of Crystal Growth* **227-228**, 51–55 (2001).

[198] Dowdy, R. A. S., Walko, D. A. & Li, X. Relationship Between Planar GaAs Nanowire Growth Direction and Substrate Orientation. *Nanotechnolgy* **24**, 35304 (2013).

[199] Drouin, D., Couture, A. R., Joly, D., Tastet, X., Aimez, V. & Gauvin, R. CASINO V2.42 - A fast and easy-to-use modeling tool for scanning electron microscopy and microanalysis users. *Scanning* **29**, 92–101 (2007).

[200] Goldstein, J., Newbury, D., Joy, D., Lyman, C., Echlm, P., Lifshin, E., Sawyer, L. & Micheal, J. *Scanning Electron Microscopy and X-ray Microanalysis - Third Edition* (Springer US, 2003).

[201] Wu, J., Wang, Z. M., Li, A. Z., Salamo, G. J., Li, S. & Salamo, G. J. Surface Mediated Control of Droplet Density and Morphology on GaAs and AlAs Surfaces. *Physica Status Solidi - Rapid Research Letters* **4**, 371–373 (2010).

[202] Horcas, I., Fernández, R., Gómez-Rodríguez, J. M., Colchero, J., Gómez-Herrero, J. & Baro, A. M. WSXM: A Software for Scanning Probe Microscopy and a Tool for Nanotechnology. *Review of Scientific Instruments* **78**, 013705 (2007).

[203] Cao, L., Garipcan, B., Atchison, J. S., Ni, C., Nabet, B. & Spanier, J. E. Insta-

bility and transport of metal catalyst in the growth of tapered silicon nanowires. *Nano Letters* **6**, 1852–1857 (2006).

[204] Kashchiev, D. Dependence of the Growth Rate of Nanowires on the Nanowire Diameter. *Crystal Growth & Design* **6**, 1154–1156 (2006).

[205] Johansson, J., Svensson, C. P. T., Mårtensson, T., Samuelson, L. & Seifert, W. Mass transport model for semiconductor nanowire growth. *The Journal of Physical Chemistry. B* **109**, 13567–13571 (2005).

[206] Glas, F. Vapor fluxes on the apical droplet during nanowire growth by molecular beam epitaxy. *Physica Status Solidi (b)* **247**, 254–258 (2010).

[207] Kashchiev, D. *Nucleation. Basic Theory with Applications* (Butterworth-Heinemann, Oxford, 2000).

[208] Markov, I. V. *Crystal Growth for Beginners - Fundamentals of Nucleation, Crystal Growth and Epitaxy* (Hackensack, New Jersey, 2003).

[209] Kim, B. J., Tersoff, J., Kodambaka, S., Reuter, M. C., Stach, E. A. & Ross, F. M. Kinetics of Individual Nucleation Events Observed in Nanoscale Vapor-Liquid-Solid Growth. *Science* **322**, 1070–1073 (2008).

[210] Sear, R. P. Nucleation at contact lines where fluid-fluid interfaces meet solid surfaces. *Journal of Physics: Condensed Matter* **19**, 466106 (2007).

[211] Hofmann, S., Sharma, R., Wirth, C. T., Cervantes-Sodi, F., Ducati, C., Kasama, T., Dunin-Borkowski, R. E., Drucker, J., Bennett, P. & Robertson, J. Ledge-flow-controlled catalyst interface dynamics during Si nanowire growth. *Nature materials* **7**, 372–375 (2008).

[212] Tersoff, J., Jesson, D. E. & Tang, W. X. Running Droplets of Gallium from Evaporation of Gallium Arsenide. *Science* **324**, 236–238 (2009).

[213] Mitch, M. G., Chase, S. J., Fortner, J., Yu, R. Q. & Lannin, J. S. Phase transition in ultrathin Bi films. *Physical Review Letters* **67**, 875–878 (1991).

[214] Hardcastle, F. D. & Wachs, I. E. The molecular structure of bismuth oxide by Raman spectroscopy. *Journal of Solid State Chemistry* **97**, 319–331 (1992).

[215] Mailhiot, C. Modulation of internal piezoelectric fields in strained-layer superlattices grown along the [111] orientation. *Journal of Vacuum Science & Technology A* **7**, 609 (1989).

[216] Yoshimoto, M., Itoh, M., Tominaga, Y. & Oe, K. Quantitative estimation of density of Bi-induced localized states in $GaAs_{1-x}Bi_x$ grown by molecular beam epitaxy. *Journal of Crystal Growth* **378**, 73–76 (2013).

[217] Mazur, Y. I., Dorogan, V. G., Schmidbauer, M., Tarasov, G. G., Johnson, S. R., Lu, X., Ware, M. E., Yu, S.-Q., Tiedje, T. & Salamo, G. J. Strong excitation intensity dependence of the photoluminescence line shape in $GaAs_{1-x}Bi_x$ single quantum well samples. *Journal of Applied Physics* **113**, 144308 (2013).

[218] Luo, X. D., Huang, J. S., Xu, Z. Y., Yang, C. L., Liu, J., Ge, W. K., Zhang, Y., Mascarenhas, A., Xin, H. P. & Tu, C. W. Alloy states in dilute $GaAs_{1-x}N_x$ alloys (x<1%). *Applied Physics Letters* **82**, 1697 (2003).

[219] Narukawa, Y., Kawakami, Y., Fujita, S., Fujita, S. & Nakamura, S. Recombination dynamics of localized excitons in In0.20Ga0.80N-In0.05Ga0.95N multiple quantum wells. *Physical Review B* **55**, R1938–R1941 (1997).

[220] Zhongying, X., Jizong, X., Weikun, G., Baozhen, Z., Junying, X. & Yuzhang, L. The excitonic properties and temperature behaviour of the photoluminescence

from GaAs-GaAlAs multiple quantum well structures. *Solid State Communications* **61**, 707–711 (1987).

[221] Martil, I., Redondo, E. & Ojeda, A. Influence of defects on the electrical and optical characteristics of blue light-emitting diodes based on III-V nitrides. *Journal of Applied Physics* **81**, 2442–2444 (1997).

[222] Sammes, N., Tompsett, G., Näfe, H. & Aldinger, F. Bismuth based oxide electrolytes - structure and ionic conductivity. *Journal of the European Ceramic Society* **19**, 1801–1826 (1999).

[223] Fergus, J. W. Electrolytes for solid oxide fuel cells. *Journal of Power Sources* **162**, 30–40 (2006).

[224] Fan, H. J., Werner, P. & Zacharias, M. Semiconductor nanowires: From self-organization to patterned growth. *Small* **2**, 700–717 (2006).

[225] Ismail, R. A. Characteristics of Bismuth trioxide film prepared by rapid thermal oxidation. *e-Journal of Surface Science and Nanotechnology* **4**, 563–565 (2006).

[226] Kumari, L., Lin, J.-H. & Ma, Y.-R. Laser oxidation and wide-band photoluminescence of thermal evaporated bismuth thin films. *Journal of Physics D: Applied Physics* **41**, 025405 (2008).

[227] Yang, B., Mo, M., Hu, H., Li, C., Yang, X., Li, Q. & Qian, Y. A rational self-sacrificing template route β-Bi2O 3 nanotube arrays. *European Journal of Inorganic Chemistry* 1785–1787 (2004).

[228] Gotić, M., Popović, S. & Musić, S. Influence of synthesis procedure on the morphology of bismuth oxide particles. *Materials Letters* **61**, 709–714 (2007).

[229] Salazar-Pérez, A. J., Camacho-López, M. A., Morales-Luckie, R. A. & Sánchez-Mendieta, V. Structural evolution of Bi_2O_3 prepared by thermal oxidation of bismuth nano-particles. *Sociedad Mexicana de Ciencia y Tecnología de Superficies y Materiales* **18**, 4–8 (2005).

[230] Gujar, T., Shinde, V. & Lokhande, C. The influence of oxidation temperature on structural, optical and electrical properties of thermally oxidized bismuth oxide films. *Applied Surface Science* **254**, 4186–4190 (2008).

[231] Huang, C. C., Wen, T. Y. & Fung, K. Z. Orientation-controlled phase transformation of Bi_2O_3 during oxidation of electrodeposited Bi film. *Materials Research Bulletin* **41**, 110–118 (2006).

[232] M. A. Zepeda, M. Picquart & Haro-Poniatowski, E. Laser induced oxidation effects in bismuth thin films. *MRS Proceedings* **1477** (2012).

[233] Trentelman, K. A note on the characterization of bismuth black by Raman microspectroscopy. *Journal of Raman Spectroscopy* **40**, 585–589 (2009).

[234] Wang, W., Liu, M., Yang, Z., Mai, W. & Gong, J. Synthesis and Raman optical properties of single-crystalline Bi nanowires. *Physica E: Low-dimensional Systems and Nanostructures* **44**, 1142–1145 (2012).

[235] Condurache-Bota, S., Rusu, G. I., Tigau, N., Drasozean, R. & Gheorghies, C. Structural and optical characterization of thermally oxidized bismuth films. *Romanian Journal of Chemistry* **54**, 205–211 (2009).

[236] Kumari, L., Lin, J.-H. & Ma, Y.-R. One-dimensional Bi(2)O(3) nanohooks: synthesis, characterization and optical properties. *Journal of Physics: Condensed Matter* **19**, 406204 (2007).

[237] Stevens, K. J., Ingham, B., Toney, M. F., Brown, S. A., Partridge, J., Ayesh, A. & Natali, F. Structure of oxidized bismuth nanoclusters. *Acta Crystallographica Section B: Structural Science* **63**, 569–576 (2007).

[238] Vila, M., Díaz-Guerra, C. & Piqueras, J. Laser irradiation-induced α to δ phase transformation in Bi_2O_3 ceramics and nanowires. *Applied Physics Letters* **101**, 071905 (2012).

[239] Lu, D. Y., Chen, J., Zhou, J., Deng, S. Z., Xu, N. S. & Xu, J. B. Raman spectroscopic study of oxidation and phase transition in $W_{18}O_{49}$ nanowires. *Journal of Raman Spectroscopy* **38**, 176–180 (2007).

[240] Shebanova, O. N. & Lazor, P. Raman study of magnetite (Fe_3O_4): Laser-induced thermal effects and oxidation. *Journal of Raman Spectroscopy* **34**, 845–852 (2003).

[241] Camacho-López, M. A., Escobar-Alarcón, L., Picquart, M., Arroyo, R., Córdoba, G. & Haro-Poniatowski, E. Micro-Raman study of the m-MoO_2 to α-MoO_3 transformation induced by cw-laser irradiation. *Optical Materials* **33**, 480–484 (2011).

[242] Rawson, M. S. R. H. & H. Bismuth trioxide glasses. *J. Soc. Glass Technol.* **41**, 347–349 (1957).

[243] Lannin, J. S., Calleja, J. M. & Cardona, M. Second-order Raman scattering in the group-Vb semimetals: Bi, Sb, and As. *Physical Review B* **12**, 585–593 (1975).

[244] Nánai, L., Vajtai, R. & F. George, T. Laser-induced oxidation of metals: state of the art. *Thin Solid Films* **298**, 160–164 (1997).

[245] Zayed, M. K. & Elsayed-Ali, H. E. Condensation on (002) graphite of liquid bismuth far below its bulk melting point. *Physical Review B* **72**, 205426 (2005).

[246] Yarnell, J. L., Warren, J. L., Wenzel, R. G. & Koenig, S. H. Phonon Dispersion Curves in Bismuth. *IBM Journal of Research and Development* **8**, 234–240 (1964).

[247] Höhne, J., Wenning, U., Schulz, H. & Hüfner, S. Temperature dependence of k=0 optical phonons of Bi and Sb. *Zeitschrift für Physik B Condensed Matter* **27**, 297–302 (1977).

[248] Gualtieri, A. F., Immovilli, S. & Prudenziati, M. Powder X-ray diffraction data for the new polymorphic compound ω-Bi_2O_3. *Powder Diffraction* **12**, 90–92 (1997).

[249] Cornei, N., Tancret, N., Abraham, F. & Mentré, O. New ϵ-Bi_2O_3 metastable polymorph. *Inorganic chemistry* **45**, 4886–4888 (2006).

[250] Atou, T., Faqir, H., Kikuchi, M., Chiba, H. & Syono, Y. A New High-Pressure Phase of Bismuth Oxide. *Materials Research Bulletin* **33**, 289–292 (1998).

[251] In, J., Yoon, I., Seo, K., Park, J., Choo, J., Lee, Y. & Kim, B. Polymorph-tuned synthesis of α- and β-Bi_2O_3 nanowires and determination of their growth direction from polarized raman single nanowire microscopy. *Chemistry - A European Journal* **17**, 1304–1309 (2011).

[252] Denisov, V. N., Ivlev, A. N., Lipin, A. S., Mavrin, B. N. & Orlov, V. G. Raman spectra and lattice dynamics of single-crystal. *Journal of Physics: Condensed Matter* **9**, 4967–4978 (1997).

[253] Lei, Y.-H. & Chen, Z.-X. Density functional study of the stability of various α-Bi_2O_3 surfaces. *The Journal of Chemical Physics* **138**, 054703 (2013).

[254] Smith, E. R. Electrostatic Energy in Ionic Crystals. In *Proceedings of the Royal Society A: Mathematical, Physical and Engineering Sciences*, vol. 375, 475–505 (1981).

[255] Tasker, P. W. The stability of ionic crystal surfaces. *Journal of Physics C: Solid State Physics* **12**, 4977–4984 (1979).

[256] Harwig, H. A. & Weenk, J. W. Phase Relations in Bismuthsesquioxide. *Zeitschrift für anorganische und allgemeine Chemie* **444**, 167–177 (1978).

[257] Glasser, L. Solid-state energetics and electrostatics: Madelung constants and Madelung energies. *Inorganic chemistry* **51**, 2420–2424 (2012).

[258] Nakayama, K., Tanabe, K. & Atwater, H. A. Plasmonic nanoparticle enhanced light absorption in GaAs solar cells. *Applied Physics Letters* **93**, 121904 (2008).

[259] Li, C., Zeng, Z. Q., Fan, D. S., Hirono, Y., Wu, J., Morgan, T. A., Hu, X., Yu, S. Q., Wang, Z. M. & Salamo, G. J. Bismuth nano-droplets for group-V based molecular-beam droplet epitaxy. *Applied Physics Letters* **99**, 243113 (2011).

[260] Lin, X., Huang, F., Wang, W. & Shi, J. Photocatalytic activity of $Bi_{24}Ga_2O_{39}$ for degrading methylene blue. *Scripta Materialia* **56**, 189–192 (2007).

[261] Chine, Z., Fitouri, H., Zaied, I., Rebey, A. & El Jani, B. Photoreflectance and photoluminescence study of annealing effects on GaAsBi layers grown by metalorganic vapor phase epitaxy. *Semiconductor Science and Technology* **25**, 065009 (2010).

[262] Mazzucato, S., Boonpeng, P., Carrère, H., Lagarde, D., Arnoult, A., Lacoste, G., Zhang, T., Balocchi, A., Amand, T., Marie, X. & Fontaine, C. Reduction of defect density by rapid thermal annealing in GaAsBi studied by time-resolved photoluminescence. *Semiconductor Science and Technology* **28**, 022001 (2013).

[263] Grant, P. C., Fan, D., Mosleh, A., Yu, S.-Q., Dorogan, V. G., Hawkridge, M. E., Mazur, Y. I., Benamara, M., Salamo, G. J. & Johnson, S. R. Rapid thermal annealing effect on GaAsBi/GaAs single quantum wells grown by molecular beam epitaxy. *Journal of Vacuum Science & Technology B* **32**, 02C119 (2014).

[264] Moussa, I., Fitouri, H., Chine, Z., Rebey, A. & El Jani, B. Effect of thermal annealing on structural and optical properties of the $GaAs_{0.963}Bi_{0.037}$ alloy. *Semiconductor Science and Technology* **23**, 125034 (2008).

[265] Lemine, O., Alkaoud, A., Avanço Galeti, H., Orsi Gordo, V., Galvão Gobato, Y., Bouzid, H., Hajry, A. & Henini, M. Thermal annealing effects on the optical and structural properties of (100) $GaAs_{1-x}Bi_x$ layers grown by Molecular Beam Epitaxy. *Superlattices and Microstructures* **65**, 48–55 (2014).

[266] White, G. K. Thermal expansion of bismuth at low temperatures. *Journal of Physics C: Solid State Physics* **2**, 575–576 (1969).

[267] Herman, I. P. Peak temperatures from Raman Stokes/anti-Stokes ratios during laser heating by a Gaussian beam. *Journal of Applied Physics* **109**, 016103 (2011).

[268] White, G. K. Thermal expansion of trigonal elements at low temperatures: As, Sb and Bi. *Journal of Physics C: Solid State Physics* **5**, 2731–2745 (1972).

[269] Childs, B. G. The Thermal Expansion of Anisotropic Metals. *Reviews of Modern Physics* **25**, 665–670 (1953).

[270] DeCamp, M. F., Reis, D. A., Bucksbaum, P. H. & Merlin, R. Dynamics and coherent control of high-amplitude optical phonons in bismuth. *Physical Review B* **64**, 092301 (2001).

[271] Renucci, J. B., Richter, W., Cardona, M. & SchÖstherr, E. Resonance raman scattering in group Vb semimetals: As, Sb, and Bi. *Physica Status Solidi (b)* **60**, 299–308 (1973).

[272] Kofstad, P. *High-temperature oxidation of metals* (Wiley, New York, 1966).

[273] Kolmogorov, A. N. On the statistical theory of crystallization of metals. *Izvestiya Rossiiskoi Akademii Nauk. Seriya Matematicheskaya* **1**, 355–359 (1937).

[274] Johnson, M. W. A., R. F. Reaction kinetics in processes of nucleation and growth. *Transactions of the American Institute of Mining and Metallurgical Engineers* **135**, 416–442.

[275] Avrami, M. Kinetics of Phase Change. I General Theory. *The Journal of Chemical Physics* **7**, 1103–1112 (1939).

[276] Yang, J. C., Evan, D. & Tropia, L. From nucleation to coalescence of Cu_2O islands during in situ oxidation of Cu(001). *Applied Physics Letters* **81**, 241 (2002).

[277] Adachi, S. *Physical properties of III-V semiconductor compounds* (John Wiley & Sons, 1992).

[278] Blakemore, J. Semiconducting and other major properties of gallium arsenide. *Journal of Applied Physics* **53**, R123–R181 (1982).

[279] Puech, P., Daran, E., Landa, G., Fontaine, C., Pizani, P. & Carles, R. MBE growth and Raman analysis of [hhk]GaAs/(Si or CaF2) highly strained heterostructures. *Microelectronics Journal* **26**, 789–795 (1995).

[280] Tuck, B. Mechanisms of atomic diffusion in the III-V semiconductors. *Journal of Physics D: Applied Physics* **18**, 557–584 (1985).